UAB
Universitat Autònoma de Barcelona

Phosphate-Based Materials for All-Solid-State Thin-Film Lithium Batteries

Fernanda Monteiro Freitas

ADVERTIMENT. L'accés als continguts d'aquesta tesi queda condicionat a l'acceptació de les condicions d'ús establertes per la següent llicència Creative Commons: https://creativecommons.org/licenses/?lang=ca

ADVERTENCIA. El acceso a los contenidos de esta tesis queda condicionado a la aceptación de las condiciones de uso establecidas por la siguiente licencia Creative Commons: https://creativecommons.org/licenses/?lang=es

WARNING. The access to the contents of this doctoral thesis it is limited to the acceptance of the use conditions set by the following Creative Commons license: https://creativecommons.org/licenses/?lang=en

Universitat Autònoma de Barcelona

PhD Programme in Materials Science

Catalonia Institute for Energy Research

Nanoionics & Fuel Cells

Doctoral Thesis

Phosphate-Based Materials for All-Solid-State Thin-Film Lithium Batteries

Author:

Fernanda Monteiro Freitas

Supervisors:

Prof. Dr. Alberto Tarancón Rubio

Dr. Alejandro Morata Garcia

Dr. Juan Carlos Gonzalez-Rosillo

Barcelona, 2026

The research leading to the results presented in this thesis received funding from the predoctoral grant PRE2020-092652, associated with the research project PID2019-107106RB-C31, funded by the Spanish Ministry of Science and Innovation.

El Prof. Dr. Alberto Tarancón Rubio, Dr. Alejandro Morata Garcia i el Dr. Juan Carlos Gonzalez-Rosillo, investigadors de l'Institut de Recerca en Energia de Catalunya (IREC), **CERTIFIQUEN:**

Que la memòria titulada **Phosphate-Based Materials for All-Solid-State Thin-Film Lithium Batteries** presentada per Fernanda Monteiro Freitas per optar al grau de Doctora en el Programa de Ciència de Materials de la Universitat Autònoma de Barcelona ha estat realitzada sota la seva direcció a l'Institut de Recerca en Energia de Catalunya (IREC).

Barcelona, 11 de juny de 2026







Prof. Alberto Tarancón Dr. Alejandro Morata Dr. Juan Carlos Gonzalez-Rosillo

Acknowledgements

A PhD is an adventure, and one that can truly change a life, not only as an academic diploma, but as a lived experience unlike any other. Returning to research, to the lab, and to "studying", five years after graduating as a chemical engineer and already settled into an office life, felt like the greatest adventure I could have imagined in 2020, in the middle of the pandemic. And despite every bureaucratic hurdle, from the exhausting fight for funding and to the demanding visa process, I arrived in Barcelona on September 6th, 2021. The journey since then has been anything but easy. Even having lived abroad before, the cultural adjustment hit hard a second time. And yet, I never had to face it alone. This thesis exists because of the people who stood by me throughout, immigrants and non-immigrants alike, who believed it was worth it, and who refused to give up on me when I had already lost the energy for the adventure myself. I am profoundly grateful to each of them.

First I thank my supervisors Albert and Alex for the opportunity to join the group and for the countless meetings and discussions about the vast world of thin-film Li batteries. Frequently, we concluded those sessions with "hay que pensar", and that was never a dead end, but a beginning. Equally, I want to thank Juan Carlos, who gave me the warmest welcome to the battery team and motivated me during the moments when exhaustion had made me feel like there was no time left to finish anything. You believed in my results more than I did, and that made all the difference because I finally started to like the data at some point. Your warmth and way of supervising taught me something I will carry with me throughout my career.

My gratitude also goes to Carolina, Natalia, José and Juande colleagues from the Nanoionics group who were already deep in their own research adventures and still found time to answer my endless questions about equipments and lab procedures. Fjorelo, thank you for the company both inside and outside the lab, and for the laughter we shared when we needed it most. Philipp and Paul, together, thank you both for the kind conversations. It was always nice to see your enthusiasm, day after day. Beatrice, Isma, Santi, and Walter for the hallway conversations and coffee breaks that I truly valued.

A special note of thanks goes to my friend Marie (Maritta, pros demais), who had the courage to pursue this opportunity abroad and who has consistently encouraged me to grow and seek out the remarkable possibilities that experiences can offer. Thank you, sister, from EQ and all the way to here, you have been present and helping me change my life for the better. Daiana and Natasha, you became far more than colleagues. Thank you for your support in the lab and mostly for your friendship, always. I would not have made it through the final year without you, and I am so happy to have found you on this side of the ocean.

Marc Nuñez, thank you for all your help and time in the lab, without which I would not have been able to spark a single plasma. The same goes for Francesco, who was always available to share his knowledge. Kevin and Olha, thank you for the kind words that came at just the right moments. Kosova, you gave me your keys and a breath at a moment when I was ready to give up and go back to Brazil. I also wish to thank others at the institute who contributed to this work or to my time there: Karol, Yudania, and María. Martí for the time and support; and Diouldé for her wisdom and counsel.

I am also grateful to the team at EMPA, who made my two-month research stay in Switzerland truly unforgettable, in the lab and beyond.

I cannot close without mentioning my Barcelona family who were part of my happiest moments in these years. E sempre, com todo o meu amor, agradeço a Inha, Dé e Felipe, que nunca me deixaram esquecer que estarão sempre ao meu lado, independentemente de qualquer aventura que eu escolha viver.

Abstract

The increasing demand for compact, safe, and reliable energy storage solutions is driving the development of all-solid-state thin-film batteries for autonomous microsystems, Internet-of-Things devices, wearable electronics, and chip-level power sources. At the microscale, these architectures offer key advantages in safety, miniaturization, thermal stability, and compatibility with on-chip fabrication. The dominant commercial architecture relies on $LiCoO_2$ cathodes, LiPON solid electrolytes, and Li metal anodes. LiPON remains the benchmark thin-film electrolyte owing to its stable interface with Li metal, low electronic conductivity, and reliable performance at micrometer scales. However, its moderate ionic conductivity has motivated the search for crystalline oxide alternatives with higher intrinsic lithium-ion transport. Simultaneously, developing alternative cathode chemistries based on safer and more sustainable materials is increasingly relevant. In this context, $LiFePO_4$ (LFP) is an attractive candidate: widely established in commercial lithium-ion batteries and stationary storage for its structural stability, low cost, and thermal safety, it has not yet found a comparable role in thin-film microbattery architectures.

This thesis focuses on the development of phosphate-based all-solid-state thin-film battery architectures using LFP as the cathode and $Li_{1+x}Al_xTi_{2-x}(PO_4)_3$ (LATP), a NASICON-type oxide, as the solid electrolyte. LATP is attractive for its relatively high ionic conductivity and air stability, but its integration into submicrometric thin films via physical vapor deposition remains largely unexplored. Its crystallization requires high-temperature processing that can compromise the underlying cathode, and it is unstable in direct contact with Li metal due to Ti^{4+} reduction. In dense carbon-free LFP thin films, the absence of conductive additives and liquid-electrolyte infiltration makes electrochemical performance critically dependent on crystallinity, microstructure, and buried interfaces. The central objective is therefore to establish processing routes that enable the fabrication, optimization, and integration of LFP and LATP thin films into functional all-solid-state architectures - a combination with very limited precedent in the thin-film battery literature.

The first part of the work investigates carbon-free LFP thin-film cathodes fabricated by pulsed laser deposition (PLD). The influence of substrate type, deposition temperature, film thickness, and rapid thermal processing (RTP) is analyzed in relation to morphology, phase formation, interfacial chemistry, and electrochemical activity. Crystalline LFP films are obtained at 600 °C under low-pressure Ar, preserving the olivine redox response. However, electrochemical utilization remains limited by the intrinsic transport properties of dense LFP and by interfacial effects at the Pt current collector. Comparison with ITO-based substrates highlights substrate engineering as a key strategy to improve cathode accessibility.

The second part addresses the fabrication of LATP thin films and their compatibility with LFP. Low-temperature PLD followed by RTP is explored to decouple film growth from electrolyte crystallization, limiting thermal exposure while recovering ionic transport. The results reveal a narrow processing window: Ar atmosphere better preserves the LFP cathode during bilayer processing, whereas oxidative conditions or excessive thermal budgets promote secondary-phase formation and structural degradation. Despite these challenges, LFP/LATP bilayers remain

Abstract

electrochemically active under the pre-optimized conditions proposed in this work, demonstrating the feasibility of integrating LATP on top of LFP thin-film cathodes.

The final part evaluates complete thin-film battery architectures. LFP/LiPON/Li cells are first fabricated as a reference platform — replacing the conventional LCO cathode with LFP while retaining LiPON as the established thin-film electrolyte. These devices preserve the LFP redox contribution near 3.45 V vs. Li/Li^+ for cathode thicknesses between 120 and 300 nm. A trade-off between areal capacity and rate capability is observed: thicker films store more charge at low rates, while thinner films show better high-current stability. At 50 ºC, the 200 nm cell reaches approximately 100 mAh g^{-1} at 5 μA cm^{-2} and maintaining around 46 mAh g^{-1} at 98 μA cm^{-2}. Impedance spectroscopy confirms that the main resistive contributions are thermally activated and that LFP transport resistance remains the dominant limitation.

Finally, LFP/LATP/LiPON/Li cells are then investigated as a proof-of-concept architecture, representing one of the first attempts to integrate a NASICON-type oxide electrolyte in thin-film form into a phosphate-based all-solid-state battery. LiPON is retained as a buffer layer to prevent direct LATP–Li contact, while LATP is evaluated at the cathode side. The LFP redox contribution remains partially accessible after LATP integration, but additional plateaus near 2.7–2.8 V reveal the participation of interfacial Fe-containing phosphate secondary phases formed at the LFP/LATP interface. The apparent capacity increase observed upon extending the voltage window therefore reflects the superposition of LFP activity with these additional interfacial redox processes, rather than improved utilization of pristine LFP.

Overall, this thesis demonstrates that phosphate-based thin films can be integrated into functional all-solid-state battery architectures, while highlighting the central role of buried interfaces, cathode microstructure, and thermal processing on device performance. The work bridges three levels of battery development: the commercial maturity of LFP in conventional lithium-ion batteries and stationary storage, the established role of LiPON in thin-film microbatteries, and the emerging potential of LATP as a crystalline oxide electrolyte for all-solid-state thin-film systems. Key limitations are identified related to LFP/current-collector reactions, cathode utilization, LATP crystallization, crack formation, and cathode/electrolyte interfacial reactivity, providing design guidelines for future optimization of thin-film cathodes, solid electrolyte processing, and interface engineering toward safer and more sustainable microbattery technologies.

Resumen

La creciente demanda de soluciones de almacenamiento de energía compactas, seguras y fiables impulsa el desarrollo de baterías de película delgada de estado sólido total para microsistemas autónomos, dispositivos del Internet de las Cosas, electrónica vestible y fuentes de alimentación a nivel de chip. A la microescala, estas arquitecturas ofrecen ventajas clave en seguridad, miniaturización, estabilidad térmica y compatibilidad con la fabricación integrada en chip. La arquitectura comercial dominante se basa en cátodos de $LiCoO_2$, electrólitos sólidos de LiPON y ánodos de litio metálico. El LiPON sigue siendo el electrólito de referencia en baterías de película delgada gracias a su interfaz estable con el litio metálico, su baja conductividad electrónica y su rendimiento fiable a escala micrométrica. Sin embargo, su conductividad iónica moderada ha motivado la búsqueda de alternativas de óxido cristalino con mayor transporte intrínseco de iones litio. Paralelamente, el desarrollo de químicas de cátodo alternativas basadas en materiales más seguros y sostenibles es cada vez más relevante. En este contexto, el $LiFePO_4$ (LFP) es un candidato atractivo: ampliamente consolidado en baterías de iones de litio comerciales y en almacenamiento estacionario por su estabilidad estructural, bajo coste y seguridad térmica, aún no ha encontrado un papel comparable en las arquitecturas de microbaterías de película delgada.

Esta tesis se centra en el desarrollo de arquitecturas de batería de película delgada de estado sólido total basadas en fosfatos, utilizando LFP como cátodo y $Li_{1+x}Al_xTi_{2-x}(PO_4)_3$ (LATP), un óxido de tipo NASICON, como electrólito sólido. El LATP es atractivo por su conductividad iónica relativamente alta y su estabilidad en aire, pero su integración en películas delgadas submicrométricas mediante deposición física en fase vapor sigue siendo poco explorada. Su cristalización requiere procesamiento a alta temperatura que puede comprometer el cátodo subyacente, y es inestable en contacto directo con litio metálico debido a la reducción del Ti^{4+}. En películas delgadas densas de LFP sin carbono, la ausencia de aditivos conductores e infiltración de electrólito líquido hace que el rendimiento electroquímico dependa críticamente de la cristalinidad, la microestructura y las interfaces enterradas. El objetivo central es, por tanto, establecer rutas de procesamiento que permitan la fabricación, optimización e integración de películas delgadas de LFP y LATP en arquitecturas de estado sólido total funcionales, una combinación con muy escasos precedentes en la literatura de baterías de película delgada.

La primera parte del trabajo investiga cátodos de película delgada de LFP sin carbono fabricados por deposición por láser pulsado (PLD). La influencia del tipo de sustrato, la temperatura de deposición, el espesor de la película y el procesamiento térmico rápido (RTP) se analiza en relación con la morfología, la formación de fases, la química interfacial y la actividad electroquímica. Se obtienen películas de LFP cristalinas a 600 ºC en Ar a baja presión, conservando la respuesta redox de la olivina. No obstante, la utilización electroquímica sigue estando limitada por las propiedades de transporte intrínsecas del LFP denso y por efectos interfaciales en el colector de corriente de Pt. La comparación con sustratos basados en ITO destaca la ingeniería de sustratos como estrategia clave para mejorar la accesibilidad del cátodo.

La segunda parte aborda la fabricación de películas delgadas de LATP y su compatibilidad con el LFP. Se explora la deposición por PLD a baja temperatura seguida de RTP para desacoplar

Resumen

el crecimiento de la película de la cristalización del electrólito, limitando la exposición térmica mientras se recupera el transporte iónico. Los resultados revelan una ventana de procesamiento estrecha: la atmósfera de Ar preserva mejor el cátodo de LFP durante el procesamiento de la bicapa, mientras que las condiciones oxidantes o los presupuestos térmicos excesivos favorecen la formación de fases secundarias y la degradación estructural. A pesar de estos desafíos, las bicapas permanecen electroquímicamente activas bajo las condiciones pre-optimizadas propuestas en este trabajo, demostrando la viabilidad de integrar LATP sobre LFP en película delgada.

La parte final evalúa arquitecturas completas de baterías de película delgada. En primer lugar, se fabrican células LFP/LiPON/Li como plataforma de referencia, sustituyendo el cátodo convencional de LCO por LFP y conservando el LiPON como electrólito de película delgada consolidado. Estos dispositivos preservan la contribución redox del LFP cerca de 3.45 V vs. Li/Li^+ para espesores de cátodo entre 120 y 300 nm. Se observa una compensación entre la capacidad areal y la capacidad de régimen: las películas más gruesas almacenan más carga a bajas velocidades, mientras que las más delgadas presentan mejor estabilidad a alta corriente. A 50 ºC, la célula de 200 nm alcanza aproximadamente 100 mAh g^{-1} a 5 μA cm^{-2} y mantiene alrededor de 46 mAh g^{-1} a 98 μA cm^{-2}.

A continuación, se investigan células LFP/LATP/LiPON/Li como arquitectura de prueba de concepto, representando uno de los primeros intentos de integrar un electrólito óxido de tipo NASICON en forma de película delgada en una batería de estado sólido total basada en fosfatos. El LiPON se conserva como capa tampón para evitar el contacto directo LATP-Li, mientras que el LATP se evalúa en el lado del cátodo. La contribución redox del LFP permanece parcialmente accesible tras la integración del LATP, pero mesetas adicionales cerca de 2.7–2.8 V revelan la participación de fases secundarias de fosfato con hierro formadas en la interfaz LFP/LATP. El aparente aumento de capacidad observado al ampliar la ventana de voltaje refleja por tanto la superposición de la actividad del LFP con estos procesos redox interfaciales adicionales, y no una mejor utilización del LFP prístino.

En conjunto, esta tesis demuestra que las películas delgadas basadas en fosfatos pueden integrarse en arquitecturas de batería de estado sólido total funcionales, destacando al mismo tiempo el papel central de las interfaces, la microestructura del cátodo y el procesamiento térmico en el rendimiento del dispositivo. El trabajo conecta tres niveles de desarrollo de baterías: la madurez comercial del LFP en baterías de iones de litio convencionales y almacenamiento estacionario, el papel consolidado del LiPON en microbaterías de película delgada, y el potencial emergente del LATP como electrólito óxido cristalino para sistemas de película delgada de estado sólido total. Se identifican limitaciones clave relacionadas con las reacciones LFP/colector de corriente, la utilización del cátodo, la cristalización del LATP, la formación de grietas y la reactividad interfacial cátodo/electrólito, proporcionando directrices de diseño para la optimización futura de cátodos de película delgada, procesamiento de electrólitos sólidos e ingeniería de interfaces hacia tecnologías de microbatería más seguras y sostenibles.

Resum

La creixent demanda de solucions d'emmagatzematge d'energia compactes, segures i fiables impulsa el desenvolupament de bateríes de pel·lícula prima d'estat sòlid total per a microsistemes autònoms, dispositius de l'Internet de les Coses, electrònica vestible i fonts d'alimentació a nivell de xip. A la microescala, aquestes arquitectures ofereixen avantatges clau en seguretat, miniaturització, estabilitat tèrmica i compatibilitat amb la fabricació integrada en xip. L'arquitectura comercial dominant es basa en càtodes de $LiCoO_2$, electròlits sòlids de LiPON i ànodes de liti metàl·lic. El LiPON continua sent l'electròlit de referència en bateríes de pel·lícula prima gràcies a la seva interfície estable amb el liti metàl·lic, la seva baixa conductivitat electrònica i el seu rendiment fiable a escala micromtètrica. Tot i això, la seva conductivitat iònica moderada ha motivat la recerca d'alternatives d'òxid cristal·lí amb un transport intrínsec d'ions liti més elevat. Paral·lelament, el desenvolupament de químiques de càtode alternatives basades en materials més segurs i sostenibles és cada vegada més rellevant. En aquest context, el $LiFePO_4$ (LFP) és un candidat atractiu: àmpliament consolidat en bateríes d'ions de liti comercials i en emmagatzematge estacionari per la seva estabilitat estructural, baix cost i seguretat tèrmica, encara no ha trobat un paper comparable en les arquitectures de microbateríes de pel·lícula prima.

Aquesta tesi se centra en el desenvolupament d'arquitectures de bateria de pel·lícula prima d'estat sòlid total basades en fosfats, utilitzant LFP com a càtode i $Li_{1+x}Al_xTi_{2-x}(PO_4)_3$ (LATP), un òxid de tipus NASICON, com a electròlit sòlid. El LATP és atractiu per la seva conductivitat iònica relativament alta i la seva estabilitat a l'aire, però la seva integració en pel·lícules primes submicrmètriques mitjançant deposició física en fase vapor continua sent poc explorada. La seva cristal·lització requereix processament a alta temperatura que pot comprometre el càtode subjacent, i és inestable en contacte directe amb liti metàl·lic a causa de la reducció del Ti^{4+}. En pel·lícules primes denses de LFP sense carboni, l'absència d'additius conductors i d'infiltració d'electròlit líquid fa que el rendiment electroquímic depengui críticament de la cristal·linitat, la microestructura i les interfícies soterrades. L'objectiu central és, per tant, establir rutes de processament que permetin la fabricació, l'optimització i la integració de pel·lícules primes de LFP i LATP en arquitectures d'estat sòlid total funcionals, una combinació amb molt escassos precedents en la literatura de bateríes de pel·lícula prima.

La primera part del treball investiga càtodes de pel·lícula prima de LFP sense carboni fabricats per deposició per làser polsat (PLD). La influència del tipus de substrat, la temperatura de deposició, el gruix de la pel·lícula i el processament tèrmic ràpid (RTP) s'analitza en relació amb la morfologia, la formació de fases, la química interfacial i l'activitat electroquímica. S'obtenen pel·lícules de LFP cristal·lines a 600 ºC en Ar a baixa pressió, conservant la resposta redox de l'olivina. No obstant això, la utilització electroquímica continua estant limitada per les propietats de transport intrínseques del LFP dens i pels efectes interfacials al col·lector de corrent de Pt. La comparació amb substrats basats en ITO posa de manifest l'enginyeria de substrats com a estratègia clau per millorar l'accessibilitat del càtode.

La segona part aborda la fabricació de pel·lícules primes de LATP i la seva compatibilitat amb el LFP. S'explora la deposició per PLD a baixa temperatura seguida de RTP per desacoblar el

Resum

creixement de la pel·lícula de la cristal·lització de l'electròlit, limitant l'exposició tèrmica mentre es recupera el transport iònic. Els resultats revelen una finestra de processament estreta: l'atmòsfera d'Ar preserva millor el càtode de LFP durant el processament de la bicapa, mentre que les condicions oxidants o els pressupostos tèrmics excessius afavoreixen la formació de fases secundàries i la degradació estructural. Malgrat aquests reptes, les bicapes romanen electroquímicament actives en les condicions preoptimitzades proposades en aquest treball, demostrant la viabilitat d'integrar LATP sobre LFP en pel·lícula prima.

La part final avalua arquitectures completes de bateria de pel·lícula prima. En primer lloc, es fabriquen cel·les LFP/LiPON/Li com a plataforma de referència, substituint el càtode convencional de LCO per LFP i conservant el LiPON com a electròlit de pel·lícula prima consolidat. Aquests dispositius preserven la contribució redox del LFP prop de 3.45 V vs. Li/Li^+ per a gruixos de càtode entre 120 i 300 nm. S'observa una compensació entre la capacitat areal i la capacitat de règim: les pel·lícules més gruixudes emmagatzemen més càrrega a baixes velocitats, mentre que les més primes presenten millor estabilitat a alta corrent. A 50 ºC, la cel·la de 200 nm assoleix aproximadament 100 mAh g^{-1} a 5 μA cm^{-2} i manté al voltant de 46 mAh g^{-1} a 98 μA cm^{-2}.

A continuació, s'investiguen cel·les LFP/LATP/LiPON/Li com a arquitectura de prova de concepte, representant un dels primers intents d'integrar un electròlit òxid de tipus NASICON en forma de pel·lícula prima en una bateria d'estat sòlid total basada en fosfats. El LiPON es conserva com a capa tampó per evitar el contacte directe LATP–Li, mentre que el LATP s'avalua al costat del càtode. La contribució redox del LFP roman parcialment accessible després de la integració del LATP, però plataformes addicionals prop de 2.7–2.8 V revelen la participació de fases secundàries de fosfat amb ferro formades a la interfície LFP/LATP. L'aparent augment de capacitat observat en ampliar la finestra de voltatge reflecteix, per tant, la superposició de l'activitat del LFP amb aquests processos redox interfacials addicionals, i no una millor utilització del LFP prístin.

En conjunt, aquesta tesi demostra que les pel·lícules primes basades en fosfats es poden integrar en arquitectures de bateria d'estat sòlid total funcionals, posant de manifest alhora el paper central de les interfícies soterrades, la microestructura del càtode i el processament tèrmic en el rendiment del dispositiu. El treball connecta tres nivells de desenvolupament de bateríes: la maduresa comercial del LFP en bateríes d'ions de liti convencionals i emmagatzematge estacionari, el paper consolidat del LiPON en microbateríes de pel·lícula prima, i el potencial emergent del LATP com a electròlit òxid cristal·lí per a sistemes de pel·lícula prima d'estat sòlid total. S'identifiquen limitacions clau relacionades amb les reaccions LFP/col·lector de corrent, la utilització del càtode, la cristal·lització del LATP, la formació d'esquerdes i la reactivitat interfacial càtode/electròlit, proporcionant directrius de disseny per a l'optimització futura de càtodes de pel·lícula prima, processament d'electròlits sòlids i enginyeria d'interfícies cap a tecnologies de microbateria més segures i sostenibles.

Table of contents

1 Introduction 2

1.1 Motivation 2

1.2 Energy storage devices and types 3

1.2.1 Electrostatic vs. Faradaic storage: a fundamental distinction 4

1.2.2 The evolution of battery technology: from aqueous to solid-state 5

1.3 Principles of Li-ion batteries 7

1.3.1 Historical development of lithium-ion batteries 8

1.3.2 Operating principle of a Li-ion cell 9

1.4 All-solid-state batteries (ASSB) 11

1.4.1 Main ASSB configurations 12

1.4.2 State-of-the-Art materials for ASSBs 12

1.5 Materials of Choice in this thesis 18

1.5.1 LATP 18

1.5.2 LFP 20

1.5.3 Compatibility between LFP cathodes and LATP solid electrolytes 24

1.5.4 Relevance to thin-film and microbattery systems 26

1.6 Scope of this thesis 27

2 Experimental methods 30

2.1 Introduction 30

2.2 Thin film fabrication 30

2.2.1 Pulsed laser deposition (PLD) 30

2.2.2 Magnetron sputtering 32

2.2.3 Thermal evaporation 33

2.2.4 Rapid Thermal Processing (RTP) 35

2.3 Structural, morphological, and elemental characterization 36

2.3.1 X-ray diffraction (XRD) 36

2.3.2 Grazing Incidence Wide-Angle X-ray Scattering (GIWAXS) 38

2.3.3 Raman spectroscopy 39
2.3.4 Atomic Force Microscopy (AFM) 40
2.3.5 Scanning electron microscopy (SEM) 40
2.3.6 Transmission electron microscopy (TEM/STEM) 41
2.3.7 Glow Discharge Optical Emission Spectroscopy (GDOES) 42
2.4 Electrochemical characterization 43
2.4.1 Electrochemical Impedance Spectroscopy (EIS) 43
2.4.2 Cyclic Voltammetry (CV) 46
2.4.3 Chronopotentiometry (CP) 48
3 Fabrication and characterization of LFP thin-film cathodes 52
3.1 Scope and motivation of the chapter 52
3.2 Fabrication conditions and samples description 53
3.3 Influence of substrate and its temperature on thin film growth and morphology 55
3.4 Structural and compositional characterization 60
3.4.1 Phase formation and thickness-dependent crystallinity 60
3.4.2 GIWAXS analysis and interfacial phase formation 63
3.4.3 Substrate and deposition temperature effects on as-deposited films 65
3.4.4 Elemental depth distribution 68
3.4.5 Effect of post-annealing by rapid thermal processing (RTP) 71
3.5 Electrochemical characterization 73
3.5.1 Electrochemical response of LFP films deposited on Pt 73
3.5.2 Electrochemical response of LFP films deposited on ITO and influence of deposition temperature 76
3.5.3 Effect of RTP on electrochemical performance 79
3.5.4 Post-cycling analysis of the optimized LFP/ITO electrode 84
3.5.5 Asymmetric constant current charge/discharge cycles 88
3.6 Conclusions 89
4 Fabrication and characterization of $Li_{1+x}Al_xT_{2-x}(PO_4)_3$ thin-film and its compatibility with $LiFePO_4$ cathodes 92

4.1 Scope and motivation of the chapter 92
4.2 Fabrication conditions and samples description 92
4.3 Growth, morphology and structural analysis of as-deposited LATP Films 94
4.4 Phase formation and structural evolution induced by RTP 99
4.5 Morphological Evolution after RTP 104
4.6 Ionic Transport Properties of LATP Thin Films 107
4.7 Integration of LATP with LFP: Bilayer Architecture 112
4.8 Electrochemical Performance of LFP/LATP Bilayer 118
4.9 Conclusions 124
5 All-solid-state thin-film batteries based on phosphates 128
5.1 Scope and motivation of the chapter 128
5.2 Sample description and experimental overview 129
5.3 Electrochemical characterization of LFP/LiPON/Li all-solid-state thin-film batteries 130
5.4 Electrochemical characterization of LFP/LATP/LiPON/Li all-solid-state thin-film battery 140
5.5 Conclusions 144
6 Conclusions of the thesis 148
References 151
Appendix A. Complementary processing and control experiments 168
Appendix B. Alternative substrate strategies 173
Scientific contributions 177

Chapter 1

Introduction

1 Introduction 2

1.1 Motivation 2

1.2 Energy storage devices and types 3

1.2.1 Electrostatic vs. Faradaic storage: a fundamental distinction 4

1.2.2 The evolution of battery technology: from aqueous to solid-state 5

1.3 Principles of Li-ion batteries 7

1.3.1 Historical development of lithium-ion batteries 8

1.3.2 Operating principle of a Li-ion cell 9

1.4 All-solid-state batteries (ASSB) 11

1.4.1 Main ASSB configurations 12

1.4.2 State-of-the-Art materials for ASSBs 12

1.5 Materials of Choice in this thesis 18

1.5.1 LATP 18

1.5.2 LFP 20

1.5.3 Compatibility between LFP cathodes and LATP solid electrolytes 24

1.5.4 Relevance to thin-film and microbattery systems 26

1 Introduction

1.1 Motivation

The relentless pursuit of a more connected, intelligent, and sustainable world is driving an unprecedented demand for advanced energy storage solutions. At the heart of this transformation is the proliferation of the Internet of Things (IoT), which foresees a world with tens of billions of interconnected autonomous devices, from wireless micro-sensors and wearable electronics to implantable medical devices and smart labels.[1,2] These microsystems require compact, safe, and reliable power sources that can be seamlessly integrated, often on-chip, and operate with minimal maintenance over extended periods. Traditional energy storage technologies, particularly those relying on liquid electrolytes, face fundamental limitations in this domain, including constraints on miniaturization, safety hazards related to leakage and flammability, and a restricted operational temperature range, typically between -20 °C and 60 °C.[3–6]

Simultaneously, the ongoing electrification of transport and the imperative for grid-scale storage to accommodate intermittent renewable energy sources necessitate batteries with ever-higher energy density, faster charging rates, and improved safety profiles.[7] While conventional lithium-ion batteries (LIBs) have been instrumental in the portable electronics revolution and the initial wave of electric vehicles, their reliance on flammable organic liquid electrolytes presents an inherent safety risk, particularly as energy densities increase. Furthermore, the quest for higher energy density is pushing the operational voltage limits of cathodes, a goal often thwarted by the limited electrochemical stability window of conventional liquid electrolytes.[8]

All-solid-state batteries (ASSBs) have emerged as a leading contender to address these converging challenges. By replacing the volatile and reactive liquid electrolyte with a solid-state electrolyte (SSE), ASSBs offer a paradigm shift in battery technology.[9] They inherently promise enhanced safety by eliminating the risk of leakage and thermal runaway. The solid electrolyte acts as both an ionic conductor and a robust physical separator, which, if sufficiently strong, can suppress the growth of metallic lithium dendrites, which is the primary cause of internal short circuits and failure in high-energy-density cells employing lithium metal anodes.[10] Moreover, many SSEs possess a much wider electrochemical stability window (ESW) than their liquid counterparts, enabling the use of high-voltage cathode materials (>4.5 V vs. Li/Li^+) to achieve higher energy densities and faster charging rates.[11]

Within the broad landscape of ASSBs, thin-film batteries (TFBs) represent a specialized and highly promising architecture, particularly well-suited for powering the aforementioned IoT microsystems.[12] In a TFB, all active components (the cathode, solid electrolyte, and anode) are deposited as dense, micrometer- or sub-micrometer-thick layers using vacuum-based deposition techniques such as pulsed laser deposition (PLD) or sputtering. This planar, thin-film geometry minimizes the ionic transport distances, effectively mitigating the impact of the moderate ionic conductivity often observed in SSEs and enabling high power densities and excellent rate

capability.[13] The ability to fabricate these devices directly onto silicon wafers or flexible substrates opens up new possibilities for monolithic integration with microelectronics, energy harvesting systems, and other functional components.

The successful realization of phosphate-based ASSTFBs hinges on overcoming critical materials science and engineering challenges. For the cathode, olivine-structured lithium iron phosphate ($LiFePO_4$, LFP) stands out for its exceptional thermal and chemical stability, low cost, and environmental benignity, making it a safe and sustainable choice.[14,15] However, its intrinsically low ionic conductivity (~10^{-14} to 10^{-12} cm^2 s^{-1} for Li^+ diffusivity)[16] and electronic conductivities (~10^{-10} to 10^{-9} S cm^{-1}), typically mitigated by carbon coating in bulk electrodes, become a critical limiting factor in dense thin-film architectures where conductive additives are absent.[17] For the electrolyte, NASICON-type $Li_{1.3}Al_{0.3}Ti_{1.7}(PO_4)_3$ (LATP) is a compelling candidate due to its high bulk ionic conductivity (up to 10^{-3} S cm^{-1}) and remarkable stability in air and moisture, a significant advantage over other leading SSEs like sulfides.[18] The prior work in our group by Siller (2020) established the feasibility of depositing high-quality LATP films by PLD[19], but the high temperatures (>700 ºC) required to crystallize the material and achieve optimal ionic conductivity present a major compatibility issue with temperature-sensitive cathode materials like LFP.

This thesis is motivated by the need to overcome this specific integration challenge. It aims to develop a new fabrication strategy that decouples the growth of the LATP electrolyte from its high-temperature crystallization, thereby enabling the creation of a functional LFP/LATP bilayer. By combining low-temperature PLD with rapid thermal processing (RTP), this work seeks to establish a pathway for realizing all-phosphate-based, all-solid-state thin-film batteries that are safe, cost-effective, and high-performing.

1.2 Energy storage devices and types

The selection of an appropriate energy storage system is inherently application-driven and is primarily dictated by the balance between specific energy (Wh kg^{-1}) and specific power (W kg^{-1}). This trade-off is commonly represented through a Ragone plot, which provides a comprehensive framework for comparing different energy storage technologies.[20] Electrochemical energy storage systems can be broadly classified according to their charge storage mechanisms, which ultimately define both their performance characteristics and their position within this diagram.[21–23]

Within this context, batteries, particularly lithium-based systems, stand out due to their high specific energy, enabling long operation times and making them the preferred choice for applications requiring sustained energy delivery. As shown in **Figure 1.1**, batteries are located in the high-energy region of the Ragone plot, although typically at lower specific power compared to capacitor-based systems. This reflects the fact that their operation relies on bulk electrochemical processes, which inherently limit the rate of charge and discharge.

Despite these limitations, continuous advances in materials design and device engineering have significantly improved the power capability of modern batteries, narrowing the gap between energy- and power-oriented storage systems. In particular, LIBs have achieved a favorable balance

between energy density and rate performance, which explains their widespread adoption in portable electronics, electric vehicles, and stationary storage applications.

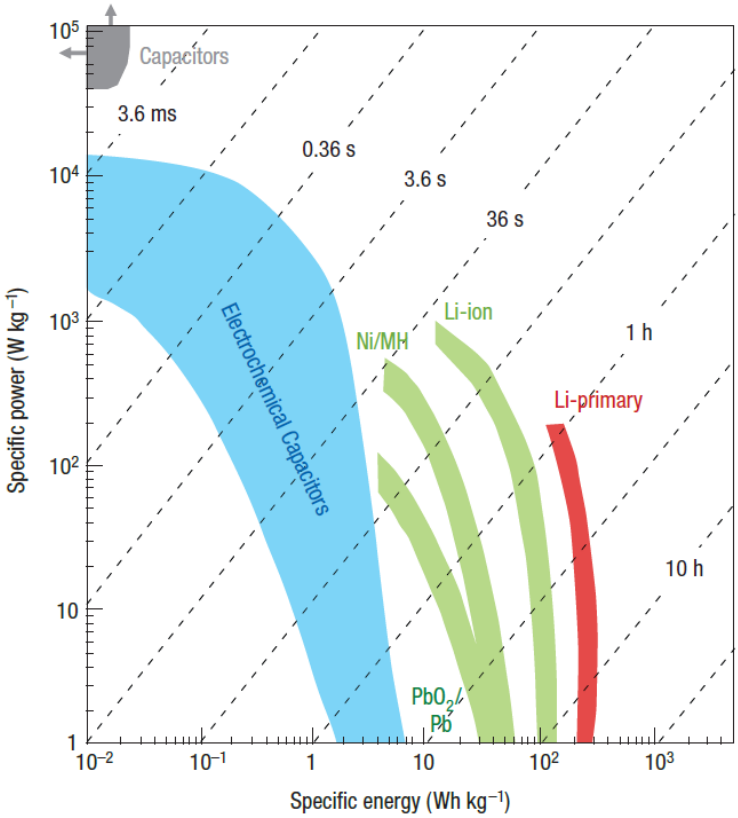


Figure 1.1 - Ragone plot showing the relationship between specific power and specific energy for electrical energy storage technologies, highlighting the position of batteries in the high-energy region. Specific energy represents the total stored energy, while specific power reflects the rate of energy delivery.[22]

In addition, the diagonal lines in the Ragone plot represent characteristic discharge times, defined by the ratio between specific energy and specific power. These lines provide a useful indication of the operational timescale of a device. In the case of batteries, their position corresponds to discharge times ranging from minutes to hours, reinforcing their role as energy-dominant systems rather than power-dominant ones.

Overall, the Ragone representation highlights the intrinsic strengths of batteries in terms of energy storage, while also emphasizing the ongoing need to improve their rate capability for high-power applications.

1.2.1 Electrostatic vs. Faradaic storage: a fundamental distinction

At the most basic level, devices are categorized by whether charge is stored at the surface (electrostatic) or within the bulk (Faradaic) of the electrode material. Supercapacitors, also known as electrochemical capacitors, are the prime example of electrostatic storage. They store energy primarily through non-Faradaic processes, i.e., the physical separation of charge at the electrode-

electrolyte interface, forming an electrical double layer.[22] This surface-confined mechanism allows for extremely fast charge and discharge rates, translating to exceptionally high specific power (up to 15 kW kg^{-1}) and remarkable cycle lives (exceeding 500,000 cycles). However, their energy density is inherently low, typically around 5-10 Wh kg^{-1}. Pseudocapacitors, a related category, achieve slightly higher energy densities through fast, reversible Faradaic redox reactions at the electrode surface, but often at some expense to cycle life. Consequently, supercapacitors are ideally suited for applications demanding short, high-power bursts, such as regenerative braking or grid frequency regulation, rather than long-term energy storage.

In contrast, batteries store energy through Faradaic redox reactions that occur within the bulk volume of the electrode materials.[24] This bulk storage mechanism enables significantly higher energy densities compared to supercapacitors, ranging from ~50 Wh kg^{-1} for lead-acid to over 250 Wh kg^{-1} for advanced Li-ion chemistries. The trade-off, however, is that the kinetics of these bulk reactions and the associated mass transport limitations (e.g., solid-state diffusion of Li^+) restrict their power capability and cycle life. ASSTFBs are strategically positioned to bridge this gap. By reducing the electrode thickness to the micrometer scale, the diffusion path for ions is drastically shortened, mitigating transport limitations and enabling higher power densities while retaining the high energy density characteristic of batteries.[11] This makes them particularly attractive for powering autonomous microsystems that require both a compact energy source and the ability to handle pulsed power demands from wireless communication.

1.2.2 The evolution of battery technology: from aqueous to solid-state

Beyond the fundamental charge storage mechanism, the evolution of battery technology over the past two centuries can be viewed as a continuous effort to improve energy density, safety, and durability, with the nature of the electrolyte playing a central and defining role. This progression is summarized in **Figure 1.2**.

The earliest rechargeable batteries were based on aqueous electrolytes. The lead-acid battery, invented by Gaston Planté in 1859, remains the oldest and one of the most widely used rechargeable battery systems to this day. [25] Its robustness, low cost, and well-established recycling infrastructure make it a continued choice for automotive starter batteries and backup power systems, despite its low specific energy (~30-50 Wh kg^{-1}). The subsequent development of alkaline electrolytes enabled nickel-based systems in the 20th century, including nickel-cadmium (Ni-Cd) and, later, the more environmentally friendly nickel–metal hydride (Ni–MH) batteries. These offered significant improvements in energy density and cycle life, dominating the portable electronics market before the advent of lithium-ion.[26]

A paradigm shift occurred with the commercialization of the lithium-ion battery (LIB) by Sony in 1991, built upon foundational discoveries by John B. Goodenough, Stanley Whittingham, and Akira Yoshino, works recognized with the Nobel Prize in Chemistry in 2019.[27] By utilizing non-aqueous, organic liquid electrolytes with a wide electrochemical stability window, LIBs enabled the use of electrode materials with much higher redox potentials. This resulted in a dramatic leap in

energy density (>200 Wh kg^{-1}) and specific energy, coupled with long cycle life and low self-discharge, cementing their position as the dominant power source for portable electronics and, increasingly, electric vehicles.[28]

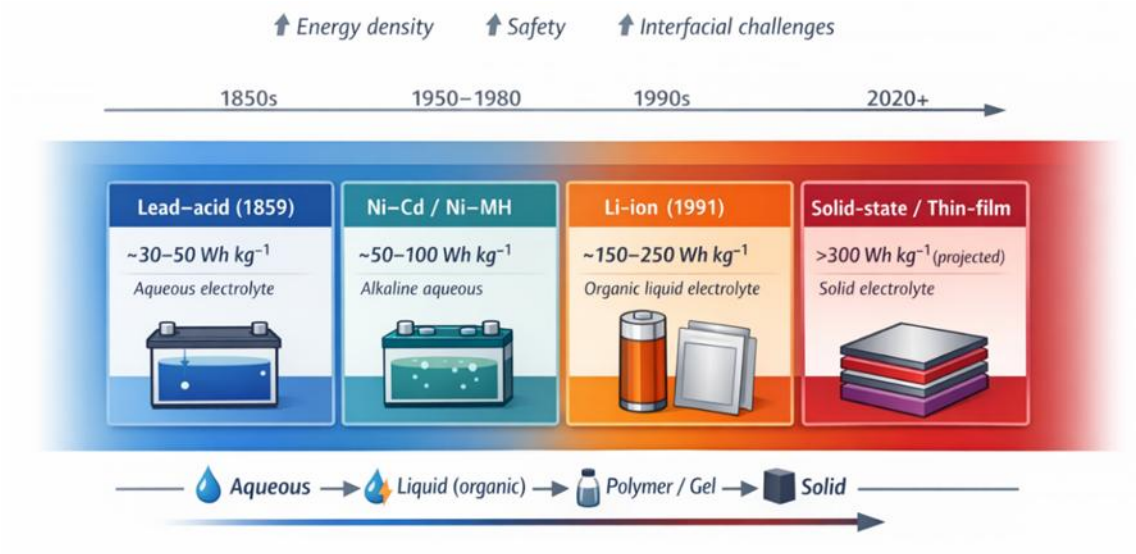


Figure 1.2 - Schematic timeline illustrating the evolution of rechargeable battery technologies as a function of electrolyte type and energy density. Approximate ranges of specific energy are indicated for each technology, together with the corresponding electrolyte nature.

Despite their immense success, the intrinsic properties of liquid electrolyte-based LIBs present fundamental limitations. The organic solvents are flammable and volatile, creating safety hazards related to leakage and thermal runaway. Furthermore, the electrolyte's limited electrochemical stability window restricts the use of high-voltage cathodes (>4.5 V vs. Li/Li^+) that are necessary to achieve higher energy densities, and its reactivity promotes the formation of unstable solid-electrolyte interphases (SEI) that can foster lithium dendrite growth.[29]

These safety and stability concerns have driven the exploration of alternative electrolyte systems, leading to the development of polymer and gel electrolytes. Solid polymer electrolytes (SPEs), typically based on polyethylene oxide (PEO), replace the liquid with a solid ion-conducting polymer matrix, offering improved safety and mechanical flexibility.[7] Gel polymer electrolytes (GPEs), which incorporate a liquid phase within the polymer matrix, represent an intermediate step, achieving higher ionic conductivity than pure SPEs while offering better safety than fully liquid systems. However, both approaches generally suffer from lower ionic conductivity at room temperature compared to their liquid counterparts.[30]

The logical culmination of this trajectory is the all-solid-state battery (ASSB) , in which the electrolyte is an entirely solid, inorganic ceramic or glass. As illustrated in **Figure 1.3**, this transition eliminates the flammable liquid component entirely, promising a step-change in intrinsic safety. Many SSEs possess a much wider electrochemical stability window compared to organic liquid ones, enabling the use of both high-voltage cathodes (>4.5 V vs. Li/Li^+) and lithium metal anodes (3860

mAh g^{-1}), which represents a pathway toward cell-level energy densities projected to exceed 500 Wh kg^{-1}, compared to the ~250-300 Wh kg^{-1} currently achieved by state-of-the-art LIBs.[31] Furthermore, a mechanically robust SSE could act as a physical barrier to suppress the penetration of lithium dendrites, a major failure mechanism in liquid-based systems.[32] As a result, ASSBs are not merely an incremental improvement but are widely regarded as a key next-generation technology for overcoming the intrinsic limitations of conventional LIBs.

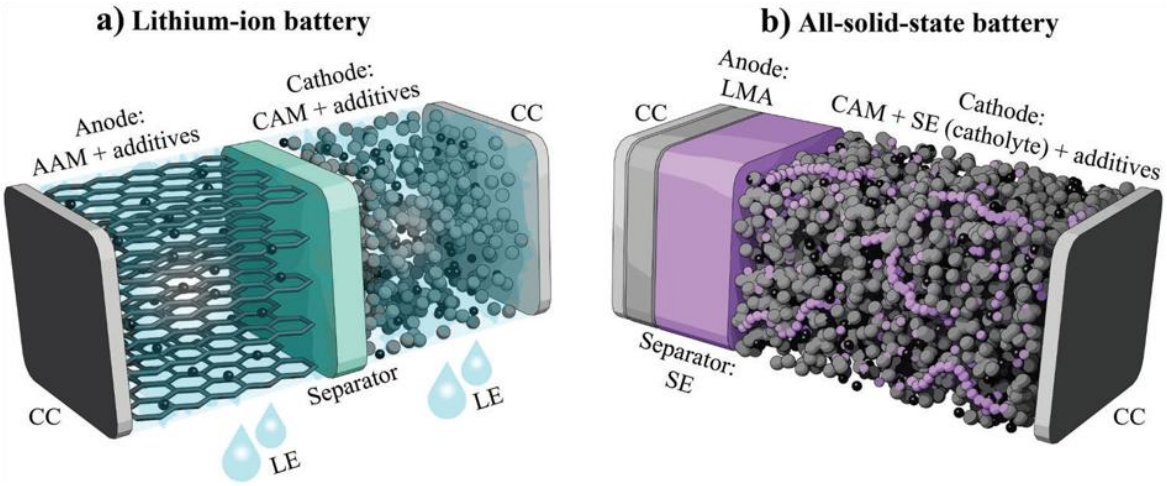


Figure 1.3 - Schematic comparison between (a) state-of-the-art conventional rechargeable lithium-ion battery architectures and (b) next-generation all-solid-state battery design. (CC, current collector; LE, liquid electrolyte; SE, solid electrolyte; AAM, anode active material; CAM, cathode active material; LMA, lithium metal anode). Reproduced from Thomas Schmaltz *et al.* (2023).[31]

This evolution from liquid to solid electrolytes, however, introduces a new set of challenges. The replacement of a compliant liquid with a rigid solid fundamentally changes the nature of the interfaces, leading to issues of high interfacial resistance, poor mechanical contact, and chemo/mechanical degradation upon cycling. These challenges are particularly acute in thin-film architectures, where the management of strain and the quality of interfaces are paramount. It is within this specific context, the drive for safe, high-energy-density storage and the challenges of solid-solid interfaces, that this thesis is situated, focusing on the development and integration of phosphate-based materials for all-solid-state thin-film batteries.

1.3 Principles of Li-ion batteries

A rechargeable battery is an electrochemical device that stores electrical energy in the form of chemical energy and converts it back into electricity when required. In its most fundamental configuration, a battery cell consists of two electrodes with different electrochemical potentials: a negative electrode (anode) and a positive electrode (cathode) separated by an electrolyte. The electrolyte provides ionic transport between both electrodes while blocking electronic conduction, thereby forcing electrons to travel through the external circuit and generate useful electrical work. In secondary (rechargeable) batteries, these electrochemical reactions must be reversible upon the application of an external current and voltage.

The practical value of any rechargeable battery technology is determined by a combination of key metrics, including safety, energy density, power capability, cycle life, shelf life, efficiency, and manufacturing cost. Among the many battery chemistries developed to date, LIBs have become dominant because they offer a highly favorable balance between gravimetric energy density, operating voltage, durability, and efficiency. Their success is closely linked to the use of non-aqueous organic electrolytes, whose electrochemical stability window is significantly wider than that of aqueous electrolytes, thereby enabling higher cell voltages and increased specific energy.

1.3.1 Historical development of lithium-ion batteries

The defining concept of modern LIBs is reversible intercalation chemistry. In this mechanism, lithium ions are inserted into and extracted from crystallographic host structures without complete disruption of the framework. Both cathode and anode materials therefore act as insertion compounds capable of reversibly accommodating Li^+ during cycling.[24,33]

This behavior differs fundamentally from metallic lithium batteries, where energy storage relies on lithium plating and stripping. Although lithium metal offers an exceptionally high theoretical capacity, repeated deposition frequently leads to dendritic growth, internal short circuits, and poor cycle stability. Intercalation electrodes largely overcome these limitations by storing lithium within structurally stable solids that undergo only moderate lattice changes during operation.

The quantity of charge that can be reversibly transferred depends on the compositional range over which insertion remains stable, as well as on kinetic factors such as ionic diffusion within the solid, charge transfer across interfaces, and electronic transport through the electrode network. Consequently, the practical capacity of real electrodes is typically lower than the theoretical value predicted from stoichiometry alone.

The emergence of LIB technology resulted from a sequence of breakthroughs that collectively transformed electrochemical energy storage and were recognized by the 2019 Nobel Prize in Chemistry. A first milestone was achieved by M. Stanley Whittingham in the 1970s, who demonstrated that layered titanium disulfide (TiS_2) could reversibly host lithium ions. Combined with a lithium metal anode, this system produced voltages above 2 V and provided the first convincing demonstration of a rechargeable lithium battery based on intercalation chemistry.[33]

A second decisive advance was reported by John B. Goodenough and co-workers in 1980 through the discovery of layered lithium cobalt oxide ($LiCoO_2$) as a cathode material.[34] Because transition-metal oxides operate at higher redox potentials than sulfides, $LiCoO_2$ enabled cell voltages approaching 4 V versus Li/Li^+, resulting in a substantial increase in energy density. This material became the foundation of early commercial LIB technology and remains widely relevant today.

The final enabling innovation was introduced by Akira Yoshino,[35] who replaced metallic lithium with a carbonaceous insertion anode. This "rocking-chair" concept, in which lithium ions

shuttle reversibly between two host electrodes, eliminated the major safety hazards associated with lithium metal and led to the first commercial LIB launched by Sony in 1991.

1.3.2 Operating principle of a Li-ion cell

The operation of a lithium-ion battery is based on the reversible transfer of lithium between two electrodes with different lithium chemical potentials. In a typical cell, lithium is stored in the negative electrode (anode) in a relatively weakly bonded state, while the positive electrode (cathode) provides a thermodynamically more stable host environment. This difference in lithium stabilization constitutes the fundamental driving force for spontaneous discharge.

As illustrated in **Figure 1.4a**, during discharge lithium atoms are effectively transferred from the anode to the cathode through two coupled transport processes: lithium ions (Li^+) migrate through the electrolyte, whereas electrons flow through the external circuit, where they provide electrical power to the connected device. To maintain electroneutrality, Li^+ insertion into the cathode is accompanied by electron uptake and reduction of a redox-active species in the host structure. During charging, the application of an external voltage higher than the equilibrium cell potential reverses these fluxes, forcing lithium ions and electrons back to the negative electrode, where energy is stored again in chemical form.

A representative example is shown in **Figure 1.4b** for a cell employing a lithiated graphite anode and an iron-phosphate cathode. In this system, lithium is relatively weakly bonded within graphite and is therefore released during discharge as Li^+ and electrons. The Li^+ ions migrate through the electrolyte, commonly $LiPF_6$ dissolved in carbonate-based organic solvents, toward the $FePO_4$ cathode, while electrons travel through the external circuit. Upon reaching the cathode, lithium ions are inserted into one-dimensional channels of the $FePO_4$ framework, forming $LiFePO_4$, while electrons are accepted primarily by Fe^{3+} centers, reducing them to Fe^{2+} and preserving charge neutrality.

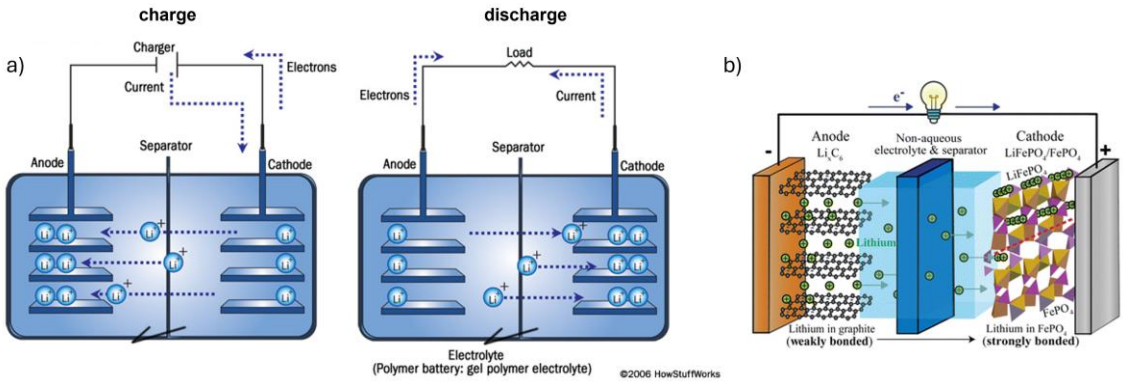


Figure 1.4 - Operating principle of a conventional lithium-ion battery. (a) Schematic representation of the charge and discharge processes, showing the migration of Li^+ ions through the electrolyte/separator and the flow of electrons through the external circuit. (b) Representative example of a graphite/$LiFePO_4$ cell, in which Li^+ ions are released from lithiated graphite during discharge and migrate through the non-

aqueous electrolyte and separator toward the $FePO_4$ cathode, where they are inserted into the olivine framework to form $LiFePO_4$.

For $LiFePO_4$-based electrodes, lithiation commonly proceeds through the coexistence of $LiFePO_4$ and $FePO_4$ phases separated by a moving phase boundary. This interface may be atomically sharp or extend over several nanometers depending on particle size, defect chemistry, and operating conditions. Such two-phase behavior is directly associated with the characteristic flat voltage plateau of $LiFePO_4$ during cycling.

The electrochemical processes described above are macroscopically observed through the cell voltage, which reflects the energy difference between lithium stored in the two electrodes. In practical terms, voltage represents the electrical work obtainable per unit charge when lithium is transferred from the anode to the cathode. Therefore, electrode materials that stabilize lithium very differently generally produce higher operating voltages and higher attainable energy density.

At open-circuit equilibrium, when no external current flows, the cell potential (E_{cell}) is determined by the difference in lithium chemical potential (μ_{Li}) between both electrodes and can be expressed as:

$$E_{cell} = \frac{\mu_{Li}^{anode} - \mu_{Li}^{cathode}}{F} \tag{1.1}$$

where F is the Faraday constant. This relation highlights that the battery voltage is fundamentally linked to the thermodynamic tendency of lithium to move from a higher-energy state in the negative electrode toward a lower-energy state in the positive electrode.[36]

During real operation, the measured voltage differs from the equilibrium voltage because current flow requires the system to overcome kinetic and transport limitations. These losses include ohmic resistance in the electrolyte, current collectors and interfaces, charge-transfer overpotentials at the electrode/electrolyte interfaces, and concentration gradients associated with ion transport in the electrolyte and solid-state diffusion within the electrode. As a result, the discharge voltage under load is lower than the equilibrium voltage, whereas the charging voltage must be higher. Minimizing these polarization losses is therefore essential for improving power capability, energy efficiency and capacity utilization.

The amount of charge stored or released by an electrode is governed by Faraday's law. For an electrochemical reaction involving n electrons per formula unit, the total charge is given by:

$$Q = \int_0^t I(t)\, dt = nFN \tag{1.2}$$

where Q is the charge, I is the current, t is time, n is the number of electrons transferred per formula unit, and N is the number of moles of electrochemically reacted species. The theoretical specific capacity of an electrode material is therefore:

$$C_{th} = \frac{nF}{3.6M} \tag{1.3}$$

where C_{th} is expressed in mAh g^{-1}, M is the molar mass of the active material in g mol^{-1}, and the factor 3.6 arises from the conversion between coulombs and mAh, since 1 mAh corresponds to 3.6 C.[36]

Despite their commercial success, conventional LIBs remain constrained by the use of flammable organic liquid electrolytes, which may decompose at highly reducing or oxidizing electrode potentials. This decomposition commonly forms passivation layers, particularly the solid electrolyte interphase (SEI) on graphite anodes. Although the SEI is electronically insulating and Li^+ conductive, its formation consumes cyclable lithium and increases interfacial resistance, contributing to capacity fade and reduced power capability.

Furthermore, the limited electrochemical stability window of liquid electrolytes restricts the use of high-voltage cathodes and lithium metal anodes, both of which are attractive routes toward higher energy density. These intrinsic limitations have strongly motivated the development of alternative electrolyte systems, especially ASSBs based on solid ion-conducting electrolytes, which offer prospects for improved safety, wider stability windows, and enhanced compatibility with lithium metal.

1.4 All-solid-state batteries (ASSB)

ASSBs replace the flammable liquid electrolyte used in conventional LIBs with a solid ion-conducting phase, typically ceramic, glassy, or polymeric in nature. Although conceptually straightforward, this substitution profoundly modifies the electrochemical cell architecture, ion transport pathways, interface chemistry, and mechanical behavior of the system. As a result, ASSBs are widely regarded as one of the most promising next-generation battery technologies for applications requiring enhanced safety, higher energy density, and longer service life.[3,31]

The principal motivation for ASSBs arises from the intrinsic limitations of liquid-electrolyte lithium-ion batteries. Conventional carbonate-based electrolytes are flammable, volatile, and thermodynamically unstable outside a relatively narrow electrochemical window. Under abusive conditions, overcharge, or internal short-circuit events, these electrolytes may trigger thermal runaway and catastrophic failure. By contrast, replacing the liquid phase with a non-flammable solid electrolyte offers an inherently safer platform with reduced leakage risk and improved thermal tolerance.[5]

Beyond safety, solid electrolytes may enable the practical use of lithium metal as the negative electrode. Metallic lithium possesses an exceptionally high theoretical specific capacity of 3,860 mAh g^{-1}, approximately ten times higher than that of graphite anodes, 372 mAh g^{-1} for LiC_6, together with the lowest electrochemical potential among practical negative electrode materials. These properties make lithium metal highly attractive for increasing cell-level energy density, although the practical gain depends strongly on cathode loading, electrolyte excess, lithium thickness, and cell

design.[10,11,29] In principle, a mechanically robust solid electrolyte can also act as a physical barrier against dendritic lithium penetration, although this issue remains far from fully resolved in practical systems.

At the same time, the replacement of a liquid by a rigid solid introduces new scientific and engineering challenges. Liquid electrolytes readily infiltrate porous electrodes and establish intimate electrode/electrolyte contact, whereas solid electrolytes require direct solid-solid interfaces for ion transfer. Imperfect contact, volume changes during cycling, interfacial reactions, and residual stresses often lead to increased impedance and progressive degradation. Consequently, interface engineering has become one of the central research themes in modern ASSBs.[10,11]

1.4.1 Main ASSB configurations

ASSBs can be implemented through different cell architectures depending on the targeted application. The most industrially pursued approach is the bulk composite configuration, in which a particulate cathode active material is mixed with solid electrolyte particles and conductive additives to form a percolating composite electrode. This strategy seeks to reproduce the high areal capacity of conventional slurry-cast electrodes while replacing the liquid phase with a solid conductor. It is currently the dominant route for electric vehicle and large-format cell development.[31]

A second important configuration is the thin-film battery, where cathode, electrolyte, and anode are sequentially deposited as dense micrometer- or sub-micrometer-thick layers by vacuum techniques such as sputtering or pulsed laser deposition. In this planar geometry, ionic diffusion distances are drastically reduced, and interfaces can be engineered with high precision. Thin-film ASSBs typically exhibit excellent cyclability, low self-discharge, and high-rate capability, making them especially attractive for microelectronics, sensors, medical implants, and autonomous microsystems.[2]

More advanced concepts include three-dimensional microbatteries, in which structured substrates increase internal surface area while preserving short transport lengths, and anode-free architectures, where lithium is plated in situ from the cathode inventory during first charge. These approaches aim to further increase volumetric energy density, although fabrication complexity and interface stability remain important barriers.[12]

1.4.2 State-of-the-Art materials for ASSBs

ASSBs represent a major paradigm shift in electrochemical energy storage by replacing the flammable liquid electrolyte of conventional LIBs with a solid ion-conducting phase. This apparently simple substitution has far-reaching consequences for battery design, since the solid electrolyte must simultaneously transport Li^+ ions, electronically isolate the electrodes, and physically separate the anode from the cathode. As a result, the performance of ASSBs is governed not only by the intrinsic properties of the cathode, anode, and electrolyte, but also by their mutual chemical, electrochemical, and mechanical compatibility across solid–solid interfaces. ASSB

development is therefore fundamentally a materials-integration challenge rather than merely a materials-discovery problem.[9,37–39]

Compared with conventional LIBs, ASSBs are expected to offer enhanced safety, wider operating windows, and potentially higher energy density through the use of lithium metal anodes and high-voltage cathodes. However, these advantages can only be realized when ionic conductivity, interfacial impedance, electronic leakage, and processing constraints are simultaneously optimized. For this reason, significant research effort has focused on the transport properties of the constituent materials, particularly their ionic and electronic conductivities, and on the engineering of stable buried interfaces.

The constituent materials of ASSBs can be broadly divided into three categories: active anode materials (AAM), solid electrolytes (SE) and cathode active materials (CAM). Within each category, multiple material families coexist, each offering different balances of ionic conductivity, electrochemical stability, mechanical compliance, density, abundance, and manufacturability. No single chemistry presently satisfies all requirements simultaneously, which explains why multiple technological routes are being pursued in parallel for bulk cells, thin-film devices, and microbattery architectures. In the following sections, these components are first discussed separately. The final part of the section then focuses on the materials selected in this thesis and on the specific compatibility issues of the LFP/LATP phosphate-based system.

1.4.2.1 Anode materials

Graphite remains the state-of-the-art negative electrode in commercial LIBs. Its success arises from its low operating potential, typically around 0.1 V vs. Li^+/Li in the fully lithiated state, good reversibility, moderate volume change during cycling, mature processing, and low cost. Graphite stores lithium through an intercalation mechanism, forming LiC_6 at full lithiation, which corresponds to a theoretical specific capacity of 372 mAh g^{-1}. Although this capacity is modest compared with metallic or alloy-type anodes, graphite provides an excellent compromise between energy density, safety, cyclability, and manufacturability.[24]

Lithium metal represents one of the most favoured choices for negative electrode in next-generation Li batteries. It can meet the requirements for high-energy ASSBs because of its exceptionally high theoretical capacity (3860 mAh g^{-1}) and low electrochemical potential. Its electronic conductivity is high (~10^5 S cm^{-1}), and transport limitations in the bulk metal are generally negligible. The major challenges instead arise from unstable plating/stripping, void formation, nonuniform current distribution, filament growth, and interphase evolution at solid interfaces.[40]

Alloy anodes such as Si, Sn, Al, and In offer significantly higher capacities than graphite. Silicon, for example, provides a theoretical capacity of ~3579 mAh g^{-1}, with lithium diffusivity in amorphous Si typically around ~10^{-14} to 10^{-12} cm^2 s^{-1}. It is considered the leading candidate to replace graphite in conventional LIBs.[41] However, these materials undergo large volume changes during cycling, which can induce fracture, voiding, and contact loss at solid electrolyte interfaces. Therefore, while alloy-type anodes are attractive from an energy-density perspective, their practical

implementation in ASSBs requires careful control of mechanical deformation and interfacial stability.[42]

1.4.2.2 Solid electrolyte families

The solid electrolyte is the defining component of ASSBs. Ideally, it should combine high lithium-ion conductivity (preferably $\geq 10^{-3}$ S cm^{-1} at room temperature), negligible electronic conductivity ($<10^{-10}$-10^{-12} S cm^{-1}), broad electrochemical stability, sufficient mechanical integrity, and scalable processing. In practice, these requirements are difficult to satisfy simultaneously, justifying the challenges faced in current researches.

In addition to ionic conductivity, the electrochemical stability window is a key parameter for selecting a solid electrolyte, since it defines the potential range within which the material is thermodynamically stable against reduction and oxidation. **Figure 1.5** compares the calculated stability windows of several representative inorganic solid electrolytes and related binary compounds versus Li metal. This comparison highlights the wide diversity of electrochemical stability among oxide, phosphate, sulfide, halide, hydride, and nitride-based materials. It also shows that high ionic conductivity alone is not sufficient for practical ASSBs, because many fast Li-ion conductors are not thermodynamically stable at the low potentials imposed by lithium metal or at the high potentials required by high-voltage cathodes. Therefore, apparent compatibility often relies on the formation of passivating interphases, kinetic stabilization, or the use of protective buffer layers.

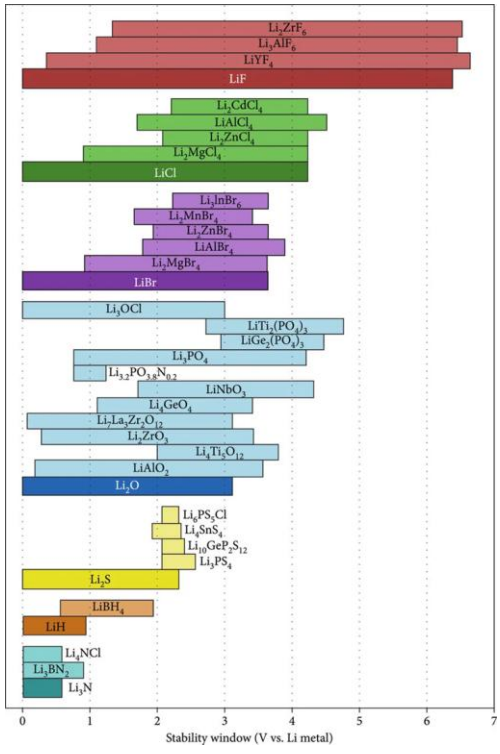


Figure 1.5 - Electrochemical stability windows of selected inorganic solid electrolytes and related binary compounds, expressed versus Li metal. Reproduced from Richards *et al.* (2016).[43]

- **Oxide electrolytes**

Oxide solid electrolytes are particularly attractive because of their high thermal robustness, relatively wide oxidative stability, and better ambient stability compared with sulfide-based electrolytes. Garnet-type $Li_7La_3Zr_2O_{12}$ (LLZO), perovskite-type $Li_{3x}La_{2/3-x}TiO_3$ (LLTO), and NASICON-type compounds such as LATP and LAGP are among the most intensively studied oxide solid electrolytes for ASSBs.

Cubic LLZO became a landmark material after Murugan *et al.* reported its fast lithium-ion conduction.[44] Stabilized cubic LLZO typically exhibits room temperature ionic conductivity in the range of ~10^{-4} to 10^{-3} S cm^{-1}, while its electronic conductivity remains extremely low, generally below 10^{-12} S cm^{-1}. These characteristics make LLZO especially attractive for pairing with lithium metal. However, high-temperature sintering (1100 ºC-1200 ºC in bulk, and up to 800ºC in thin films), grain-boundary resistance, brittleness, poor wetting against lithium and its tendency to form lithium carbonate on the surface remain persistent challenges.

Perovskite-type LLTO exhibits bulk ionic conductivity approaching ~10^{-3} S cm^{-1}, among the highest values reported for oxide electrolytes.[45] Nevertheless, total conductivity is often reduced to ~10^{-5}–10^{-4} S cm^{-1} by grain-boundary resistance, and reduction of Ti^{4+} to Ti^{3+} near lithium metal interfaces can introduce undesirable electronic leakage.

Among oxide solid electrolytes, NASICON-type phosphates, such as LATP and LAGP combine attractive room-temperature ionic conductivity, typically in the 10^{-4}-10^{-3} S cm^{-1} range for optimized ceramic compositions, with good thermal stability, low electronic conductivity, and comparatively good air and moisture tolerance. Their robust phosphate framework makes them particularly appealing for oxide-based solid-state batteries. However, Ti- and Ge-containing NASICON electrolytes are not stable in direct contact with lithium metal because Ti^{4+} or Ge^{4+} can be reduced at low potentials, leading to interfacial degradation and increased electronic conductivity. Therefore, their integration with modern anodes generally requires protective interlayers or cell configurations that avoid direct contact with lithium metal. [10,46,47] LATP is especially relevant to this thesis because of its phosphate chemistry, relatively high ionic conductivity, environmental stability, and compatibility with thin-film deposition routes. A more detailed discussion of LATP and its compatibility with LFP is provided in the Materials of Choice section.

- **Sulfide electrolytes**

Sulfide electrolytes currently provide the highest room-temperature ionic conductivities among practical solid electrolytes, in some cases rivaling liquid electrolytes. Representative systems include $Li_7P_3S_{11}$, LGPS-type materials, and argyrodites such as Li_6PS_5Cl. Kamaya *et al.* reported $Li_{10}GeP_2S_{12}$ (LGPS) with ionic conductivity of ~1.2×10^{-2} S cm^{-1}, marking a major milestone in the field.[48] Optimized argyrodites frequently exhibit conductivities in the 10^{-3}–10^{-2} S cm^{-1} range. Their electronic conductivity is usually low (~10^{-8} to 10^{-10} S cm^{-1}), although often higher than that of oxides. The relatively soft mechanical nature of sulfides facilitates densification by cold pressing

and improves interparticle contact in composite electrodes, making them highly attractive for bulk ASSBs. However, sulfides suffer from moisture sensitivity, H_2S evolution, narrow electrochemical stability windows, and pronounced reactivity with both oxide cathodes and lithium metal. Protective coatings such as $LiNbO_3$ or Li_3PO_4 are therefore commonly employed.

- **Halide electrolytes**

Halide electrolytes have emerged more recently as a promising class because they combine moderate-to-high ionic conductivity with improved oxidative stability toward high-voltage cathodes. Typical compounds include Li_3YCl_6, Li_3YBr_6, and Li_3InCl_6, with room-temperature conductivities commonly in the ~10^{-4} to 10^{-3} S cm^{-1} range.[49] Their main current limitations concern moisture sensitivity, cost of some metal precursors, and early-stage manufacturing maturity.

- **Polymer and hybrid electrolytes**

Polymer electrolytes, especially polyethylene oxide (PEO)-based systems, offer flexibility, ease of processing, low density, and excellent interfacial conformity. Their ionic conductivity is typically ~10^{-7} to 10^{-5} S cm^{-1} at room temperature, increasing to ~10^{-4} S cm^{-1} or higher above 60 ºC, while electronic conductivity is generally below 10^{-12} S cm^{-1}.[50] Their lower room-temperature conductivity and narrower oxidative stability window often favor coupling with lower-voltage cathodes such as LFP. Hybrid electrolytes combining polymers with ceramic fillers or continuous ceramic networks seek to combine the mechanical compliance of polymers with the superior transport properties of ceramics.

- **Thin film LiPON**

Lithium phosphorus oxynitride (LiPON) remains the benchmark electrolyte for thin-film microbatteries. LiPON typically exhibits room-temperature ionic conductivity of ~10^{-6} S cm^{-1} and extremely low electronic conductivity of ~10^{-14}-10^{-13} S cm^{-1}. Although modest in bulk terms, this conductivity is sufficient in sub-micrometer films where transport distances are very short. More importantly, LiPON combines excellent electrochemical stability, negligible electronic leakage, and remarkable compatibility with lithium metal, explaining its unmatched long-term cyclability in thin-film batteries. The pioneering work of Bates *et al.* on amorphous lithium electrolyte thin films and rechargeable thin-film batteries was foundational in this regard. [51,52]

1.4.2.3 Cathode active materials

Cathode active materials largely determine the operating voltage, specific capacity, and energy density of lithium batteries. **Figure 1.6** presents a voltage versus specific capacity comparison of representative cathode materials, including layered oxides, spinels, high-voltage spinels, and olivine phosphates. Layered oxides provide high capacity and high energy density,

spinel oxides offer high-voltage operation and good rate capability, whereas olivine LFP provides a safer and more chemically robust alternative for solid-state battery architectures.

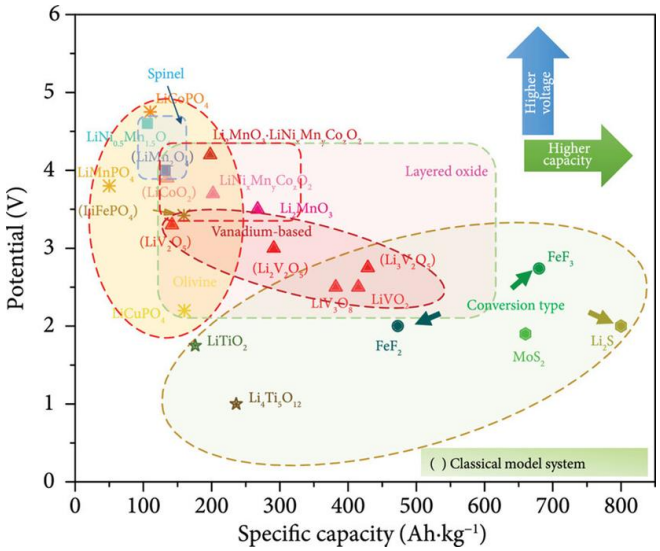


Figure 1.6 - Comparison of representative cathode materials in terms of average operating voltage versus theoretical specific capacity. Reproduced from Qi & Wang (2020).[53]

In ASSBs, however, cathode selection is not governed only by capacity and redox potential, but also by chemical compatibility with the solid electrolyte, mechanical stability during cycling, and the ability to maintain low-resistance solid-solid interfaces. For this reason, the choice of cathode material is strongly coupled to the selected solid electrolyte and processing route.

Layered oxide cathodes

Layered transition-metal oxides remain the dominant high-energy cathode family. $LiCoO_2$ (LCO), introduced by Mizushima *et al.* in 1980,[54] has a theoretical capacity of 274 mAh g^{-1}, although practical cycling is usually limited to approximately 140-160 mAh g^{-1} to avoid structural degradation. It exhibits electronic conductivity of ~10^{-4} to 10^{-3} S cm^{-1} in partially delithiated states and lithium diffusivity typically between ~10^{-12} and 10^{-9} cm^2 s^{-1}. Owing to its high density and compatibility with sputtering or PLD, LCO demonstrate particular importance in thin-film microbatteries.

Nickel-rich layered oxides, such as NMC and NCA, offer higher specific capacities, often in the range of 180-220 mAh g^{-1}, and dominate electric-vehicle batteries. Their electronic conductivity commonly lies in the ~10^{-4} to 10^{-2} S cm^{-1} range, with lithium diffusivities around ~10^{-12} to 10^{-10} cm^2 s^{-1} depending on composition and state of charge. However, larger volume changes, oxygen release tendencies, and particle cracking become more problematic in rigid solid-state environments.[55]

Spinel cathodes

$LiMn_2O_4$ (LMO) and high-voltage $LiNi_{0.5}Mn_{1.5}O_4$ (LNMO) provide three-dimensional lithium transport pathways and relatively good rate capability. LMO operates near 4.0 V vs. Li^+/Li

with a theoretical capacity of 148 mAh g-1, whereas LNMO operates around 4.7 V vs. Li^+/Li with a theoretical capacity close to 147 mAh g^{-1}. The high voltage of LNMO is attractive for increasing energy density, but it also imposes stricter requirements on the oxidative stability of the solid electrolyte and the cathode/electrolyte interface.[56]

Olivine phosphate cathodes

LFP, firstly reported by Padhi and colleagues in 1997,[14] offer a different balance of properties. LFP operates at approximately 3.45 V vs. Li^+/Li and has a theoretical specific capacity of 170 mAh g^{-1}, corresponding to the reversible extraction/insertion of one Li^+ per formula unit through the Fe^{2+}/Fe^{3+} redox couple. Although its gravimetric energy density is lower than that of Ni-rich layered oxides, LFP is low-cost, environmentally benign, thermally stable, and structurally robust. The strong covalent P-O framework suppresses oxygen release and contributes to its superior intrinsic safety. These characteristics make LFP especially attractive for safe, long-life, and phosphate-based solid-state battery architectures. Its detailed structure, thin-film processing, and compatibility with LATP are discussed in the Materials of Choice section.

1.5 Materials of Choice in this thesis

Based on the material families discussed above, this thesis focuses on a phosphate-based thin-film battery platform composed of LFP as the cathode, LATP as the solid electrolyte, LiPON as a lithium-compatible electrolyte or interlayer, and thermally evaporated lithium metal as the negative electrode. This materials selection is motivated by the combination of safety, chemical robustness, environmental stability, and compatibility with vacuum-based thin-film processing. At the same time, integrating these materials introduces a specific processing challenge, since LATP requires crystallization or post-deposition thermal treatment to achieve high ionic conductivity, whereas LFP can undergo structural and chemical degradation under prolonged thermal exposure, particularly in oxidative atmospheres.

1.5.1 LATP

Among oxide solid electrolytes, NASICON-type phosphates have attracted considerable attention because they combine relatively high Li^+ conductivity, low electronic conductivity, good thermal stability, and remarkable tolerance to ambient air and moisture. The NASICON framework was originally identified in compounds of the general formula $NaM_2(PO_4)_3$, where M = Ge, Ti, or Zr, and later adapted to lithium-ion conductors by replacing Na+ Na^+ with Li^+. In this structure, corner-sharing MO_6 octahedra and PO_4 tetrahedra generate a three-dimensional polyanionic framework containing interstitial sites and bottlenecks through which lithium ions can migrate.[57] This structural robustness, together with the strong covalency of the phosphate units, makes NASICON-type materials especially relevant for ASSBs requiring chemical and thermally stable electrolytes.

The parent compound $LiTi_2(PO_4)_3$ (LTP) already exhibits lithium-ion mobility within the NASICON framework, but its total room-temperature conductivity is limited by grain-boundary

resistance and insufficient densification. A major improvement is achieved by partial aliovalent substitution of Ti^{4+} by trivalent cations, most commonly Al^{3+}, leading to the family $Li_{1+x}Al_xTi_{2-x}(PO_4)_3$ (LATP). This substitution introduces additional Li^+ ions for charge compensation and modifies the NASICON framework, thereby increasing the number of mobile charge carriers and facilitating Li^+ transport. Aono *et al.* first demonstrated the strong enhancement in ionic conductivity upon trivalent cation substitution in lithium titanium phosphate-based solid electrolytes, with Al-substituted compositions showing particularly attractive transport properties.[58] Subsequent studies confirmed that compositions close to $Li_{1.3}Al_{0.3}Ti_{1.7}(PO_4)_3$ are among the most conductive LATP formulations, because they provide an effective compromise between carrier concentration and framework size.[18,59,60]

The conduction mechanism in LATP is closely related to the distribution of Li^+ over different crystallographic sites. In undoped LTP, lithium preferentially occupies the M1 site, which limits long-range mobility. Upon Al incorporation, additional Li^+ ions are introduced into interstitial positions, often described as M3-type sites, creating migration pathways between adjacent lithium sites.[61] Therefore, the size and polarizability of the triangular oxygen bottlenecks formed between Ti/AlO_6 octahedra and PO_4 tetrahedra are critical descriptors of Li^+ transport. Neutron diffraction, NMR, and computational studies have shown that Li^+ diffusion in LATP involves M1–M3–M3–M1-type pathways and that Al substitution affects both the Li-site occupancy and the local framework distortion.[46]

For dense ceramic LATP, bulk ionic conductivities in the range of 10^{-4}–10^{-3} S cm^{-1} at room temperature are commonly reported, with bulk activation energies often around 0.15–0.30 eV. However, the total conductivity is frequently lower than the intrinsic grain conductivity because Li^+ transport across grain boundaries is hindered by pores, cracks, secondary phases, local compositional deviations, or highly disordered intergranular regions.[62,63] In this sense, LATP conductivity is not only a crystallographic property, but also a microstructural one. Optimized densification, sintering, and control of grain-boundary chemistry are therefore essential to approach the high intrinsic conductivity of the NASICON lattice.

The role of secondary phases in LATP is particularly important. Phases such as $AlPO_4$, TiO_2, and $LiTiOPO_4$ may appear depending on stoichiometry and thermal history. Their effect is not always straightforward: insulating phases can block Li^+ migration when they segregate continuously at contact and promote densification. Therefore, a balance must be achieved between phase purity, crystallinity, densification, and the formation of ion-conducting or blocking intergranular regions. Raman spectroscopy is particularly useful in this context because it enables the identification of the LATP framework vibrations as well as secondary phosphate or titanate phases, including $AlPO_4$, TiO_2, and $LiTiOPO_4$.[19,64]

Compared with sulfide solid electrolytes, LATP offers lower ionic conductivity but much better stability in air and easier handling, avoiding the moisture sensitivity and H_2S evolution typical of sulfide systems. Compared with LiPON, LATP can reach higher intrinsic ionic conductivity, but it usually requires crystallization or post-deposition thermal treatment to achieve optimal transport.

This makes LATP highly attractive for thin-film solid-state batteries, provided that its crystallization temperature can be made compatible with the electrode stack. In this respect, the previous work of Siller demonstrated that LATP thin films deposited by large-area PLD can reach ionic conductivities around 10^{-6} S cm^{-1} in the as-deposited state, comparable to LiPON thin films, and that post-deposition annealing can increase the conductivity by approximately two orders of magnitude, approaching 10^{-4} S cm^{-1} with activation energies close to 0.37 eV.[65]

Despite these advantages, LATP is not stable in direct contact with metallic lithium. At low potentials, Ti^{4+} can be reduced to Ti^{3+}, increasing local electronic conductivity and promoting interfacial degradation. This limits the direct use of LATP with Li-metal anodes unless protective interlayers or artificial buffer layers are introduced. Nevertheless, this limitation is less critical when LATP is coupled with positive electrode materials or with electrode configurations operating at higher potentials. For this reason, LATP remains a highly relevant electrolyte candidate for phosphate-based all-solid-state thin-film batteries, particularly when combined with LFP cathodes. The chemical affinity between phosphate electrode and phosphate electrolyte, together with the good air stability and processability of LATP, motivates the development of low-temperature crystallization or rapid thermal processing strategies capable of integrating LATP with temperature-sensitive LFP thin films.[47,65]

1.5.2 LFP

Since the seminal report which established olivine LFP as a promising cathode, LFP has become one of the most important positive electrode materials in lithium batteries because of its low cost, low toxicity, thermal stability, and structural robustness. In that original work,[14] capacities of about 100-110 mAh g^{-1} were obtained at low current density, although lithium extraction was limited to about 0.6 Li per formula unit, already indicating the kinetic limitations intrinsic to this material.

In contrast with layered oxide cathodes, the strong covalent P–O framework suppresses oxygen release and contributes to the superior intrinsic safety of LFP in LIBs, which explains its extensive deployment in electric mobility and stationary storage systems. Structurally, LFP crystallizes in the orthorhombic olivine structure (space group *Pnma*), where lithium transport occurs through one-dimensional channels parallel to the [010] direction (**Figure 1.7**)Error! Reference source not found..[66,67] This anisotropic diffusion pathway strongly couples electrochemical performance to crystallographic orientation, particle morphology, antisite defects, and grain boundaries. Consequently, experimentally reported lithium diffusivities span several orders of magnitude, typically from ~10^{-16} to 10^{-12} cm^2 s^{-1} depending on methodology and microstructure.[16,68] In ideal crystals, higher intrinsic values are predicted, indicating that real microstructural constraints often dominate practical kinetics. A second limitation of pristine LFP is its low electronic conductivity, commonly reported around ~10^{-10} to 10^{-9} S cm^{-1} at room temperature.[17] This drawback motivated the widespread use of carbon coatings, aliovalent doping, and particle downsizing, which collectively transformed LFP into a commercially viable cathode.

In conventional porous composite electrodes, nanosized LFP particles embedded in conductive carbon matrices minimize both ionic and electronic transport lengths.

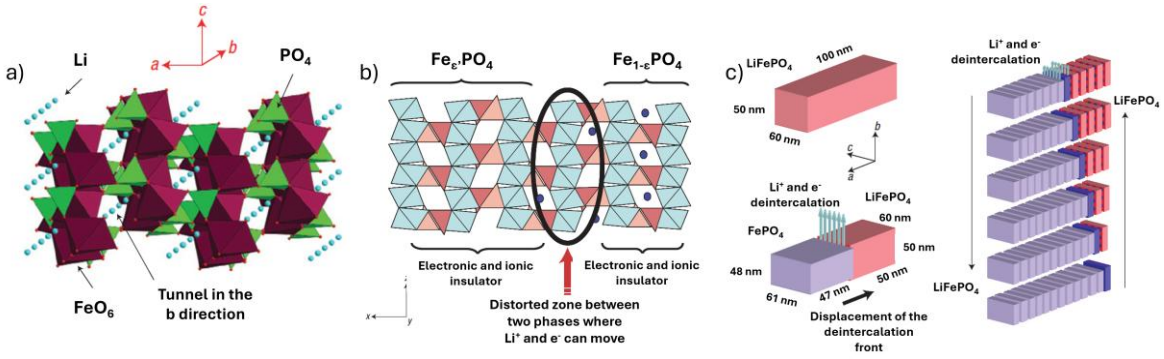


Figure 1.7 - (a) Olivine crystal structure highlighting 1D lithium diffusion channels. (b) Distorted interfacial region between lithiated $LiFePO_4$ and delithiated $FePO_4$ phases during cycling. (c) Schematic representation of the domino-cascade phase-transformation mechanism in $LiFePO_4$ particles. Adapted from Delmas *et al.* (2008).[69]

For thin-film batteries, however, the transport penalties of low-conductivity materials are substantially alleviated because dense active layers are only hundreds of nanometers thick. In such geometries, both ionic and electronic path lengths are drastically shortened, allowing carbon-free LFP to become viable even without conventional composite electrode design. At the same time, thin-film configurations are particularly valuable for fundamental studies because they suppress many of the complexities present in composite porous electrodes, such as binder effects, conductive additives, and tortuous liquid-electrolyte pathways. This makes LFP thin films an ideal model system for studying the intrinsic coupling between crystallinity, orientation, film morphology, buried interfaces, and electrochemical utilization.

This concept motivated some studies using pulsed laser deposition (PLD), sputtering, and related vacuum techniques, where stoichiometric transfer and precise thickness control can yield crystalline LFP films with competitive electrochemical performance. Among the different preparation routes, PLD emerged early as one of the most effective techniques for LFP thin films because of its good stoichiometric transfer and precise thickness control. One of the first clear demonstrations was reported by Sauvage *et al.* in 2004,[70] who obtained well-crystallized, homogeneous carbon-free LFP films about 300 nm thick on Pt-capped Si substrates in a one-step in situ process. The optimized deposition conditions involved a substrate temperature of 600 ºC, an Ar pressure of 8×10^{-2} mbar, a target–substrate distance of 3 cm, and a 1 h deposition using a KrF laser. These films exhibited the characteristic electrochemical signature of triphylite LFP and were notable because they were crystallized without any post-deposition annealing. This result was particularly important because it showed that in situ crystallization was possible within a narrow deposition window, whereas earlier reports often relied on post-annealing or suffered from poor crystallinity. In parallel, Iriyama *et al.* deposited LFP films by PLD at room temperature for 30 min or 3 h under Ar (23 Pa), followed by annealing at 500 ºC for 3 h in Ar.[71] Their films were close to

stoichiometric and polycrystalline after annealing, and they showed only the expected anodic/cathodic peaks around 3.4 V vs Li/Li^+. The authors emphasized that the thin geometry strongly reduced the impact of LFP's poor electronic conductivity, as evidenced by the fact that the capacity estimated from CV at 100 mV s^{-1} still retained 69% of the value obtained at 1 mV s^{-1}.

A related study by Yada *et al.* in 2005 systematically investigated the influence of annealing temperature on PLD-grown films deposited at room temperature for 30 min and then annealed for 3 h under Ar between 400 and 700 ºC.[71] Films annealed at 500 and 600 ºC showed the expected LFP redox peaks at 3.4 V vs Li/Li^+, while 400 ºC was insufficient to crystallize the phase and 700 ºC promoted impurity formation. Interestingly, the 500 ºC film, composed of finer grains (~50 nm), exhibited better rate capability, whereas the 600 ºC film showed slightly higher absolute capacity. This led to the conclusion that the optimum lies in a compromise window between 500 and 600 ºC.

A key next step in the field was the recognition that electrochemical activity in LFP thin films depends not only on phase purity, but also strongly on texture and morphology. Sauvage *et al.* explored this in detail in their 2005 study on PLD-grown carbon-free LFP films with thicknesses ranging from 12 to 600 nm.[72] Under optimized PLD conditions (600 ºC, 8×10^{-2} mbar Ar), they found that thinner films were nearly amorphous, whereas increasing thickness promoted crystallization and a preferential (120) orientation up to about 600 nm; thicker films eventually lost this preferred texture and became more polycrystalline. Importantly, however, the measured capacities remained far below the expected values for the full film thickness, leading the authors to conclude that only a fraction of the film was actually electrochemically active and that ionic conductivity, rather than purely electronic conductivity, was the main limitation in these oriented olivine films.

Because pristine LFP remains limited by low electronic conductivity, in 2007 Lu *et al.* introduced a small amount of silver into PLD-grown LFP films by preparing a dense $LiFePO_4$-Ag target and depositing composite films on $Si/SiO_2/Ti/Pt$ substrates.[73] Under optimized deposition conditions (600 ºC, 0.15 mbar Ar, 1 h), they obtained uniform films about 200 nm thick containing about 2 at.% Ag distributed through the film thickness. The room-temperature conductivity increased to about 1.29×10^{-3} S cm^{-1}, roughly six orders of magnitude above that reported for bare LFP films. Electrochemically, the 200 nm $LiFePO_4$-Ag film delivered a reversible discharge capacity of 46.3 μAh cm^{-2} μm^{-1}, corresponding to >135 mAh g^{-1}, at 8 μA cm^{-2} (about 0.7 C), and still retained more than 65% of this capacity at ~14 C. Under overcharge/overdischarge conditions, the film even approached ~93% of theoretical capacity.[73]

The same group then replaced Ag with carbon by preparing $LiFePO_4$-C PLD targets using PVA as both binder and carbon source.[74] The films were deposited under similar conditions (600 ºC, 0.15 mbar Ar, 300 mJ laser energy, 10 Hz) and further optimized by varying carbon content and post-deposition annealing. The authors reported that 2 mol% C gave the best performance, while annealing at 600 ºC for 6 h in the deposition chamber improved coulombic efficiency and high-rate capability, although sometimes at the cost of lower specific capacity. They reported capacity in areal-

thickness-normalized units rather than mAh g^{-1}, but values around 55-60 μAh cm^{-2} μm^{-1} were achieved in optimized cycling windows, corresponding to near-theoretical utilization. These Ag- and C-modified films clearly demonstrated that conductivity enhancement can dramatically improve the utilization of LFP thin films. At the same time, such approaches also move the system away from the ideal model of a pure thin-film cathode, which is less suitable when the objective is to understand the intrinsic limitations of dense carbon-free LFP.

The emphasis on texture and partial utilization was reinforced by later structural studies in 2010. Legrand *et al.* compared traditional-geometry and off-axis PLD deposition of LFP on Si substrates and showed that the deposition geometry strongly affects both the preferential orientation and the defect structure of the films.[75] In particular, off-axis growth promoted highly oriented films but also produced unusual protrusions and iron-rich protuberances, while traditional geometry led to more polycrystalline morphologies. Their study highlighted that PLD chamber geometry itself can influence the final electrochemical behavior through its effect on microstructure and compositional heterogeneity.

Tang *et al.* then investigated the relationship between morphology, crystallinity, and performance in carbon-free PLD-grown films deposited on Ti substrates at 400–700 ºC and 10-40 Pa Ar.[76] They identified 500 ºC and 20–30 Pa Ar as an optimum window for obtaining well-crystallized pure olivine LFP. The films were about 300 nm thick, slightly textured, and showed their best electrochemical performance at elevated temperature. Under 1/20 C and 45 ºC, the optimized films reached about 83% of the theoretical capacity, corresponding to roughly 141 mAh g^{-1}. Moderate post-annealing further increased utilization, whereas deposition at too high temperature or annealing for too long introduced Fe^{3+}-containing impurity phases such as $Li_3Fe_2(PO_4)_3$ and $Fe_4(P_2O_7)_3$.

In 2011, the same group later used PLD-grown 300 nm LFP films on Ti substrates for kinetic analysis by CV, GITT, and EIS.[77] These films were deposited at 500 ºC under 20 Pa Ar and showed a voltage plateau around 3.4 V with 58% of the theoretical capacity at a current density of 1.67 μA cm^{-2} (reported as C/4 in the article). The apparent chemical diffusion coefficients extracted by different methods spanned from about 10^{-14} to 10^{-18} cm^2 s^{-1} depending on state of charge and method, again underlining the strong methodological and microstructural dependence of kinetic parameters in LFP thin films.

In parallel with PLD, radio-frequency sputtering was developed as an alternative route more compatible with microbattery manufacturing. Zhu *et al.* deposited LFP films by RF magnetron sputtering on Pt/Ti/quartz substrates using a $LiFePO_4$/C target with added Li_2O, under Ar at 2.7 Pa and 100 W, with substrate temperatures between room temperature and 500 ºC.[78] The films were about 400 nm thick and 1.77 cm^2 in area. They found that films deposited at 25 and 300 ºC were amorphous or poorly crystallized, whereas deposition at 400 ºC yielded crystalline LFP with the best electrochemical performance. At this optimum temperature, the film delivered an initial discharge capacity of 56 μAh cm^{-2} μm^{-1} at 10 μA cm^{-2} between 3.0 and 4.3 V, with good cyclability.

At 500 ºC, however, an impurity phase identified as $Li_3Fe_2(PO_4)_3$ developed and small surface particles appeared, likely carbon agglomerates or decomposition products.

A more recent sputtering-based study by Sugiawati *et al.* focused on porous Li–Fe–P–O films prepared by RF sputtering for microbatteries.[79] Their as-deposited films were amorphous, dense, and about 1.6 μm thick, deposited at room temperature under 7 mTorr Ar and 3 W cm^{-2} for 12 h. Annealing in air between 400 and 700 ºC progressively crystallized the films, but also induced phase evolution from LFP toward $Li_3Fe_2(PO_4)_3$. At 500 ºC, crystalline porous LFP was obtained and delivered about 17.9 μAh cm^{-2} μm^{-1} at C/5 after 100 cycles, with a voltage plateau around 3.45 V. At 700 ºC, the film transformed predominantly into NASICON-type $Li_3Fe_2(PO_4)_3$ and delivered 22.1 μAh cm^{-2} μm^{-1} at 2.8 V; at C/10 the areal capacity approached ~27 μAh cm^{-2} μm^{-1}, roughly nine times the as-deposited value. This study is important for the LFP thin-film literature because it shows how easily sputtered Li–Fe–P–O films can drift toward secondary phosphate phases during thermal treatment, especially in air. It also highlights that high areal capacities in this materials system do not necessarily correspond to phase-pure LFP.

A recent development is the move away from classic dense intercalation cathodes deposited entirely by vacuum methods. In 2024, Ke *et al.* proposed a hybrid architecture combining tape-cast LFP thick films with sputtered LiPON (~3 μm) and either pressed Li, evaporated Li, or sputtered Si anodes.[80] Their aim was to avoid the high-temperature crystallization step normally required by sputtered thin-film cathodes and to increase mass loading while adopting a thin-film solid electrolyte. In their system, the LFP slurry was tape-cast with a 25 μm scraper and dried at 120 ºC for 12 h, completely avoiding post-annealing. The resulting LFP/LiPON/Evaporated-Li cells delivered 12.3 μAh cm^{-2} with 93.21% retention after 50 cycles, while the LFP/LiPON/pressed-Li cells maintained 9.6 μAh cm^{-2} after 180 cycles with an average coulombic efficiency above 99.1%. Although this architecture is not a "classic" dense and carbon-free LFP thin film in the strict sense, it reflects an important recent trend in the field: reconciling microbattery integration with higher mass loading and lower processing temperature. It also reinforces that the design space of "thin-film cathodes" is broadening beyond dense PLD and sputtered layers.

From the perspective of ASSBs, LFP is especially attractive because its moderate working voltage and exceptional structural robustness reduce the chemical driving force for electrolyte decomposition compared with Ni-rich layered oxides or high-voltage spinels. Although its gravimetric energy density is lower than that of advanced layered cathodes, its reliability, safety, and sustainability continue to make LFP one of the most strategically important cathode materials for next-generation thin-film and solid-state battery systems.

1.5.3 Compatibility between LFP cathodes and LATP solid electrolytes

The integration of LFP with LATP is particularly attractive because both materials are phosphate-based compounds, which suggests a higher degree of chemical affinity compared with combinations involving oxide cathodes and phosphate electrolytes. In contrast to layered or spinel oxide cathodes, where large differences in lithium and phosphate content can promote severe

interdiffusion and decomposition during high-temperature processing, LFP and LATP share a polyanionic phosphate framework. This anionic similarity has been identified as one of the main reasons why olivine cathodes generally exhibit better thermochemical compatibility with LATP than conventional oxide cathodes.

Gellert *et al.*[81] systematically compared LATP with several cathode materials and showed that oxide cathodes can react rapidly with LATP at temperatures as low as 500 ºC, whereas olivine phosphate cathodes are substantially more stable. Among the olivine systems investigated, LFP showed the most promising behavior, with no XRD-detectable secondary phases after co-sintering with LATP up to 700 ºC under reducing atmosphere. However, electron microscopy revealed minor interfacial secondary phases, tentatively assigned to $Li_2FeTi(PO_4)_3$, indicating that compatibility does not imply complete chemical inertness. The thermal atmosphere plays a decisive role in determining the reaction pathway between LFP and LATP. Under reducing or inert conditions, LFP/LATP mixtures can remain comparatively stable up to intermediate temperatures, although higher temperatures promote Fe redistribution and the formation of Fe-containing NASICON-type or orthophosphate phases. In the study by Gellert *et al.*, no additional phases were detected by XRD for LFP/LATP up to 700 ºC, but at 800 ºC a significant fraction of $Li_2FeTi(PO_4)_3$ and $AlPO_4$ was observed. The authors proposed that Fe loss from the LFP phase can lead either to Fe-substituted LATP or to orthorhombic $Li_{1+x}Fe_xTi_{2-x}(PO_4)_3$-type phases, which may still be ionically conductive and electrochemically active.[81]

In contrast, studies performed under air or oxidative conditions reveal a different degradation route. Yu *et al.* investigated the high-temperature chemical stability of $Li_{1.4}Al_{0.4}Ti_{1.6}(PO_4)_3$ with several cathode materials between 500 and 900 ºC in air. For the LFP/LATP system, they observed that a major fraction of LFP transformed into a Fe-rich NASICON-type phase, simplified as $Li_3Fe_2(PO_4)_3$, after heating at 500 ºC for 2 h. With increasing temperature, the fraction of $Li_3Fe_2(PO_4)_3$ increased while the LATP fraction decreased. This result indicates that LFP/LATP compatibility is strongly atmosphere-dependent: while inert or reducing environments suppress Fe^{2+} oxidation and delay severe phase transformation, oxidative conditions favor the formation of Fe^{3+}-containing NASICON phases at much lower temperatures.[82]

More recent microscopy-based studies have provided a spatially resolved picture of the interface evolution in LFP/LATP composites. Malaki *et al.* investigated co-sintered all-phosphate LFP–LATP cathode–solid electrolyte composites between 650 and 850 ºC using advanced STEM-based techniques. Their results showed that LFP particles retain good structural stability over this temperature range, whereas LATP undergoes stronger phase transformation. At 650 ºC, Fe_{Li} antisite defects were observed near LFP grain boundaries, while between 750 and 850 ºC Fe diffused into the LATP phase, leading to the transformation of rhombohedral LATP into orthorhombic $Li_{1.3+x}Al_{0.3}Fe_xTi_{1.7-x}(PO_4)_3$ phases with Pbca and Pbcn symmetries. Importantly, these transformed phases were not completely inactive: the discharge capacity of the composite decreased from 148 mAh g^{-1} at 650 ºC to 130 mAh g^{-1} at 850 ºC, confirming that the newly formed Fe-containing phosphate phases can still participate electrochemically.[83]

Beaupain *et al.* further examined LFP/LATP compatibility in a battery-relevant composite cathode configuration.[84] In their work, porous LATP–LFP composite cathodes were prepared by tape casting using carbon-coated LFP and LATP powders, followed by debinding and co-sintering under N_2 between 650 and 850 ºC. These sintered composite tapes were infiltrated either with conventional liquid electrolyte or with a PEO-based polymer electrolyte and tested as Li-metal half-cells. The study showed that reaction layers form between LATP and LFP during co-sintering and that, above 750 ºC, rhombohedral LATP transforms into orthorhombic $Li_{1.3+x}Al_{0.3-\gamma}Fe_{x+\gamma}Ti_{1.7-x}(PO_4)_3$ phases due to Fe diffusion into the NASICON structure. Despite this phase evolution, high capacities were still obtained after electrolyte infiltration, reaching 134 mAh g^{-1} with liquid electrolyte and 125 mAh g^{-1} with PEO electrolyte.

A particularly relevant aspect of the work by Beaupain *et al.* is the electrochemical identification of redox contributions from LATP-derived and Fe-containing NASICON-type phases. By extending the discharge window down to 2.0 V, they showed that pristine LATP and co-sintered LATP–LFP composites exhibit additional redox activity below the conventional LFP plateau. Features around 2.75–2.78 V were assigned to Fe^{3+}/Fe^{2+} redox processes in NASICON-type phases, comparable to $Li_3Fe_2(PO_4)_3$, whereas processes below 2.4 V were attributed to Ti^{4+}/Ti^{3+} redox activity in LATP-derived phases. This distinction is important because it demonstrates that, in LFP/LATP systems, capacity measured over an extended voltage window cannot always be assigned exclusively to the $LiFePO_4/FePO_4$ redox couple. Instead, secondary phosphate phases and interfacial reaction products may contribute to charge storage.

Overall, the literature indicates that LFP and LATP represent one of the most promising phosphate-based cathode/electrolyte combinations for oxide solid-state batteries, but their interface remains chemically active under thermal processing. The main reaction pathways involve Fe redistribution, Fe substitution into the LATP framework, partial transformation of rhombohedral LATP into orthorhombic Fe-containing NASICON phases, and the possible formation of $AlPO_4$, $Li_2FeTi(PO_4)_3$, $Li_{1+x}Fe_xTi_{2-x}(PO_4)_3$, or $Li_3Fe_2(PO_4)_3$ depending on atmosphere and thermal history. These reactions can be detrimental when they reduce ionic conductivity or block transport pathways, but they can also generate electrochemically active interphases. For thin-film architectures, this dual character is especially relevant: the reduced transport distances may mitigate some bulk limitations, but the high interfacial area and the thermal budget required for LATP crystallization make the LFP/LATP interface a critical design parameter. Therefore, processing strategies that minimize prolonged high-temperature exposure, such as low-temperature LATP deposition followed by rapid thermal processing, are essential for enabling functional phosphate-based all-solid-state thin-film batteries.

1.5.4 Relevance to thin-film and microbattery systems

Although much of the present ASSB literature focuses on bulk composite cathodes and large-format cells for electric vehicles, thin-film batteries constitute a distinct and technologically mature branch of the field. Their relevance is particularly strong for autonomous microsystems,

sensors, medical implants, and on-chip power sources, where footprint, safety, long cycle life, and reliability are often more critical than maximizing total stored energy.

In thin-film ASSBs, all active layers are commonly deposited by vacuum-based methods such as sputtering, pulsed laser deposition, evaporation, or ALD. Because transport distances are drastically reduced, materials with only moderate bulk ionic conductivity can still perform effectively. For example, LiPON with ~10^{-6} S cm^{-1} is highly successful when deposited as ~1 μm dense films, while cathodes such as LFP can achieve competitive rate performance when fabricated as nanometric layers.

Within this broader context, phosphate-based thin-film systems are especially compelling. LFP offers a safe and structurally stable cathode platform, while LATP provides a promising oxide electrolyte with relatively high ionic conductivity and environmental stability. However, the thermal budget required for LATP crystallization is often incompatible with temperature-sensitive cathodes such as LFP. This compatibility gap directly motivates the materials-processing strategy developed in this thesis, namely the decoupling of electrolyte growth from high-temperature crystallization to enable functional phosphate-based all-solid-state thin-film batteries.

1.6 Scope of this thesis

This thesis is devoted to the development and integration of phosphate-based thin-film materials, specifically $LiFePO_4$ (LFP) cathodes and $Li_{1.3}Al_{0.3}Ti_{1.7}(PO_4)_3$ (LATP) solid electrolytes, into functional all-solid-state thin-film battery architectures. The central challenge addressed is the incompatibility between the high thermal budget required for LATP crystallization and the thermal sensitivity of LFP, which motivates a processing strategy based on low-temperature pulsed laser deposition (PLD) combined with rapid thermal processing (RTP) to decouple film growth from electrolyte crystallization. The thesis is organized as follows:

- **Chapter 1** introduces the scientific and technological context of this work. Starting from the motivation for compact and safe energy storage in autonomous microsystems, it reviews the fundamental principles of lithium-ion batteries and the evolution toward all-solid-state architectures. The specific materials selected for this thesis, LFP as cathode, LATP as NASICON-type oxide electrolyte, and LiPON as a Li-compatible buffer layer, are presented in detail, along with the known compatibility challenges at the LFP/LATP interface.
- **Chapter 2** describes the experimental methods and equipment common to the entire thesis. The thin-film fabrication techniques used to prepare all active layers are presented, including PLD, RF magnetron sputtering, thermal evaporation, and RTP. The structural, morphological, and compositional characterization tools are then introduced, followed by the electrochemical techniques employed to assess ionic transport, redox activity, and full-battery performance. This chapter establishes the shared experimental framework underlying the results presented in subsequent chapters.

- **Chapter 3** addresses the fabrication and characterization of carbon-free LFP thin-film cathodes deposited by PLD. The influence of substrate type (Pt vs. ITO), deposition temperature, film thickness, and RTP post-treatment is systematically investigated with respect to phase formation, microstructure, interfacial chemistry, and electrochemical activity in a liquid electrolyte half-cell configuration. A set of optimized deposition conditions is established as the starting point for the subsequent chapters.
- **Chapter 4** focuses on the fabrication of LATP thin-film solid electrolytes and their integration with LFP cathodes in a bilayer architecture. The structural and morphological evolution of LATP films under low-temperature PLD followed by RTP is analyzed, the resulting ionic transport properties are characterized by impedance spectroscopy, and the compatibility of the LFP/LATP bilayer is evaluated through combined structural, elemental, and electrochemical analysis. A narrow but viable processing window in Ar atmosphere is identified that preserves LFP integrity while enabling partial LATP crystallization.
- **Chapter 5** presents the electrochemical characterization of complete all-solid-state thin-film battery devices. LFP/LiPON/Li cells are first investigated as a reference platform, demonstrating reversible LFP activity and exploring the trade-off between cathode thickness, areal capacity, and rate capability. LFP/LATP/LiPON/Li cells are then evaluated as a proof-of-concept architecture, revealing the electrochemical signature of interfacial Fe-containing phosphate secondary phases and establishing a framework for interpreting the combined redox contributions from LFP and reaction interphases.
- **Chapter 6** summarizes the main conclusions of the thesis and highlights key design guidelines for future optimization of thin-film cathodes, solid electrolyte processing, and interface engineering toward safer and more sustainable microbattery technologies.

Chapter 2

Experimental methods

2 Experimental methods 30

2.1 Introduction 30

2.2 Thin film fabrication 30

2.2.1 Pulsed laser deposition (PLD) 30

2.2.2 Magnetron sputtering 32

2.2.3 Thermal evaporation 33

2.2.4 Rapid Thermal Processing (RTP) 35

2.3 Structural, morphological, and elemental characterization 36

2.3.1 X-ray diffraction (XRD) 36

2.3.2 Grazing Incidence Wide-Angle X-ray Scattering (GIWAXS) 38

2.3.3 Raman spectroscopy 39

2.3.4 Atomic Force Microscopy (AFM) 40

2.3.5 Scanning electron microscopy (SEM) 40

2.3.6 Transmission electron microscopy (TEM/STEM) 41

2.3.7 Glow Discharge Optical Emission Spectroscopy (GDOES) 42

2.4 Electrochemical characterization 43

2.4.1 Electrochemical Impedance Spectroscopy (EIS) 43

2.4.2 Cyclic Voltammetry (CV) 46

2.4.3 Chronopotentiometry (CP) 48

2 Experimental methods

2.1 Introduction

This chapter describes the experimental methods used throughout this thesis for the fabrication and characterization of thin-film materials and all-solid-state battery architectures. **Section 2.2** describes the deposition and processing techniques employed for the preparation of the different thin-film layers present in this thesis: $LiFePO_4$ (LFP) cathodes, $Li_{1+x}Al_xTi_{2-x}(PO_4)_3$ (LATP) and $Li_xPO_yN_z$ (LiPON) solid electrolytes, and Li metal anodes. Then, the structural, morphological, and compositional characterization methods are described in **Section 2.3**. Finally, the electrochemical techniques used to evaluate ionic transport, redox activity, and battery performance are presented in **Section 2.4**.

Overall, this chapter establishes the common experimental framework used to investigate the thin-film materials and multilayer architectures developed in this thesis. By combining fabrication, structural and compositional characterization, and electrochemical analysis in the results presented in **Chapters 3**, **4**, and 5. It should be noted that the theoretical descriptions provided in this chapter are not intended to serve as an exhaustive review of each fabrication and characterization technique, but rather as a concise guide to support the interpretation of the specific experimental results. The reader is encouraged to consult dedicated reference literature for a detailed and comprehensive understanding.

2.2 Thin film fabrication

The thin-film materials and multilayer battery architectures investigated in this thesis were fabricated by combining different physical vapor deposition and thermal processing techniques. In this way, dense and continuous cathode, electrolyte, and anode films could be sequentially integrated into model half-cell and all-solid-state thin-film battery configurations. The following subsections describe the principles of each fabrication technique and summarize the specific experimental conditions used in this thesis.

2.2.1 Pulsed laser deposition (PLD)

Pulsed laser deposition (PLD) is a physical vapor deposition technique widely used for the fabrication of complex oxide and phosphate thin films, including materials for all-solid-state thin-film batteries. The method is based on the interaction between a high-energy pulsed laser beam and a solid target. When the laser pulse reaches the target surface, the absorbed energy induces rapid local heating, melting, evaporation, and ablation of the material, generating a highly energetic plasma plume composed of atoms, ions, molecules, clusters, and electrons. This plume expands toward the substrate, where the ablated species condense, diffuse, and rearrange to form a thin film.[85–87]

One of the main advantages of PLD is its capacity for congruent ablation, making it highly suitable for depositing complex multicomponent materials. In principle, this near-stoichiometric transfer is ideal for lithium-containing systems like LFP and LATP, where even minor deviations

in cation ratios can trigger secondary-phase formation, alter crystallinity, or degrade ionic and electronic transport.[88–90]

In practice, however, maintaining stoichiometric transfer is highly challenging when dealing with volatile and light elements. In lithium-based compounds, lithium loss frequently occurs via thermal re-evaporation at elevated substrate temperatures, preferential scattering of light Li species within the plasma plume, or post-deposition ambient degradation.[91] Because lithium non-stoichiometry directly reduces the concentration of mobile Li^+ charge carriers, precisely optimizing deposition conditions is critical to preserving the electrochemical performance of these battery thin films and their interfaces. Because lithium non-stoichiometry directly reduces the concentration of mobile Li^+ charge carriers, precisely optimizing deposition conditions is critical to preserving the electrochemical performance of these battery thin films and their interfaces.

Therefore, the final film composition, crystallinity, morphology, density, and interfacial quality are strongly governed by the deposition parameters. The laser fluence determines the ablation regime and the kinetic energy of the ablated species; insufficient fluence may result in unstable ablation and low deposition rates, whereas excessive fluence can promote droplet formation, target damage, or non-congruent material transfer. The pulse repetition frequency controls the growth rate and the time available for surface diffusion between consecutive pulses, which can influence film compactness and roughness. The target-to-substrate distance affects the spatial distribution, energy, and angular spread of the plume species reaching the substrate. Substrate temperature plays a central role in surface mobility, crystallization, grain growth, and film densification; however, excessively high temperatures may also promote Li loss or interfacial reactions with the substrate. Finally, the nature and pressure of the background gas influence plume expansion, scattering, oxidation state, and kinetic energy of the arriving species. In phosphate-based battery materials, this parameter is particularly important because oxidizing or inert atmospheres can favor different phase formation pathways and oxidation states. [92,93]

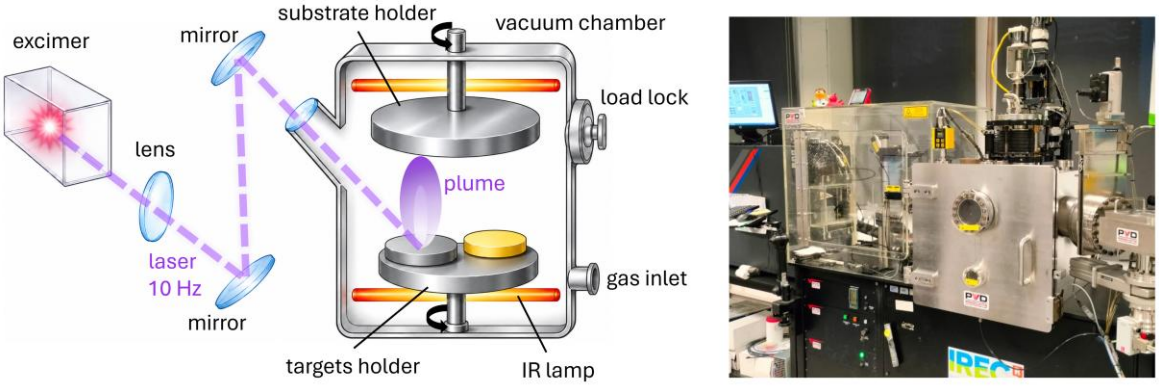


Figure 2.1 - Schematic representation of the PLD method and photograph of the PLD system used in this thesis.

In this thesis, PLD depositions for fabrication of the phosphate-based thin films were carried out using a large-area PLD system from PVD Products (PLD-5000) equipped with a KrF

excimer laser source, Lambda Physik (COMPex PRO 205), operating at a wavelength of 248 nm (**Figure 2.1**). The target-to-substrate distance was kept fixed at 90 mm for all depositions, while the laser pulse frequency was set to 10 Hz. The nominal laser fluence was set to 4.2-2.8 J cm^{-2}, corresponding to an estimated fluence of approximately 1.2-0.8 J cm^{-2} at the target surface after optical losses, with a laser spot area of approximately 10-15 mm^2. LFP thin films were deposited from a commercial $LiFePO_4$ target (3 inch diameter, Toshima Manufacturing Co., Ltd.) whereas LATP films were deposited from a homemade $Li_{1+x}Al_xTi_{2-x}(PO_4)_3$ target (3 inch diameter) fabricated and optimized in the group.[19] Constant rotation of both the substrate holder and the target carousel was applied during deposition to improve thickness homogeneity and target surface wear, enabling the simultaneous deposition of up to eight samples in a single PLD run.

The atmosphere and substrate temperature were adjusted according to the material requirements. For LFP, depositions were mainly carried out under low-pressure Ar, 1 mTorr (1.3×10^{-3} mbar), in order to favor the formation of the olivine phase and preserve Fe^{2+} during growth.[76] The temperature was varied between 300 and 600 °C. For LATP, based on the previous optimization carried out in our group,[19] depositions were performed under O_2 pressure of 80 mTorr, since an oxidizing environment is required to promote the formation of the phosphate-based NASICON-type structure. In this thesis, the substrate temperature was reduced from the previously optimized high-temperature condition of 700 °C to 300 °C, and rapid thermal processing was explored as a post-deposition strategy to promote crystallization while reducing the overall thermal budget. All PLD films were deposited as 8 x 8 mm^2 squares onto 10 x 10 mm^2 substrates. Specific deposition parameters and processing routes are detailed at the start of their respective results chapters.

2.2.2 Magnetron sputtering

Magnetron sputtering is a physical vapor deposition technique based on the erosion of a solid target by energetic ions generated within a plasma. In this process, an inert working gas, typically argon, is ionized and the resulting Ar^+ ions are accelerated toward a negatively polarized target surface. Upon impact, momentum transfer from the incident ions leads to the ejection of target atoms, which are subsequently transported through the plasma and deposited onto a substrate, where thin-film growth takes place. The ion bombardment of the target also produces secondary electrons, which play a crucial role in maintaining the plasma by promoting further ionization of the working gas. In magnetron configurations, a magnetic field is applied in the vicinity of the target, forcing the emitted electrons to follow spiral trajectories along the magnetic field lines. This confinement of electrons near the target region significantly enhances the local plasma density, thereby increasing the sputtering efficiency and deposition rate compared to conventional sputtering systems. As a result, high deposition rates can be achieved at relatively low operating pressures and with short target–substrate distances.[94]

Film growth and properties are strongly influenced by deposition parameters such as substrate temperature, working gas pressure, applied power, and substrate bias. In contrast to PLD, magnetron sputtering is frequently performed at lower substrate temperatures, which typically yields

amorphous as-deposited films. Consequently, post-deposition annealing is often required to induce the desired crystalline phases and, in the case of oxides, to ensure proper oxygen stoichiometry. Furthermore, achieving congruent transfer from multicomponent targets is inherently more complex than in PLD due to the disparate sputtering yields of the constituent elements, meaning that target compositions or plasma parameters must be carefully tailored to avoid cation deviations.

In the case of insulating materials, such as oxide thin films, radio-frequency (RF) sputtering is generally preferred because the alternating electric field enables stable plasma generation while minimizing charge accumulation at the target surface.[95] Reactive sputtering further expands the versatility of the process through the controlled addition of reactive gases. For instance, introducing oxygen ensures the growth of fully oxidized films and avoids reduced phases, while nitrogen can be deliberately introduced to modify film chemistry. A relevant example is the sputtering of Li_3PO_4 in a nitrogen-containing atmosphere, which enables nitrogen incorporation into the amorphous phosphate matrix and leads to the formation of LiPON. Nitrogen incorporation is a key factor behind the enhanced ionic conductivity of LiPON compared with undoped lithium phosphate.[96,97]

In this work, LiPON solid electrolyte was sputtered using an Orion sputtering system (AJA International Inc.) at the Laboratory for Thin Films and Photovoltaics, Swiss Federal Laboratories for Materials Science and Technology (EMPA). LiPON layer covered the entire LFP or LATP previously deposited by PLD. Layers of 1 μm were obtained by RF cosputtering in a confocal arrangement of Li_3PO_4 (99.95%, 2", Kurt J Lesker Co.) and Li_2O (99.9%, 2", Toshima Manufacturing) commercial targets at rates of 0.7 nm/min and 0.6 nm/min and power densities of 5.92 $W.cm^{-2}$ and 4.93 $W.cm^{-2}$ respectively. Target-to-substrate distance was set to 25 cm. Chamber environment was kept constant during the entire deposition (4×10^{-3} mbar pressure, and 50 sccm of N_2). **Figure 2.2** presents a schematic illustration of the co-sputtering process, showing two magnetron sources operating simultaneously inside the vacuum chamber to deposit the desired material onto a common substrate.

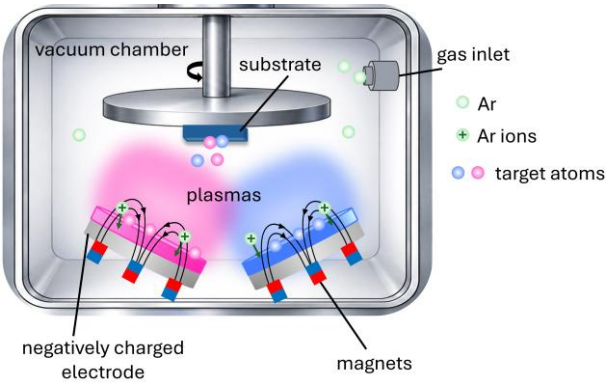


Figure 2.2 - Schematic representation of the RF co-sputtering work principle.

2.2.3 Thermal evaporation

Thermal evaporation is a physical vapor deposition technique in which a source material is heated under high vacuum until a sufficient vapor pressure is reached for evaporation. The

evaporated species then travel mainly in a line-of-sight trajectory through the vacuum chamber and condense onto the substrate surface, forming a thin film. The source material is typically placed in a crucible or boat at the bottom of the chamber, while the substrate is positioned facing the source in order to collect the evaporated material. Heating can be achieved either by resistive heating, using a high electrical current through a filament, boat, or crucible, or by electron-beam evaporation, in which an accelerated electron beam locally heats the source material.

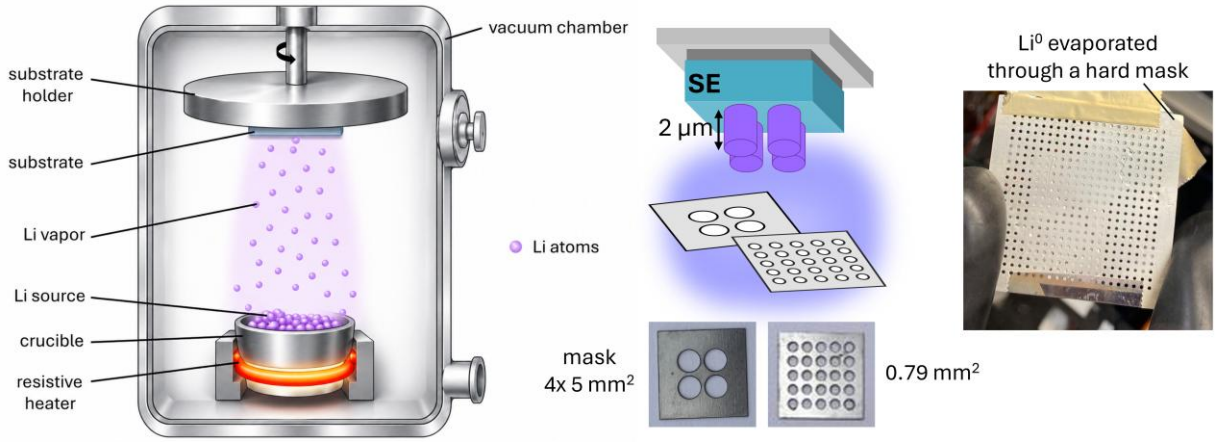


Figure 2.3 - Schematic representation of the thermal evaporation process used for Li metal anode deposition and shadow masks used to pattern independent Li reservoirs on top of the solid electrolyte layer.

Thermal evaporation is particularly attractive for the preparation of lithium metal anodes in thin-film batteries, since it enables the deposition of ultrathin Li layers ranging from tens of nanometers to a few micrometers under clean and controlled vacuum conditions. Compared with conventional rolled Li foils, evaporated Li films can offer improved thickness control, better surface homogeneity, and higher purity, since evaporation preferentially transfers metallic Li while many impurity-containing species remain in the source. This is especially relevant for thin-film and low-excess-Li battery architectures, where the thickness, purity, and interfacial quality of the Li anode strongly influence electrochemical performance. Evaporated Li electrodes have been used for several decades in all-solid-state thin-film microbatteries, commonly in combination with LiPON solid electrolytes, and have also been reported to improve the effective contact at solid electrolyte/Li interfaces.[51,98–101]

In this thesis, resistive thermal evaporation of Li metal anodes was employed using a Nexdep evaporator (Angstrom Engineering Inc), at the Laboratory for Thin Films and Photovoltaics, in EMPA. The deposition was carried out from Li metal pellets (99+%, Thermo Fischer Scientific Inc.) using a stainless-steel crucible arc-coated with alumina. Lithium layers with a thickness of 2 µm were deposited on the LiPON solid electrolyte surfaces at a rate of 25 Å s^{-1} under a vacuum of 10×10^{-6} mTorr. Shadow masks were used to define independent Li reservoirs for separated cells on the same substrate and to control the anode geometry, with active areas of either 5 or 0.79 mm^2 depending on the cell configuration. A schematic representation of the thermal

evaporation process and the shadow-mask configuration used to define the Li anode area is shown in **Figure 2.3**. The evaporation system was integrated into an Ar-filled glovebox line for thin-film battery fabrication, allowing in situ transfer between the sputtering and evaporation chambers and minimizing exposure of the Li metal and solid electrolyte layers to air and moisture.

2.2.4 Rapid Thermal Processing (RTP)

RTP is a short-duration thermal annealing technique widely used in the semiconductor manufacturing industry. This method allows fast processing of silicon wafers by rapidly heating them to high temperatures (200 – 1500 °C) within seconds using high-intensity lamps, such as tungsten halogen lamps or lasers. Thermocouples and pyrometers monitor temperatures to ensure that the samples are heated and cooled according to the programmed profile with ramp rates typically ranging from 20 to 200°C s^{-1}. In contrast to conventional furnace treatments, RTP can largely reduce the thermal budget of the fabrication process. Depending on the heating source and process design, rapid annealing technologies can operate over very different time scales. Conventional lamp-based rapid thermal annealing typically involves dwell times in the order of seconds, whereas flash-lamp, dynamic surface and nanosecond laser annealing can reduce the effective annealing time to the millisecond, microsecond and nanosecond regimes, respectively. These approaches were originally developed to achieve high-temperature activation while limiting unwanted diffusion processes in semiconductor devices.[102,103]

In this context, RTP is particularly attractive for thin-film systems, where post-deposition crystallization or microstructural optimization is often required without exposing the complete stack to long high-temperature treatments. Previous works have demonstrated its effectiveness for different functional oxide films, including highly oriented $LiTaO_3$ thin films prepared by sol–gel processing, crystalline $LiCoO_2$ cathodes for all-solid-state thin-film batteries, and dense Gadolinium-Doped Ceria (GDC) diffusion barrier layers for solid oxide cells. [104–106]

In this thesis, the RTP treatments were carried out using an ANNEALSYS AS-One 100 system, which consists of a stainless-steel cold-wall chamber equipped with parallel infrared halogen lamps, that provide radiative heating of the sample stage. The samples were placed on a silicon wafer carrier supported by quartz pins inside the chamber (**Figure 2.4**). During processing, the chamber walls are water-cooled, while the lamps are air-cooled, enabling fast thermal cycling and limiting heating of the surrounding components. Temperature control is achieved using an optical pyrometer positioned below the wafer carrier, while K-type thermocouples can be used for calibration and for monitoring processes at lower temperatures. The system also allows treatments under different process gases, which is important for controlling oxidation or reduction during annealing.

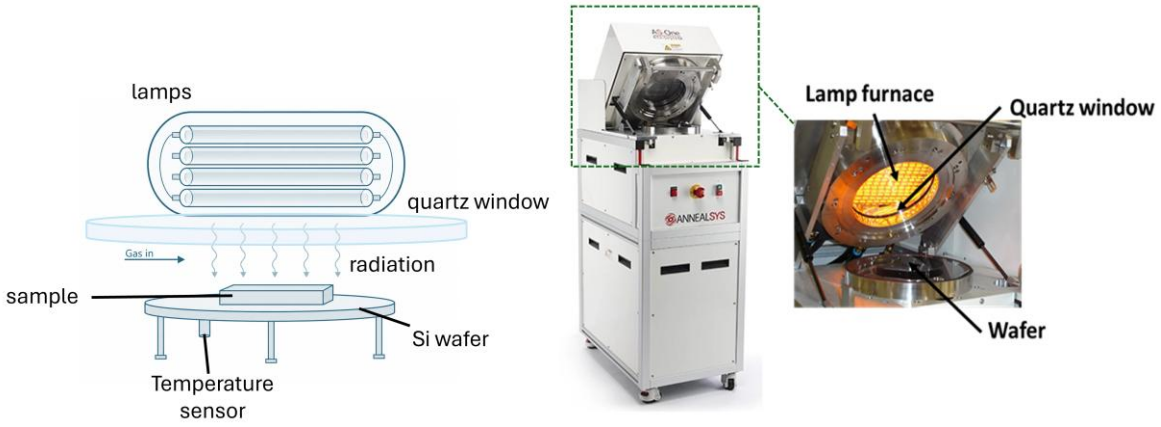


Figure 2.4 - Schematic representation rapid thermal processing and photographs of the ANNEALSYS AS-One 100 system equipment used for post-deposition thermal treatments of thin films.

In the experiments reported in this work, the RTP chamber pressure was fixed at 250 mbar, while the heating/cooling ramp rate was set to either 10 or 50 °C s^{-1}, depending on the specific experiment. The maximum temperature, dwell time and processing atmosphere were adjusted according to the film composition and the stack configuration. For LATP single layers, RTP treatments were explored over a broad temperature window, typically between 700 and 1000 °C, with short dwell times ranging from 1 to 60 s under either Ar or O_2 atmospheres. A longer 300 s treatment was also performed to assess the effect of extended thermal exposure. For LFP single layers, milder RTP conditions were employed, mainly at 700 °C for 60 s under Ar. For LFP/LATP bilayers, the RTP window was restricted mainly to Ar atmospheres, with treatments between 800 and 900 °C and dwell times from 1 to 60 s. Overall, RTP was selected as a processing route to access high-temperature annealing conditions under reduced thermal budgets, enabling the balance between LATP crystallization, ionic conductivity enhancement, and interfacial stability in PLD-grown phosphate-based thin-film systems to be evaluated.

2.3 Structural, morphological, and elemental characterization

A comprehensive set of structural, morphological, and compositional characterization techniques was employed to correlate thin-film properties with processing conditions and electrochemical performance.

2.3.1 X-ray diffraction (XRD)

X-ray diffraction (XRD) was used in this thesis as one of the main techniques to evaluate the crystalline structure of the prepared materials. The technique provides information on phase formation, crystallinity, lattice-related features, and, in thin films, possible preferential orientation. Its relevance arises from the fact that X-ray wavelengths are comparable to interatomic distances in crystalline solids, allowing the periodic arrangement of atoms to be probed through diffraction phenomena.

In a crystalline material, atoms are arranged in periodically repeated planes. When an incident monochromatic X-ray beam interacts with this ordered structure, part of the radiation is scattered by the atoms in the lattice. For most incident angles, the scattered waves cancel each other out. However, at specific angles, the waves scattered from consecutive crystallographic planes remain in phase and produce constructive interference. These constructive interference conditions generate diffraction peaks, whose angular positions are characteristic of the interplanar distances and symmetry of the crystalline phase. Therefore, the resulting diffraction pattern acts as a structural fingerprint of the material.

The diffraction condition is commonly expressed by Bragg's law:

$$n\lambda = 2d_{hkl}\sin\theta \tag{2.1}$$

where n is an integer corresponding to the diffraction order, λ is the wavelength of the incident X-ray beam, d_{hkl} is the spacing between crystallographic planes with Miller indices (hkl), and θ is the diffraction Bragg angle. This relation can be understood by considering the additional distance travelled by X-rays scattered from adjacent lattice planes. Constructive interference occurs when this path difference is equal to an integer multiple of the X-ray wavelength.

Depending on the type of sample and the depth region of interest, two different XRD geometries were used in this work: conventional θ-2θ scans and grazing-incidence X-ray diffraction (GIXRD). In conventional θ-2θ geometry, typically implemented in Bragg–Brentano configuration, the incident angle and detector angle are coupled. The sample is tilted by an angle θ, while the detector moves at 2θ, allowing the diffracted beam to be collected under the specular diffraction condition. This geometry probes planes predominantly parallel to the sample surface and generally provides a relatively large penetration depth. For this reason, it is well suited for the analysis of powders, ceramic targets, and bulk-like materials, where the diffracted signal originates from a significant sample volume. For thin-film samples, conventional θ-2θ measurements can be limited by the strong contribution of the substrate or current collector, especially when the film thickness is low or when the underlying substrate is highly crystalline or metallic. Therefore, grazing-incidence X-ray diffraction was also employed when enhanced surface sensitivity was required . In GIXRD, the incident angle is fixed at a shallow value chosen carefully with respect to the material's critical angle for total external reflection. Below this critical angle, X-rays are completely reflected, creating an evanescent wave that only penetrates the top few nanometers of the sample surface. By setting the fixed incident angle slightly above this critical threshold, the X-ray path length within the film is maximized while drastically reducing penetration into the underlying substrate. This configuration effectively isolates and enhances the diffraction signal of the thin film while minimizing dominant background contributions from highly crystalline or metallic current collectors like Pt or ITO. In addition, because the incident and diffracted angles are not coupled as in conventional geometry, GIXRD can sample a broader population of crystallographic planes, and the relative peak intensities may differ from those obtained in the conventional geometry, even when the peak positions remain governed by Bragg's law.

A comparison between the conventional θ-2θ and grazing-incidence XRD geometries used in this thesis is schematically represented in **Figure 2.5**.

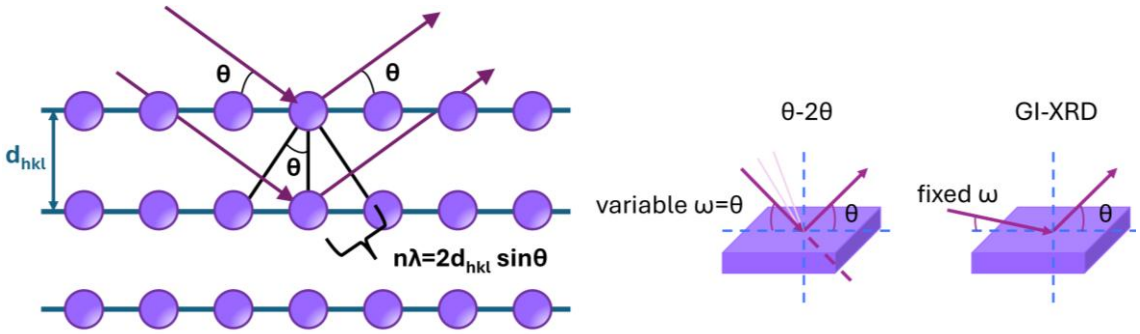


Figure 2.5 - Schematic representation of X-ray diffraction geometry, including Bragg diffraction from crystallographic planes and the comparison between conventional θ-2θ XRD and grazing-incidence XRD configurations.

In the present work, conventional θ-2θ scans were performed to ceramic target of $LiFePO_4$ and LATP thin-film samples using a Bruker D8 Advance diffractometer equipped with Cu Kα radiation (λ = 1.54 Å), Ni filter and a LynxEye 1D detector.

GIXRD measurements were carried out for LFP thin-film samples deposited on Pt or ITO using a X'pert Pro MRD from Malvern-Panalytical diffractometer, at the facilities of ICN2, equipped with a horizontal ω-2θ goniometer (320 mm radius) in a four-circle geometry and a ceramic X-ray tube with Cu Kα radiation (λ = 1.54 Å). The detector used is a PIXcel which is a fast X-ray detector based on Medipix2 technology with a 256x256 pixels array. The measurements were set with ω=0.8º, 2θ range = 10-45º, step size: 0.02º, time per step: 500s.

Phase identification was performed using X'Pert HighScore Plus® software in combination with the ICDD reference database. Throughout this thesis, XRD was used to confirm the formation of the olivine $LiFePO_4$ phase in cathode thin films and the NASICON-type LATP structure in solid electrolyte layers. The corresponding structural results are discussed in **Chapters 3** and **4**, where they are correlated with deposition conditions, thermal treatments, morphology, and electrochemical performance.

2.3.2 Grazing Incidence Wide-Angle X-ray Scattering (GIWAXS)

To further probe the structural arrangements and crystallographic texture of the battery thin films beyond the capabilities of laboratory diffractometers, synchrotron-based GIWAXS was employed. This advanced technique combines grazing-incidence surface sensitivity with high-brilliance synchrotron radiation and pixelated 2D area detectors, allowing the collection of vast regions of reciprocal space in a single exposure. Unlike conventional 1D scans that sample a very restricted population of crystallographic planes parallel to the surface, 2D GIWAXS captures a comprehensive map of both the in-plane (q_{xy}) and out-of-plane (q_z) scattering vectors. This makes

it an invaluable method for evaluating preferred crystal grain orientation and structural texturing within thin-film architectures.[107]

However, GIWAXS is a highly complex technique involving non-trivial data treatment. The geometry of a flat area detector intersecting a curved Ewald sphere introduces severe spatial distortions that require rigorous re-meshing and correction algorithms. Furthermore, the planar thin-film geometry inherently blocks a portion of the diffracted rays pointing directly along the surface normal, manifesting as a diagnostic "missing wedge" of information along the q_z axis in the reconstructed q-space. Given these inherent complexities, GIWAXS was utilized in this thesis primarily as an exploratory tool to complement standard laboratory XRD techniques. Specifically, experiments were carried out at the NCD-SWEET beamline of the ALBA Synchrotron (Cerdanyola del Valles, Barcelona, Spain). The measurements leveraged a granted beam time proposal aimed at exploring angle-dependent GIWAXS. By systematically varying the grazing incidence angle from values below the critical angle to angles well above it, the study aimed to retrieve depth-resolved structural information regarding phase purity, crystallization gradients, and interfacial structures throughout the depth of the battery thin films. The fundamental analytical and experimental framework governing these synchrotron measurements follows the extensive protocols outlined by Steele *et al.* (2023), a comprehensive guide co-developed by the ALBA NCD-SWEET beamline scientists.[107]

2.3.3 Raman spectroscopy

Raman spectroscopy is a non-destructive vibrational spectroscopy technique widely used for the structural and chemical characterization of solid materials. The technique is based on the interaction between monochromatic light, typically provided by a laser source, and the vibrational modes of a material. When the incident photons interact with the sample, most of the scattered radiation preserves the same energy as the incident light, corresponding to elastic or Rayleigh scattering. However, a small fraction of the photons undergoes inelastic scattering, exchanging energy with the vibrational or rotational modes of the material. This process gives rise to Raman scattering, which appears as a shift in frequency with respect to the excitation laser and is commonly reported as Raman shift in cm^{-1}.[108]

The energy shift observed in a Raman spectrum is directly related to the vibrational energy of specific chemical bonds or structural units. Therefore, each crystalline phase, local coordination environment, or molecular group can present characteristic Raman bands, which act as a fingerprint of the material. Raman spectroscopy is particularly useful for identifying crystalline phases, detecting secondary phases, evaluating local structural disorder, and following changes in bonding environments that may not be easily detected by conventional X-ray diffraction, especially in thin films, poorly crystallized materials, or nanostructured systems.

The Raman measurements in this work were performed using a HORIBA Scientific iHR320 spectrometer equipped with a HORIBA syncerity CCD (1024 x 256, pixel size 26 μm x 26 μm), with green laser (λ = 532 nm), 100x magnification objective and 1800 lines mm^{-1} grating. The laser

power and acquisition time were adjusted according to the sample response in order to obtain a sufficient signal-to-noise ratio while minimizing local heating, laser-induced degradation, or modification of the thin-film surface. For LFP single layers in **Chapter 3**, a laser power of 0.925 mW was used, with 10s of acquisition time. Whereas for LATP and LFP/LATP bilayers in **Chapter 4**, 9.25 mW and 2s were employed.

2.3.4 Atomic Force Microscopy (AFM)

AFM is a non-destructive surface characterization technique for thin films, that maps surface topography with sub-nanometer resolution to determine key parameters like roughness, grain size, film thickness, and structural defects. It is based on the controlled scanning of a sharp probe, mounted at the end of a flexible cantilever, across the sample surface. During scanning, the tip-surface interaction is affected by short- and long-range forces, including van der Waals, electrostatic, adhesive and repulsive contributions. These interactions modify the cantilever deflection or oscillation response, which is monitored optically by reflecting a laser beam from the back side of the cantilever onto a position-sensitive photo detector. The recorded signal is then converted into a three-dimensional topographic map of the surface. AFM can be operated in different modes, including contact, non-contact and tapping modes. In tapping mode, the cantilever oscillates and briefly taps the surface of the sample at the bottom of its swing.[109]

In this work, a Park Systems XE15 AFM operating in tapping mode was employed to evaluate the nanoscale surface topography and root-mean-square roughness (RMS) of LFP thin films and bare Pt and ITO current collectors, as discussed in **Chapter 3**.

2.3.5 Scanning electron microscopy (SEM)

SEM is a powerful technique for the morphological and microstructural analysis of materials, in which a focused electron beam is scanned across the sample surface, producing different electron–matter interactions within a near-surface interaction volume. The emitted signals provide information about the surface morphology, local contrast, and internal features of the analyzed material. Among the detected signals, secondary electrons and backscattered electrons are the most commonly used for microstructural characterization. Secondary electrons are generated close to the sample surface and are therefore highly sensitive to topographic variations, making them especially suitable for evaluating surface morphology, grain structure, porosity, and defects. Backscattered electrons, in contrast, originate from deeper regions of the interaction volume and provide contrast related mainly to differences in atomic number, which can be useful for distinguishing layers or phases with different compositions.[110,111]

In this thesis, SEM was employed to investigate the morphology and structural integrity of the deposited thin films. Top-view images were used to examine surface coverage, grain morphology, roughness-related features, cracks, and defects, whereas cross-sectional SEM was used to determine film thickness and to assess the continuity of the different layers in the thin-film stacks. This analysis as particularly relevant for evaluating the growth of LFP and LATP films, as well as the preservation of the layers after deposition and thermal treatments. SEM measurements were

carried out using a Zeiss Auriga SEM at low 2 kV and 2 mm working distance to minimize charging effects and to gain higher resolution.

2.3.6 Transmission electron microscopy (TEM/STEM)

Transmission electron microscopy (TEM) and scanning transmission electron microscopy (STEM) are advanced electron microscopy techniques that enable the investigation of materials with nanometric to atomic-scale spatial resolution. In contrast to surface-sensitive techniques such as SEM, TEM-based methods require electron-transparent specimens, typically prepared as thin cross-sectional lamellae with thicknesses in the range of a few tens of nanometers.

In TEM, a high-energy electron beam is transmitted through the thin specimen, and the image is formed from the electrons that pass through or are scattered by the material. Image contrast can arise from differences in mass-thickness, diffraction conditions, or phase contrast. Bright-field and dark-field imaging provide information about microstructural features, defects, grains, and crystalline regions, while high-resolution TEM can be used to directly visualize lattice fringes and local crystallographic ordering. In STEM mode, the incident electron beam is focused into a fine probe and raster-scanned across the sample. The transmitted and scattered electrons are then collected by detectors positioned at different angular ranges, allowing complementary imaging modes to be obtained. Among the STEM imaging modes, bright-field (BF), annular dark-field (ADF), and high-angle annular dark-field (HAADF) are commonly used. HAADF-STEM is especially useful for multilayer thin-film systems because the intensity of the detected signal depends strongly on the atomic number of the elements present in the sample, providing so-called Z-contrast. As a result, layers or regions with different average composition can be distinguished more clearly, making this technique particularly suitable for evaluating interfaces, interdiffusion, secondary phases, and local heterogeneities.[112]

Chemical analysis can be performed in STEM by combining imaging with energy-dispersive X-ray spectroscopy (EDX). In this mode, characteristic X-rays emitted from the sample under electron-beam irradiation are collected to generate elemental maps or line profiles.[111] Electron energy-loss spectroscopy (EELS) can also be coupled to TEM or STEM to obtain complementary chemical information. EELS is based on the analysis of the energy lost by transmitted electrons after inelastic interactions with the sample. The resulting spectra provide information about elemental composition, bonding environment, oxidation state, and electronic structure. Compared with X-ray-based microanalysis, EELS can be particularly useful for detecting light elements and for evaluating changes in local chemistry, although careful acquisition conditions are required to minimize possible beam-induced damage in sensitive battery materials.

Crystallographic information from TEM/STEM images can be further extracted using Fast Fourier Transform (FFT) analysis of high-resolution images, which allows local lattice spacings and crystallographic orientations to be evaluated. Selected area electron diffraction (SAED) can also be employed to obtain diffraction patterns from specific regions of the lamella, providing information

about crystallinity, phase formation, preferred orientation, and the coexistence of crystalline and amorphous domains at the nanoscale.

In **Chapter 4** of this thesis, TEM-based characterization was applied to selected LFP/LATP thin-film architectures in order to investigate the local microstructure, interfacial stability, and elemental distribution across the cathode/electrolyte stack. The measurements were carried out in collaboration at the Department of Electronics and Biomedical Engineering and the Institute of Nanoscience and Nanotechnology (IN2UB) at the University of Barcelona. Cross-sectional TEM lamellae were prepared from representative regions of the samples, before and after electrochemical test, using focused ion beam scanning electron microscopy (FIB-SEM, Thermo Fisher Scientific Helios 5). High-resolution TEM images were acquired using a JEOL JEM 2010F, while HAADF-STEM imaging, STEM-EDX elemental mapping, and EELS analyses were performed using a JEOL NeoARM microscope. Both instruments operated at an accelerating voltage of 200 kV and were located at the CCiTUB facilities, corresponding to the ICTS ELECMI node in Barcelona. These analyses were used to evaluate the continuity of the deposited layers, the structural integrity of the LFP/LATP interface, possible intermixing between the cathode and electrolyte, and local chemical modifications induced by rapid thermal processing or electrochemical cycling. All these measurements and analyses were done in collaboration with Dr. Lluís Yedra.

2.3.7 Glow Discharge Optical Emission Spectroscopy (GDOES)

Glow Discharge Optical Emission Spectroscopy (GDOES) is a destructive technique is particularly suitable for multilayer systems because it enables elemental analysis as a function of depth. In a glow discharge source, the sample acts as the cathode and is exposed to a low-pressure Ar plasma. When a sufficiently high voltage is applied, energetic Ar ions progressively sputter the sample surface, removing material layer by layer. The sputtered atoms are excited in the plasma and subsequently relax by emitting light at characteristic wavelengths, which is collected by a collection of optical spectrometers to identify the elements present in the analyzed region.

For lithium-ion battery materials, GDOES is especially useful because it can provide depth-resolved information on light elements such as Li, which are difficult to quantify by many conventional techniques. This technique has been successfully used to obtain depth profiles from the electrode surface to the current collector and showing that the Li emission intensity could be correlated with Li contents determined by ICP-MS.[113] Recently, work on PLD-grown $LiMn_2O_4$ thin-film solid-state microbatteries in our group used GDOES to evaluate the compositional depth profile of the cathode, revealing variations in the Li signal across the film thickness (<1μm) and highlighting the usefulness of the technique for detecting Li-rich regions in complex oxide thin films.[114]

In this thesis, GDOES measurements were performed to determine the compositional depth profiles across the LFP-based thin films deposited by PLD on Pt and ITO substrates in **Chapter 3.** The analyses were carried out using a Spectruma GDA 750 HR instrument equipped with a 2.5

mm-diameter anode. Measurements were conducted under 700 V and 2.5 hPa Ar pressure, conditions that promoted stable sputtering and flat and homogeneous crater, enabling reproducible depth profiling to compare different samples (**Figure 2.6**).

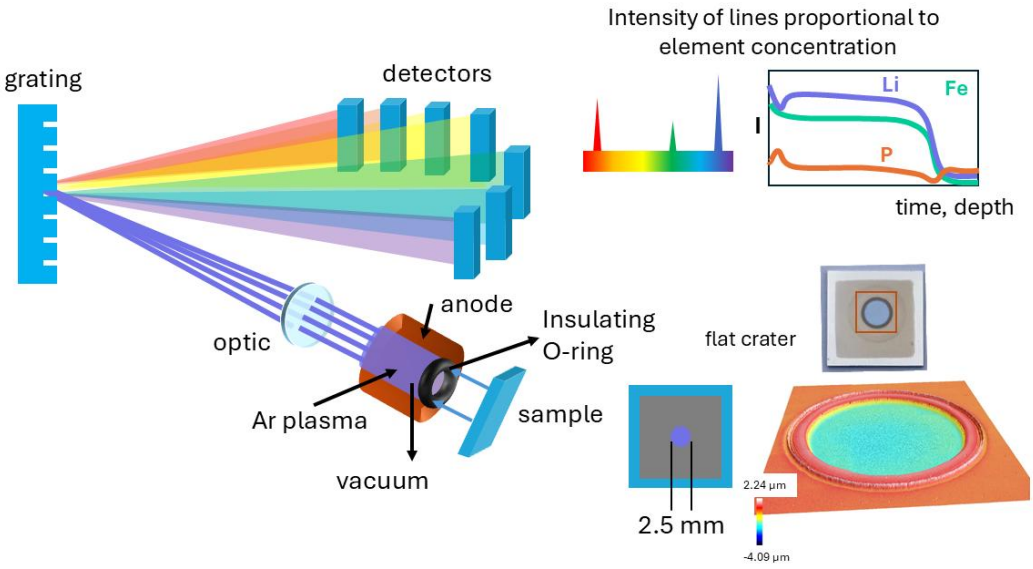


Figure 2.6 - Schematic representation of the Glow Discharge Optical Emission Spectroscopy (GDOES) principle. A representative confocal microscopy profile of the GDOES crater and a photograph of the analyzed samples are also shown.

2.4 Electrochemical characterization

2.4.1 Electrochemical Impedance Spectroscopy (EIS)

Electrochemical impedance spectroscopy (EIS) is used to evaluate the frequency-dependent response of electrochemical systems under a small alternating perturbation. In potentiostatic electrochemical impedance spectroscopy. In potentiostatic EIS (PEIS), a low-amplitude sinusoidal voltage is applied, and the corresponding sinusoidal current response is recorded). The impedance is then obtained as a complex, frequency-dependent quantity, Z (ω), which describes how the system opposes the flow of alternating current at each applied frequency.

To ensure that the measured response reflects the intrinsic properties of the system, the AC perturbation must be sufficiently small for the electrochemical cell to remain within the linear response regime. Under these conditions, the current response occurs at the same angular frequency as the applied voltage, but it may be shifted in phase due to capacitive, resistive, inductive, or diffusional contributions (**Figure 2.7**). The time-dependent voltage and current signals can be described as:

$$V(t) = V_m \cdot \sin(\omega t) \quad (2.2)$$

$$I(t) = I_m \cdot \sin(\omega t + \varphi) \quad (2.3)$$

where V_m and I_m are the voltage and current amplitudes, respectively, ω is the angular frequency ($\omega = 2\pi f$), and φ is the phase difference between the applied voltage and the measured current.[115–117]

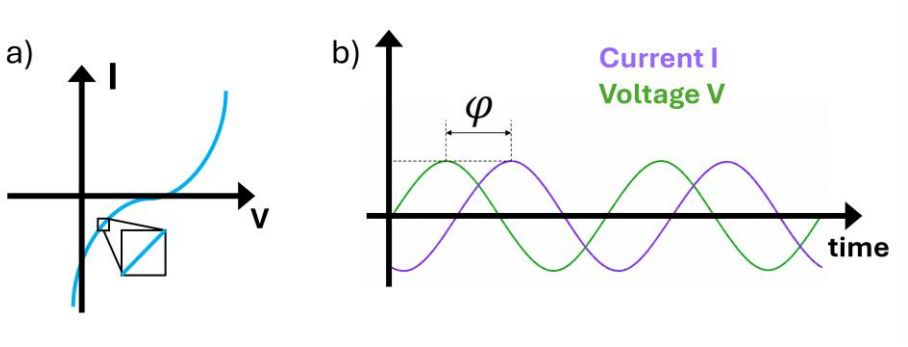


Figure 2.7 - Representation EIS principle with (a) generalized current-voltage curve showing the linear approximation for small perturbations and (b) sinusoidal voltage perturbation and corresponding current response as a function of time, showing the phase shift φ.

The complex impedance Z(ω) is calculated from the ratio between applied voltage and current response in the frequency domain, and can be expressed in terms of real and imaginary components:

$$Z(\omega) = \frac{V(\omega)}{I(\omega)} = |Z|e^{j\varphi} = |Z|(\cos\varphi + j\sin\varphi) = Z' + jZ'' \quad (2.4)$$

where Z' is the real component of the impedance, associated mainly with resistive contributions, and Z" is the imaginary component, associated with phase-shifted processes such as capacitive, inductive, and diffusion-related responses.

In real electrochemical systems, the measured impedance rarely arises from a single ohmic contribution. Instead, the total response reflects the combined effect of several processes occurring at different length scales and time constants. These may include ionic conduction through the electrolyte or solid electrolyte, transport across grain boundaries, charge accumulation at interfaces, charge transfer at electrode/electrolyte boundaries, interfacial polarization, and diffusion of electroactive species within the electrolyte or electrode material. Because each process responds differently to the applied AC frequency, EIS allows these contributions to be partially separated in the frequency domain.

The impedance response is commonly analyzed using both Bode and Nyquist plots. Bode plots show the impedance magnitude and phase angle as a function of frequency, making them useful for identifying the frequency range in which each process dominates. Nyquist plots, in contrast, display the imaginary component of the impedance as a function of the real component, allowing resistive intercepts, semicircular arcs, and diffusion-related features to be visualized more

directly. In practice, the spectra are interpreted by fitting the experimental data to equivalent electrical circuits whose elements are selected according to the physical processes expected for the system. Resistors are used to describe ohmic or kinetic resistances, capacitors or constant phase elements are used to represent ideal or non-ideal capacitive behavior, and Warburg-type elements are used when the response is influenced by mass transport.

A representative example is the Randles circuit, shown in **Figure 2.8**, which is frequently used as a first approximation for faradaic electrochemical systems. In this model, the resistance, R_u, in series with a parallel interfacial branch, containing the double-layer capacitance, C_{dl}, and the faradaic pathway composed of the charge-transfer resistance, R_{ct}, and the Warbug diffusion impedance, Z_w. The corresponding Nyquist response contains a semicircular region at higher and intermediate frequencies, associated mainly with charge-transfer kinetics and double-layer charging, followed by a low-frequency linear region related to mass-transport control. The high-frequency intercept provides Ru, while the characteristic frequency of the semicircle is related to the interfacial time constant, approximately given by $\omega_{max} = 1/(R_{ct}C_{dl})$ for ideal RC response. Thus, the Randles circuit provides a useful framework for connecting the shape of the impedance spectrum with physically meaningful electrochemical processes.

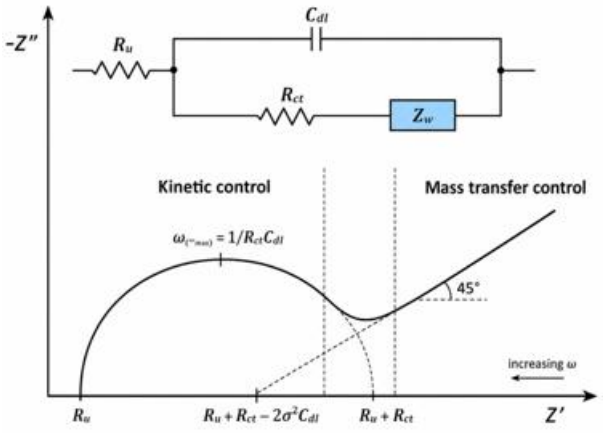


Figure 2.8 - Randles equivalent circuit and corresponding Nyquist response for a faradaic electrochemical system. Reproduced from Lazanas & Prodromidis.[117]

In this thesis, temperature-dependent PEIS was used to investigate the ionic transport properties of LATP thin-film solid electrolytes. Measurements were performed on LATP layers deposited on Si_3N_4 insulating substrates using parallel Au electrodes in an in-plane configuration, which enabled the effective lateral resistance of the films to be determined. The samples were mounted in a Linkam LTS600 probe station equipped with a resistive heating stage, as shown in **Figure 2.9a**, and the impedance response was recorded using a Novocontrol Alpha-A impedance spectrometer. Spectra were acquired from 10 MHz to 100 mHz with an AC perturbation amplitude of 100 mV and no applied DC bias. All measurements were carried out in ambient air. From the

fitted resistance values, the effective ionic conductivity was calculated using the geometrical factor of the in-plane electrode configuration, while the temperature-dependent conductivity was used to extract the activation energy for Li^+ transport, as discussed in **Chapter 4**.

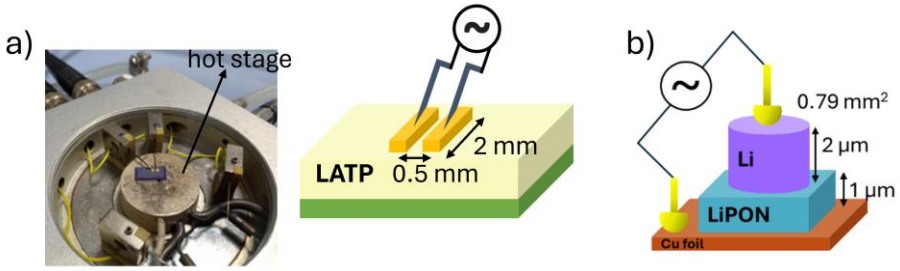


Figure 2.9 - (a) Station setup and schematic of the system for in-plane PEIS measurements of Au/LATP/Au mounted on a resistive heating stage. (b) Schematic of the system for through-plane PEIS measurements of Cu/LiPON/Li stack.

PEIS was also used to characterize LiPON solid electrolyte layers and complete all-solid-state thin-film batteries (LFP/LiPON/Li), as discussed in **Chapter 5**. In this case, samples measured inside an Ar-filled glovebox in order to avoid exposure of the Li metal anode and LiPON-containing stacks to air and moisture. The impedance spectra were collected using a Squidstat Prime potentiostat (Admiral Instruments) with an AC perturbation amplitude of 10 mV and no DC bias, in the frequency range of 2 MHz-200mHz for the Cu/LiPON/Li stack (**Figure 2.9b**), and 2 MHz-500 mHz for the LFP/LiPON/Li all-solid-state device. For these measurements, the electrochemical response was acquired in the through-plane configuration of the full multilayer stack, with the active area defined by the evaporated Li electrode.

2.4.2 Cyclic Voltammetry (CV)

CV is a dynamic potentiostatic technique widely used to investigate the electrochemical activity of electrode materials. In this method, the potential of the working electrode is swept linearly with time between two selected potential limits, while the resulting current response is continuously recorded. Once the upper or lower potential limit is reached, the direction of the scan is reversed, generating a triangular potential waveform (**Figure 2.10a**). The resulting voltammogram, in which current is plotted as a function of applied potential, provides information on the redox processes occurring in the electrode, the potential range in which they take place, and their degree of reversibility.

The position of the redox peaks in a cyclic voltammogram is related to the equilibrium potential of the corresponding electrochemical reaction. For a generic redox couple involving an oxidized species O and a reduced species R, this equilibrium potential can be described by the Nernst equation:

$$E = E^{0\prime} + \frac{RT}{nF}\ln\frac{(a_O)}{(a_R)} \tag{2.5}$$

where $E^{0'}$ is the formal potential of the redox couple under the experimental conditions, R is the gas constant, T is the absolute temperature, n is the number of electrons transferred, F is the Faraday constant, and a_O and a_R are the activities of the oxidized and reduced species, respectively. At equilibrium, the electrode potential is determined by the relative activities of both redox states. In insertion electrodes such as $LiFePO_4$, this relation provides the thermodynamic basis for the potential associated with the $FePO_4/LiFePO_4$ redox couple, while deviations from the ideal equilibrium response arise from kinetic and transport limitations.

For battery electrodes, oxidation and reduction processes appear as anodic and cathodic current peaks, respectively (**Figure 2.10b**). The peak position is related to the potential of the corresponding redox reaction, while the peak intensity reflects the amount of charge involved and the kinetics of the electrochemical process. In an ideal reversible system, the oxidation process observed during the forward scan is followed by a corresponding reduction process during the reverse scan. In practical battery materials, however, the peak separation, peak broadening, and changes in peak intensity can be affected by charge-transfer resistance, ion diffusion, structural transformations, interfacial polarization, and side reactions. Therefore, CV is particularly useful as a diagnostic technique to identify electrochemically active phases and to evaluate the reversibility of lithium insertion and extraction processes.

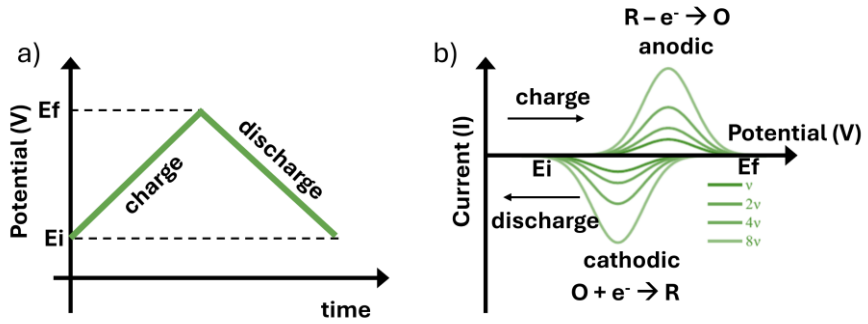


Figure 2.10 - Schematic representation of cyclic voltammetry: (a) triangular potential waveform applied between two selected potential limits and (b) representative current response showing anodic and cathodic peaks associated with oxidation and reduction processes.

Measurements performed at different scan rates (ν) can be used to assess whether the electrochemical response is mainly controlled by diffusion, surface-related processes, or kinetic limitations. The scan rate is defined as the rate at which the applied potential changes with time:

$$\nu = \frac{dE}{dt} \tag{2.6}$$

For a reversible redox process limited by semi-infinite linear diffusion, the peak current is described by the Randles–Sevcik equation. After normalization by the electrode area, this relation can be written as:

$$j_p = \frac{i_p}{A} = 0.4463\ nFC\left(\frac{nFD\nu}{RT}\right)^{1/2} \quad (2.7)$$

where j_p is the peak current density, i_p is the peak current, A is the electrode area, C is the concentration of the electroactive species, D is the diffusion coefficient, and ν is the scan rate. Therefore, under diffusion-controlled conditions, the peak current density scales linearly with the square root of the scan rate ($j_p \propto \nu^{1/2}$). Although the Randles–Sevcik equation was originally derived for reversible solution-phase redox systems, the j_p–$\nu^{1/2}$ dependence is commonly used in insertion-type electrodes as an indication of diffusion-related lithium transport. In $LiFePO_4$ thin films, the apparent response may also include contributions from solid-state Li transport, phase-boundary motion, film texture, interfacial kinetics, and microstructural heterogeneity.

A more general description of the scan-rate dependence can be obtained using the empirical power-law relation:

$$j_p = a(\nu)^b \quad (2.7)$$

where a is a proportionality constant and b indicates the dominant charge-storage mechanism. Values of b close to 0.5 are generally associated with diffusion-controlled behavior, whereas values approaching 1 indicate surface-controlled or capacitive contributions.

This approach was used in **Chapter 3** to compare the kinetic response of the PLD-grown LFP thin films in a three-electrode half-cell configuration (**Figure 2.12a**) . The LFP thin film on Pt or ITO substrate was used as the working electrode (WE), while a Pt electrode and an Ag/AgCl introduced in 3 M KCl solution electrode were used as counter (CE) and reference (RE) electrodes, respectively. The measurements were carried out in 1 M Li_2SO_4 aqueous electrolyte (AE), with the exposed active area of the film defined by an O-ring. The same setup was used to measure the LFP/LATP bilayer in **Chapter 4**, where the top LATP solid electrolyte was in contact with the liquid.

2.4.3 Chronopotentiometry (CP)

CP is a galvanostatic electrochemical technique in which a constant current is applied to the cell while the potential response is recorded as a function of time. In the context of battery characterization, this method is commonly referred to as galvanostatic charge–discharge cycling, since the current direction is reversed between charge and discharge steps. While cyclic voltammetry is based on controlling the electrode potential and measuring the resulting current response, CP imposes a defined current and follows the voltage evolution. During a CP measurement, a positive or negative current is applied until the potential reaches a predefined cut-off value. For a charge step, the potential typically increases until the upper voltage limit, E_2, is reached, while during discharge the current polarity is reversed and the potential decreases toward the lower voltage limit, E_1, as schematically represented in **Figure 2.11**. The shape of the resulting voltage–capacity profile reflects the electrochemical processes taking place in the material. In insertion electrodes, voltage

plateaus or sloping regions are associated with lithium extraction and insertion reactions, while the difference between charge and discharge profiles provides information on polarization and kinetic limitations. Therefore, the x axis is directly associated with the amount of charge storage in the system.

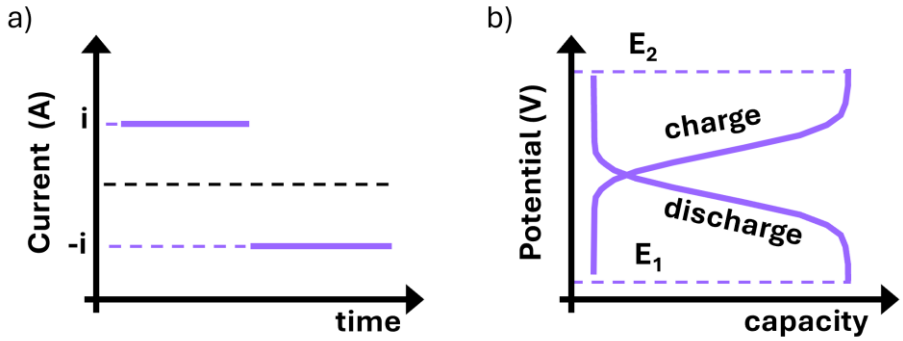


Figure 2.11 - Schematic representation of chronopotentiometry/galvanostatic charge–discharge measurements. (a) Constant current profile applied during charge and discharge steps, where the current polarity is reversed between both processes. (b) Representative potential–capacity response obtained between the lower and upper cut-off potentials.

In this thesis, CP measurements were used to evaluate the electrochemical performance of both LFP thin-film and LFP/LATP bilayers in half-cell configuration, in **Chapter 3** and **Chapter 4** respectively, and of complete all-solid-state thin-film batteries (LFP/LiPON/Li and LFP/LATP/LiPON/Li) in **Chapter 5**. For the half cells, liquid-electrolyte tests were carried out using the three-electrode setup in **Figure 2.12a**. The all-solid-state cells stacks are represented in **Figure 2.12b**. The specific measurement conditions, as well as geometric dimensions (thicknesses and areas) are detailed in the corresponding results chapters.

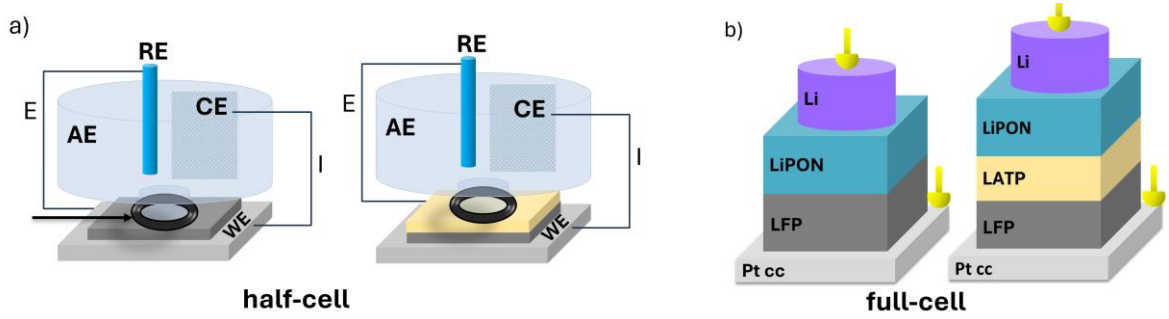


Figure 2.12 - Schematic representation of the electrochemical configurations used in this thesis: (a) three-electrode half-cell and (b) all-solid-state full-cell architectures based on LFP/LiPON/Li and LFP/LATP/LiPON/Li stacks.

Chapter 3

Fabrication and characterization of $LiFePO_4$ thin-film cathodes

3.1 Scope and motivation of the chapter 52

3.2 Fabrication conditions and samples description 53

3.3 Influence of substrate and its temperature on thin film growth and morphology 55

3.4 Structural and compositional characterization 60

3.4.1 Phase formation and thickness-dependent crystallinity 60

3.4.2 GIWAXS analysis and interfacial phase formation 63

3.4.3 Substrate and deposition temperature effects on as-deposited films 65

3.4.4 Elemental depth distribution 68

3.4.5 Effect of post-annealing by rapid thermal processing (RTP) 71

3.5 Electrochemical characterization 73

3.5.1 Electrochemical response of LFP films deposited on Pt 73

3.5.2 Electrochemical response of LFP films deposited on ITO and influence of deposition temperature 76

3.5.3 Effect of RTP on electrochemical performance 79

3.5.4 Post-cycling analysis of the optimized LFP/ITO electrode 84

3.5.5 Asymmetric constant current charge/discharge cycles 88

3.6 Conclusions 89

3 Fabrication and characterization of LFP thin-film cathodes

3.1 Scope and motivation of the chapter

$LiFePO_4$ is a well-established cathode material for lithium-ion batteries due to its structural stability, low cost, environmental compatibility, and flat redox plateau associated with the Fe^{2+}/Fe^{3+} couple.[14,15] However, its direct implementation in thin-film battery architectures remains challenging because carbon-free $LiFePO_4$ suffers from intrinsically low electronic and ionic conductivity. In conventional composite electrodes, these limitations are mitigated not only by reducing the particle size, but also by incorporating conductive additives, designing porous electrode architectures, and enabling liquid-electrolyte infiltration throughout the electrode, thereby shortening both ionic and electronic transport pathways.[118–120] In dense thin-film electrodes, by contrast, the electrochemical response depends strongly on the crystallinity, grain orientation, microstructure, thickness, and quality of the interfaces formed during deposition, since these parameters determine both the accessible active volume and the transport pathways for Li^+ and electrons.

Within this context, this chapter investigates the fabrication and characterization of carbon-free $LiFePO_4$ thin-film cathodes deposited by pulsed laser deposition (PLD). The objective is to establish how the processing conditions control the morphology, phase formation, interfacial chemistry, and electrochemical activity of the films. Particular attention is given to the influence of substrate type, deposition temperature, and rapid thermal processing (RTP), since these parameters directly affect nucleation, grain growth, densification, crystallinity, and the formation of secondary or interfacial phases.

The chapter first examines the growth behavior of LFP films on two different conducting substrates: Pt, a highly stable metallic current collector, and ITO, a conductive transparent mixture of indium(III) oxide (In_2O_3) and tin(IV) oxide (SnO_2). Pt is used as a reference current collector for electrochemical testing and comparison with the all-solid-state cells discussed later in this thesis, while ITO is explored as an alternative current-collector configuration to modify the LFP/substrate interface and improve the accessible fraction of the cathode.

The role of deposition temperature during PLD growth is then evaluated in order to determine the conditions required to obtain crystalline and electrochemically active LFP . In parallel, selected films deposited at low-temperature are subjected to RTP to assess whether short post-deposition annealing can activate poorly crystallized layers while limiting the thermal budget of the process. This approach is also relevant for the subsequent development of LFP/LATP bilayers in **Chapter 4**, since LATP typically requires thermal treatment to improve its structural ordering, and therefore the thermal stability of the underlying LFP layer must be assessed before cathode/electrolyte integration.

Structural and compositional characterization are conducted and the observations on the microstructure, the phase formation and the interfacial reactions are correlated and linked to the electrochemical performance. Grazing-incidence X-ray diffraction, synchrotron-based GIWAXS,

Raman spectroscopy, and GDOES depth profiling are combined to evaluate the formation of olivine $LiFePO_4$, the possible presence of secondary phases, and the redistribution of Fe near the current collector. This analysis is particularly important because interfacial reactions at the earliest stages of growth can reduce the amount of electrochemically accessible LFP and therefore influence the capacity measured later in electrochemical experiments. In addition, understanding the structural and chemical stability of LFP after thermal exposure provides an essential basis for interpreting the more complex interfaces formed in LFP/LATP bilayers.

Finally, the electrochemical behavior of selected films is evaluated in aqueous-electrolyte half-cell configuration. These measurements are used as a rapid and practical way to assess the intrinsic activity of the PLD-grown LFP thin films before their integration into complete all-solid-state thin-film batteries. The electrochemical response of LFP films deposited on Pt is used as a baseline, while the LFP films deposited on ITO are used to evaluate the impact of substrate engineering and RTP on capacity, reversibility, and rate capability. These results also provide a reference for distinguishing the intrinsic LFP response from additional electrochemical contributions that may arise after integration with LATP. Overall, this chapter establishes the processing–structure–interface–performance relationships of PLD-grown LFP thin-film cathodes and provides the foundation for their subsequent integration into LFP/LiPON/Li and LFP/LATP-based solid-state battery architectures.

3.2 Fabrication conditions and samples description

Several series of $LiFePO_4$ thin films were prepared in order to investigate how deposition conditions, substrate chemistry, film thickness, and post-deposition thermal treatment influence the structural and electrochemical properties of carbon-free LFP cathodes. All LFP films discussed in this chapter were fabricated by pulsed laser deposition from a commercial $LiFePO_4$ target under Ar atmosphere. The use of an inert low-pressure atmosphere was selected to favor the stabilization of Fe^{2+} and the formation of crystalline olivine $LiFePO_4$ phase, on the comparison between films deposited at 80 mTorr and 1 mTorr Ar (**Figure A.1**, Appendix A). An argon pressure of 1 mTorr was selected for subsequent depositions.

Two main current-collector configurations were investigated: $Pt/Ti/SiO_2/Si$ and $ITO/Pt/Ti/SiO_2/Si$. Pt-coated substrates were used as the reference metallic current collector because they are compatible with electrochemical measurements and with the all-solid-state thin-film cells discussed later in this thesis. In addition, Pt has been commonly employed as a current collector for PLD-grown LFP thin films in previous studies. Based on this reference configuration, ITO-coated Pt substrates were also explored as an alternative current-collector configuration, with the aim of modifying the LFP/substrate interface, improving surface homogeneity, and increasing the electrochemically accessible fraction of the cathode.

The first group of samples was designed to evaluate the influence of deposition temperature. LFP films were deposited on Pt-based substrates at temperatures 300 and 600 ºC, while films on ITO/Pt substrates were prepared at 400, 500, and 600 ºC. These samples were used to correlate

substrate temperature with surface morphology, film densification, crystallinity, elemental redistribution, and electrochemical response.

A second group of samples was prepared to investigate the effect of film thickness. For this purpose, LFP films were deposited on Pt current collectors at 600 ºC with nominal thicknesses of approximately 120, 200, and 300 nm. These films were used to study the transition from early-stage island growth to more continuous and compact layers. The same thickness series also provides the structural and electrochemical reference for the LFP/LiPON/Li all-solid-state cells discussed in **Chapter 5**.

In order to provide some flexibility on future device fabrication and enhance compatibility with the rest of the components, the effect of processing temperature has been explored. For this purpose, a third group of samples was prepared, consisting of selected LFP films deposited on ITO/Pt substrates at 400, 500, and 600 ºC. These were submitted to RTP at 700 ºC for 60 s under Ar atmosphere, using heating and cooling ramps of 10 ºC s^{-1}. This treatment was applied to evaluate whether short thermal exposure can improve the crystallinity and electrochemical activity of films deposited at lower substrate temperature. In addition, this experiment provides relevant information for the subsequent development of LFP/LATP bilayers, since LATP generally requires thermal treatment to improve its structural ordering, and the thermal stability of the underlying LFP layer must therefore be assessed before cathode/electrolyte integration.

For electrochemical characterization, selected LFP films were evaluated in aqueous-electrolyte half-cell configuration. The 300 nm-think LFP film deposited on Pt was used as a baseline to establish the intrinsic electrochemical response of PLD-grown LFP on the metallic Pt current collector. In parallel, LFP films deposited on ITO/Pt, both as-deposited and RTP-annealed, were tested to determine how substrate engineering and post-deposition thermal treatment affect capacity, reversibility, and rate capability. The use of an aqueous electrolyte in a half-cell configuration provides a rapid and controlled way to evaluate the activity of the cathode films before their integration into half-cells with a solid electrolyte (**Chapter 4**) and complete all-solid-state thin-film battery architectures (**Chapter 5**).

The main sample families investigated in this chapter are summarized in **Figure 3.1**.

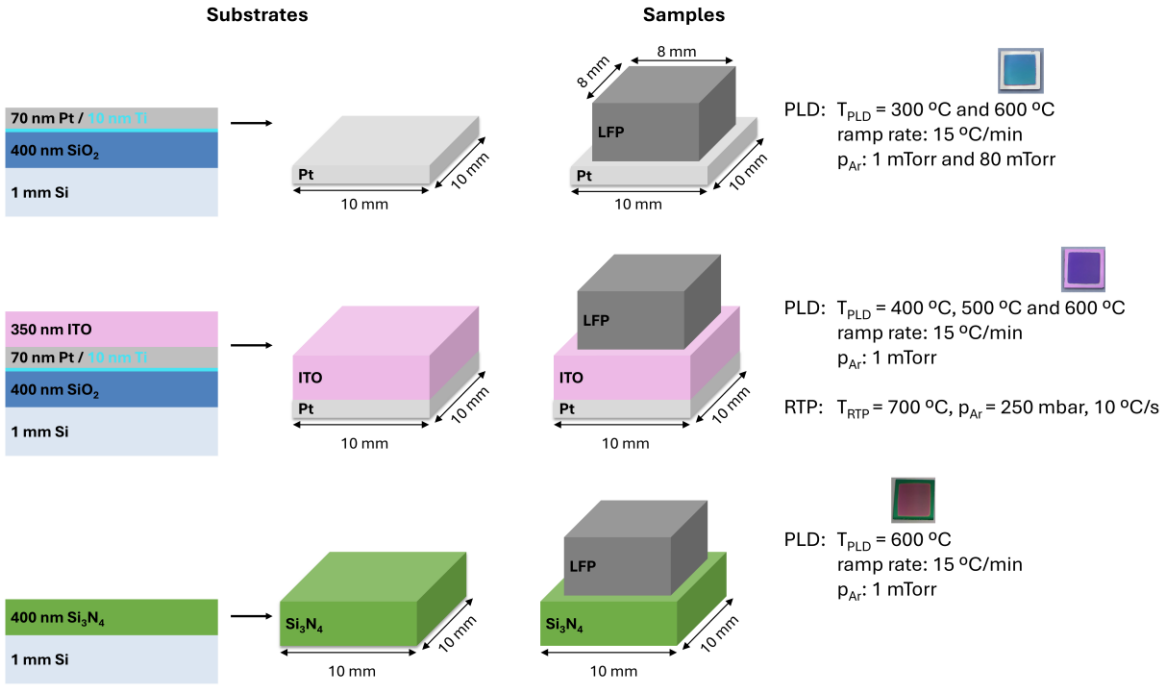


Figure 3.1 - Illustration of different substrates (Pt/Ti/SiO_2/Si, ITO/Pt/Ti/SiO_2/Si, and Si_3N_2/Si stacks), and PLD-deposited LFP samples. Photographs on the right show representative LFP films deposited at 600 °C.

This experimental design allows the chapter to progress from film growth and morphology toward structural, compositional, and electrochemical interpretation. The Pt-based samples provide a reference for understanding the behavior of LFP grown on a metallic current collector and for connecting this chapter with the LFP/LiPON/Li all-solid-state cells discussed later in **Chapter 5**. The ITO/Pt-based samples provide a complementary route to evaluate whether current-collector engineering can reduce unfavorable interfacial effects and improve the accessible active fraction of LFP. Together, these sample series establish the processing framework required to identify the main limitations and optimization pathways for PLD-grown LFP thin-film cathodes.

3.3 Influence of substrate and its temperature on thin film growth and morphology

The growth behavior and morphology of the LFP thin films were investigated as a function of substrate type, deposition temperature, and film thickness. These parameters are known to strongly influence nucleation mechanisms, grain growth, and the resulting microstructure of PLD-grown films.[87,121]

To first assess the role of the substrate, the surface morphology of the bare Pt- and ITO-coated substrates was analyzed after thermal exposure under PLD deposition conditions (600 °C, Ar atmosphere, 1 mTorr). The Pt substrate exhibits a relatively smooth and homogeneous surface, with low roughness values (RMS ~ 2.8–3.0 nm) and smaller grains, as confirmed by AFM (**Figure 3.2a,b**). The ITO-coated substrate also presents a homogenous surface (**Figure 3.2c,d**), with densely packed nanometric grains and low roughness (RMS ~ 5.5 nm).

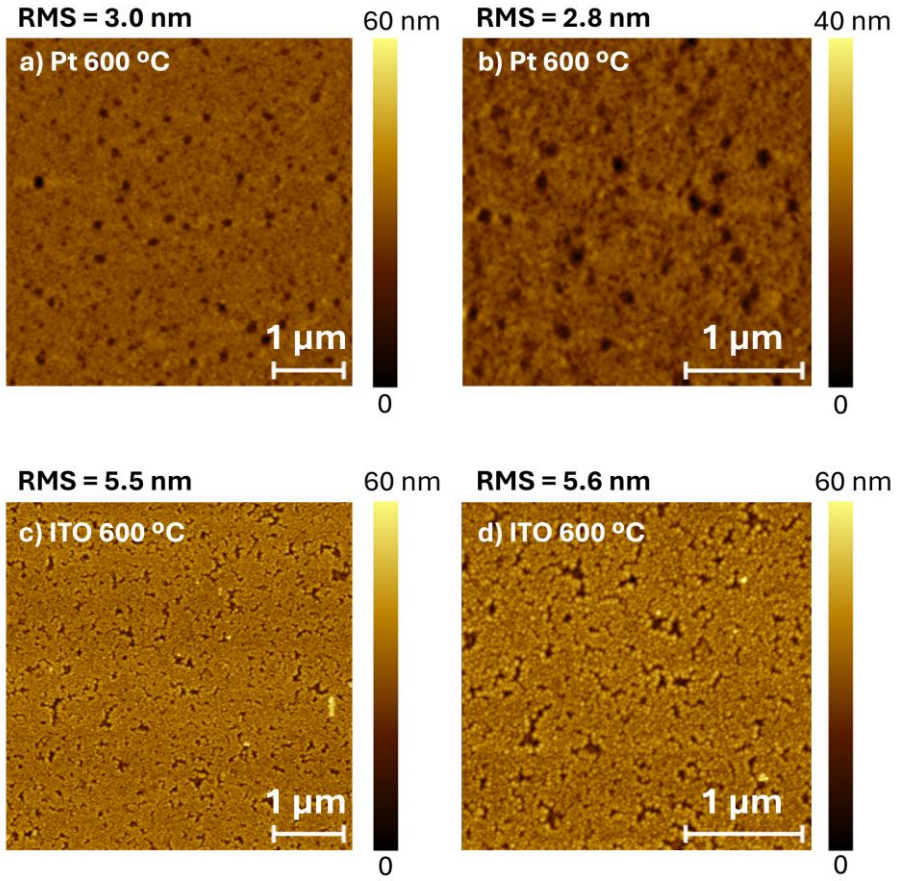


Figure 3.2 - AFM topography images of bare substrates after thermal treatment under deposition conditions in the PLD (600 ºC, Ar atmosphere, 1 mTorr): (a,b) Pt and (c,d) ITO. Images (a,c) correspond to larger scan areas (5x5 μm^2), while (b,d) show higher magnification (3x3 μm^2).

Complementary top-view SEM images of the same thermally treated substrates are presented in **Figure 3.3**, providing higher-magnification surface information through a different imaging technique.

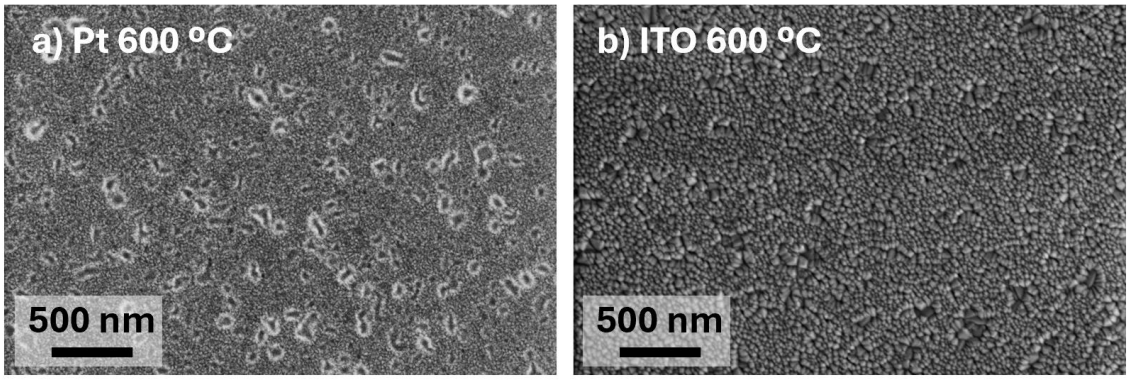


Figure 3.3 - Top-view SEM images of (a) Pt and (b) ITO bare substrates submitted to thermal treatment under PLD conditions at 600 ºC.

AFM topography images of ~300 nm-thick LFP films deposited at 600 ºC (**Figure 3.4)** reveal a clear substrate-dependent morphology. The film grown on Pt exhibits pronounced height variations, with RMS roughness values of approximately 26-28 nm (**Figure 3.4a,b**). In contrast, the film deposited on ITO shows a smoother and more homogeneous surface, displaying a dense morphology composed of closely packed polygonal grains, with lower RMS values of approximately 10-11 nm (**Figure 3.4c,d**). Same features are observed through microscopic images (**Figure 3.6c,d** and **Figure 3.7e,f**).

Based on grain-boundary contrast and linear-intercept analysis, the apparent surface grain size of LFP deposited on ITO was estimated to be 170 ± 35 nm, with some elongated grains reaching lateral dimensions of approximately 250-300 nm. For the film deposited on Pt, a slightly smaller apparent surface grain size of 145 ± 50 nm was obtained. However, in this case, the delimitation of individual grain boundaries is less straightforward, which may be related to stronger grain coalescence and/or limitations in image contrast and focusing. These results suggest that the substrate influences nucleation, grain coalescence, and growth dynamics during PLD, leading to distinct surface roughness and grain morphologies.

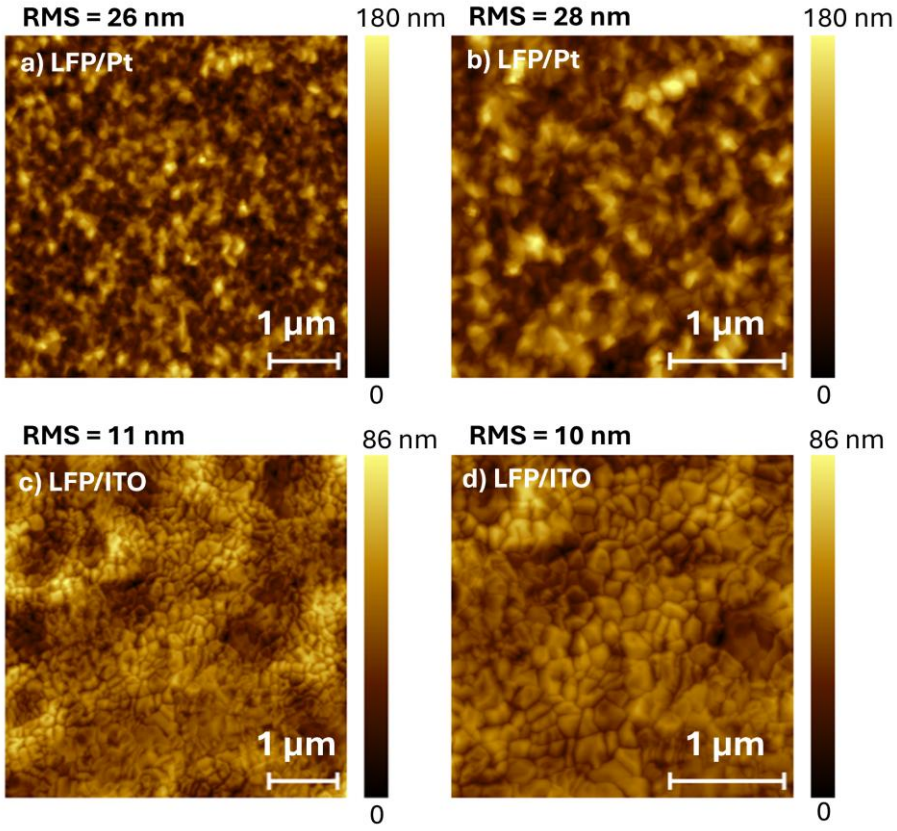


Figure 3.4 - AFM topography images of $LiFePO_4$ thin films (300 nm) deposited at 600 ºC by PLD on (a,b) Pt and (c,d) ITO substrates. Images (a,c) correspond to larger scan areas, while (b,d) show higher-magnification views of the surface morphology.

Additional insight into the substrate-dependent growth was obtained from early-stage LFP films deposited for 15 min under the same PLD conditions (600 ºC, 1 mTorr, Ar) (see **Figure A.3**, Appendix A). The early-stage film on ITO shows a finer and more homogeneous morphology, whereas Pt leads to island-like coverage, characteristic of a Volmer–Weber (island-growth) mechanism.[87,122] This morphological behavior indicates a thermodynamically limited wettability of LFP on the platinum surface, where the interfacial free energy, and the surface energy of the film exceed the surface energy of the metallic substrate. Under the energetic conditions of the PLD plasma and the high deposition temperature of 600 ºC, the enhanced thermal mobility of adatoms on the surface favors diffusion and segregation into isolated three-dimensional clusters before complete coalescence. Additionally, this effect is severely accentuated by the pronounced structural and lattice mismatch between the orthorhombic olivine-type LFP phase and the face-centered cubic (*fcc*) structure of platinum, which prevents the stabilization of two-dimensional layer-by-layer growth.

As deposition proceeds at 600 ºC, these islands progressively grow and coalesce, forming a continuous but initially irregular and porous network. This transition is clearly reflected in the thickness-dependent microstructure of films deposited at 600 ºC in **Figure 3.5** (see also **Figura A.4**, Appendix A). The 120 nm-thick film exhibits a rough and porous morphology with incomplete merging of crystalline domains. The 200 and 300 nm films show reduced porosity, dense and compact microstructures with coarsened grains on the surface.

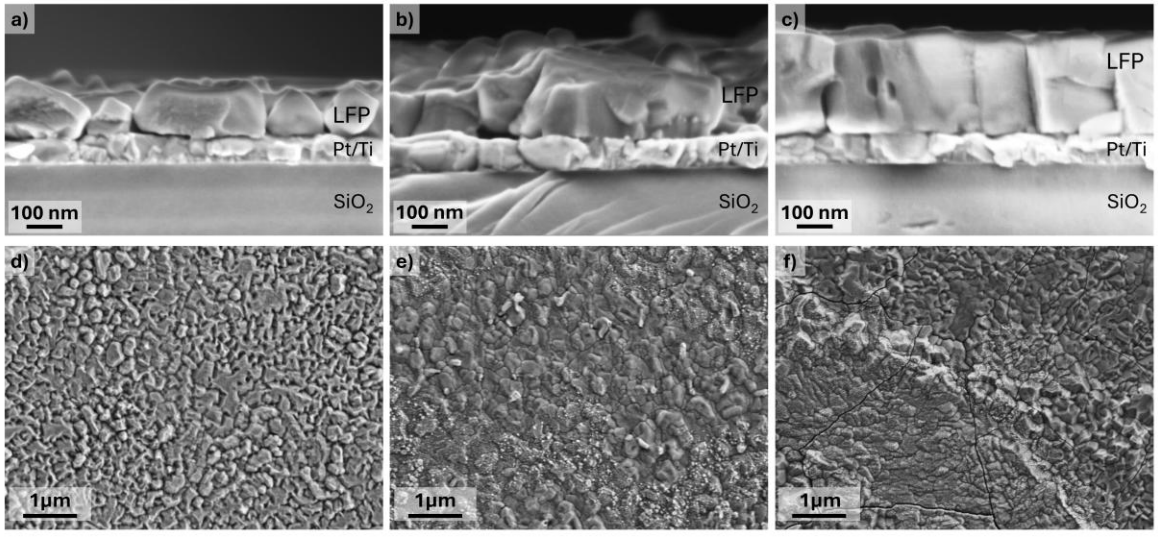


Figure 3.5 - (a–c) Cross-sectional and (d–f) top-view FE-SEM images of LFP thin films deposited on Pt-coated substrates at 600 ºC with different thicknesses: 120 nm (a,d), 200 nm (b,e), and 300 nm (c,f).

The influence of deposition temperature on film morphology was further investigated by SEM. For films deposited on Pt substrates (**Figure 3.6**), a clear evolution of the surface morphology is observed when increasing the substrate temperature from 400 ºC to 600 ºC. At 400 ºC, the film exhibits a smooth surface with some dispersed nanoscale bright features, consistent with a predominantly amorphous matrix containing only a small fraction of incipient crystalline nuclei. At

600 ºC, the film develops a fully dense crystalline morphology, consistent with the results previously observed by AFM, and indicating that this temperature provides sufficient thermal energy to drive complete crystallization of the $LiFePO_4$ phase. From the cross-sectional perspective SEM analysis (**Figure 3.6e,f**), the increase of temperature from 300 ºC to 600 ºC promotes interfacial roughening and noticeable changes in the metallic substrate. In particular, the bright layer (Pt/Ti) appears to become thicker, changing from ~80 nm to ~100 nm thickness.

For films deposited on ITO (**Figure 3.7**), increasing the deposition temperature from 400 ºC to 600 ºC leads to more visible grain-boundary-related features, while maintaining a well-defined and continuous LFP/ITO interface. Notably, the film deposited on ITO at 500 ºC shows surface grains that appear to be embedded within a smoother surrounding region, analogous to the interpretation proposed for the Pt-deposited films, a partially crystalline microstructure in which crystalline grains coexist with an amorphous LFP matrix. Overall, these results demonstrate that LFP thin film growth on Pt substrate proceeds via an initial island nucleation stage followed by coalescence and grain growth. While deposition temperature primarily controls grain size, crystallinity, and densification, the substrate plays a critical role in determining nucleation density, surface roughness and LFP/substrate interface quality. These combined effects ultimately define the microstructure of the films and are expected to strongly influence their electrochemical properties, as discussed in the following sections.

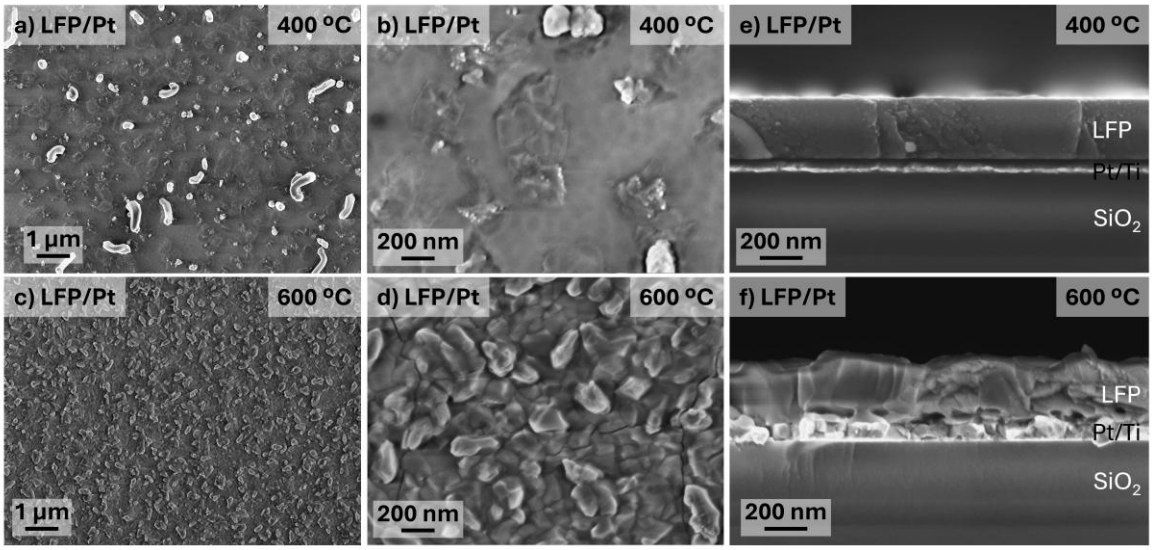


Figure 3.6 - FE-SEM images of LFP thin films deposited by PLD on Pt-coated substrates at different temperatures. Top-view images of 220 nm-thick layers deposited at (a,b) 400 ºC and (c,d) 600 ºC. Images on the left correspond to lower magnification, while those on the right show higher-magnification. Cross-sectional images of 300 nm-thick layers deposited at (e) 300 ºCand (f) 600 ºC.

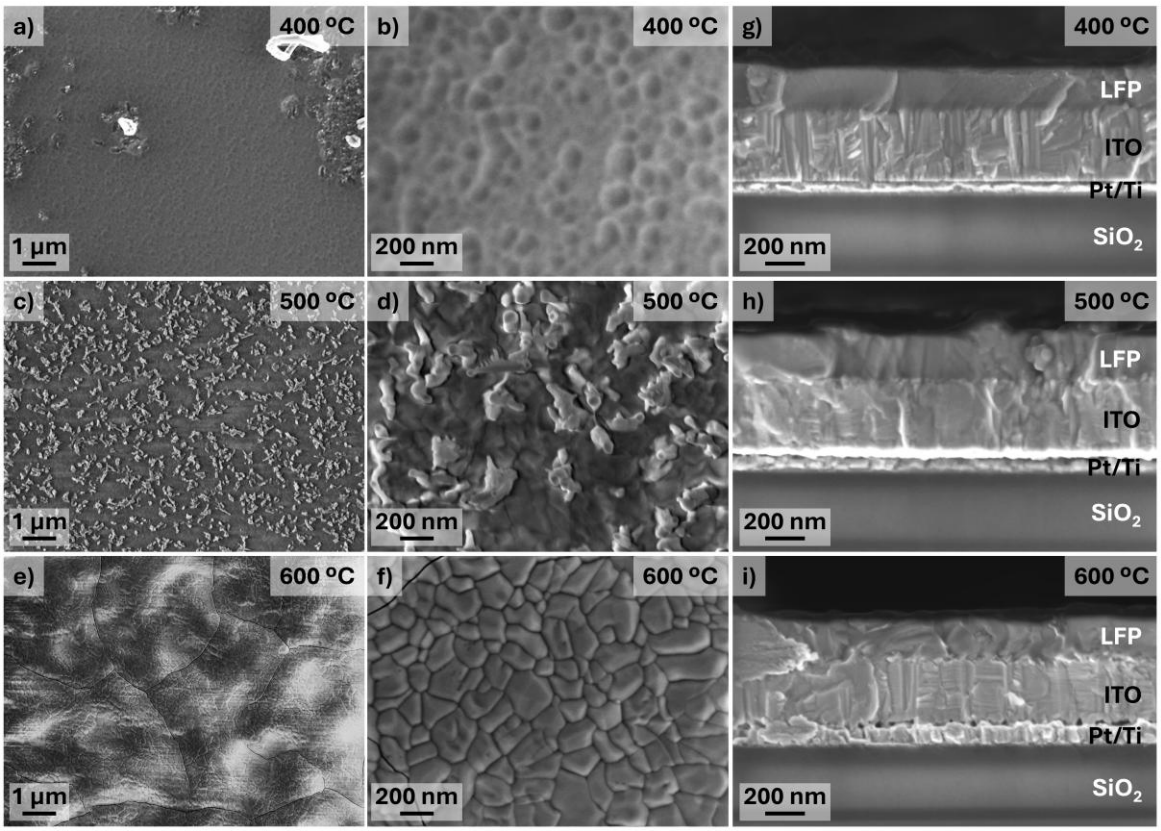


Figure 3.7 - FE-SEM images of LFP thin films deposited by PLD on ITO-coated substrates at different temperatures. Top-view images of 220 nm-thick layers deposited at (a,b) 400 ºC , (c,d) 500 ºC and (e,f) 600 ºC. Images on the left correspond to lower magnification, while those on the right show higher-magnification. Corresponding cross-sectional images of the layers deposited at (g) 400 ºC, (h) 500 ºC and (i) 600 ºC.

3.4 Structural and compositional characterization

Following the analysis of film growth and morphology, the structural and compositional properties of the LFP thin films were investigated using GIXRD, synchrotron-based GIWAXS, Raman spectroscopy, and GDOES depth profiling. These complementary techniques provide insight into phase formation, crystallinity, interfacial reactions, and elemental distribution within the films.

3.4.1 Phase formation and thickness-dependent crystallinity

The structural properties of LFP thin films deposited on Pt current collectors at 600 ºC were first evaluated by combining GIXRD and Raman spectroscopy as shown in **Figure 3.8**.

The diffractograms of the 120 and 200 nm-thick films are presented in **Figure 3.8a**, together with that of the commercial $LiFePO_4$ target used for the deposition. The observed diffraction peaks can be indexed to the olivine $LiFePO_4$ phase with orthorhombic structure (Pnma, JCPDS 01-083-2092), confirming the successful formation of the LFP phase under the selected PLD conditions. The 120 nm-thick film exhibits only weak features, suggesting limited crystallinity

and/or a reduced amount of diffracting material, consistent with an early growth stage dominated by island nucleation and incomplete coalescence, as previously observed by SEM. In contrast, the 200 nm-thick film displays sharper and more intense reflections at approximately 17.2º, 20.8º, 22.8º, 25.7º, 29.7º, 35.7º, 36.7º, 38.0º and 39.7º, confirming the development of a more crystalline and continuous LFP layer.

For the 200 nm-thick film, the reflection at approximately 22.8º, assigned to the (210) plane of olivine $LiFePO_4$, exhibits a relatively high intensity compared to the reference and LFP target patterns. This suggests that the film presents some degree of preferential crystallographic orientation rather than a fully random powder-like structure. A similar effect has been reported by Sauvage *et al.*, who studied LFP thin films grown on Pt-coated Si substrates under comparable conditions (600 ºC, Ar atmosphere).[72] In their work, the authors observed a single and well-defined Bragg reflection near this same position for films up to 600 nm in thickness, which they briefly ascribed to a specific interaction between the deposited film and Pt. However, as the film becomes thicker, this preferential orientation may gradually diminish due to strain relaxation and the reduced templating effect of the substrate, leading to a more randomly oriented polycrystalline structure.

Such preferential orientation may influence electrochemical performance because Li^+ transport in olivine LFP is highly anisotropic and occurs mainly along one-dimensional channels parallel to the [010] direction, or b-axis.[16] Therefore, the orientation of the grains with respect to the electrolyte interface can affect the accessibility of Li^+ diffusion pathways and contribute to reduced practical capacity, together with other factors such as film continuity, electronic connectivity, interfacial contact, density, and structural defects.

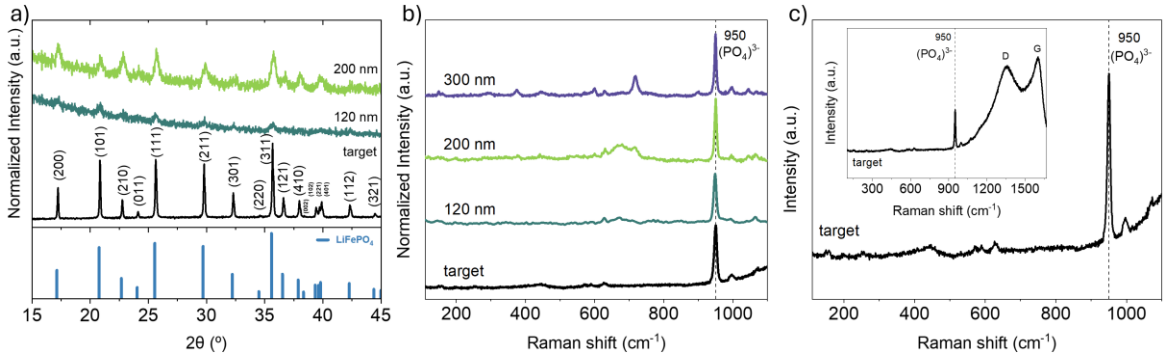


Figure 3.8 - Structural characterization of LFP thin films deposited on Pt (111)-coated substrates by PLD at 600 ºC as a function of thickness. (a) GIXRD patterns of 120 and 200 nm-thick LFP films, together with the XRD pattern of the commercial $LiFePO_4$ target. Vertical lines at the bottom correspond to the reference olivine $LiFePO_4$ diffractogram (JCPDS 01-083-2092). (b) Raman spectra of LFP thin films with thicknesses of 120, 200, and 300 nm. (c) Raman spectrum of the target.

Raman spectroscopy was employed to further probe the structural characteristics of 120, 200, and 300 nm-thick films deposited on Pt at 600 ºC (**Figure 3.8b**). The corresponding spectrum of the commercial target is also displayed for direct comparison. All spectra exhibit a dominant and sharp band centered at approximately ~950 cm^{-1}, which is assigned to the symmetric stretching

vibration of the PO_4^{3-} tetrahedra (ν_1 , A_g mode), characteristic of olivine $LiFePO_4$ structure. In addition, weaker bands are observed in the region between ~990 and 1070 cm^{-1}, corresponding to asymmetric stretching modes of the PO_4^{3-} units. The presence and relative sharpness of these features indicate that the phosphate tetrahedra remain structurally well-defined and largely undistorted within the films.[123,124]

Additional weak bands are observed in the intermediate Raman-shift region, particularly between approximately 690 and 800 cm^{-1}, and become more evident as the film thickness increases. These features may indicate minor secondary phosphate-related contributions or local structural distortions, although no unambiguous secondary crystalline phase is detected by GIXRD. In our previous studies,[125] similar broad features have been tentatively associated with iron oxide species such as Fe_3O_4 at the surface by using tip-enhanced Raman spectroscopy (TERS). However, in the present case, no unambiguous evidence of such phase is observed by GIXRD. Therefore, a direct assignment of these features to specific impurity phases remains inconclusive. In particular, relatively sharp peaks observed at approximately ~724 cm^{-1} and ~1038 cm^{-1} deserve particular attention, as directly evidenced in the Raman spectrum collected during the nucleation stage of film growth (**Figure 3.9c** and **Figure A.2**, Appendix A). These features are detected at early stages of film growth, prior to the full development of the characteristic $LiFePO_4$ signature at 950 nm^{-1}. Based on their spectral positions, these modes may be tentatively associated with lithium pyrophosphate-like environments, such as $Li_4P_2O_7$, due to P–O–P symmetric and antisymmetric stretching vibrations.[126] This interpretation remains tentative, but it is consistent with the possibility of local Fe depletion in some regions of the film, especially considering the Fe redistribution toward Pt discussed later in this section. This interpretation could be also supported by the scattering of lighter elements (Li, P, and O), resulting in a relative enrichment of Fe at the interface. As a consequence, the initial stages of film growth may promote both the formation of $FePt_3$ at the substrate interface and the stabilization of $Li_4P_2O_7$ within the film. To further assess the influence of direct contact with the Pt layer on film growth, ITO-coated substrates were also investigated, with the ITO layer acting as an oxide interlayer between LFP and Pt, allowing the interfacial reactivity, and electrochemical behavior to be evaluated.

Finally, the Raman response of the commercial target is shown in **Figure 3.8c** with more detail. In addition to the characteristic phosphate bands, the target exhibits D and G bands in the high-wavenumber region (1355 and 1600 cm^{-1}), associated with carbonaceous surface contamination. These features are not observed in the deposited films, indicating that the pre-ablation step prior to deposition combined with the high temperature effectively removed surface contaminants and ensured a cleaner transfer of material. The necessity of target pre-ablation is well established in the literature, as it plays a crucial role in stabilizing the composition and reproducibility of the ablation process.[86,101,121] In the present work, this effect is also experimentally evidenced by the progressive reduction of Raman signals associated with the D and G bands upon continued use of the target across successive depositions. This evolution, shown in **Figure A.2** (Appendix A), confirms that repeated laser exposure leads to the removal of surface contaminants and contributes to a cleaner LFP Raman signature.

3.4.2 GIWAXS analysis and interfacial phase formation

To gain further structural insight, synchrotron-based GIWAXS measurements were performed on the 120 nm-thick film deposited on Pt (111)-coated substrate at 600 ºC. The 2D scattering pattern (**Figure 3.9a**) shows diffraction rings corresponding to $LiFePO_4$. However, the intensity is not fully homogeneous along the rings, indicating a polycrystalline film with a certain degree of crystallographic texture rather than a completely random orientation.

The azimuthally integrated profiles from the GIWAXS data (**Figure 3.9b**) reveal, in addition to the $LiFePO_4$ reflections, a set of additional peaks located at approximately 16.2, 23.0, 28.0, 32.5, and 46.0 nm^{-1}. These peaks are attributed to the formation of $FePt_3$ phase (**Figure 3.9b**). The presence of this phase indicates interfacial reactions between Fe species from the plasma and the Pt current collector under reducing PLD conditions (600 ºC, 1 mTorr, Ar). Such conditions are necessary to maintain Fe^{2+} and avoid the formation of secondary iron oxide or phosphate phases ($Li_3Fe_2(PO_4)_3$, Fe_2O_3 or Fe_3O_4), but they simultaneously promote interdiffusion and alloy formation at the interface. Importantly, the intensity of the $FePt_3$-related reflections decreases significantly at lower incidence angles, while the $LiFePO_4$ reflections become more prominent. This depth-dependent behavior confirms that the $FePt_3$ phase is localized near the LFP/Pt interface. In particular, the reflections at $q \approx 28.0$ and 32.5 nm^{-1}, corresponding to 2θ values of approximately 40.2° and 47.0° for Cu Kα radiation, overlap with characteristic Fe_2P diffraction peaks reported at 2θ = 40.28° and 47.31°, assigned to the (111) and (210) planes of the hexagonal Fe_2P phase.[127] Therefore, a minor contribution from Fe_2P at these reflections cannot be fully excluded.

To confirm the substrate-dependent origin of this phase, GIWAXS measurements were also performed on ~180 nm films deposited on Si_3N_4 under the same conditions (**Figure 3.10a**). In this case, only LFP reflections are observed, with no evidence of secondary phases. In contrast, films deposited on Pt consistently exhibit additional reflections associated with $FePt_3$ (**Figure 3.10b**). This comparison demonstrates that the extra peaks are not intrinsic to LFP deposition, nor do they arise from LFP decomposition, but instead result from a chemical interaction with the Pt substrate.

The possible formation of Fe_2P at the LFP/Pt interface during the initial PLD growth stages is chemically plausible and can be rationalized through a carbon-assisted reduction mechanism. The commercial LFP target carries a surface layer of carbonaceous contamination, directly evidenced by the D and G bands in its Raman spectrum (**Figure 3.8**). Despite the pre-ablation protocol, the first laser pulses ablate material from the target surface where carbon is most concentrated, and adventitious carbon on the Pt surface constitutes an additional source. Carbonaceous species entrained in the early plasma plume therefore arrive at the hot substrate together with Li, Fe, P, and O species, creating transiently more reducing local conditions at the very onset of film growth. In $LiFePO_4$/C composite systems, it is well established that carbon provides an environment favourable for Fe^{3+} reduction and, under sufficiently reducing conditions, can drive the formation of Fe_2P through a self-oxidation–reduction reaction:

$$4\ LiFePO_4 + C \rightarrow 2\ Fe_2P + 2\ Li_4P_2O_7 + P\uparrow + CO_2\uparrow$$

Although this reaction is observed at 938 °C in bulk carbothermal synthesis,[128] thermodynamic analysis of the Li_2CO_3-Fe_2O_3-$NH_4H_2PO_4$-C/CO system demonstrates that Fe_2P can form at temperatures as low as ~244 °C when elemental or partially reduced Fe is present.[129] In the PLD context, the transient carbon contamination from the target during the first ablation pulses mimics this carbothermal effect, intensifying the local reducing character at the LFP/Pt interface precisely at the earliest stages of nucleation. Simultaneously, partially over-reduced Fe^0 species interdiffuse into the Pt lattice at 600 °C, promoting $FePt_3$ alloying. This selective removal of Fe from the phosphate network produces a Li–P–O-rich residual layer with pyrophosphate character ($Li_4P_2O_7$), whose P–O–P vibrational signature is captured in the nucleation-stage Raman spectrum at ~724 and ~1038 cm^{-1} (**Figure 3.9c**). Once the transient carbon is consumed and the Pt surface is covered by a continuous LFP layer, interfacial reactivity is suppressed and the bulk of the film grows as stoichiometric olivine LFP.

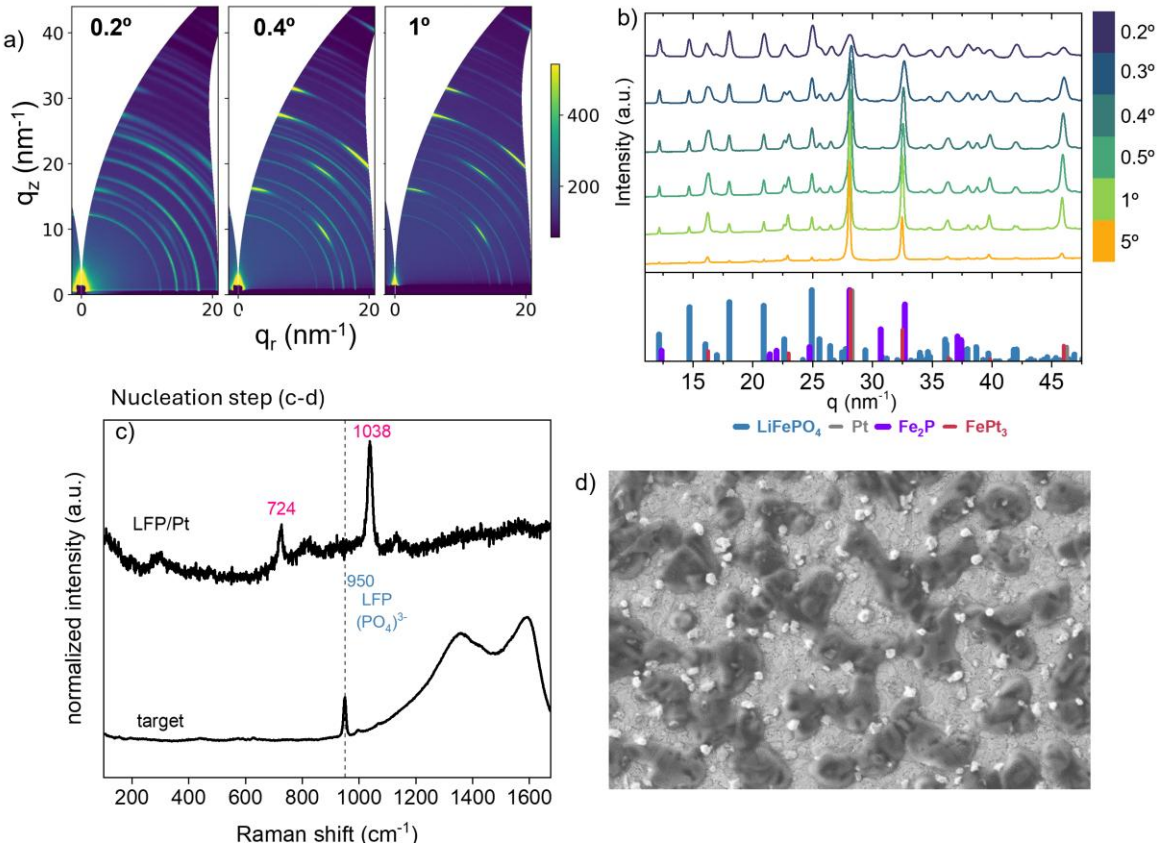


Figure 3.9 – (a) 2D GIWAXS data of a LFP thin film (120 nm) grown on Pt (111)-coated substrate (70 nm) at three incidence angles (0.2°, 0.4°, and 1°). (b) Pseudo XRD data extracted from GIWAXS within the range $10 < q < 50$ nm^{-1}. Reference patterns of $LiFePO_4$ (JCPDS card 01-083-2092, Pnma), $FePt_3$ (JCPDS card 29-0716, Pm-3m), Fe_2P (JCPDS card 51-0943, P-$\bar{6}$2m), and Pt (01-071-5031, Fm-3m) are present at the bottom (vertical lines). (c) Raman spectrum and (d) SEM top-view image collected at the nucleation stage of LFP growth on Pt.

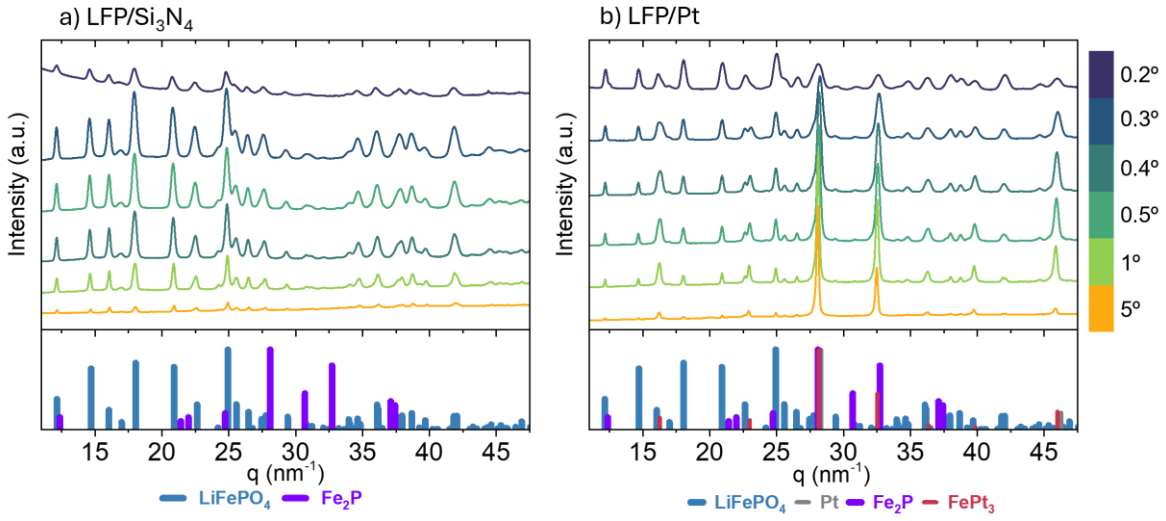


Figure 3.10 - GIWAXS data from 11 to 47 nm^{-1} (q) of 180 nm LFP thin film deposited by PLD on (a) Si_3N_4 and (b) Pt substrates. Vertical lines correspond to references diffractograms of $LiFePO_4$ (JCPDS card 01-083-2092), $FePt_3$ (JCPDS card 01-071-5031), Fe_2P (JCPDS card 51-0943, P-$\bar{6}$2m), and Pt (JCPDS card 01-087-0640).

3.4.3 Substrate and deposition temperature effects on as-deposited films

After establishing the thickness-dependent crystallization of LFP on Pt and the formation of $FePt_3$ at the LFP/Pt interface, the influence of the current collector and deposition temperature was evaluated by combining GIXRD (acquired at the ICN2 facilities) and Raman spectroscopy. **Figure 3.11** compares the diffraction response of ~200 nm-thick films deposited at 600 ºC on ITO and Pt substrates, together with Raman spectra of as-deposited films grown at different temperatures on both substrates. Raman spectra of the corresponding bare substrates submitted to the same thermal conditions are also included to distinguish film-related vibrational features from possible substrate contributions.

The GIXRD measurements were performed at a fixed incidence angle of 0.8º over the 2θ range of 10–45º. The reference diffraction patterns of the LFP target and bare substrates were collected in conventional Bragg–Brentano θ–2θ geometry, rather than in grazing-incidence configuration. For the film deposited on ITO, multiple reflections, at approximately 17.3º, 22.6º, 25.6º, 29.6º, 32.1º, 35.5º, and 39.5º corresponding to the $LiFePO_4$ phase are clearly observed, indicating a well-crystallized structure (**Figure 3.11a**). A pronounced diffraction feature is observed at approximately ~37.4º, with an intensity comparable to that of the peak at ~35.5º. This peak falls within the angular region spanned by the $LiFePO_4$ (121) and (410) reflections at 36.5º and 37.9º, respectively, and its origin could not be unambiguously established. A possible contribution from a preferred crystallographic orientation of specific $LiFePO_4$ planes cannot be excluded; however, if a pronounced texture were responsible, a correlated intensity variation across the doublet in the 35–40º region would be expected, which is not clearly observed. Similarly, a feature at approximately ~22.7º is present in the RT-deposited film on ITO; a tentative assignment to Li_3PO_4 is considered but cannot be confirmed, as the PO_4 stretching bands of Li_3PO_4 overlap with those of $LiFePO_4$

near 950 cm^{-1}, precluding Raman confirmation. The origin of these features is therefore left open, and further depth-resolved or surface-sensitive structural analysis would be required for a definitive assignment. The peak observed at approximately ~35º, originating from the ITO layer, overlaps with the $LiFePO_4$ (311) reflection.

For the film deposited directly on Pt, fewer $LiFePO_4$ reflections are clearly distinguishable, although the observed peaks remain consistent with the olivine structure. The most evident peaks are located at approximately 17.2º (200), 23.1º (210), 35.5º (311), and 37.9º (410), which are highlighted in **Figure 3.11b**. It should be noted that, given the grazing-incidence geometry employed (0.8º), the diffraction signal is predominantly sensitive to the film volume and is not expected to contain contributions from the buried substrate or from the interfacial $FePt_3$ layer identified by GIWAXS. Two additional reflections are observed at approximately 23.1º and 40.5º that do not correspond to $LiFePO_4$. Possible assignments include Li_3PO_4 or Fe_2P secondary phases, consistent with the interfacial decomposition processes discussed in **Section 3.4.2**; however, a definitive identification could not be established from the available data. Interdiffusion at the LFP/Pt interface, evidenced by GIWAXS and GDOES, likely modifies the local film chemistry and may give rise to these additional features.

The Raman spectra further highlight the influence of deposition temperature and substrate chemistry (**Figure 3.11c,d**). In all samples, the characteristic $LiFePO_4$ band at approximately 950 cm^{-1} is observed, confirming the presence of the phosphate framework. However, films deposited at lower temperature, particularly at 400 ºC, show broader and less intense Raman features, consistent with a larger amorphous contribution and lower structural ordering.

For films deposited on ITO, additional Raman bands are observed at approximately ~667, ~540, and ~304 cm^{-1}. These bands are close to the characteristic Raman-active modes of magnetite-like Fe_3O_4.[130,131] Peaks in these regions suggest the presence of Fe–O related species. Since these features are not observed with the same intensity in Pt-based samples, their presence may be related to substrate chemistry and possible interfacial processes involving excess Fe diffusion toward the ITO layer. Considering that ITO is based on In_2O_3/SnO_2, local Fe incorporation into the oxide substrate or the formation of Fe-rich oxide environments at the interface could give rise to Raman signatures resembling spinel-type iron oxides. Such behavior is consistent with Fe-doped $Sn_{1-x}Fe_xO$ systems, where Fe incorporation into the oxide lattice leads to modifications in structural and vibrational properties.[132] This interpretation is further supported by the absence of these features in Pt-based samples, where excess Fe is involved with $FePt_3$, highlighting the critical role of substrate chemistry in governing interfacial reactions and phase stability in thin-film configurations.

The presence of Fe–O-related Raman bands may also be associated with partial oxidation of the film surface, possibly connected with the surface features observed by SEM later in this chapter. Since Raman spectroscopy is highly sensitive to local order variations, a thin oxidized layer or nanoscale Fe-rich oxidized particles could be detected even if no crystalline iron oxide phase is observed by GIXRD. However, an interfacial origin related to Fe diffusion toward the oxide-based ITO layer cannot be excluded. Therefore, the assignment remains tentative, and further surface-

sensitive or depth-resolved analyses would be required to determine whether these species are located at the surface or at the LFP/ITO interface.

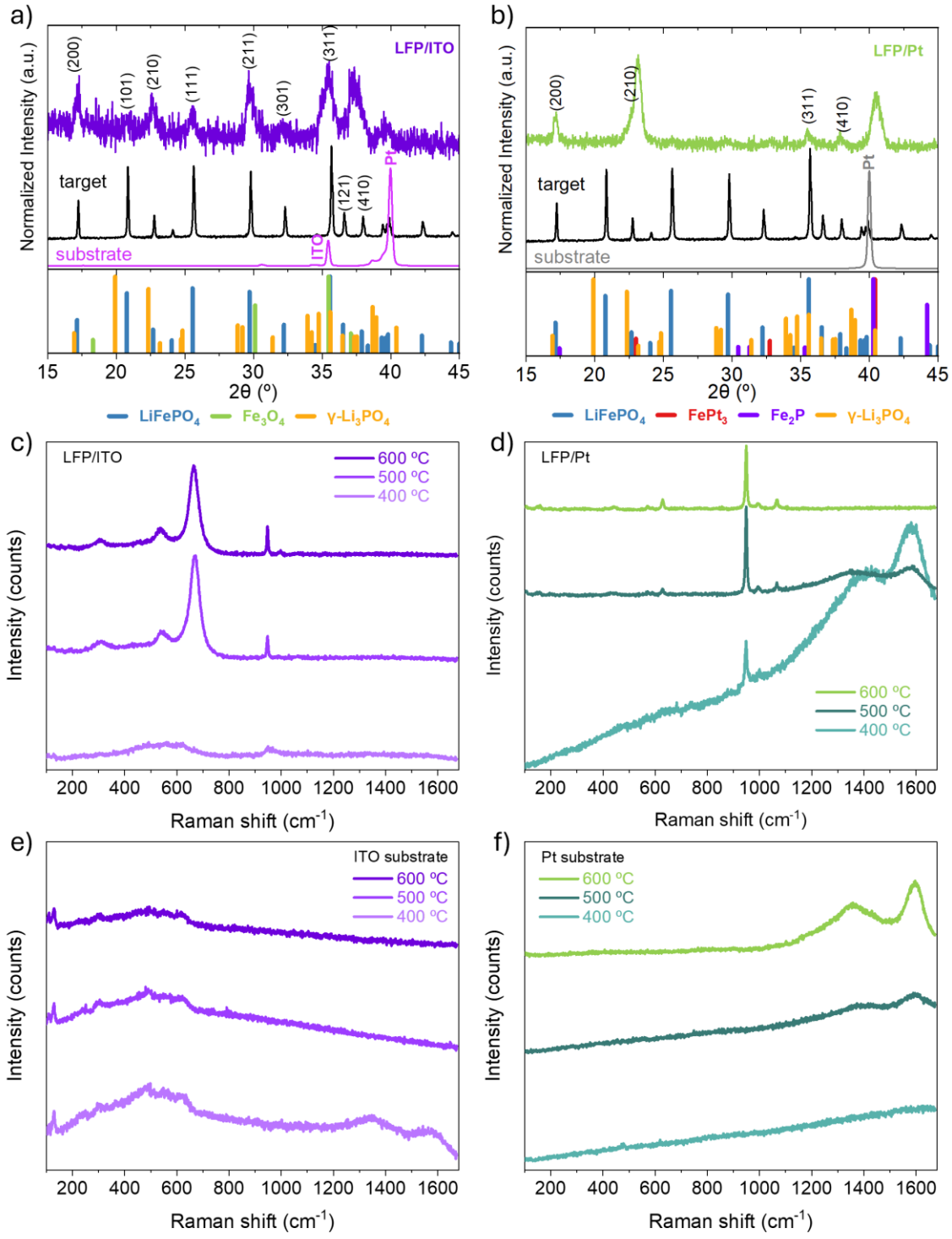


Figure 3.11 - Structural comparison of as-deposited $LiFePO_4$ thin films as a function of substrate and deposition temperature. a,b) GIXRD patterns of ~220 nm-thick LFP films deposited by PLD at 600 ºC on

(a) ITO/Pt- and (b) Pt- coated substrates. Vertical lines correspond to references diffractograms of $LiFePO_4$ (JCPDS card 01-083-2092), γ-Li_3PO_4 (ICSD 77095, Pnma), Fe_3O_4 (JCPDS 19-0629, Fd-3m), $FePt_3$ (JCPDS card 01-071-5031), Fe_2P (JCPDS card 51-0943, P-$\bar{6}$2m), and Pt (JCPDS card 01-087-0640). c,d) Raman spectra of as-deposited LFP thin films deposited at different substrate temperatures, 400–600 ºC, on c) ITO/Pt and d) Pt substrates. e,f) Raman spectra of the corresponding bare e) ITO/Pt and f) Pt substrates submitted to the same thermal conditions.

3.4.4 Elemental depth distribution

Elemental depth profiles obtained by GDOES for the LFP films deposited by PLD under same conditions at 600 ºC for 2h (72k pulses, 10 Hz) on Pt and ITO substrates are presented in **Figure 3.12**, showing the evolution of the elemental signals as a function of sputtering time.

For the film deposited on Pt (**Figure 3.12a**) LFP signal appears stable from 0.8 to 10.6 s, while the Pt signal exhibits a steep increase, indicating a relatively well-defined interface. The Fe signal overlaps with the Pt one, becoming more pronounced within the substrate region. This overlap arises, in part, from the proximity of the spectral emission lines of both elements detected in the Fe channel (λ = 271.9 nm) (**Figure 3.15b**).

For the sample on ITO (**Figure 3.12b**), LFP signal appears stable from 0.8 to 13.2 s. For this sample, the Fe and Pt signals overlap but maintain comparable intensities within the substrate region, without the marked increase of Fe observed in the Pt-based sample.

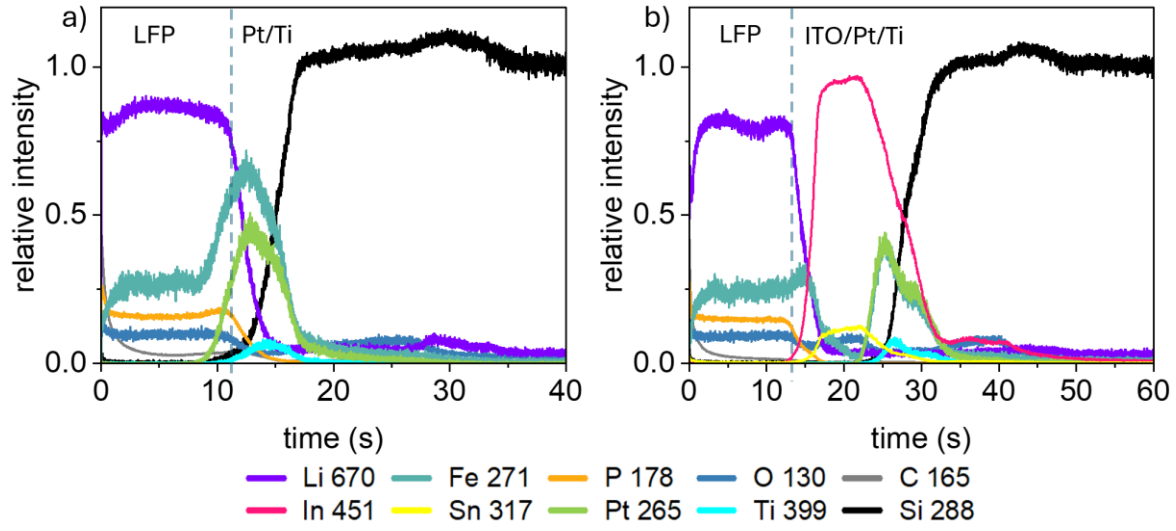


Figure 3.12 - GDOES elemental profiles of $LiFePO_4$ thin films deposited at 600 ºC on (a) Pt and (b) ITO substrates. Legend indicates the specific wavelength (nm) detected.

In both samples, the gradual decrease of Li, P and O and the persistence of Fe signal beyond the film region suggest a certain degree of elemental interdiffusion towards the substrate. Although a detailed mechanistic interpretation is beyond the timeframe of this analysis, these observations are consistent with the trends previously inferred from Raman and XRD measurements, where indications of interfacial interactions and compositional modifications were identified. An

additional feature observed for sample deposited on Pt is the accumulation of Li at the SiO_2/Si interface, which is assigned to thermally activated Li diffusion across the thin Pt/Ti layers.

The cross-sectional ESB image (**Figure 1.13**) further highlights a region of distinct contrast at the LFP/ITO interface. Although SEM contrast alone cannot provide definitive compositional identification, the combined SEM and GDOES results support the presence of a Fe-rich interfacial region near the LFP/ITO boundary.

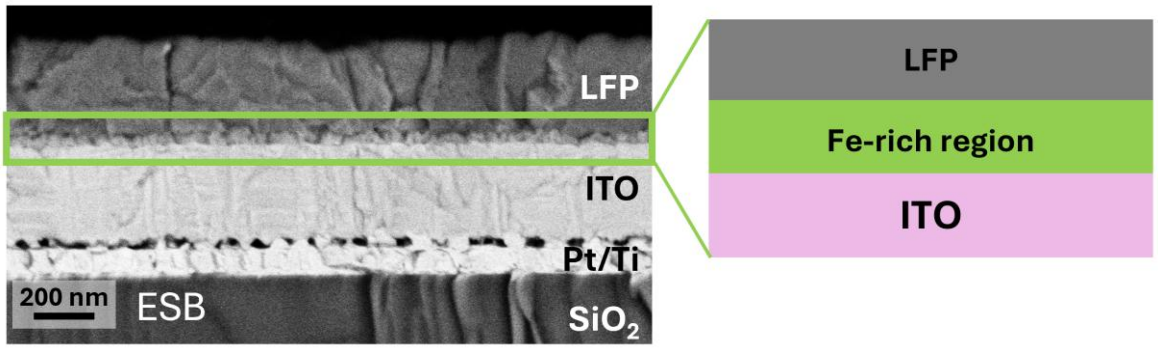


Figure 3.13 - The cross-sectional ESB image of LFP thin film deposited by PLD on ITO-coated substrate at 600 ºC.

After the comparison between samples deposited at 600ºC on Pt and ITO substrates, the influence of deposition temperature (300 - 600 ºC) on the elemental distribution and interfacial characteristics was further examined for LFP films deposited on Pt (**Figure 3.14**).

The profiles reveal a clear dependence of the Fe and Li distribution and the film/substrate interface on the deposition temperature. At 300 ºC, transition between the film and Pt-coated substrate is sharp with almost vertical lines separating the layers, comparable to the bare substrate (**Figure 3.15**). The Fe signal oscillates and does not show interfacial enrichment, suggesting a limited interdiffusion of excess Fe towards the substrate. This behavior is consistent with the reduced atomic mobility at lower deposition temperatures, which also limits the extent of LFP crystallization. Li signal, on the other hand, shows an enrichiment at both surface and interface with Pt. Based on this analisis, and also with evidence from the GIXRD measurements presented in the following **Section 3.4.5**, the Li-rich region in the first 2 seconds is attributed to an amorphous lithium phosphate (Li_3PO_4) secondary phase due to the low deposition temperature and/or lithium carbonate (Li_2CO_3) driven by the high reactivity of fresh lithium with atmospheric moisture and carbon dioxide. Intermediate behaviors are observed for the samples deposited at 400 and 500 ºC, where a progressive broadening of the reaction region between Pt and Fe with increasing temperature is indicated by the higher accumulation of Fe at the interface level. The Fe signal begins to show a progressive tendency, although less pronounced than in the 600 ºC case where the signal become flat within the crystalline LFP layer. Overall, these results demonstrate that increasing the deposition temperature promotes a progressive redistribution of Fe toward the LFP/substrates interface.

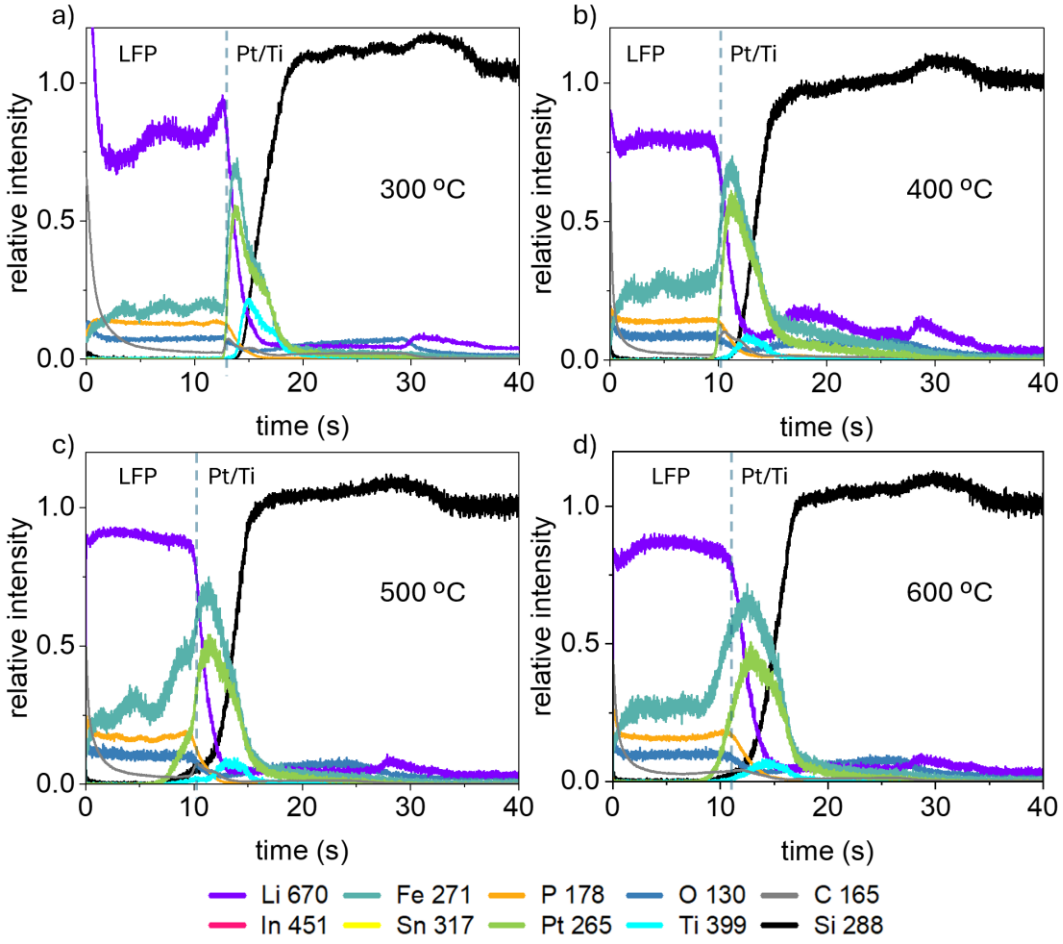


Figure 3.14 - GDOES elemental profiles of $LiFePO_4$ thin films deposited on Pt at different substrate temperatures: (a) 300 ºC, (b) 400 ºC, (c) 500 ºC, and (d) 600 ºC.

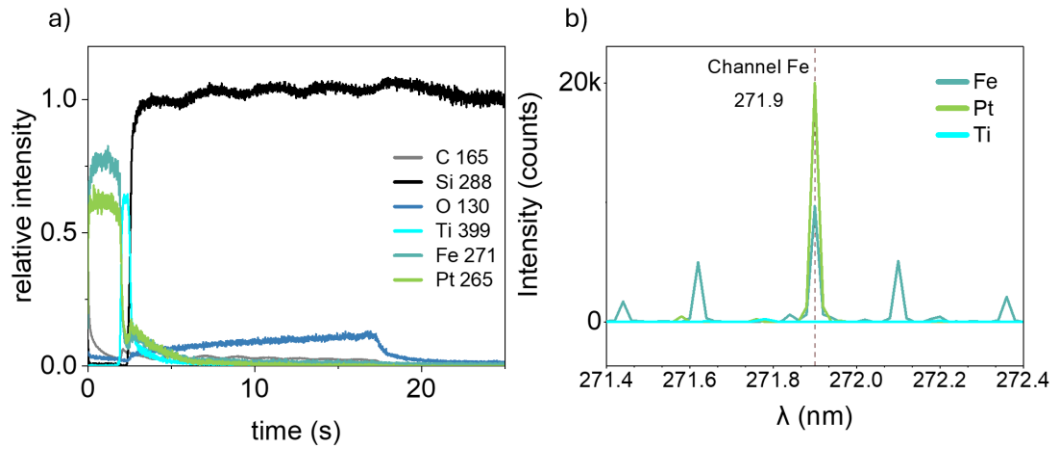


Figure 3.15 – (a) GDOES elemental profiles of pristine Pt-coated substrate. (b) Characteristic emission wavelengths (λ) of spectral lines from excited Fe, Pt, and Ti atoms. The vertical line at 271.9 nm indicates the nominal wavelength of the Fe analytical channel used in the GDOES system.

3.4.5 Effect of post-annealing by rapid thermal processing (RTP)

The effect of RTP on the crystallinity of $LiFePO_4$ thin films was evaluated for samples deposited on ITO at different substrate temperatures (400, 500 and 600 ºC). The post-annealing conditions were kept constant for all samples: 700 ºC for 60 s under Ar atmosphere, with heating and cooling ramp rates of 10 ºC s^{-1}. The annealing temperature was selected as a compromise between promoting crystallization and preserving film integrity. Specifically, 700 ºC is above the standard PLD deposition temperature used in this work to obtain crystalline LFP films, 600 ºC, and therefore provides an additional thermal driving force for crystallization, particularly for films deposited at lower substrate temperatures. Higher RTP temperatures were avoided because processing above this temperature range may favor the formation of secondary phases and/or induce detrimental morphological changes. This limitation was supported by additional SEM observations of LFP films deposited on Pt and annealed at higher temperatures, where pronounced surface restructuring and film degradation were observed (**Figure A.5**, Appendix A).

Films deposited at 400 ºC and 600 ºC after RTP treatment show multiple reflections consistent with the $LiFePO_4$ phase (**Figure 3.16a**), similar to the as-deposited film grown at 600 ºC shown in **Figure 3.11a**Error! Reference source not found. In contrast, the film deposited at 500 ºC exhibits a markedly anomalous diffraction profile, characterized by a single sharp and dominant reflection at approximately $2\theta = 22.7^{\circ}$, together with broad features near ~35.5º and within the 36.8–38.5º region, and a notably reduced number of other reflections.

The primary hypothesis for this anomalous profile is that the LFP film grown at 500 ºC develops a strong preferred orientation after RTP, so that only a limited set of crystallographic planes contributes significantly to the diffraction pattern. In this scenario, the dominant reflection at $2\theta = 22.7^{\circ}$ is assigned to the $LiFePO_4$ (210) plane, and the RTP-treated film may exhibit a preferential orientation with the (210) planes approximately parallel to the substrate surface. The broad features near 35.5º and 36.8–38.5º remain compatible with the $LiFePO_4$ (311) and (131)/(400) reflections, respectively. In this case, the Li-ion diffusion direction of olivine $LiFePO_4$, [010] would be slightly tilted with respect to both the surface normal and the film plane. Therefore, such texture may positively influence Li-ion kinetics and material utilization, although it does not correspond to an ideal out-of-plane alignment of the [010] diffusion channels.

Alternatively, the distinct surface morphology, particularly the particles observed by SEM at the film surface (**Figure 3.16d,e**) may dominate the diffracted intensity in the grazing-incidence geometry, making the measured pattern less representative of the underlying continuous active layer. Finally, the dominant peak at $2\theta = 22.7^{\circ}$ could theoretically align with a highly oriented γ-Li_3PO_4 phase,[133,134] although an extensive insulating surface layer of this nature is difficult to reconcile with the electrochemical properties shown in next sections. This interpretation is directly supported by the θ–2θ diffraction pattern of a reference γ-Li_3PO_4 thin film deposited by PLD on Pt-coated substrates at room temperature and annealed by RTP at 600 ºC for 60 s under Ar (**Figure 3.16b**). The dominant reflection in that pattern is observed at $2\theta = 22.46^{\circ}$.

The Raman spectra before and after RTP, shown in **Figure 3.16c**, provide complementary evidence of structural improvement. For the film deposited at 400 ºC, the characteristic LFP band at ~950 cm^{-1} becomes more defined after annealing, while the spectral background decreases significantly. This indicates a reduction in amorphous contributions and an improvement in local phosphate ordering. The same trend is observed for the film deposited at 500 ºC, although the change is less pronounced, consistent with the fact that this film already exhibits a higher degree of crystallinity in the as-deposited state. For the sample deposited at 400 ºC, features centred around ~670, ~540, and ~307 cm^{-1} become evident after RTP. These bands correspond to the A_{1g} (~670 cm^{-1}), T_{2g} (~540 cm^{-1}), and E_g (~307 cm^{-1}) Raman-active modes of magnetite Fe_3O_4,[130] and their emergence after RTP is consistent with thermally activated Fe redistribution toward the LFP/ITO interface, where Fe incorporation into the In_2O_3/SnO_2 matrix or local oxidation at the interface can produce iron oxide environments with spinel-type Raman signature.[135]

The dominant contribution of the Fe_3O_4 signal in the 500 ºC+RTP film, despite the relatively thin iron oxide layer expected, is further rationalized by a resonance enhancement effect. The 532 nm excitation wavelength used in these measurements falls within the strong optical absorption band of magnetite, arising from Fe^{2+}/Fe^{3+} charge-transfer transitions in the 400–700 nm range,[130] which selectively amplifies the Fe_3O_4 Raman cross-section relative to the non-absorbing $LiFePO_4$ matrix. This resonance effect explains why the Fe_3O_4 Raman bands dominate the spectrum even when the iron oxide volume fraction is below the GIXRD detection limit. Notably, although Fe_3O_4 is unambiguously identified by Raman spectroscopy as a surface phase in both RTP-annealed films, no corresponding XRD signal is detected in GIXRD, consistent with a nanocrystalline or low-volume-fraction iron oxide phase at the film surface and LFP/ITO interface.

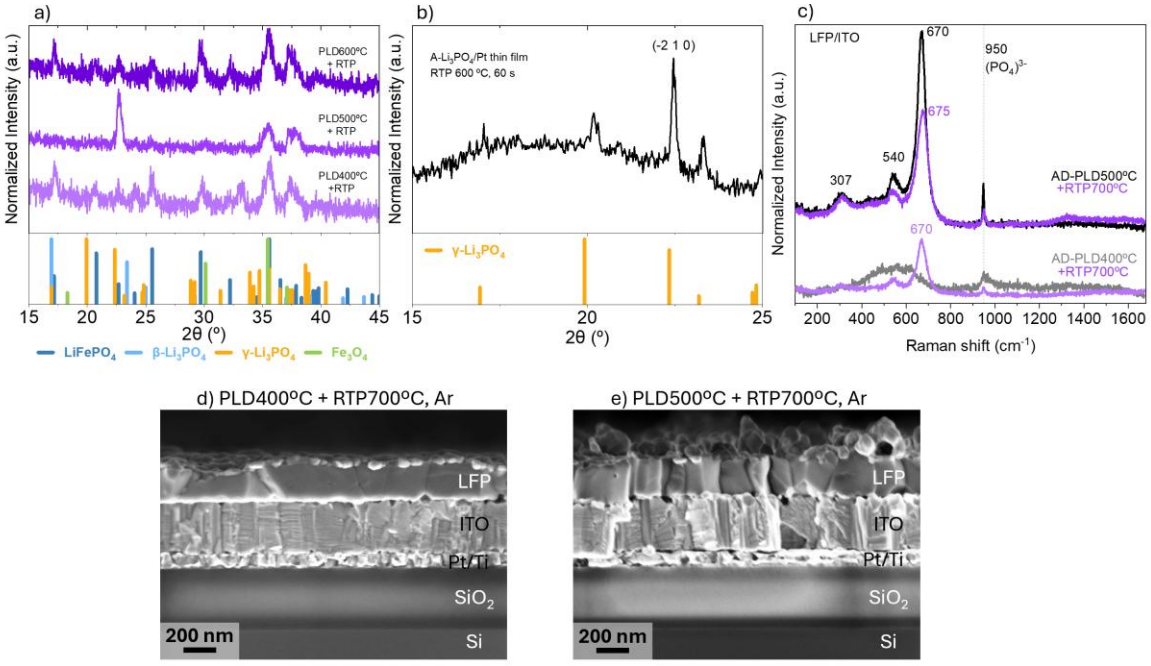


Figure 3.16 – (a) GIXRD patterns of LFP thin films deposited on ITO at 400, 500, and 600 ºC followed by RTP. Reference reflection markers for olivine $LiFePO_4$ (JCPDS 01-083-2092), β-Li_3PO_4 (JCPDS 15-

0760, $Pmn2_1$), γ-Li_3PO_4 (ICSD 77095, Pnma), and magnetite Fe_3O_4 (JCPDS 19-0629, Fd-3m). (b) θ-2θ diffraction pattern of a reference Li_3PO_4 thin film deposited by PLD on Pt-coated substrate at room temperature and annealed by RTP at 600 ºC for 60 s under Ar atmosphere. (c) Raman spectra of LFP thin films deposited on ITO at 400 ºC and 500 ºC before and after RTP treatment. Cross-sectional SEM micrographs of RTP-annealed LFP films deposited at (d) 400 ºC and (e) 500 ºC. All RTP-treated samples were annealed at 700 ºC for 60 s under Ar atmosphere, with heating and cooling ramp rates of 10 ºC s^{-1}.

3.5 Electrochemical characterization

The electrochemical behavior of selected LFP thin films was evaluated in liquid-electrolyte half-cell configuration to assess their intrinsic activity. The measurements were performed in a three-electrode configuration using the LFP thin film as the working electrode, Ag/AgCl as the reference electrode, Pt as the counter electrode, and 1 M Li_2SO_4 aqueous electrolyte. The response was analyzed by cyclic voltammetry and galvanostatic charge–discharge measurements, with particular attention to the effect of current collector, deposition temperature, and rapid thermal processing.

The electrochemical analysis is first established using a 300 nm-thick LFP film deposited directly on Pt, which serves as the reference case for PLD-grown LFP on a metallic current collector, as reported in the literaure. This baseline is then compared with LFP films deposited on ITO/Pt in order to evaluate whether current-collector engineering can improve the accessible fraction of the cathode and reduce the impact of interfacial reactions. Finally, RTP-treated films are examined to determine whether short post-deposition thermal treatment can activate films deposited at lower substrate temperature.

3.5.1 Electrochemical response of LFP films deposited on Pt

The electrochemical response of the 300 nm-thick LFP film deposited on Pt at 600 ºC was first evaluated in aqueous electrolyte in order to establish the baseline behavior of PLD-grown LFP on the reference metallic current collector. **Figure 3.17** shows the cyclic voltammograms recorded at scan rates between 0.25 and 2 mV s^{-1}. The curves exhibit the characteristic redox response of the Fe^{2+}/Fe^{3+} couple in olivine $LiFePO_4$, confirming the electrochemical activity of the deposited film. The reduction and oxidation peaks are centered at approximately 0.15 and 0.26 V vs Ag/AgCl, respectively, corresponding to the reversible reaction. Similar redox features and potential shifts have been reported for PLD-grown carbon-free $LiFePO_4$ thin films measured in aqueous electrolyte, confirming that the response observed here is consistent with lithium insertion/extraction in crystalline LFP thin film cathode.[70,136]

The relatively narrow and symmetric peaks indicate a reversible lithium insertion/extraction process. However, the peak separation increases with scan rate, from approximately 113 mV at 0.25 mV s^{-1} to 159 mV at 2 mV s^{-1}, revealing the onset of polarization at faster electrochemical rates. This behavior is expected for carbon-free $LiFePO_4$ thin films, where the absence of conductive additives makes the electrochemical response strongly dependent on the intrinsic ionic and electronic transport properties of the LFP layer, as well as on the quality of the film/current-collector interface. Previous studies have shown that the low electronic conductivity of pristine $LiFePO_4$ can strongly limit rate capability, whereas the incorporation of conductive additives, such

as carbon or metallic Ag, can improve charge transport but at the expense of a more complex electrode architecture.[73,74]

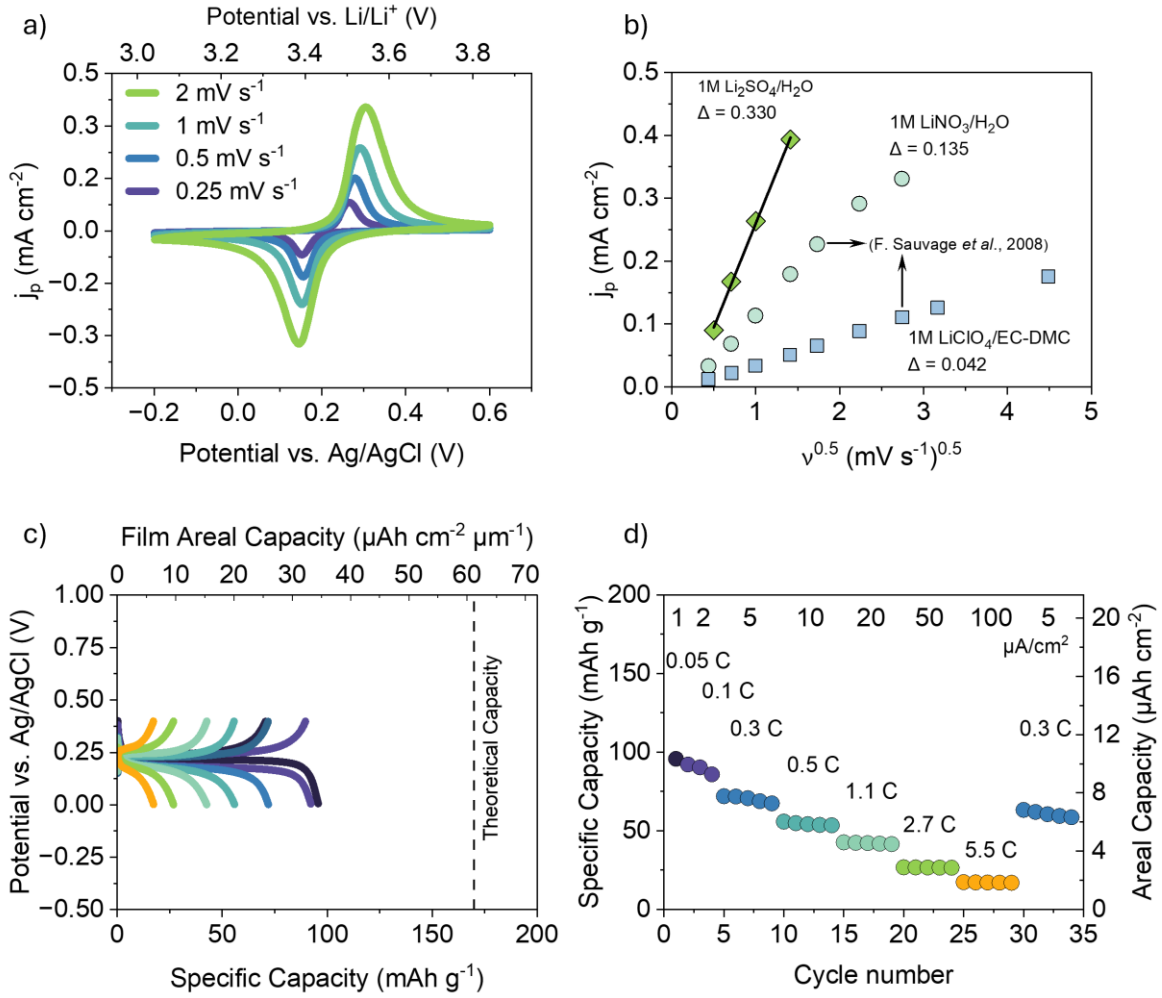


Figure 3.17 - Electrochemical behavior of a 300 nm-thick $LiFePO_4$ thin film deposited on Pt at 600 ºC and measured in aqueous electrolyte. (a) Cyclic voltammograms recorded at scan rates of 0.25, 0.5, 1, and 2 mV s^{-1}. (b) Linear dependency of the peak current density per area (j_p) as a function of $\nu^{0.5}$. (c) Galvanostatic charge–discharge voltage profiles measured at different current densities. (c) Evolution of discharge capacity as a function of cycle number. Measurements were performed in a three-electrode configuration using 1 M Li_2SO_4 aqueous electrolyte, Ag/AgCl reference electrode, and Pt counter electrode.

The areal capacity estimated from the CV curves reaches approximately 79.6 mAh g^{-1} (8.59 μAh cm^{-2}) at 0.25 mV s^{-1}, corresponding to about 46.8 % of the theoretical capacity expected for a dense 300 nm-thick $LiFePO_4$ film. When the scan rate is increased to 2 mV s^{-1}, the capacity decreases to approximately 7.21 μAh cm^{-2}, indicating that part of the active material becomes less accessible under faster polarization conditions. This decrease is consistent with kinetic limitations associated with lithium diffusion and charge transport across the carbon-free LFP layer. Even so, the capacity obtained here is higher than values previously reported for thicker PLD-grown

$LiFePO_4$ films measured under comparable aqueous half-cell conditions, where limited utilization of the theoretical capacity was also observed. [136]

The relationship between peak current and scan rate (**Figure 3.17b**) further indicates that the electrochemical response is mainly governed by diffusion-controlled lithium insertion. The average chemical diffusion coefficient of Li^+, in accordance with the Randless-Sevcik eaquation and estimated from the anodic peak currents, is approximately 2.82×10^{-12} cm^2 s^{-1}. This value falls within the broad range reported for $LiFePO_4$, where the apparent diffusion coefficient can vary significantly depending on the experimental method, film microstructure, lithium content, and crystallographic orientation. In particular, kinetic studies combining CV, GITT, and EIS have shown that Li^+ transport in LFP is highly sensitive to both measurement conditions and structural defects.[66,76] This is also consistent with the anisotropic nature of Li^+ diffusion in olivine $LiFePO_4$, where lithium transport occurs preferentially along one-dimensional channels and can be strongly affected by grain orientation and channel blocking.[16]

Galvanostatic charge–discharge measurements further confirm the partial utilization of the LFP/Pt electrode (**Figure 3.17c,d**). At low current density, the film delivers approximately 96 mAh g^{-1} at 1 μA cm^{-2} and 92 mAh g^{-1} at 2 μA cm^{-2}. At 100 μA cm^{-2}, the discharge capacity decreases to approximately 20 mAh g^{-1}, reflecting the stronger influence of transport limitations at high current density. Importantly, the capacity is largely recovered when the current is returned to lower values, indicating that the capacity decrease at high current is mainly associated with rate limitations rather than irreversible degradation of the LFP phase.

At low current density, however, a gradual capacity loss is observed over long cycling times. This behavior is possibly due to bulk degradation of the LFP film, but may also arise from time-dependent parasitic processes at the electrode/electrolyte interface. Previous studies have shown that $LiFePO_4$ can undergo surface reactions in aqueous media, including Fe^{2+} dissolution, partial surface delithiation, hydration, and the formation of passivating layers, especially when the electrode remains for long periods within the operating potential window.[137–139] Therefore, the more pronounced fading observed during low-current cycling can be attributed, at least in part, to cumulative surface processes promoted by the longer residence time in contact with the aqueous electrolyte.

Despite the clear electrochemical activity of the LFP/Pt electrode, the measured capacity remains significantly below the theoretical value of $LiFePO_4$. This limited utilization is consistent with the structural and compositional results discussed earlier in this chapter. In particular, the island-like growth behavior on Pt, the rougher surface morphology, and the formation of an $FePt_3$ interfacial phase can reduce the effectively accessible LFP volume and hinder homogeneous ionic/electronic access across the film. Therefore, the LFP/Pt electrode provides a useful baseline that confirms the activity of PLD-grown LFP while also highlighting the limitations associated with direct deposition on Pt current collectors. These limitations may have contributed to the limited continuation of early LFP/Pt thin-film studies toward all-solid-state battery architectures based on this cathode configuration.

3.5.2 Electrochemical response of LFP films deposited on ITO and influence of deposition temperature

After establishing the electrochemical baseline of LFP deposited directly on Pt, the response of LFP films deposited on ITO/Pt was evaluated as a function of deposition temperature. **Figure 3.18a-c** shows the cyclic voltammograms of as-deposited films grown at 400, 500, and 600 ºC. Three consecutive cycles were recorded at each scan rate to assess the reproducibility of the response.

The film deposited at 400 ºC exhibits low-intensity redox features, indicating limited electrochemical activation in the as-deposited state. In contrast, the films deposited at 500 and 600 ºC show more defined oxidation and reduction peaks, located around 0.30–0.35 V and 0.20–0.25 V vs Ag/AgCl, respectively. This evolution agrees with the structural results discussed earlier in this chapter, where increasing the deposition temperature improves the crystallinity and ordering of the LFP phase. For all samples, the peak current increases with scan rate, while the anodic and cathodic peaks shift slightly toward higher and lower potentials, respectively. This behavior reflects the increase in polarization under faster electrochemical conditions. The repeated cycles remain stable at each scan rate, indicating good reversibility within the investigated potential window.

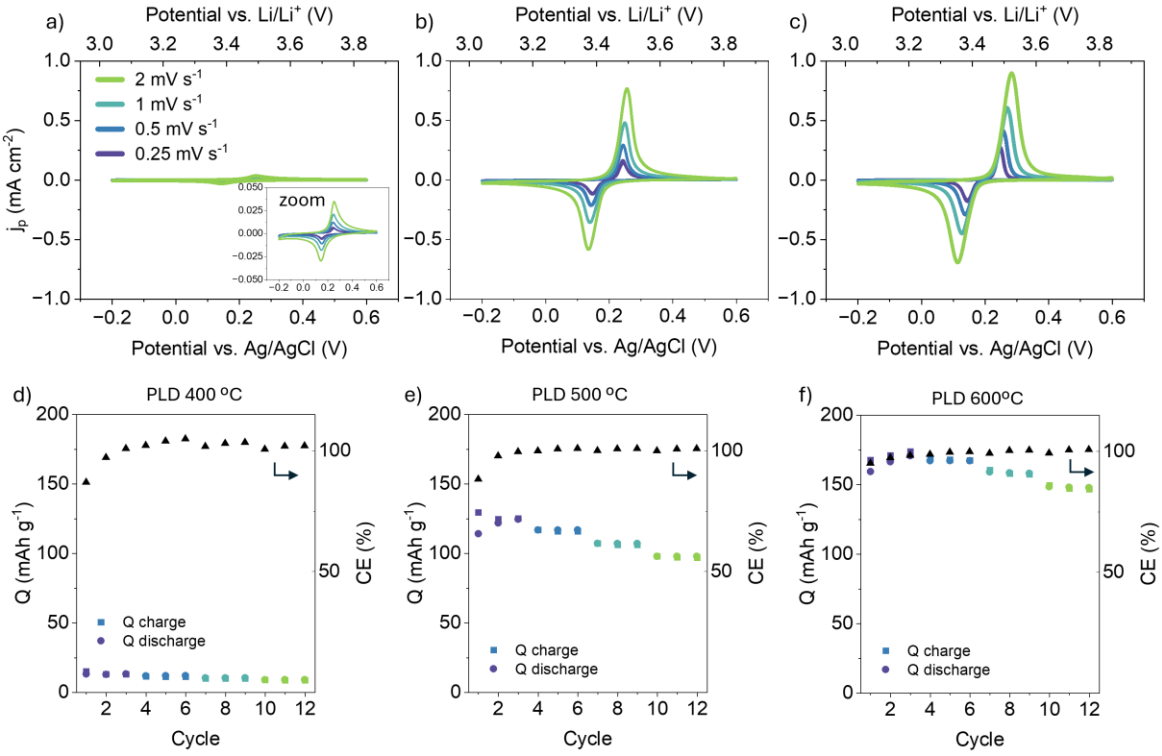


Figure 3.18 - Cyclic voltammograms of as-deposited LFP thin films fabricated by PLD at substrate temperatures of (a) 400 ºC, (b) 500 ºC and (c) 600 ºC. Measurements were performed at scan rates of 0.25, 0.5, 1 and 2 mV s^{-1}. Specific discharge capacity obtained from the integration of the cyclic voltammetry curves and corresponding coulombic efficiency as a function of cycle number for the as-deposited thin films deposited at (d) 400 ºC, (e) 500 ºC and (f) 600 ºC.

The discharge capacities obtained from the integration of the cathodic current are summarized in **Figure 3.18d-f**, together with the corresponding coulombic efficiency. The 400 ºC film delivers capacities below approximately 15 mAh g^{-1}, confirming its poor electrochemical activity. The 500 ºC film reaches approximately 120 mAh g^{-1}, while the 600 ºC film delivers the highest capacity, close to 160 mAh g^{-1} at the lowest scan rate. A slight activation is observed during the first cycles at 0.25 mV s^{-1} for the 500 and 600 ºC samples, whereas the response becomes more stable at higher scan rates.

As expected, the accessible capacity decreases with increasing scan rate due to kinetic limitations. Between 0.25 and 2 mV s^{-1}, the capacity decrease is approximately 15 % for the 500 ºC film, and only 8 % for the 600 ºC film.

The same trend is confirmed by galvanostatic charge-discharge measurements, shown in **Figure 3.19**Error! Reference source not found.. Five consecutive cycles were recorded at each current step before increasing the applied current. The voltage profiles display the characteristic $LiFePO_4/FePO_4$ plateau around 0.2 V vs Ag/AgCl (~3.44 V vs Li/Li^+), with increasing polarization at higher current densities.

The film deposited at 400 ºC delivers only 7.6 mAh g^{-1} at 2 μA cm^{-2}, decreasing to 2.5 mAh g^{-1} at 100 μA cm^{-2} (**Figure 3.19a,b**). A much higher capacity is obtained for the film deposited at 500 ºC, which decreases from 120.5 to 71.3 mAh g^{-1} over the same current range (**Figure 3.19c,d**). The best performance among the as-deposited samples is obtained for the 600 ºC film, which delivers 163.3 mAh g^{-1} at 2 μA cm^{-2} and retains 100.9 mAh g^{-1} at 100 μA cm^{-2} (**Figure 3.19d,e**).

The capacity decrease at high current density is mainly associated with rate limitations, as the capacity is largely recovered when the current is returned to a lower value at the end of the sequence. This recovery indicates that the high-current capacity loss is not primarily caused by irreversible degradation, but by limited lithium-ion diffusion and charge transport under faster cycling conditions.

Compared with the LFP/Pt baseline presented in **Figure 3.17**, the optimized LFP/ITO films exhibit significantly higher electrochemical utilization. In particular, the 600 ºC LFP/ITO film approaches the theoretical capacity of $LiFePO_4$ under low-rate conditions, whereas the 300 nm LFP/Pt electrode shows only partial utilization. This comparison reinforces the role of the current collector and film/substrate interface in determining the effective active volume of PLD-grown LFP cathodes.

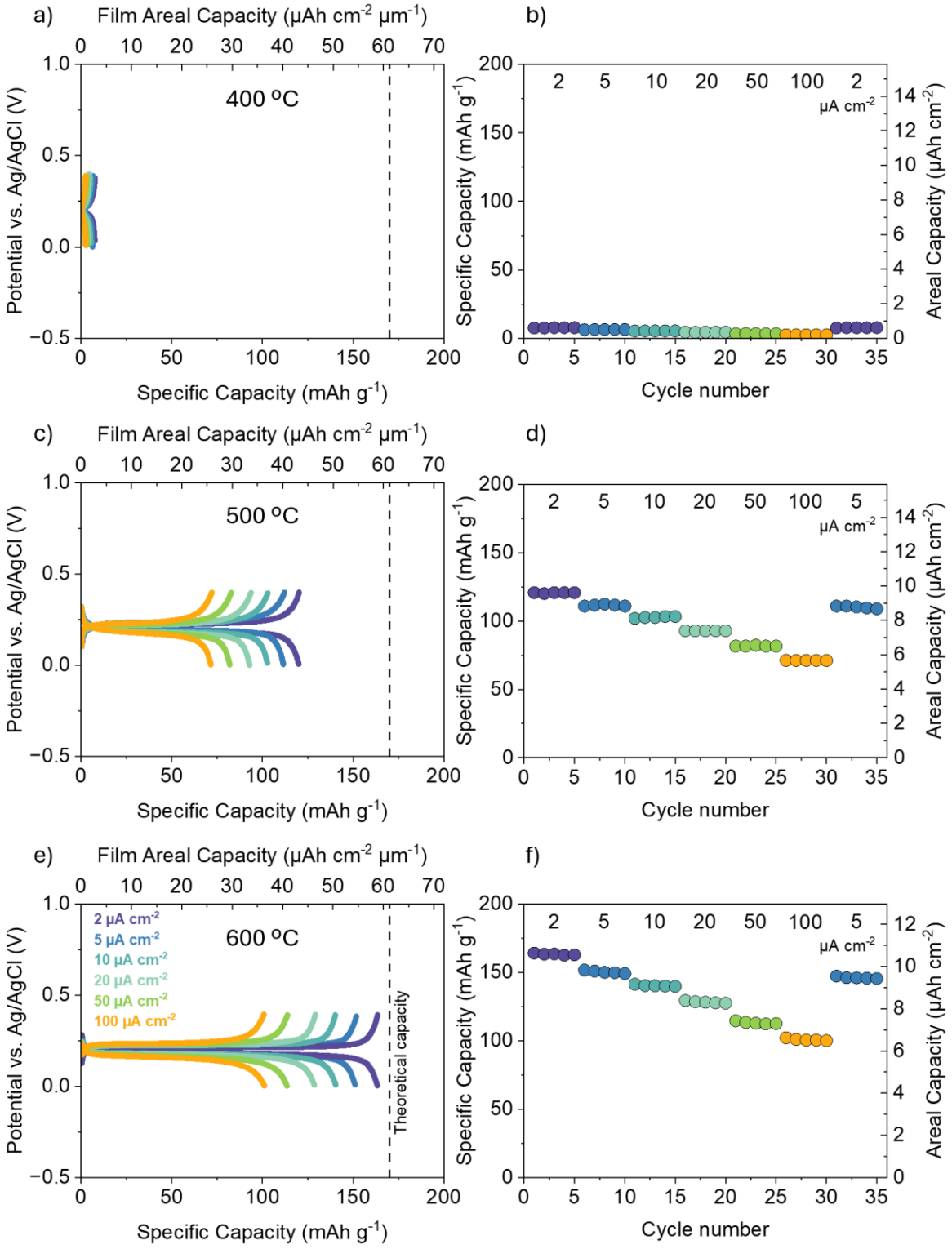


Figure 3.19 - Galvanostatic charge–discharge behavior of the as-deposited $LiFePO_4$ thin films deposited at a,b) 400 ºC, c,d) 500 ºC, and e,f) 600 ºC on ITO/Pt current collector. Left: potential versus capacity profiles measured at different applied currents. The bottom axis corresponds to the specific capacity (mAh g^{-1}), while the top axis shows the areal capacity normalized by film thickness (μAh cm^{-2} μm^{-1}). Right:

evolution of discharge capacity as a function of cycle number, expressed as specific capacity (mAh g^{-1}, left axis) and areal capacity (μAh cm^{-2}, right axis). Five cycles were performed at each current step.

3.5.3 Effect of RTP on electrochemical performance

The influence of rapid thermal processing on the electrochemical behavior of LFP films deposited on ITO/Pt was evaluated for samples grown at 400, 500, and 600 ºC and subsequently annealed at 700 ºC for 60 s under Ar atmosphere. The aim of this treatment was to determine whether short thermal exposure could improve the electrochemical activity of films deposited at lower substrate temperature, while preserving the integrity of the LFP/current-collector interface.

Figure 3.20 shows the cyclic voltammetry response of the RTP-treated films. Compared with the as-deposited state, the most pronounced improvement is observed for the film deposited at 400 ºC, which changes from a weakly active electrode to a clearly defined LFP redox response after annealing. This indicates that RTP promotes the crystallization and electrochemical activation of the initially poorly ordered layer. The film deposited at 500 ºC also benefits from the treatment, reaching the highest CV-derived capacity among the annealed samples, whereas the 600 ºC film maintains a high capacity but does not show further improvement relative to its as-deposited counterpart.

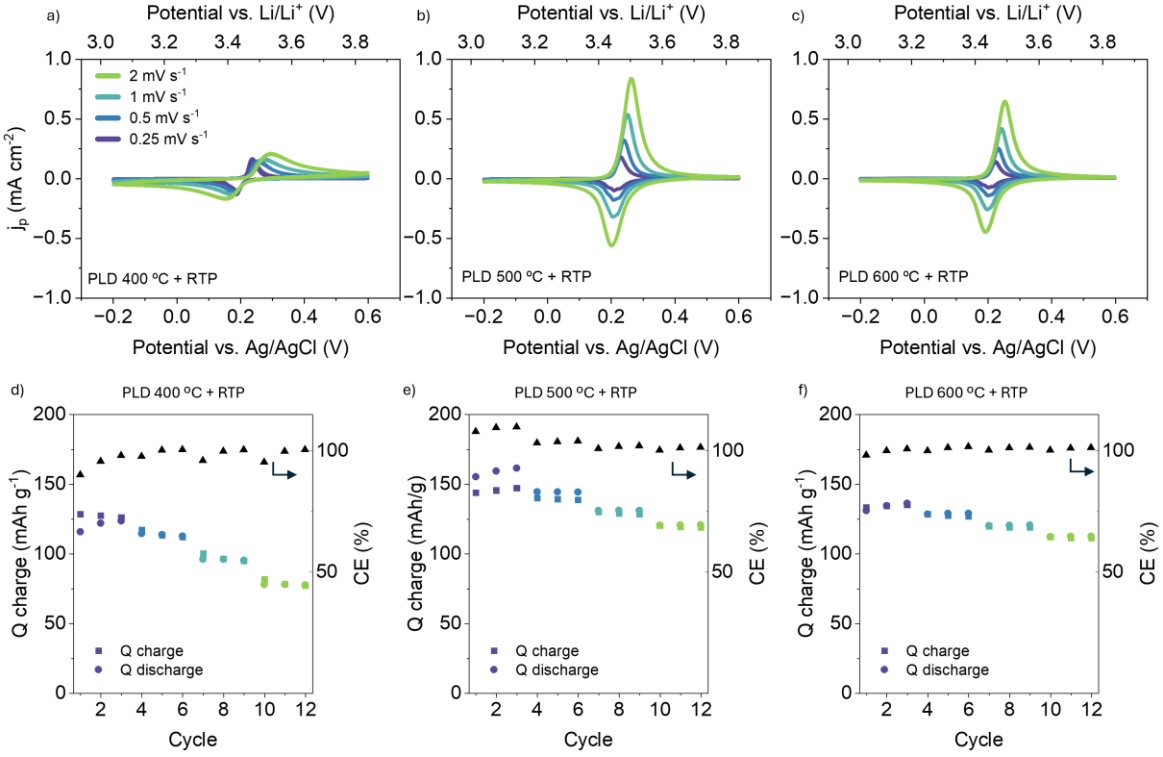


Figure 3.20 - Cyclic voltammograms of RTP-annealed $LiFePO_4$ thin films deposited by PLD on ITO/Pt substrates at (a) 400 ºC, (b) 500 ºC, and (c) 600 ºC. All samples were subjected to rapid thermal processing at 700 ºC for 1 min under Ar atmosphere with a heating and cooling ramp of 10 ºC s^{-1}. Specific discharge capacity obtained from the integration of the cyclic voltammetry curves and corresponding coulombic efficiency as a function of cycle number.

At the lowest scan rate, the RTP-treated films deposited at 400, 500, and 600 ºC deliver approximately 120, 159, and 135 mAh g^{-1}, respectively. As the scan rate increases to 2 mV s^{-1}, the capacities decrease to approximately 78, 121, and 113 mAh g^{-1}. Therefore, although the 500 ºC + RTP sample provides the highest capacity at low scan rate, the annealed sample deposited at 600 ºC sample shows the smallest relative capacity loss, suggesting better rate capability after annealing.

The galvanostatic charge–discharge results, shown in **Figure 3.21**, follow the same general trend. The RTP-treated film deposited at 400 ºC delivers approximately 118 mAh g^{-1} at the lowest current step, decreasing to 32.5 mAh g^{-1} at the highest current density. For the one deposited 500 ºC, the capacity decreases from approximately 148 to 88.6 mAh g^{-1}, while the annealed sample already deposited at 600 ºC decreases from approximately 127 to 81 mAh g^{-1}. These results confirm that RTP is particularly effective for activating films deposited at 400 ºC and, to a lesser extent, improving the performance of the 500 ºC sample.

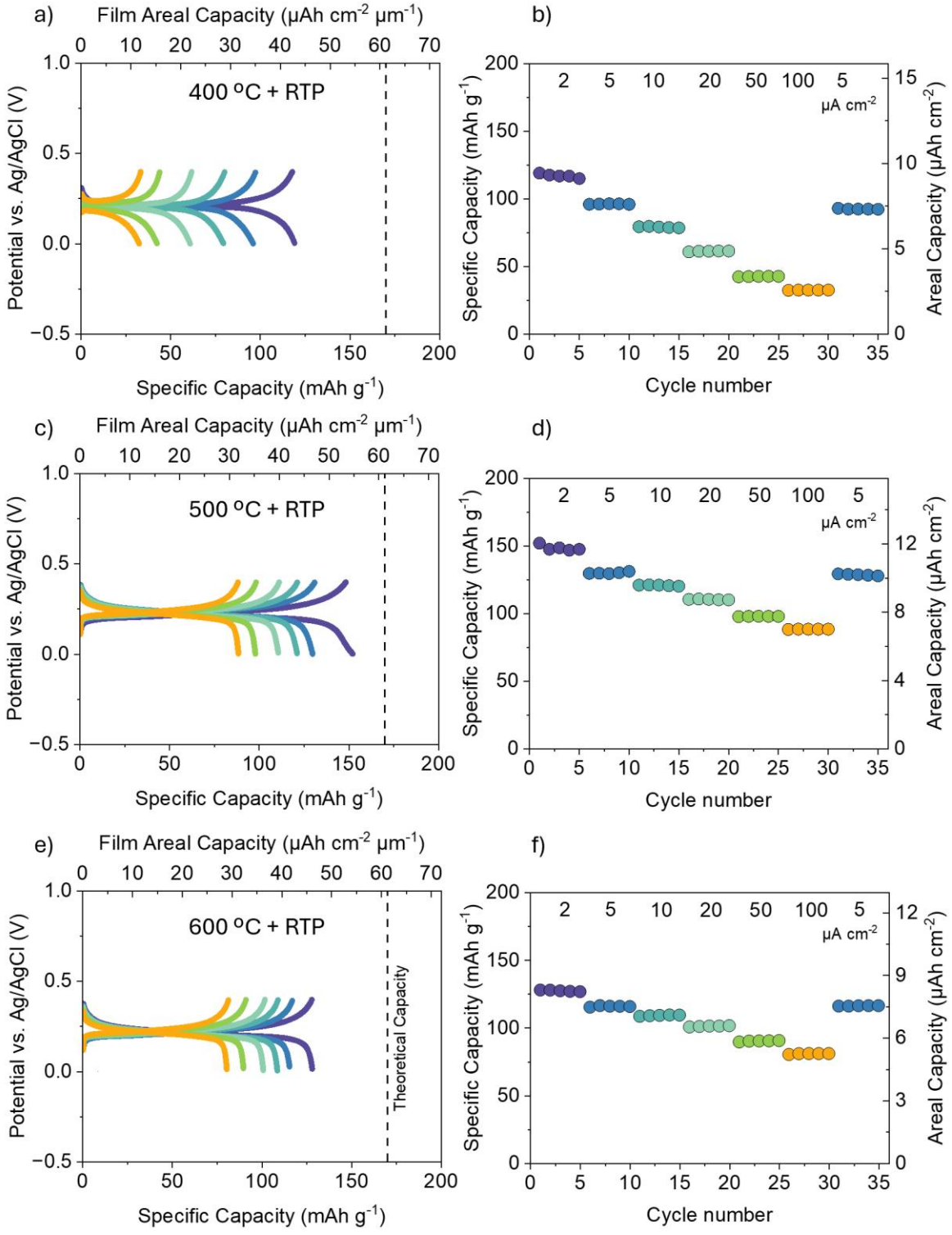


Figure 3.21 - Galvanostatic charge–discharge curves and summary of the discharge capacities over the cycles of RTP annealed LFP thin films deposited by PLD on ITO substrates at (a,b) 400 ° C, (c,d) 500 ºC and (e,f) 600 ºC. All samples were annealed in Ar at 700ºC for 60 s with 10 ºC/s ramp rate during heating and cooling.

A direct comparison between as-deposited and RTP-treated films is summarized in **Table 3.1**. Instead of focusing only on the capacity loss at high current density, the table highlights the capacity variation induced by RTP, which is more relevant to evaluate the effect of the post-treatment. For the 400 ºC film, the capacity increases from 7.6 to 118 mAh g^{-1} at 2 μA cm^{-2}, corresponding to a gain of more than one order of magnitude. For the 500 ºC film, the improvement is noticed, increasing from 120.5 to 148 mAh g^{-1}. In contrast, the 600 ºC film decreases from 163.3 to 127 mAh g^{-1} after RTP, indicating that additional thermal treatment is not beneficial once the film is already well crystallized during deposition.

Table 3.1 - Comparison of the discharge capacities of as-deposited and RTP-treated LFP thin films deposited on ITO. The percentage in parenthesis highlights the capacity variation induced by RTP at low and high current density.

Deposition temperature	State	Capacity at 2 μA cm^{-2} mAh g^{-1}	Capacity at 100 μA cm^{-2} mAh g^{-1}
400 ºC	As-deposited	7.6	2.5
400 ºC	RTP-treated	118	32.5
500 ºC	As-deposited	120.5	71.3
500 ºC	RTP-treated	148	88.6
600 ºC	As-deposited	163.3	100.9
600 ºC	RTP-treated	127	81

Overall, these results show that RTP is an effective fabrication strategy for LFP films deposited at lower substrate temperature, but its benefit depends strongly on the initial microstructure of the as-deposited layer. While annealing can compensate for the poor crystallinity of the 400 ºC film and enhance the 500 ºC sample, it may induce less favorable microstructural changes in films that are already highly active in the as-deposited state. Therefore, the best electrochemical response is obtained by balancing the deposition temperature and post-treatment conditions, rather than by maximizing the thermal budget of the process.

To compare the apparent kinetic response of the LFP thin films, the anodic peak current density (j_p), extracted from CV measurements, was plotted as a function of the square root of the scan rate ($\nu^{0.5}$), as shown in **Figure 3.22**. For insertion-type electrodes, the dependence of peak current on $\nu^{0.5}$ is commonly associated with diffusion-related lithium insertion.

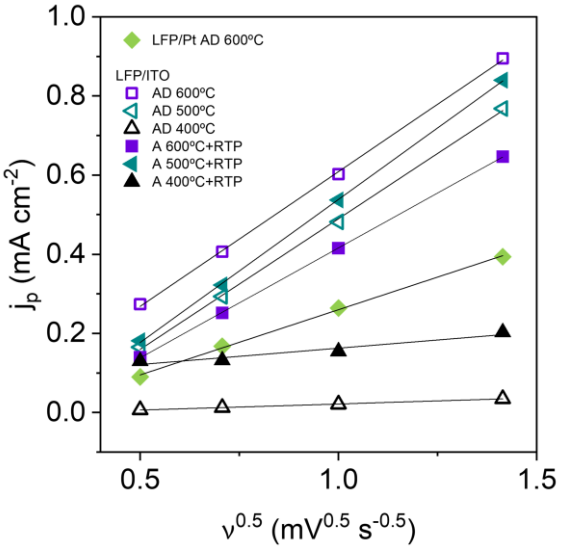


Figure 3.22 - Peak-current analysis of LFP thin films from cyclic voltammetry. Linear dependence of the anodic peak current density, j_p, as a function of the square root of the scan rate, $\nu^{0.5}$, for LFP films as-deposited (AD) on Pt and ITO, and annealed (A) by RTP at 700 ºC for 60 s under Ar atmosphere.

The extracted slopes and the corresponding apparent Li^+ diffusion coefficients are summarized in **Table 3.2**. The as-deposited LFP/ITO films grown at 500 and 600 ºC show higher slopes of 0.660 and 0.681 mA $s^{0.5}$ cm^{-2} $mV^{-0.5}$, respectively, corresponding to apparent D_{Li} values close 1.2×10^{-11} cm^2 s^{-1}. These higher values are consistent with the larger capacities obtained for the optimized LFP/ITO electrodes and suggest a more accessible redox-active LFP fraction.

Table 3.2 - Apparent Li^+ diffusion coefficients (D_{Li}) calculated from the Randles-Sevcik equation.

Deposition temperature	State	Slope mA $s^{0.5}$ cm^{-2} $mV^{-0.5}$	Apparent D_{Li} cm^2 s^{-1}
400 ºC	As-deposited	0.031	2.53×10^{-14}
400 ºC	RTP-treated	0.083	1.82×10^{-13}
500 ºC	As-deposited	0.660	1.16×10^{-11}
500 ºC	RTP-treated	0.723	1.39×10^{-11}
600 ºC	As-deposited	0.681	1.23×10^{-11}
600 ºC	RTP-treated	0.555	8.20×10^{-12}
600 ºC	As-deposited	0.330	2.89×10^{-12}

The 400 ºC as-deposited film shows a much lower slope and an apparent D_{Li} of only 2.5×10^{-14} cm^2 s^{-1}, in agreement with its weak electrochemical response. After RTP, the 400 ºC sample shows a moderate increase in slope but remains kinetically limited compared with the films deposited at higher temperature. The highest slope is obtained for the 500 ºC + RTP sample, whereas the 600 ºC + RTP film shows a lower value than its as-deposited counterpart. This confirms that RTP is beneficial mainly for activating initially under-crystallized films, while it does

not necessarily improve films already grown under optimized high-temperature conditions. For the films deposited at lower temperature, RTP enhances LFP crystallinity and promotes more efficient Li^+ transport within the active material and the charge transfer on the surface, leading to an upward shift of the trend lines and an increase in their slopes.

These D_{Li} values (**Table 3.2**.) are broadly consistent with those reported in the literature for $LiFePO_4$ thin-film electrodes, while lying above the range typically obtained for bulk composite electrodes. For bulk $LiFePO_4$ powder with carbon-black addition, Prosini *et al.* determined D_{Li} values ranging from 1.8×10^{-14} to 2.2×10^{-16} cm^2 s^{-1} by GITT and impedance spectroscopy, with a minimum near the two-phase transition at $x \approx 0.5$ in $Li_{1-x}FePO_4$.[140] For $LiFePO_4$ thin films prepared by RF magnetron sputtering, Xie *et al.* reported an apparent D_{Li} of 1.93×10^{-14} cm^2 s^{-1} by cyclic voltammetry using the Randles-Sevcik equation (the same method employed in this study) and values in the range of 10^{-14} to 10^{-12} cm^2 s^{-1} by PITT and EIS; importantly, the authors showed that these values were independent of Ag content in the films, confirming that they reflect intrinsic Li^+ transport in the $LiFePO_4$ lattice.[141] The D_{Li} values obtained in the present work for the optimized films deposited at 500 and 600 ºC (approximately $1.2\text{-}1.4 \times 10^{-11}$ cm^2 s^{-1}) are considerably higher than those reported by Xie *et al.* by CV, which may reflect differences in film microstructure, grain crystallinity, and the higher deposition temperature in the PLD employed here. The lower value obtained for the 400 ºC as-deposited film (2.5×10^{-14} cm^2 s^{-1}) falls within the range reported for the sputtered thin films by CV, consistent with its poorer crystallinity.

3.5.4 Post-cycling analysis of the optimized LFP/ITO electrode

To further investigate the state-dependent electrochemical response of the optimized LFP/ITO electrode, PEIS measurements were performed after 30 min of open-circuit relaxation in the charged and discharged states (**Figure 3.23e**). These measurements complement the GDOES depth profiles shown in **Figure 3.23a–c**, which confirm lithium extraction after charging and lithium re-insertion after discharge. The corresponding galvanostatic voltage profiles in **Figure 3.23d** indicate the electrochemical states at which the electrodes were stopped before the post-cycling analyses.

The Nyquist plots (**Figure 3.23e**) reveal a clear difference in the low-frequency response depending on the lithiation state of the film. In the charged state, where the LFP layer is more delithiated and therefore closer to $FePO_4$, the low-frequency tail becomes more vertical. This response suggests that the impedance is not governed by a classical semi-infinite diffusion process, but rather by a finite-thickness or capacitive-like response. In this regime, the characteristic penetration depth of the electrochemical perturbation becomes comparable to, or larger than, the effective thickness of the electrochemically accessible film. Therefore, the low-frequency response can sense the finite geometry of the thin-film electrode and the presence of the buried current collector as a blocking boundary for Li^+ transport.

Importantly, this interpretation does not imply that Li^+ ions physically migrate through the entire film and enter the current collector. Instead, it indicates that the concentration perturbation

associated with Li^+ insertion, together with the required electronic/polaronic compensation from the current collector, extends through a significant fraction of the film thickness. Since the ITO current collector provides electronic conduction but does not act as a lithium-insertion phase, the lower interface behaves as a blocking boundary for the chemical diffusion of lithium. As a result, the response progressively approaches a more capacitive behavior associated with lithium redistribution and charge accumulation within a finite film volume.

By contrast, in the discharged state, where the film is more lithiated and closer to $LiFePO_4$, the low-frequency tail is more inclined, approaching the characteristic response of a Warburg-type diffusion process. This behavior is consistent with an apparently semi-infinite diffusion regime within the frequency range investigated. Although the electrode is physically a thin film, the AC perturbation does not fully reach the opposite boundary of the film during the measurement. Therefore, the system responds as if the diffusion length were still smaller than the effective film thickness. This may be associated with a more localized diffusion-controlled response in the $LiFePO_4$-rich state, where lithium transport occurs through a nearly lithiated framework and can be constrained by the availability of lithium vacancies, phase-boundary motion, and coupled ionic/electronic transport.

This interpretation is schematically summarized in **Figure 3.23f**. In the present thin-film geometry, the liquid electrolyte contacts the top surface of the LFP layer, whereas the ITO current collector is located underneath the film. Therefore, Li^+ insertion/extraction from the electrolyte-facing surface must be coupled with electronic or polaronic compensation from the buried current collector. The different low-frequency PEIS responses suggest that the depth over which this coupled electrochemical perturbation propagates changes with the state of lithiation. The charged, $FePO_4$-rich state shows a more vertical response, consistent with a finite-thickness response and partial capacitive accumulation at a blocking boundary. The discharged, $LiFePO_4$-rich state shows a more Warburg-like response, consistent with an apparently semi-infinite diffusion regime within the frequency range investigated.

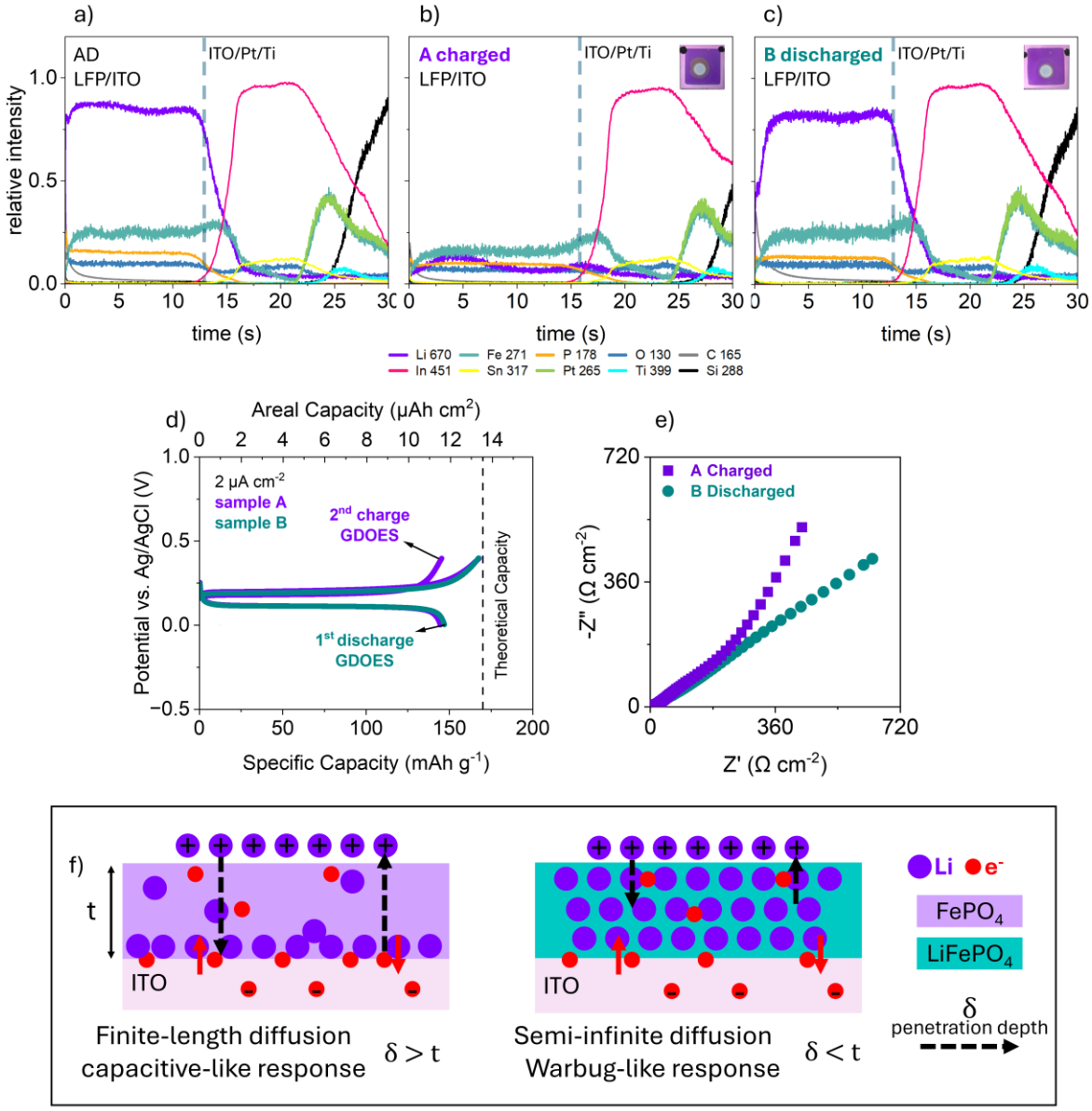


Figure 3.23 - GDOES elemental depth profiles: of (a) as-deposited film before electrochemical testing, (b) after charging, corresponding to the delithiated $FePO_4$-rich state of sample A, and (c) after discharging, lithiated $LiFePO_4$-rich state of sample B. (d) Galvanostatic charge–discharge voltage profiles of samples A and B measured at 2 μA cm^{-2}. (e) Nyquist plots obtained from PEIS measurements in the charged and discharged states. (f) Schematic interpretation of the low-frequency PEIS response.

Additional SEM observations were performed to evaluate morphological changes induced by electrochemical cycling (**Figure 3.24**). After cycling and stopping the electrode in the discharged state, the overall multilayer structure remains preserved, indicating that the film does not undergo delamination during electrochemical operation (**Figure 3.24c**). However, the cycled electrode shows a more heterogeneous contrast distribution, and internal boundaries within the film become more evident. In top view (**Figure 3.24d**), the surface appears with localized porosity and bright features that are attributed to crystallized electrolyte residues remaining on the surface after cycling.

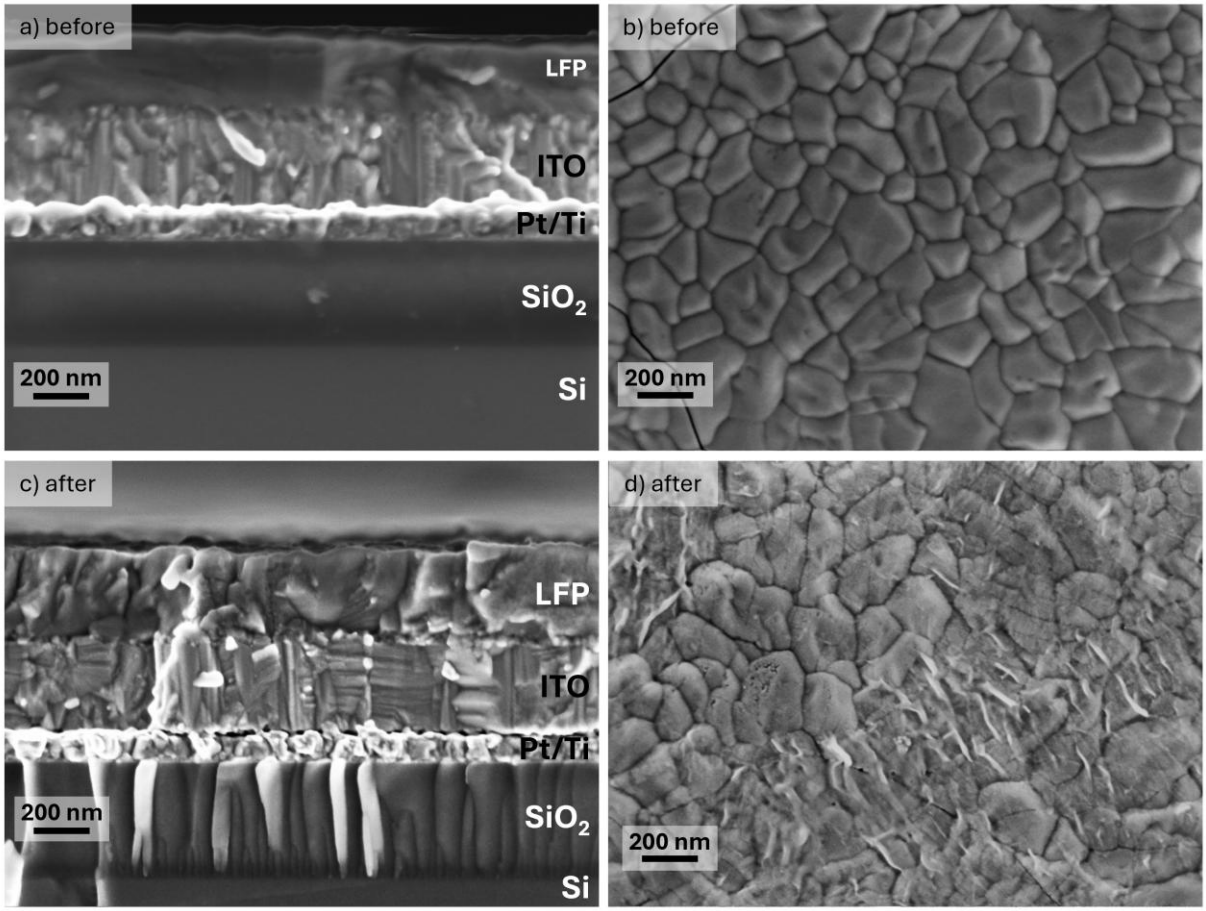


Figure 3.24 - (a) Cross-sectional and (b) top-view SEM images of the as-deposited electrode before electrochemical testing. (c) Cross-sectional and (d) top-view SEM image of the electrode after electrochemical cycling.

To further compare the effect of the current collector on lithium accessibility, normalized GDOES profiles of the Li signal and the corresponding substrate element marker were plotted for LFP/Pt and LFP/ITO electrodes fabricated at 600 ºC in the as-deposited and charged states, as shown in **Figure 3.25**. The profiles were normalized to facilitate visual comparison between different samples and should therefore be interpreted qualitatively. In the case of 120 nm thick LFP on Pt, charging was performed at a very low current density of 0.16 μA cm^{-2}, with the aim of extracting the maximum possible amount of Li from the film. Even under these slow delithiation conditions, the charged profile still exhibits a residual and broadened Li contribution extending toward the region where the Pt signal increases.

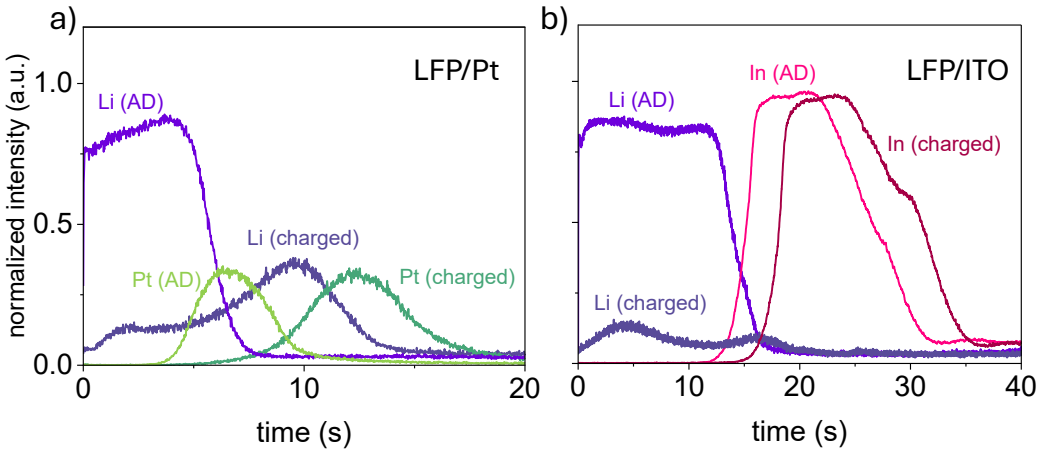


Figure 3.25 - Normalized GDOES profiles comparing the Li signal and the substrate marker signal for LiFePO4 thin films in the as-deposited and charged states: (a) LFP deposited on Pt, and (b) LFP deposited on ITO.

In contrast, the 220 nm LFP on ITO shows a much weaker residual Li signal after charging at 2 μA cm^{-2}, while the In signal clearly marks the ITO layer. This indicates a more effective delithiation of the LFP layer deposited on ITO, consistent with the higher reversible capacities measured for this configuration. Overall, this comparison reinforces that replacing direct contact with Pt by an ITO interlayer improves the electrochemically accessible fraction of the LFP film. The stronger Li retention observed for LFP/Pt, despite the lower charging current used, supports the interpretation that heterogeneous growth and interfacial reactions limit the reversible participation of the full cathode volume.

3.5.5 Asymmetric constant current charge/discharge cycles

To close the electrochemical performance study of LFP electrode on ITO, a 180 nm film was tested under symmetric and asymmetric galvanostatic conditions to evaluate whether charge or discharge is more rate-limiting. Under symmetric conditions, with charge and discharge both performed at 2 μA cm^{-2} (2 cycles), the electrode delivered a stabilized discharge capacity of 164.5 mAh g^{-1}, with a coulombic efficiency of 99.2%. When the charge current density was increased to 10 μA cm^{-2} while the discharge was kept at 2 μA cm^{-2}, the average discharge capacity over 5 cycles remained high, reaching 153.8 mAh g^{-1}, with a coulombic efficiency of 99.8%. This indicates that fast delithiation is relatively well tolerated by the LFP/ITO electrode. In contrast, when the discharge current density was increased to 10 μA cm^{-2} while charging was performed at 2 μA cm^{-2}, the average discharge capacity over 5 cycles decreased to 145.1 mAh g^{-1}, with a coulombic efficiency of 98.2%. The increase in polarization is modest but measurable: the average voltage hysteresis rises from 44.1 mV under symmetric cycling to 48.5 mV for fast charge and 50.3 mV for fast discharge. These results suggest that Li^+ insertion during discharge/lithiation is the more kinetically limited step.

Symmetric and asymmetric galvanostatic charge–discharge profiles of the same LFP/ITO thin-film electrode deposited at 600 ºC. Voltage profiles measured using: (a) the same current density for charge and discharge, 2 μA cm^{-2}; (b) fast charge at 10 μA cm^{-2} followed by slow discharge at 2 μA cm^{-2}; and (c) slow charge at 2 μA cm^{-2} followed by fast discharge at 10 μA cm^2.

3.6 Conclusions

This chapter demonstrated the successful fabrication of carbon-free $LiFePO_4$ thin-film cathodes by pulsed laser deposition and established the main processing–structure–interface–performance relationships governing their electrochemical response. The results show that the electrochemical activity of PLD-grown LFP films is not controlled by crystallinity alone, but by the combined effect of deposition temperature, substrate chemistry, film morphology, interfacial reactions, and the fraction of the cathode volume that remains electrochemically accessible.

The morphology of the films was strongly dependent on the current collector. LFP deposited directly on Pt exhibited rougher surface and strongly coalesced grains, with evidence of island-like nucleation during the early stages of growth. In contrast, films deposited on ITO showed a smoother and more homogeneous morphology, with a dense surface composed of well-defined polygonal grains. This difference indicates that the ITO interlayer improves the wetting and nucleation behavior of LFP, leading to a more continuous and homogeneous cathode layer.

The structural analysis confirmed the formation of olivine $LiFePO_4$ under optimized deposition conditions, particularly at 500–600 ºC and 1 mTorr Ar. Films deposited at lower temperature showed broader Raman features and poorer electrochemical activity, while increasing the deposition temperature promoted crystallinity, grain development, and higher capacity. However, the results also show that high-temperature deposition can promote interfacial reactions, especially when LFP is deposited directly on Pt. GIWAXS revealed the formation of $FePt_3$-related reflections at the LFP/Pt interface, and GDOES indicated temperature-dependent Fe redistribution toward the Pt-containing substrate. These interfacial processes provide a plausible explanation for the limited electrochemical utilization of LFP/Pt electrodes, despite the formation of crystalline $LiFePO_4$.

The comparison between Pt and ITO current collectors was one of the central outcomes of this chapter. The 300 nm LFP/Pt electrode delivered approximately 92 mAh g^{-1} at 2 μA cm^{-2} and decreased to about 20 mAh g^{-1} at 100 μA cm^{-2}, indicating partial utilization and strong kinetic limitations. In contrast, the optimized as-deposited LFP/ITO electrode grown at 600 ºC reached 163.3 mAh g^{-1} at 2 μA cm^{-2}, approaching the theoretical capacity of $LiFePO_4$, and retained 100.9 mAh g^{-1} at 100 μA cm^{-2}. This improvement demonstrates that replacing direct LFP/Pt contact by an ITO/Pt current collector substantially increases the accessible active fraction of the LFP film and improves rate capability.

Raman spectroscopy also revealed additional Fe–O-related bands in some LFP/ITO samples, located near the characteristic region of magnetite-like Fe_3O_4 vibrational modes. However, these contributions were not clearly detected as crystalline secondary phases by GIXRD. Importantly,

their presence did not prevent high electrochemical performance in the optimized LFP/ITO electrodes. This suggests that, within the detection and processing conditions explored here, these minor Fe–O-related contributions do not dominate the electrochemical response of the films.

Rapid thermal processing was shown to be an effective activation strategy for poorly crystallized films, but its benefit depended strongly on the initial deposition temperature. For the film deposited at 400 ºC, RTP increased the discharge capacity from 7.6 to 118 mAh g^{-1} at 2 μA cm^{-2}, corresponding to more than one order of magnitude improvement. For the 500 ºC film, RTP produced a more moderate enhancement, from 120.5 to 148 mAh g^{-1}. In contrast, the 600 ºC film decreased from 163.3 to 127 mAh g^{-1} after RTP, indicating that additional thermal treatment is not advantageous once the LFP layer is already well crystallized during deposition. The appearance of surface particles or local roughening after RTP remains inconclusive in terms of chemical origin, but the electrochemical data indicate that these features do not necessarily limit performance when the underlying LFP layer is sufficiently crystalline and accessible.

The apparent kinetic parameters extracted from cyclic voltammetry further support these trends. The as-deposited LFP/ITO films grown at 500 and 600 ºC showed apparent Li^+ diffusion coefficients close to 1.2×10^{-11} cm^2 s^{-1}, whereas the poorly active 400 ºC film showed a much lower value of 2.5×10^{-14} cm^2 s^{-1}. After RTP, the 500 ºC sample reached the highest apparent diffusion coefficient, 1.39×10^{-11} cm^2 s^{-1}, while the 600 ºC film decreased to 8.2×10^{-12} cm^2 s^{-1}. These values are higher than those reported in the literature, which typically range from 10^{-16} to 10^{-14} cm^2 s^{-1} for bulk composite C-LFP electrodes,[140] and from 10^{-14} to 10^{-12} cm^2 s^{-1} for thin-film configurations.[141]

Post-cycling GDOES and SEM analyses confirmed the reversible participation and structural stability of the optimized LFP/ITO electrode. The Li signal decreased markedly after charging and was largely recovered after discharge, providing direct qualitative evidence of reversible Li extraction and insertion within the LFP layer. SEM images after 35 charge–discharge cycles showed that the multilayer architecture was preserved with small changes likely associated with repeated Li insertion/extraction, local strain during the LFP/$FePO_4$ phase transformation. Nevertheless, the preservation of the film/substrate stack confirms that the LFP/ITO configuration provides sufficient mechanical and electrochemical stability under the tested conditions.

Overall, this chapter shows that the most favorable route for obtaining high-performance PLD-grown LFP thin-film cathodes is the direct deposition of LFP on ITO/Pt at 600 ºC under low-pressure Ar. This condition combines good crystallinity, homogeneous morphology, improved interfacial contact, high accessible capacity, and enhanced apparent Li^+ transport. In contrast, direct deposition on Pt leads to stronger interfacial reactions and lower utilization of the active material. These conclusions provide the basis for using optimized LFP/ITO electrodes as model cathodes and establish the processing guidelines required for the subsequent integration of LFP with solid electrolytes in all-solid-state thin-film battery architectures.

Chapter 4

Fabrication and characterization of $Li_{1+x}Al_xT_{2-x}(PO_4)_3$ thin-film and its compatibility with $LiFePO_4$ cathodes

4 Fabrication and characterization of $Li_{1+x}Al_xT_{2-x}(PO_4)_3$ thin-film and its compatibility with $LiFePO_4$ cathodes 92

4.1 Scope and motivation of the chapter 92

4.2 Fabrication conditions and samples description 92

4.3 Growth, morphology and structural analysis of as-deposited LATP Films 94

4.4 Phase formation and structural evolution induced by RTP 99

4.5 Morphological Evolution after RTP 104

4.6 Ionic Transport Properties of LATP Thin Films 107

4.7 Integration of LATP with LFP: Bilayer Architecture 112

4.8 Electrochemical Performance of LFP/LATP Bilayer 118

4.9 Conclusions 124

4 Fabrication and characterization of $Li_{1+x}Al_xT_{2-x}(PO_4)_3$ thin-film and its compatibility with $LiFePO_4$ cathodes

4.1 Scope and motivation of the chapter

The development of all-solid-state thin-film batteries requires the integration of electrochemically active electrodes with solid electrolytes that combine high ionic conductivity, chemical stability, and compatibility with adjacent layers. In **Chapter 3**, $LiFePO_4$ (LFP) thin-film cathodes were successfully fabricated by pulsed laser deposition (PLD), demonstrating promising electrochemical performance under optimized deposition conditions. The next critical step toward device integration is the incorporation of a compatible solid electrolyte layer that can be processed without degrading and/or reacting with the underlying cathode.

Among the different solid electrolyte materials, NASICON-type $Li_{1+x}Al_xT_{2-x}(PO_4)_3$ (LATP) is particularly attractive due to its relatively high ionic conductivity and chemical stability. However, the fabrication of LATP thin films presents several challenges. High-temperature processing under oxidative atmospheres and prolonged times, typically required to achieve crystallization and optimal ionic transport, can lead to lithium loss, formation of secondary phases, and degradation of temperature-sensitive electrode materials such as LFP when co-sintering is performed. Therefore, strategies that enable the formation of crystalline LATP under reduced thermal budgets are essential for the realization of integrated thin-film architectures.

In this context, the present chapter investigates the fabrication and post-treatment of LATP thin films deposited by pulsed laser deposition, with particular emphasis on low-temperature growth combined with rapid thermal processing as a strategy to decouple film deposition from crystallization. By depositing LATP at reduced temperature and subsequently applying short, high-temperature RTP treatments, this approach aims to promote structural ordering while limiting the thermal exposure time, lithium volatilization, and interfacial degradation. First, LATP films deposited on different substrates are examined to evaluate the influence of deposition temperature, annealing atmosphere (O_2 vs Ar), RTP temperature, and dwell time on phase formation, microstructure, and ionic transport. Then, selected processing conditions are transferred to LFP/LATP bilayer architectures in order to assess the feasibility of integrating LATP as a solid electrolyte on top of LFP thin-film cathodes. Particular attention is therefore given to the main limitations associated with this configuration, including defects, secondary-phase formation, and interfacial stability, with the final aim of determining whether the resulting bilayers are suitable for further implementation in all-solid-state thin-film battery architectures as proposed in **Chapter 5**.

4.2 Fabrication conditions and samples description

The experimental work presented in this chapter was designed to evaluate LATP thin films both as individual solid electrolyte layers and as part of LFP/LATP bilayer architectures. The study was therefore divided into two main stages. First, LATP single layers were prepared on different substrates (Pt or Si_3N_4) in order to investigate the influence of deposition temperature and post-

deposition rapid thermal processing on their structure, morphology, and ionic transport properties. Then, selected LATP processing conditions were transferred to LFP-coated substrates to assess the compatibility of the electrolyte layer with the LFP cathode. The overall fabrication route of LATP single-layers and the LFP/LATP bilayers are schematically summarized in **Figure 4.1**.

For the single-layer study, LATP films were deposited by pulsed laser deposition using a homemade $Li_{1.3}Al_{0.3}T_{1.7}(PO_4)_3$ target, same fabricated and used in previous studies of our group. Two processing approaches were considered including direct deposition at elevated temperature, using optimized conditions proposed by Siller; and specially at low-temperature deposition followed by RTP, aimed at decoupling film growth from crystallization. The latter strategy was explored to reduce the thermal load during deposition while still allowing the NASICON phase to crystallize during a subsequent short annealing step. The effect of RTP temperature, dwell time, and atmosphere was investigated using treatments performed in either O_2 or Ar. The structural and morphological consequences of these processing conditions, including phase formation, surface evolution, densification, and crack development, are discussed in **Section 4.3** based on SEM, Raman spectroscopy, and XRD analyses.

The ionic transport properties of selected LATP single layers were then evaluated by electrochemical impedance spectroscopy using an in-plane configuration with parallel metallic electrodes deposited on top of the films. This geometry provides an effective conductivity value that enables comparison between samples processed under different conditions in **Section 4.4**.

After identifying the most relevant LATP processing conditions from the single-layer study, selected treatments were applied to LFP/LATP bilayers. In these samples, LFP was used as the cathode layer and LATP as the solid electrolyte layer. The LATP deposition temperature was kept low (300 ºC) to minimize degradation or oxidation of the underlying LFP film, while subsequent RTP treatments were used to promote LATP crystallization at 800ºC and 900 ºC. Particular attention was given to Ar atmospheres, which are more compatible with the preservation of LFP than strongly oxidizing conditions. The structural and microstructural integrity of the resulting bilayers, including the possible formation of secondary phases and the chemical stability of the LFP/LATP interface, is examined in **Section 4.5** by SEM, Raman spectroscopy, and TEM/STEM-EDX analyses.

Finally, the electrochemical response of selected LFP/LATP bilayers was investigated in order to evaluate whether the processed multilayer structures could retain functional behavior after LATP integration. These measurements provide an initial assessment of the suitability of the bilayer architecture for further implementation in all-solid-state thin-film battery configurations, as proposed in Chapter 5. The electrochemical results and structural observations post-cycling are discussed in **Section 4.6.** Overall, this experimental strategy allows the LATP processing window to be evaluated progressively, from single-layer crystallization and transport properties to its compatibility with LFP-based multilayer devices.

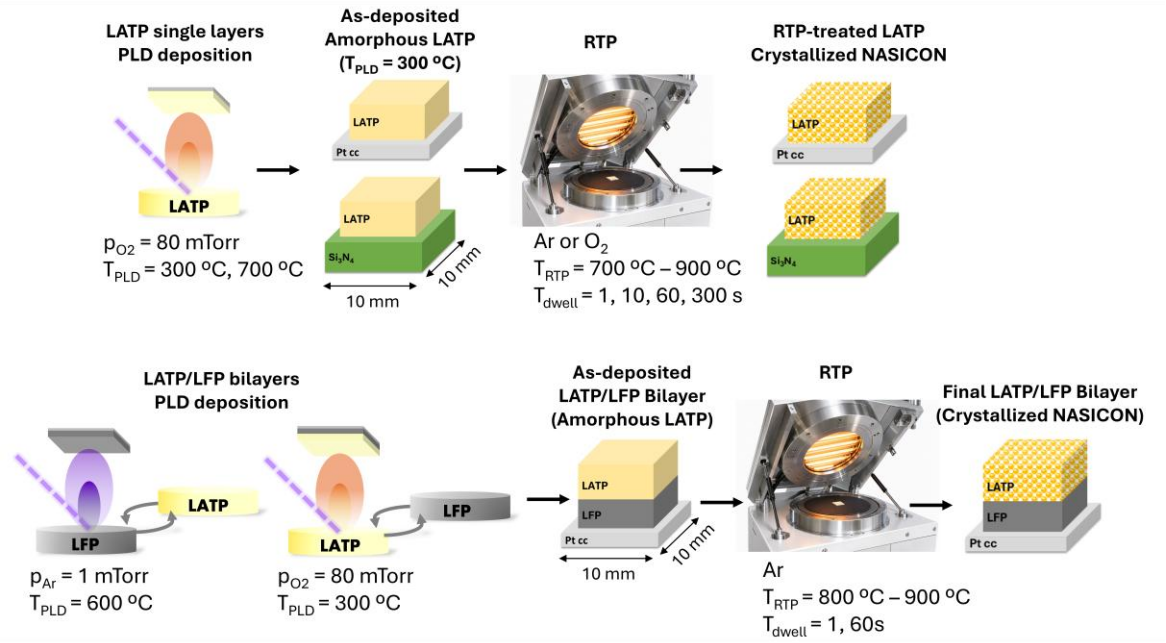


Figure 4.1 - Schematic representation of the experimental strategy followed for the fabrication of LATP single layers and LFP/LATP bilayers.

4.3 Growth, morphology and structural analysis of as-deposited LATP Films

The morphology of the LATP thin films was investigated by SEM in both top-view and cross-sectional perspectives to evaluate surface coverage, microstructural evolution, and film thickness under different deposition conditions. Films deposited on Pt were used for Raman characterization, whereas films grown on Si_3N_4 were selected for in-plane PEIS measurements. In this section, particular emphasis is placed on comparing the reference high-temperature deposition condition with lower-temperature growth, which is more relevant for the future integration of LATP in LFP/LATP bilayer architectures.

As shown in **Figure 4.2a,b**, the LATP film deposited on Pt at 700 ºC exhibits a continuous, highly dense, and crack-free nanocrystalline microstructure uniformly covering the underlying substrate. The surface is composed of closely packed nanograins displaying a hybrid morphology consisting of platelet-like and semi-rounded geometries, with lateral dimensions ranging approximately between 50 and 150 nm. The dense packing of these nanostructures yields highly defined grain boundaries across the film surface. The corresponding cross-sectional images (**Figure 4.3a,b**) confirm the formation of a continuous and dense layer with a thickness of about 780 nm, obtained after 48k laser pulses. No major cracks or large discontinuities are observed in the analyzed areas of this specific sample.

In contrast, the film deposited on Pt at 300 ºC displays a markedly different surface texture, finer and smoother, as observed in **Figure 4.3c,d**. The smaller rounded nanodomains, with lateral dimensions in the 30-80 nm range, are consistent with an amorphous structure, as confirmed by

Raman spectroscopy and XRD, and discussed later in this section. Cross-sectional SEM images (**Figure 4.3c,d**) reveal that, despite the cracked surface, the film forms a dense and structurally coherent layer with a well-defined columnar morphology extending throughout its full thickness of about 880 nm, obtained after 64k laser pulses. While the columnar boundaries remain largely intact through the film depth, the surface cracks represent a non-negligible structural feature. Depending on their depth and connectivity, such defects may act as preferential pathways for current leakages or Li dendrite formation, a consideration that will be revisited when evaluating transport properties in **Section 4.6.**

To further assess the origin of the crack formation, a thinner LATP film deposited on Pt at 300 ºC was also examined. As shown in **Figure 4.4**, the 250 nm thick layer, obtained after 24k laser pulses, does not exhibit evident surface cracking, indicating that the defects observed in the thicker low-temperature film are mainly associated with thickness-related stress accumulation rather than with the reduced deposition temperature itself.

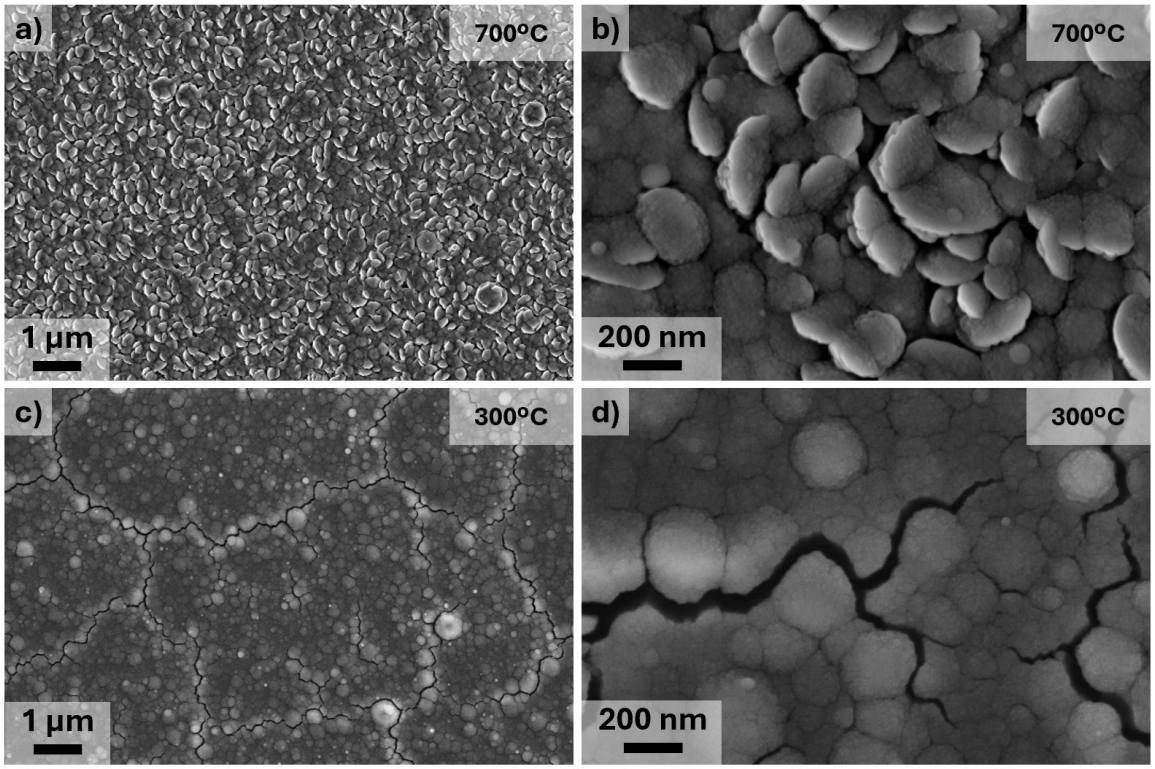


Figure 4.2 - Top-view SEM images of LATP thin films deposited on Pt under O_2 at 80 mTorr: (a,b) film deposited at 700 ºC and (c,d) film deposited at 300 ºC, shown at low and high magnification, respectively.

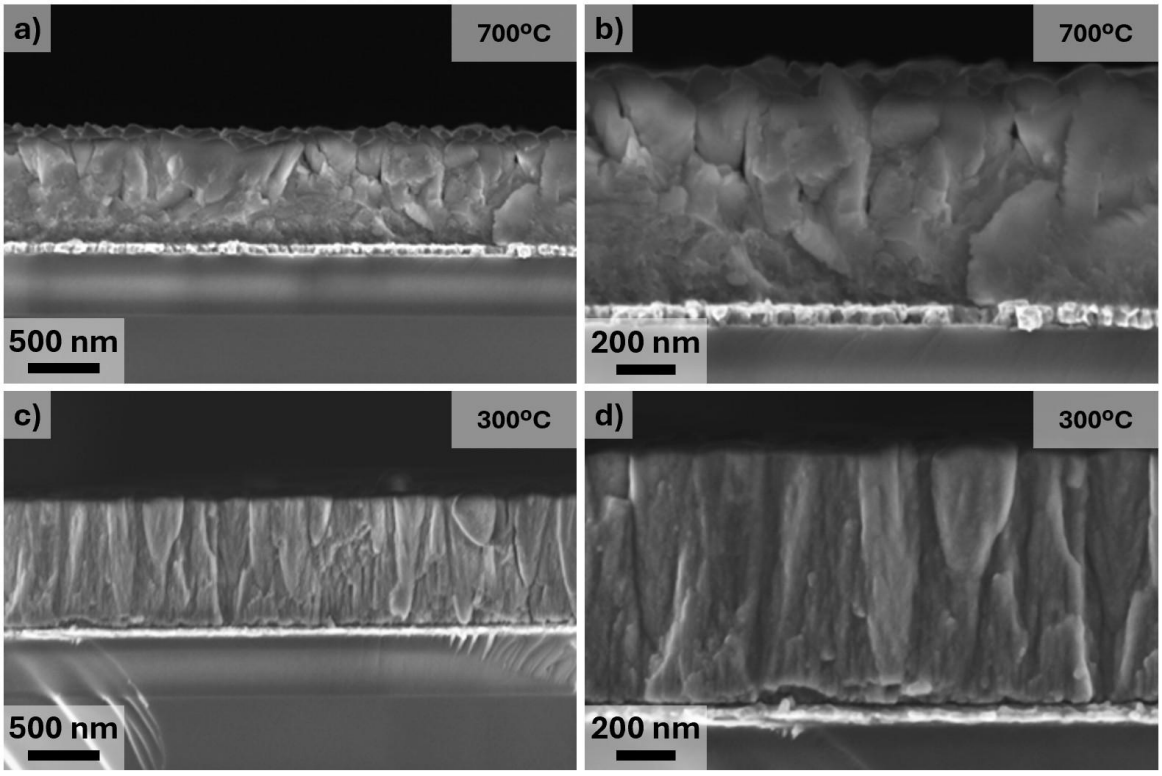


Figure 4.3 - Cross-sectional SEM images of LATP thin films deposited on Pt under O_2 at 80 mTorr: (a,b) 780 nm film deposited at 700 ºC and (c,d) 880 nm film deposited at 350 ºC, shown at two different magnifications.

Overall, the SEM results indicate that both the 700 ºC and 300 ºC films can be considered dense, despite their clearly different microstructural features. However, the presence of cracks in thicker films highlights the need for careful thickness optimization when LATP is intended for use as a thin-film solid electrolyte in all-solid-state batteries. In the absence of further processing optimization to suppress crack formation in thicker layers, the use of thinner LATP films appears more suitable to preserve film integrity and ensure reliable integration in multilayer battery architectures.

To complete the SEM analysis of the as-deposited films, the morphology of the thick LATP layer deposited at 300 ºC on Si_3N_4 was also examined (**Figure 4.5**). As shown in **Figure 4.5a**, the surface morphology is very similar to that observed for the corresponding film deposited on Pt under the same conditions (**Figure 4.2c,d**). Likewise, the cross-sectional image (**Figure 4.5b**) reveals the same well-defined columnar microstructure across the film thickness. These observations indicate that the microstructural features developed under low-temperature deposition

are not specific to the Pt-coated substrate but are also reproduced on Si_3N_4-coated one, which was the substrate used for the in-plane PEIS measurements discussed in **section 4.6**.

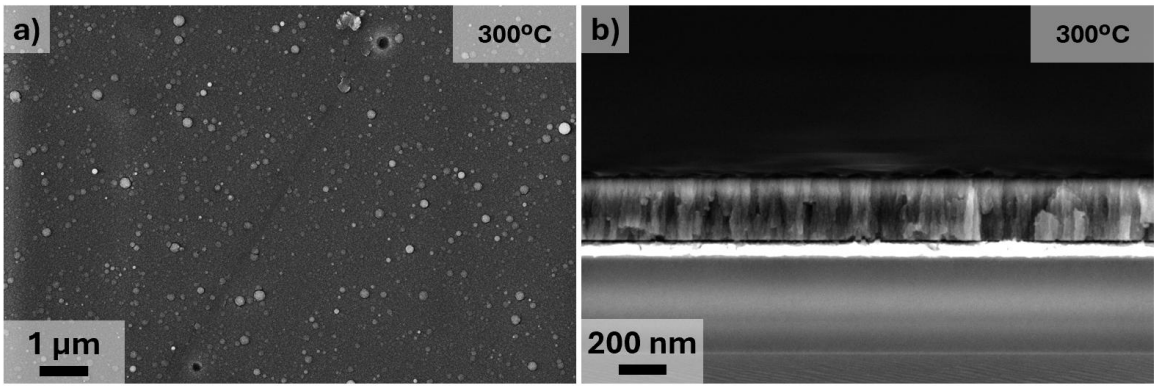


Figure 4.4 – Top-view and cross-sectional SEM images of a 250 nm LATP thin film deposited on Pt under O_2 at 80 mTorr and 300 ºC.

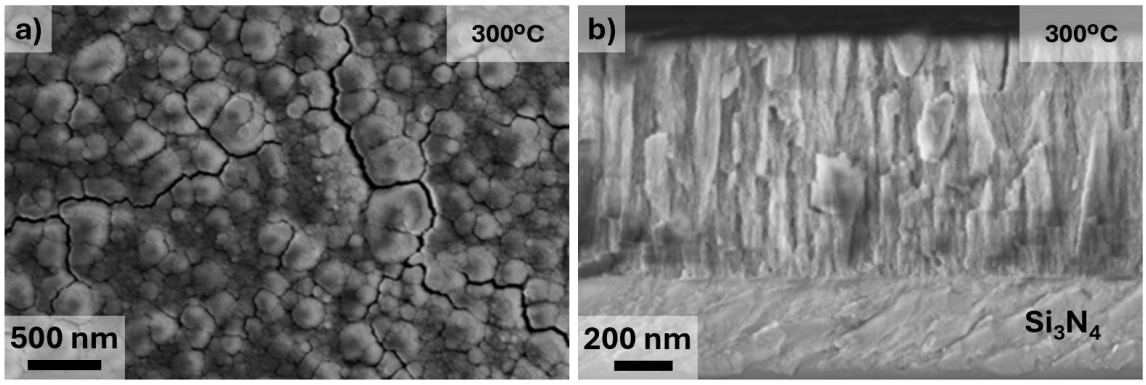


Figure 4.5 - SEM images of the thick as-deposited LATP film grown on Si_3N_4 at 300 ºC under O_2 at 80 mTorr from (a) top-view, and (b) cross-sectional perspectives.

Raman spectroscopy was used to assess the local structural environment of the as-deposited LATP films grown on Pt at 350 ºC and 700 ºC (**Figure 4.6**). The commercial $Li_{1.3}Al_{0.3}Ti_{1.7}(PO_4)_3$ target is used as the crystalline NASICON structure reference, associated with the $R\bar{3}c$ space group. The Raman spectrum of LATP can be broadly divided into three main vibrational regions. In the high-frequency range, between 950 and 1200 cm^{-1}, the symmetric (ν_1) and asymmetric (ν_3) stretching modes of the P–O bonds within the $(PO_4)^{3-}$ tetrahedral units are observed, with a prominent band located at approximately 982 cm^{-1}. The splitting of adjacent bands in this region reflects local symmetry distortions induced by the partial isomorphic substitution of Ti^{4+} by Al^{3+} within the NASICON framework. The intermediate region, from 400 to 700 cm^{-1}, comprises contributions from the asymmetric stretching vibrations of TiO_6 octahedra, typically observed near 640 cm^{-1}, together with the bending modes, ν_2 and ν_4, of the phosphate groups, located between approximately 414 and 480 cm^{-1}. In addition, the band centered around 547 cm^{-1} is commonly associated with Li–O vibrational dynamics within the interstitial sites involved in lithium-ion transport. Finally, the

low-frequency region below 350 cm^{-1} is mainly assigned to collective lattice modes and translational motions of heavier metal cations.[64]

As shown in **Figure 4.6b**, the film deposited at 700 ºC exhibits broad Raman features located in similar spectral regions to those of the reference target, suggesting the development of a LATP-related local structure despite the lower degree of order of the thin film. In contrast, the film deposited at 300 ºC shows only poorly defined spectral modulations, with no clear correspondence to the main bands of the target, indicating amorphous structure consistent with the SEM analysis.

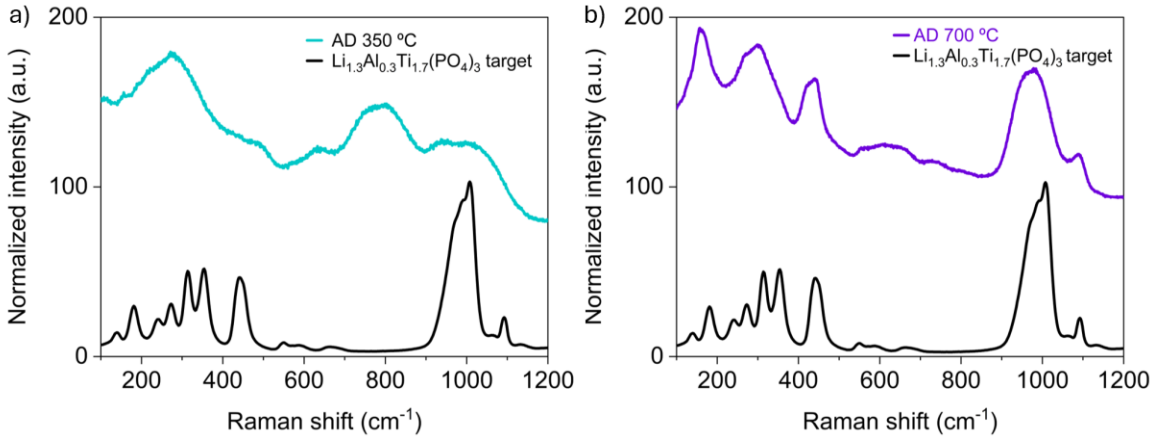


Figure 4.6 - Raman spectra of as-deposited LATP thin films grown on Pt at (a) 700 ºC and (b) 350 ºC, compared with the commercial $Li_{1.3}Al_{0.3}Ti_{1.7}(PO_4)_3$ target as reference for the crystalline NASICON phase.

A post-deposition treatment is still required to crystallize the NASICON thin films deposited at 300 ºC and to enhance Li^+ transport for their use as solid electrolytes. As previously mentioned, the high-temperature processing route reported by Siller (2021),[19] involving PLD deposition at 700 ºC followed by long post-annealing treatment in air at 700 ºC for 5 h, effectively promotes film crystallization. However, secondary phases such as TiO_2 and $AlPO_4$ were reported in both as-deposited and annealed films, as a consequence of lithium loss during high-temperature processing.[91]

The formation of secondary phases in LATP should therefore be interpreted in a nuanced manner. On the one hand, crystalline TiO_2, AlPO4, or related phosphate phases generally indicate partial lithium loss, off-stoichiometry, or decomposition of the NASICON framework during high-temperature processing. In particular, Li_2O volatilization has been reported to promote the partial transformation of LATP into $AlPO_4$ and oxide phases, generating local stress and microcracking when the thermal budget becomes excessive.[142] These phases can reduce the fraction of the film crystallized as the Li^+-conducting LATP phase and, when they segregate continuously at grain boundaries, may behave as poorly conducting or blocking regions that increase the overall resistance to Li^+ transport.

On the other hand, the improvement in conductivity after thermal treatment cannot be assigned only to the crystallization of the NASICON phase, but should also be related to the development of a more interconnected microstructure. In LATP, where grains can become highly faceted and undergo abnormal growth, a limited amount of segregated amorphous Al-phosphate-rich material at intergranular regions may act as a bridging or sintering-aid phase. Although this phase is not expected to be as conductive as LATP itself, it may fill gaps between poorly connected crystallites, increase the effective contact area between LATP grains, and promote a more continuous percolation pathway for Li^+ transport. This interpretation is consistent with reports showing that optimized thermal processing can improve LATP densification and conductivity, whereas excessive secondary-phase formation, Li loss, grain coarsening, and microcracking become detrimental.[143,144] From this perspective, rapid thermal processing (RTP) is explored in the following sections as a strategy to promote LATP crystallization and intergrain connectivity while limiting prolonged thermal exposure, lithium loss, and uncontrolled secondary-phase growth that could compromise stoichiometry and hinder future integration in LFP/LATP bilayers.

4.4 Phase formation and structural evolution induced by RTP

To evaluate the efficacy of rapid thermal processing (RTP) for thin-film crystallization, a representative RTP-treated LATP film was first compared with conventionally annealed films previously studied in our group. This comparison allows assessing whether fast thermal kinetics can promote the formation of the NASICON-type LATP phase while mitigating the growth of secondary phases associated with prolonged high-temperature exposure. The section then examines the influence of annealing atmosphere, temperature, and dwell time, before correlating the Raman observations with X-ray diffraction results.

Figure 4.7 compares the Raman response of LATP thin films subjected to conventional annealing and RTP. **Figure 4.7a** shows the Raman spectra data of LATP films previously studied by Siller *et al.* in our research group,[19] including a film deposited at high temperature, 700 ºC, in the as-deposited state (AD) and after conventional oven annealing at 800 ºC for 5 h in ambient air, using a heating rate of 5 ºC min^{-1} (A-oven). In contrast, **Figure 4.7b** presents a film deposited at low temperature, 350 ºC, before and after RTP at 850 ºC for 10 s, using a fast ramp rate of 50 ºC s^{-1}. After RTP, the Raman spectrum develops well-defined bands in the spectral regions characteristic of NASICON-type LATP, confirming that short high-temperature treatments are sufficient to induce crystallization even in films initially grown under low-temperature conditions.

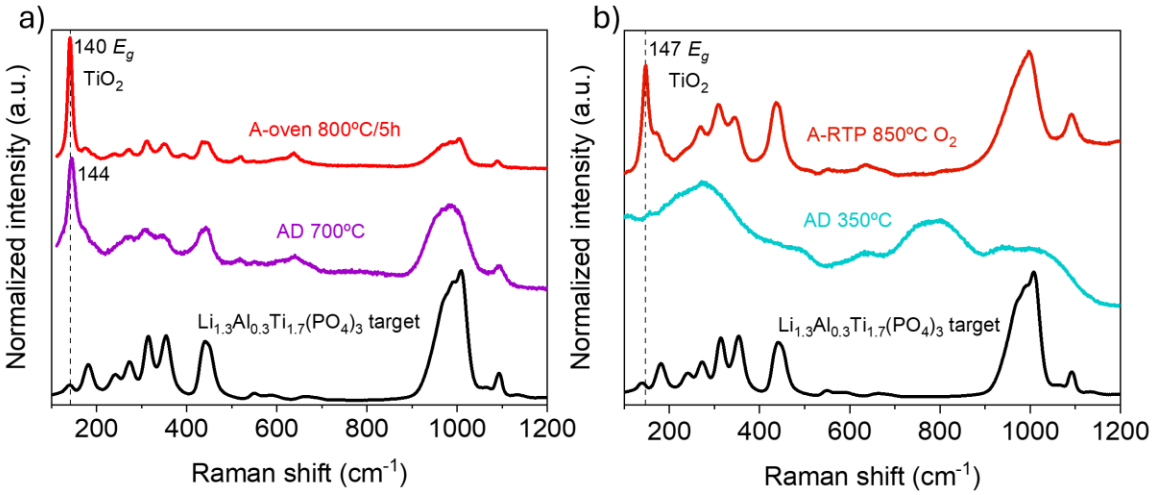


Figure 4.7 - Raman spectra of LATP thin films after post-deposition thermal treatment (a) Spectra of LATP thin films previously studied by our group (Siller, 2020)[19], including the sample deposited at 700 ºC in the as-deposited state (AD) and after conventional annealing at 800 ºC in ambient air for 5 h (A-oven). (b) Raman spectra of a LATP thin film deposited at 300 ºC in the AD state and after rapid thermal processing in O_2 at 850 ºC for 10s (A-RTP).

Importantly, for the RTP-annealed sample, the relative intensity of the main band of LATP at 997 cm^{-1} with respect to the anatase TiO_2 secondary-phase contribution, particularly evident in the E_g vibrational mode near 147 cm^{-1}, is significantly higher than in the conventionally annealed sample. However, this comparison should be interpreted qualitatively rather than quantitatively, since anatase TiO_2 is highly Raman-active and a strong Raman band does not necessarily imply a large amount of TiO_2 phase. In other words, the Raman spectra are very sensitive to small amounts of anatase, especially if it is locally crystallized or segregated at the surface or at grain-boundary regions.

Under high temperature deposition and conventional annealing, the anatase TiO_2 band becomes more intense than the principal LATP band, which is consistent with more severe lithium loss during the high-temperature treatment. This comparison indicates that RTP is a promising route to reduce lithium loss while still promoting LATP crystallization. Nevertheless, the persistence of the TiO_2 band suggests that phase purity remains highly sensitive to the thermal budget. As shown in the following paragraphs, both the annealing atmosphere and the dwell time strongly affect the balance between NASICON crystallization and secondary-phase segregation.

The effect of annealing atmosphere and temperature during RTP is compared in **Figure 4.8**. **Figure 4.8a** presents the Raman spectra of films treated in O_2 for 10 s between 700 and 850 ºC with heating and cooling ramping rates of 50 ºC s^{-1}, whereas **Figure 4.8b** shows the corresponding series treated in Ar between 700 and 1000 ºC with 10 ºC s^{-1}. In the Ar series, the dwell time was reduced from 10 s to 1 s for temperatures of 800 ºC and above. This adjustment was introduced to reduce the total thermal budget at higher temperatures, aiming to promote crystallization while minimizing lithium depletion and possible film/substrate interactions.

For films treated in O_2, increasing the RTP temperature progressively enhances the definition of LATP-related Raman features, indicating improved local structural ordering. However, this evolution is accompanied by the appearance and progressive increase of the anatase TiO_2 band near 147 cm^{-1}. This behavior suggests that RTP in O_2 promotes crystallization but also favors secondary-phase formation when the thermal budget becomes too high. In contrast, the Ar-treated films show a more gradual development of the LATP-related Raman features, while the anatase TiO_2 contribution is strongly reduced or absent. Therefore, this comparison indicates that the annealing atmosphere plays a decisive role in controlling the competition between LATP crystallization and TiO_2 segregation.

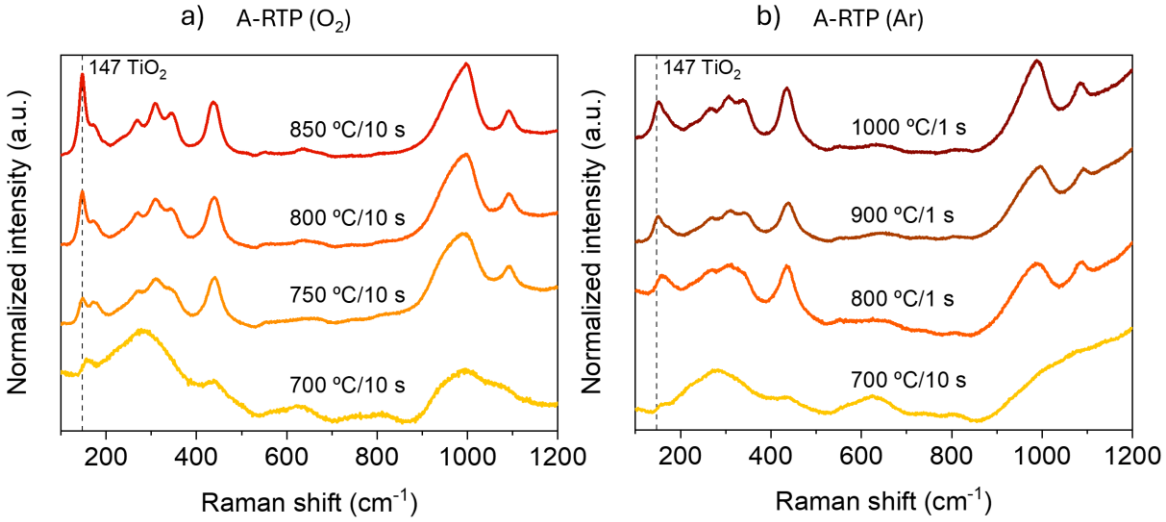


Figure 4.8 - Raman spectra of LATP thin films after rapid thermal processing under different annealing atmospheres and temperatures. (a) Films treated in O_2, from 700 to 850 °C, with 50 °C s^{-1}. (b) Films treated in Ar, from 700 to 1000 °C, with 10 °C s^{-1}.

Raman spectroscopy was performed on $Pt/Ti/SiO_2/Si$ substrates after exposure to the same RTP treatments in O_2 used for the LATP films to evaluate a possible substrate contribution to the measured spectra. As shown in **Figure 4.9a**, the intensity of a band near 147 cm^{-1}, assigned to anatase TiO_2, increases with treatment temperature. Nevertheless, the overall Raman response of the treated substrate remains weak. In comparison with the spectra of the RTP-treated LATP films (**Figure 4.9b**), this contribution is negligible, indicating that the main Raman features observed after annealing arise predominantly from the LATP layer rather than from the substrate.

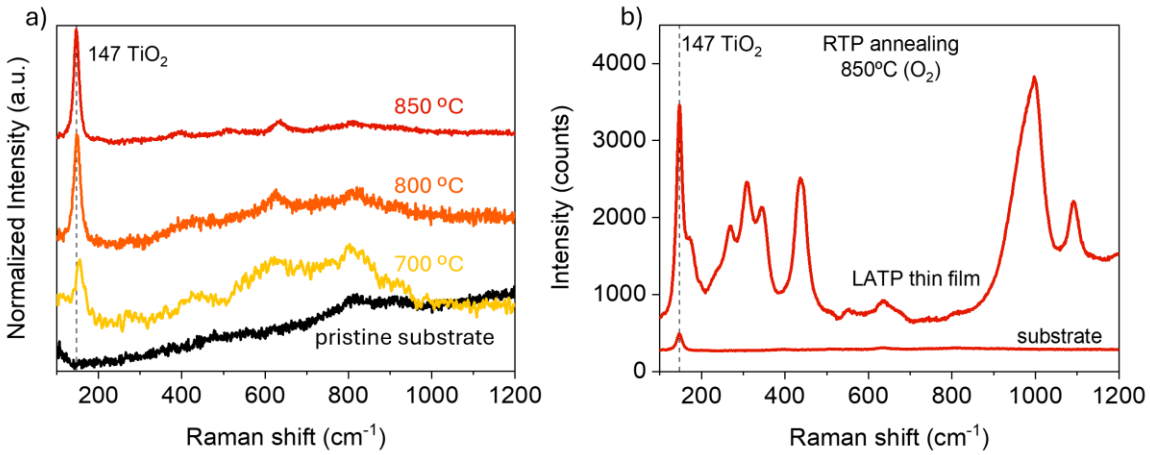


Figure 4.9 – (a) Normalized Raman spectra of pristine and RTP-treated Pt/Ti/SiO_2/Si substrates annealed in O_2 at 700, 800, and 850 °C for 10 s, using a ramp rate of 50 s^{-1}. (b) Comparison between the Raman spectra of the LATP thin film and the bare substrate after RTP at 850 °C.

The influence of dwell time under O_2 is further examined in **Figure 4.10**. At both 700 and 750 ºC, increasing the dwell time from 10 to 60 s improves the definition of the LATP-related Raman bands, confirming that longer thermal exposure promotes crystalline structural ordering. However, the same increase in dwell time also enhances the anatase TiO_2 band near 147 cm^{-1} revealing a clear trade-off between crystallinity and phase purity. A comparison between 750 ºC for 60 s and 800 ºC for 10 s shows that a similar degree of LATP crystallization can be achieved with a shorter treatment at higher temperature, while maintaining a lower TiO_2 contribution. These results suggest that, under O_2, short dwell times at moderately higher temperatures provide a more favorable balance than longer treatments at lower temperature.

Although an equivalent dwell-time series was not available for Ar, the spectra in **Figure 4.8b** indicates that Ar treatments of 1s do not produce the same pronounced increase in the TiO_2-related Raman contribution observed under O_2. This suggests that Ar provides a wider processing margin against TiO_2 segregation up to 1000 ºC, even though crystallization appears more gradual. This point is particularly relevant for LFP/LATP bilayer integration, since Ar is also required to avoid oxidation of the underlying $LiFePO_4$ cathode during post-deposition processing.

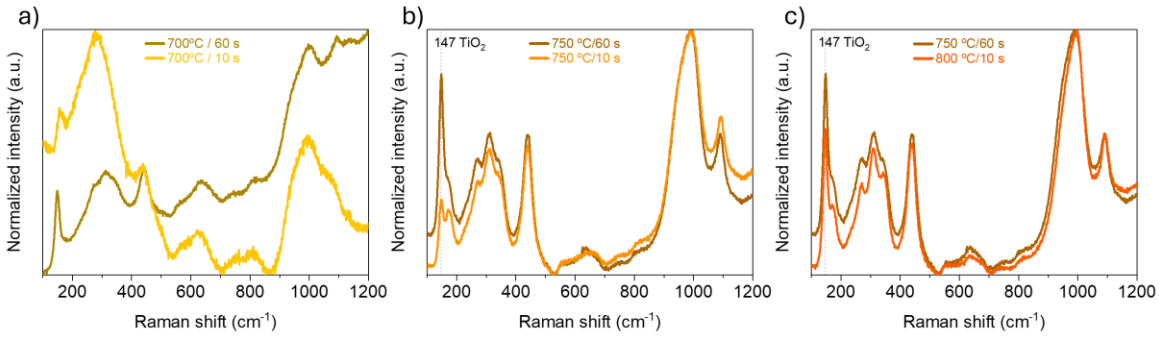


Figure 4.10 - Raman spectra of LATP thin films after RTP treatment in O_2 with fixed 10 ºC s^{-1} ramp, showing the effect of dwell time and temperature: (a) 700 ºC for 10 s and 60 s, (b) 750 ºC for 10 s and 60 s, and (c) comparison between 750 ºC for 60 s and 800 ºC for 10 s.

The structural evolution induced by RTP was further assessed by X-ray diffraction. **Figure 4.11** shows the diffractograms of 880 nm LATP thin films deposited on $Si_3N_4/SiO_2/Si$ substrates at 300 ºC under pO_2 = 80 mTorr, either in the as-deposited state (AD) or after post-deposition thermal treatments in oven for 5h or RTP for 1s. Grey lines correspond to the substrate contribution, while black vertical markers indicate the reference pattern of the NASICON-type $LiTi_2(PO_4)_3$ phase (JCPDS 00-035-0754). Secondary phases are assigned to $AlPO_4$ (JCPDS 01-072-116) and anatase TiO_2 (JCPDS 01-073-1764) polymorphs based on literature reports.[145,146]

The as-deposited film does not show diffraction peaks, confirming its amorphous character, consistent with the Raman spectra and microstructure previously discussed. After annealing, diffraction peaks emerge at approximately 2θ ≈ 20.8º, 24.5º, and 29.6º, which can be indexed to the NASICON-type $LiTi_2(PO_4)_3$ phase structure. This confirms that RTP can induce crystallization of the LATP-related phase within a very limited thermal budget, even for dwell times as short as 1 s at high temperature and fast 10 ºC s^{-1} rates.

In contrast, only the sample annealed in air at 800 ºC for 5 h exhibits an additional diffraction peak near 25.4º, which can be attributed to anatase TiO_2. The formation of TiO_2 is widely associated with lithium loss during high-temperature processing, leading to the destabilization of the LATP phase.[65,147] This behavior is expected, as lithium deficiency is a well-known issue in PLD-grown films due to the high volatility of lithium.[148] As previously discussed, the formation of secondary phases such as $AlPO_4$ may also arise from lithium deficiency, which disrupts the NASICON framework and limits the incorporation of Al into the structure.[149] In this scenario, excess aluminum reacts with phosphate groups, forming electrically insulating phases that can hinder lithium-ion transport.[142,150]

Interestingly, while Raman spectroscopy reveals traces of anatase in several RTP-treated films, especially under O_2, no corresponding TiO_2 reflections are detected by XRD. This can be explained by the high Raman scattering efficiency of the anatase mode near 147 cm^{-1}, which allows the detection of small amounts of this secondary phase that remain below the detection limit of conventional XRD. In addition, any TiO_2 formed during the short RTP treatments may be highly

dispersed, too small, or amorphous to generate coherent Bragg reflections. Therefore, the combined Raman and XRD results indicate that RTP effectively promotes NASICON-type crystallization while strongly limiting the formation of crystalline secondary phases compared with conventional annealing.

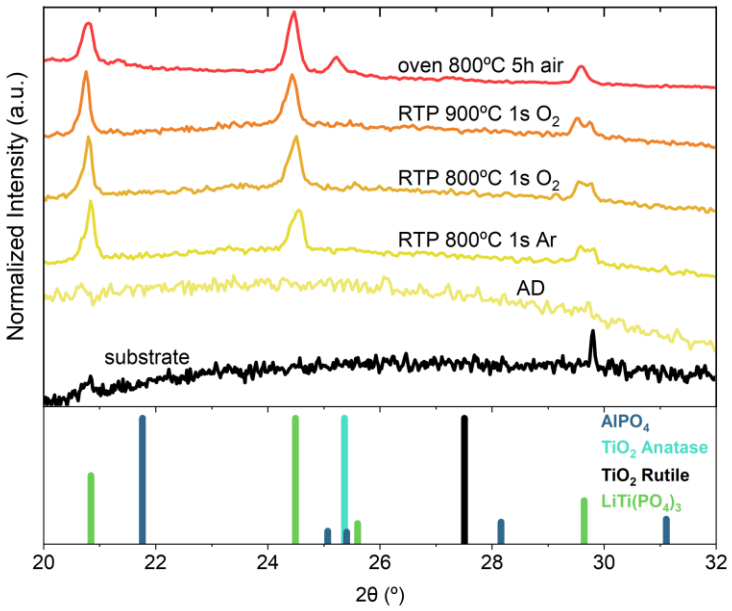


Figure 4.11 - X-ray diffraction patterns of LATP thin films deposited on $Si_3N_4/SiO_2/Si$ substrates by PLD at 300 ºC in the as-deposited state and after post-deposition thermal treatments, including RTP for 1 s with 10 ºC s^{-1} rate in Ar or O_2, and conventional long-duration annealing in air. Grey line corresponds to the substrate contribution, while vertical lines (bottom) indicate reference patterns for $LiTi_2(PO_4)_3$ (JCPDS 00-035-0754), anatase TiO_2 (JCPDS 01-073-1764), rutile TiO_2 (JCPDS 01-078-1510) and $AlPO_4$ (JCPDS 01-072-116).

4.5 Morphological Evolution after RTP

To further correlate the structural evolution induced by RTP, as detected by XRD (**Figure 4.11**), with the corresponding morphological changes, **Figure 4.12** compares the top-view SEM images of the same 880 nm thick LATP film on Si_3N_4, before and after RTP annealing at 900 ºC for 1 s under Ar or O_2.

After RTP, a pronounced morphological evolution is observed in both annealing atmospheres. The regions between cracks become more compact and smoother, indicating densification and coalescence of the initial granular structure. Although the film annealed in Ar retains a slightly rougher texture, with a higher density of round surface protrusions (**Figure 4.12c,d**), whereas the sample treated in O_2 appears more homogeneous and more strongly smoothed (**Figure 4.12e,f**).

As discussed in **Section 4.3,** the amorphous film deposited at low temperature already exhibits a crack network, mainly associated with thickness-related stress accumulation. After annealing, the cracks become bigger, with wider openings. This apparent trade-off between densification and crack

widening has been previously reported in LATP ceramics and thin films, where thermal treatments can enhance structural ordering while simultaneously amplifying stress-induced cracking due to thermal expansion mismatch and constrained shrinkage.[142] The cross-sectional SEM images of the film annealed at 900 °C in O_2 (**Figure 4.12g,h**) further confirm that some cracks are not limited to the surface, but extend deeply into the LATP layer and, in some regions, may approach or reach the substrate. The slight shrinkage after RTP from 880 nm to ~730 nm agrees with the densification of LATP and broadening of the defects. This feature is particularly undesirable for a solid-electrolyte layer, since through-thickness cracks can act as preferential pathways for leakage currents, electrolyte penetration, or direct contact between adjacent electrodes in a cross-plane device configuration.

Additionally, these cracks may also interrupt lateral percolation pathways and increase effective measured resistance, contributing to a lower apparent in-plane conductivity, as discussed in **Section 4.6**. Therefore, although RTP improves LATP crystallization and densification, the associated crack widening represents a critical limitation for the use of thick LATP films as reliable solid electrolytes in multilayer battery architectures. Further optimization of film thickness, deposition conditions, and RTP parameters is therefore required to ensure the fabrication of high-quality thin LATP electrolytes with sufficient structural integrity for device integration.

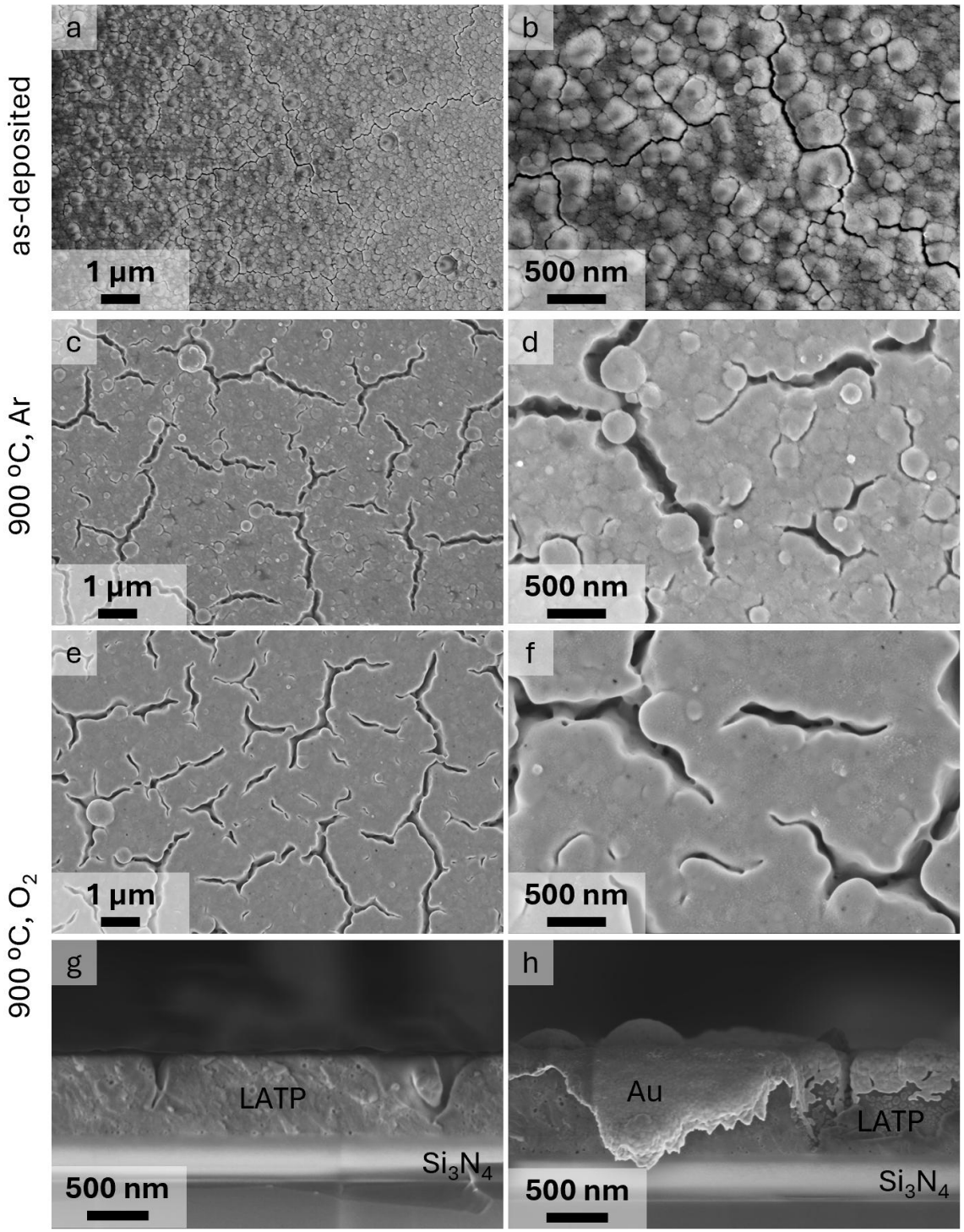


Figure 4.12 - Top-view SEM images of LATP films grown on Si_3N_4 at 300 ºC (a,b) in the as-deposited state, and after RTP at 900 ºC for 1 s (c,d) in Ar and (e,f) in O_2. (g,h) Cross sectional views of the O_2-treated film.

Extending the RTP dwell time at 900 °C in Ar from 1 s to 300 s leads to a clear change in the surface morphology (**Figure 4.13**). After longer annealing, the improvement in densification and crystallization of the LATP layer is accompanied by a more roughened surface, with visible small particles and grain boundaries.

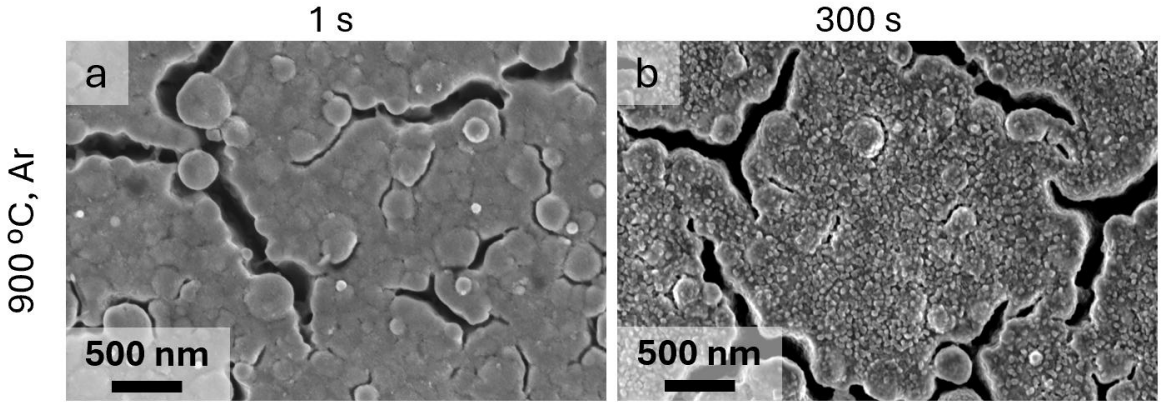


Figure 4.13 - Top-view SEM images of 730 nm LATP films grown on Si_3N_4 at 300 °C and annealed by RTP at 900 °C in Ar for (a) 1 s and (b) 300 s.

4.6 Ionic Transport Properties of LATP Thin Films

To evaluate whether the structural and morphological changes in RTP treated samples is accompanied by improved ionic transport, the LATP thin films were further investigated by in-plane PEIS. Measurements were performed between room temperature and 300 ºC, allowing 10 min of thermal stabilization before the acquisition of each spectrum.

Since the final objective is to use LATP as a solid electrolyte in LFP-based thin-film devices, the measurements of films annealed in both O_2 and Ar were investigated, as LFP is highly sensitive to oxidation. Therefore, the motivation is to enhance the ionic transport properties of LATP while contributing to the preservation of the electrochemically active LFP phase in a bilayer configuration.

Figure 4.14a shows the measurement geometry configuration used in this study, consisting of two parallel Au electrodes of 2 mm length separated by 0.5 mm, deposited on the film surface. The LATP film thicknesses were 730 nm or 250 nm, resulting in effective areas of 1.46×10^{-5} cm^2 or 0.5×10^{-5} cm^2 respectively. The simplified equivalent circuit $Rs + (R_{LATP} \| CPE_g) + [(R_{ct} + Z_w) \| CPE_{dL})$ adopted to describe the main contributions to the impedance response is also presented in this figure (**Figure 4.14b**).

This simplification assumes that the grain and grain-boundary resistive contributions cannot be clearly distinguished in the complex impedance plane, since their semicircular responses overlap and are further masked by the high geometric capacitance associated with the Si_3N_4 layer on the Si substrate.[19] As a result, the high-frequency response is described by an apparent LATP resistance (R_{LATP}) in parallel with this dominant capacitive contribution (CPE_g).

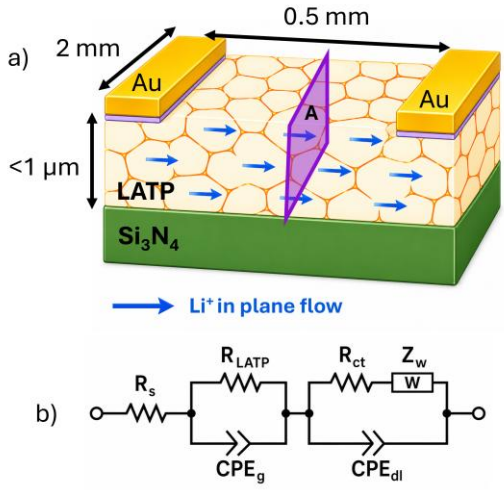


Figure 4.14 – (a) Schematic illustration of the in-plane PEIS configuration used to evaluate LATP thin films using two parallel Au electrodes deposited on the film surface. (b) Simplified equivalent circuit used to fit the impedance response.

At lower frequencies, the impedance response can be described by a Randles-type circuit, commonly used to represent phenomena at the electrode/electrolyte interfaces and possibly with the formation of a lithium-containing interdiffusion layer. This response is represented by a charge-transfer resistance (R_{ct}) in series with a Warburg element (Z_W), accounting for diffusional processes coupled to charge transfer, both in parallel with a constant phase element associated with the double layer (CPE_{dl})..[151–153]

The in-plane PEIS response of the LATP thin films, measured at 300 °C, is presented in the Nyquist plots together with the corresponding fitted curves (**Figure 4.15**). After RTP, the high-frequency contribution $R_{LATP} \| CPE_g$ is generally located in the 10^2 - 10^3 Hz range. In the as-deposited films (**Figure 4.15a**), both contributions are shifted to much lower frequencies, indicating poor ionic transport within the amorphous LATP layer than the RTP-treated samples. The 250 nm film shows a slightly larger areal impedance than the 730 nm film, although both spectra are dominated by broad and depressed semi circles responses. The as-deposited films present the highest R_{LATP} values, in the range of ~600-800 Ω cm^2 whereas RTP in Ar reduces this value by almost two orders of magnitude.

For the 730 nm films annealed in Ar (**Figure 4.15b**), increasing the RTP temperature from 800 to 900 °C shifts the spectra toward lower impedance values, indicating improved ionic transport at the higher annealing temperature. The area-normalized R_{LATP} resistance decreases from 13.26 Ω cm^2 to 11.41 Ω cm^2. This improvement is attributed to enhanced LATP crystallization and densification, which promotes Li^+ transport within the solid electrolyte phase and improves the connectivity of the conducting layer. A similar comparison at 800 °C in Ar (**Figure 4.15c**) shows that the 250 nm film exhibits a lower R_{LATP} than the 730 nm film, decreasing from 13.26 Ω cm^2 for the 730 nm film to 9.72 Ω cm^2 for the 250 nm film. This is consistent with the slightly higher

apparent in-plane conductivity calculated for the thinner film. These results suggest that fast superficial thermal treatment by RTP is more effective in thinner layers, where the reduced thickness may facilitate crystallization and densification throughout a larger fraction of the film.

The effect of dwell time at 900 °C in Ar is shown in **Figure 4.15d**. Extending the treatment from 1 s to 300 s further decreases R_{LATP} from 11.41 to 7.13 Ω cm^2, indicating an additional improvement in the main LATP transport contribution. However, the overall decrease in the impedance response is relatively limited because the lower-frequency contribution becomes more pronounced. This spectral evolution suggests that prolonged treatment improves the crystallized LATP phase, while it may also promote surface roughening or interfacial heterogeneity, increasing the non-ideal blocking contribution at the LATP/Au interface.

As a conclusion, although most of the transport improvement is already achieved during the short 1 s RTP treatment, prolonged annealing still enhances the high-frequency LATP contribution.

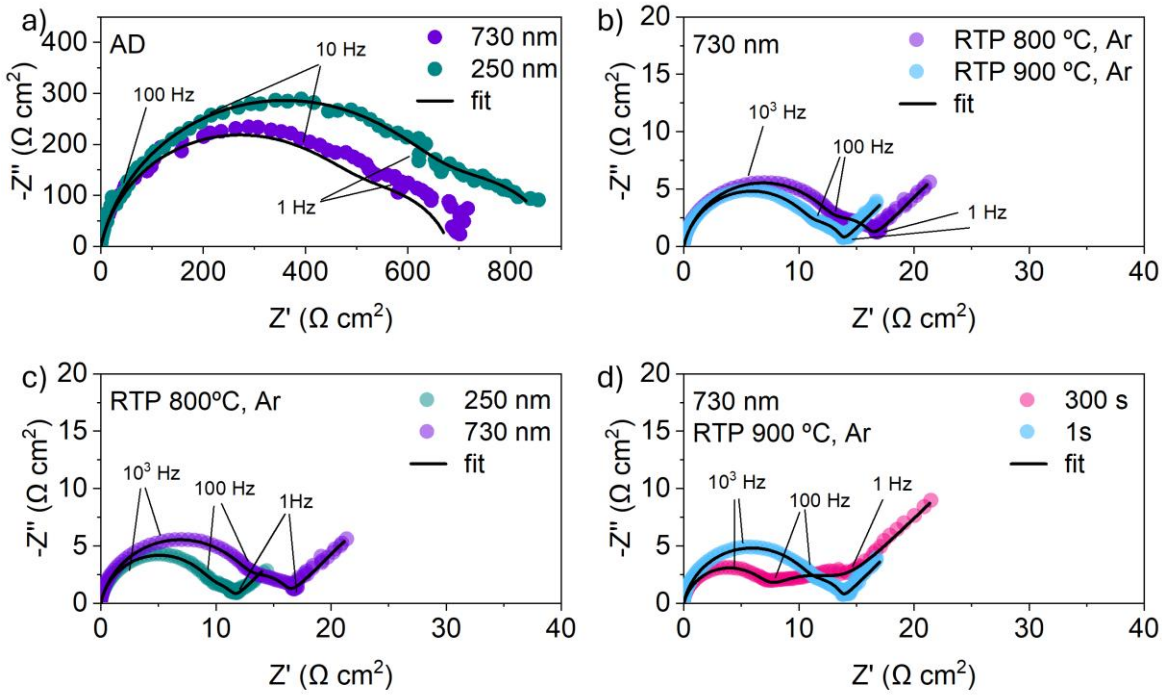


Figure 4.15 - Area-normalized Nyquist plots and fitting curves of LATP thin films measured by in-plane PEIS at 300 ºC. Pannels compare the spectra of (a) as-deposited 730 and 250 nm films; (b) 730 nm films treated at 800 and 900 ºC in Ar; (c) 250 and 730 nm films treated at 800 ºC in Ar; (d) 730 nm films treated at 900 ºC in Ar for 1 and 300 s.

The ionic conductivities, σ, were estimated from the resistances associated with the LATP semicircle contributions according to Ohm's Second Law:

$$\sigma = \frac{L}{R_{LATP}\, A} \tag{4.1}$$

where L is the electrode spacing, R_{LATP} is the resistance attributed to the LATP thin film, and A is the effective cross-sectional area for in-plane transport. Although this approach yields an overall in-plane conductivity, it provides a consistent basis for comparing the different processing conditions.

The temperature dependence of the ionic conductivity was then analyzed, assuming a thermally activated transport process. In solid electrolytes, Li^+ migration occurs through successive jumps between neighboring sites, requiring the ions to overcome an energy barrier. This behavior can be described by an Arrhenius-type relation combined with the temperature dependence of conductivity:

$$\sigma = \frac{\sigma_0}{T} \exp\left(-\frac{E_a}{RT}\right) \tag{4.2}$$

where σ_0 is the pre-exponential factor, E_a is the activation energy for Li^+ transport, R is the gas constant and T is the absolute temperature. Equivalently, this expression can be written as:

$$\ln(\sigma T) = \ln(\sigma_0) - \frac{E_a}{RT} \tag{4.3}$$

Thus, plotting $\ln(\sigma T)$ as a function of 1/T allows E_a to be extracted from the slope of the linear fit. A lower activation energy indicates a reduced energy barrier for Li^+ migration and, consequently, more favorable ionic transport.

The temperature dependence of the ionic conductivity is summarized in **Figure 4.16**. In the Arrhenius plot (**Figure 4.16a**), all RTP-treated samples exhibit linear behavior, consistent with thermally activated Li^+ transport. The conductivity at room temperature σ_{RT} (S cm^{-1}) was estimated by extrapolation of the linear Arrhenius fit to T = 298 K. For all annealed samples the σ_{RT} values fall within the 10^{-6} S cm^{-1} range, with limited variation between processing conditions. The highest value is obtained for the sample annealed at 900 ºC in O_2 (6.4×10^{-7} S cm^{-1}), while the film treated at 800 ºC in O_2 shows the lowest conductivity among the RTP samples (1.0×10^{-7} S cm^{-1}). The films annealed in Ar display intermediate and very similar values (~3.4 - 4.0×10^{-7} S cm^{-1}), indicating a weaker dependence on temperature under inert atmosphere.

Overall, the conductivities indicate that RTP effectively activates Li^+ transport in low-temperature-deposited LATP films. The as-deposited film grown at 350 ºC shows a much lower conductivity, 9.3×10^{-11}, about four orders of magnitude below the RTP-treated samples. This strong increase confirms that the crystallization induced by RTP is essential to recover the ionic transport properties of the NASICON-type phase. Although the film annealed in O_2 at 900 ºC reaches the highest conductivity, all RTP-treated films remain within the same order of magnitude and

approach values commonly reported for LiPON thin-film electrolytes.[154] Therefore, from the perspective of electrolyte resistance, LATP is not expected to be the limiting component in an integrated microbattery, provided that the layer remains mechanically continuous.

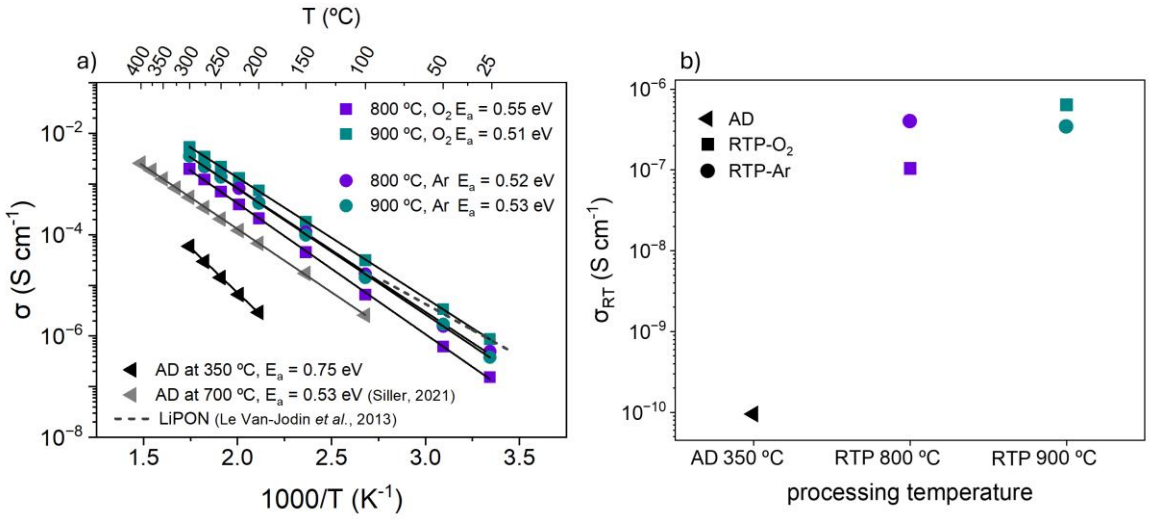


Figure 4.16 - Ionic conductivity of 730 nm-think LATP thin films as a function of temperature and processing conditions. (a) Arrhenius plots for as-deposited and RTP-treated films under O_2 or Ar. (b) Room-temperature conductivity σ_{RT} extracted from the Arrhenius fits as a function of processing condition. Marker shape distinguishes annealing atmosphere (squares: O_2, circles: Ar) and as-deposited state (triangle).

The as-deposited film grown at 350 °C exhibits a higher activation energy, 0.75 eV, whereas the RTP-treated samples show lower values in the range of 0.51–0.55 eV. These values are close to those obtained for films deposited directly at high temperature. Nevertheless, the values obtained for σ and E_a remain relatively high compared with ideal bulk LATP, suggesting that Li^+ transport is still at least partially limited by grain boundaries and intergranular regions.

Although extended annealing in air at high temperature is known to promote an amorphous matrix upon formation of Li_3PO_4, P_2O_5, $LiTiPO_5$ and even $AlPO_4$, detected by Li, P, and Al enrichment at grain boundaries, acting as the sintering aid and therefore improving densification and the contact area between domains of different orientations,[155,156] such redistribution is unlikely to be achieved under the short RTP times used here.

In addition to grain-boundary effects, the crack network described in **Section 4.5** must also be considered when interpreting the in-plane conductivity values. Since the current path in the PEIS configuration runs laterally along the film, cracks can interrupt percolation pathways and increase the effective measured resistance. Therefore, the extracted conductivities should be considered effective in-plane values that include both the intrinsic transport properties of the crystallized LATP phase and the morphological limitations associated with cracking. In cross-plane solid-state devices, the effect of cracks may differ depending on their depth and connectivity; however, through-

thickness cracks remain highly undesirable because they may provide leakage pathways or enable direct contact between adjacent electrodes.

4.7 Integration of LATP with LFP: Bilayer Architecture

After establishing in Chapter 3 the deposition conditions for LFP thin-film cathodes, and after demonstrating in the present chapter that low-temperature LATP films can be crystallized by RTP, both materials were combined into sequential LFP/LATP bilayer architectures on Pt-coated substrates. Based on the results discussed in **Section 4.3**, a thinner LATP layer was selected for bilayer fabrication in order to reduce excessive crack formation, which could compromise the ionic continuity of the electrolyte film. Thus, the LATP thickness in the bilayers was reduced to approximately 250 nm, aiming to improve the mechanical integrity of the top electrolyte layer while preserving continuous coverage of the underlying LFP cathode.

In this architecture, the LFP layer was first deposited on Pt at 600 ºC under Ar, followed by LATP deposition at 300 ºC under O_2. The transition between both depositions was carried out inside the PLD chamber by changing the target without exposing the sample to air, so that the full stack remained under vacuum throughout the process. This procedure was adopted to minimize interfacial contamination and to better assess the compatibility of both layers during sequential growth.

The morphology of the as-deposited bilayer is shown in **Figure 4.17**. The cross-sectional image in **Figure 4.17a** confirms the formation of a continuous multilayer structure on Pt, with the LATP top layer covering the underlying LFP film. The top-view image in **Figure 4.17b** reveals a granular LATP surface with a fine crack network, consistent with the morphology previously observed for low-temperature LATP films on Pt and Si_3N_4. However, the crack network appears less severe than that observed in the thicker standalone LATP films discussed in **Sections 4.3** and **4.5**, likely because of the lower LATP thickness in the bilayer architecture. No evident delamination is observed in the as-deposited state, indicating that sequential PLD deposition leads to a well-preserved bilayer architecture.

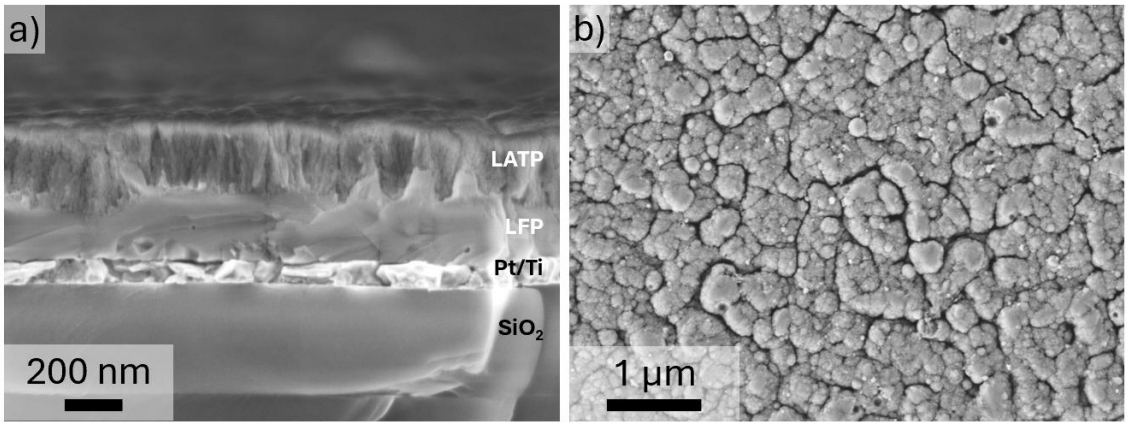


Figure 4.17 - SEM images of the as-deposited LFP/LATP bilayer grown on a Pt substrate: (a) cross-sectional view and (b) top-view image.

To evaluate the effect of post-deposition treatment, the bilayers were subjected to RTP in Ar for 1 s at 800 and 900 ºC. The corresponding cross-sectional and top-view SEM images are presented in **Figure 4.18**. The cross-sectional views reveal a clear dependence of the bilayer integrity on RTP temperature. After annealing at 800 ºC in Ar (**Figure 4.18a,c**), the multilayer architecture remains comparatively well preserved, with the stack still appearing continuous and recognizable. This indicates that the LATP crystallization treatment can be applied without completely disrupting the LFP/LATP bilayer when the thermal budget is sufficiently limited.

In contrast, after annealing at 900 ºC in Ar (**Figure 4.18b**), the bilayer no longer maintains the same uniform and well-defined stacked structure, suggesting stronger structural degradation during the thermal treatment. The top-view images show the same tendency. After RTP at 800 ºC in Ar (**Figure 4.18c**), the regions between cracks appear more compact, in agreement with the densification observed for standalone LATP films, with very small finer particles distributed on the surface. However, after RTP at 900 ºC in Ar (**Figure 4.18d**), the LATP surface exhibits stronger coarsening but also the appearance of bright particles or protrusions inter grains, like a composite. These features indicate that the increase in RTP temperature may promote not only LATP crystallization and densification, but also local degradation, secondary-phase segregation, with material redistribution within the bilayer. Secondary-phase formation during annealing was also observed for bilayers treated at 800 ºC for 1 s in O_2, as shown in **Figure 4.19**. In this case, the surface contains bright, faceted plate-like particles dispersed over the granular matrix, suggesting local phase segregation and a different crystallization during the oxidative RTP treatment. Although their composition cannot be determined from SEM alone, these features indicate that O_2 promotes degradation of the LFP/LATP bilayer, supporting the selection of Ar as the preferred annealing atmosphere for its integration.

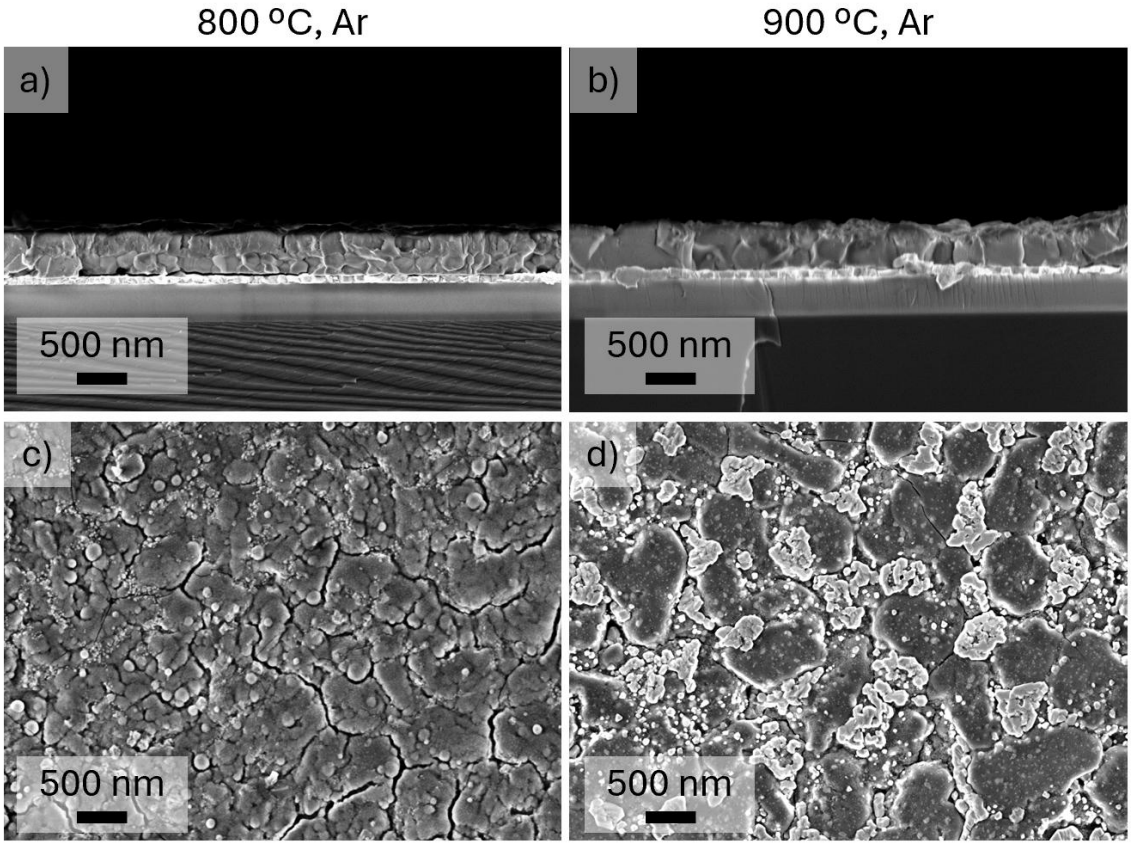


Figure 4.18 - SEM images of LFP/LATP bilayers on Pt after rapid thermal processing in Ar for 1 s: (a) cross-sectional view after annealing at 800 ºC, (b) cross-sectional view after annealing at 900 ºC, (c) top-view image after annealing at 800 ºC, and (d) top-view image after annealing at 900 ºC.

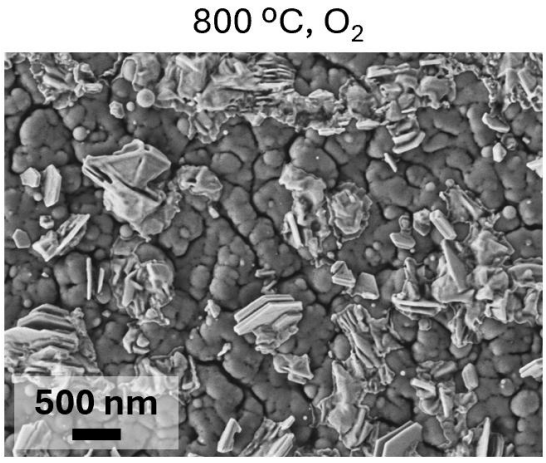


Figure 4.19 - Top-view SEM image of the LFP/LATP bilayer on Pt after rapid thermal processing at 800 ºC for 1 s under O_2.

Based on these observations, the subsequent bilayer processing was restricted to RTP under Ar. This condition represents a compromise between the thermal budget required to promote

LATP crystallization and the need to preserve the structural and chemical integrity of the underlying LFP cathode.

Raman spectroscopy was then used to evaluate the structural evolution of the LFP/LATP bilayer after this optimized treatment, using the commercial $LiFePO_4$ and $Li_{1.3}Al_{0.3}Ti_{1.7}(PO_4)_3$ targets as phase references (**Figure 4.20a**). The as-deposited bilayer exhibits a weak Raman response dominated by a band near 950 cm^{-1}, mainly associated with the underlying LFP layer, while characteristic LATP features are not clearly detected due to its amorphous nature. This result indicates that Raman probing depth can extend through the relatively thin LATP top layer and detect the bottom cathode.

After RTP at 800 ºC for 1 min in Ar, the spectrum becomes more structured, with the appearance of bands in the same spectral regions as the target, particularly between 250–450 cm^{-1} and 1000–1100 cm^{-1}. At the same time, the band near 950 cm^{-1} remains present, indicating continued contribution from the underlying LFP layer. These results suggest that RTP successfully promotes the crystallization of the LATP top layer while preserving the bilayer character of the system, as observed in the top-view SEM images in **Figure 4.20b,c**.

The structural and compositional integrity of the annealed LFP/LATP bilayers was further evaluated by cross-sectional BF-TEM and HAADF-STEM/EDX mapping on prepared FIB lamellae extracted from RTP-treated bilayers under Ar atmosphere. These analyses were carried out on samples prepared for subsequent electrochemical cycling in aqueous electrolyte, so that the fresh state could be used as a reference for the post-cycling characterization discussed in **Section 4.8**. In this way, the defects already introduced during bilayer fabrication and thermal processing can be distinguished from those generated or amplified during electrochemical testing.

The sample treated at 800 °C for 60 s preserves a recognizable bilayer configuration, with the LATP layer clearly distinguishable from the underlying LFP cathode(**Figure 4.21a,b**). In the LFP layer, grain boundaries and intragranular defects can already be identified, indicating that local structural defects are present before electrochemical cycling. The corresponding EDX maps confirm that Ti and Al remain mainly associated with the LATP layer, while Fe is primarily confined to the LFP cathode, although local heterogeneities are observed around cracks and grain/domain boundaries (**Figure 4.23a**).

The sample treated at 800ºC for 60 s preserves the bilayer configuration, with the LATP layer clearly distinguishable from the underlying LFP cathode In the LFP layer, grain boundaries and intragranular defects can be identified, indicating that the cathode already contains local structural defects before electrochemical cycling. In contrast, the sample treated at 900 °C for 1 s shows a much more pronounced compositional redistribution. The Ti-rich and Al-rich regions are no longer uniformly distributed as a continuous LATP layer, while Fe, P and O also show a more heterogeneous distribution across the cross-section. The presence of localized Al- and Ti-rich regions, together with the loss of a clearly defined stacked morphology, confirms that the higher

RTP temperature promotes chemical segregation and partial decomposition of the initial LFP/LATP bilayer architecture (**Figure 4.21c,d** and **Figure 4.23 b**).

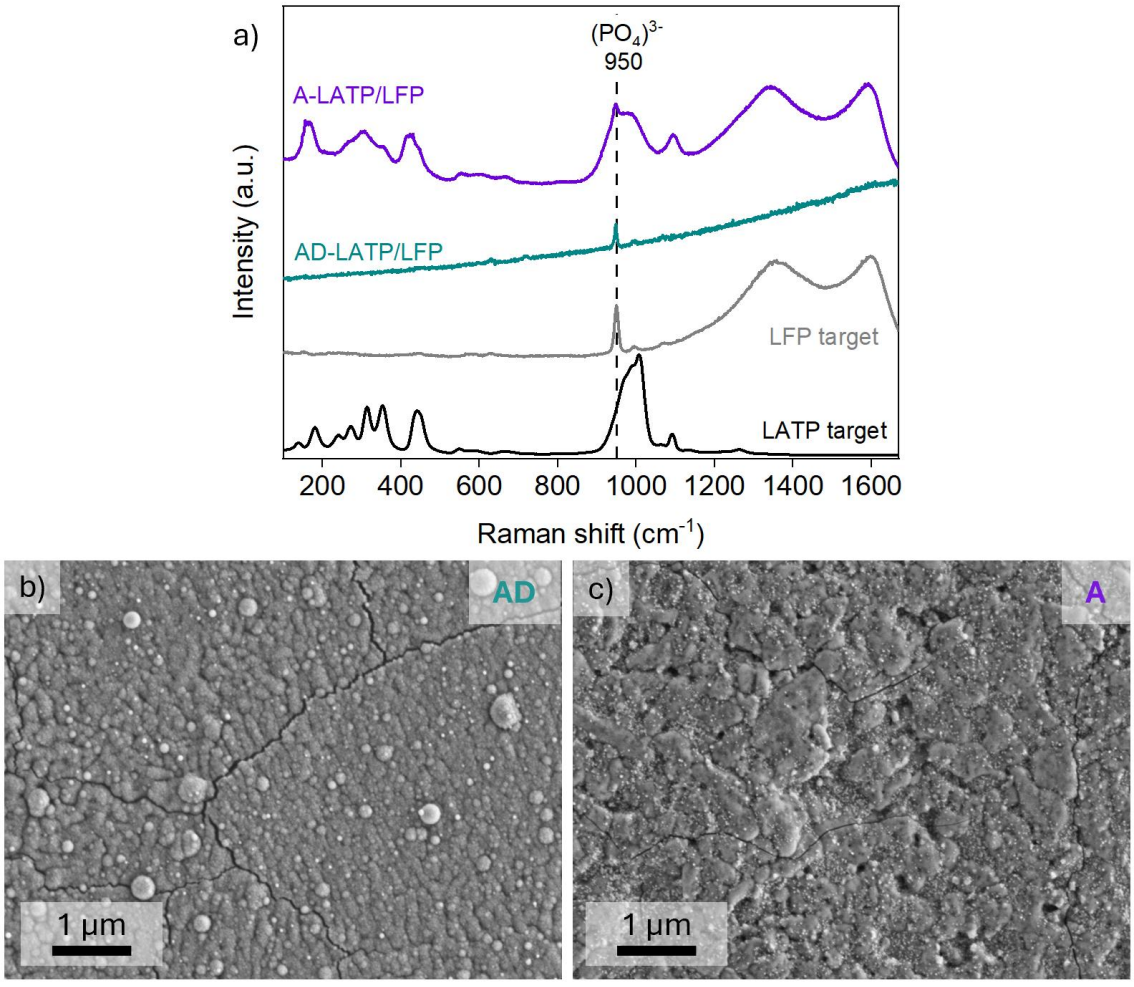


Figure 4.20 - Raman spectra of the LFP/LATP bilayer deposited on Pt in the as-deposited state (AD-LATP/LFP) and after RTP at 800 ºC for 1 min in Ar (A-LATP/LFP), compared with the $LiFePO_4$ and $Li_{1.3}Al_{0.3}Ti_{1.7}(PO_4)_3$ targets used as reference materials.

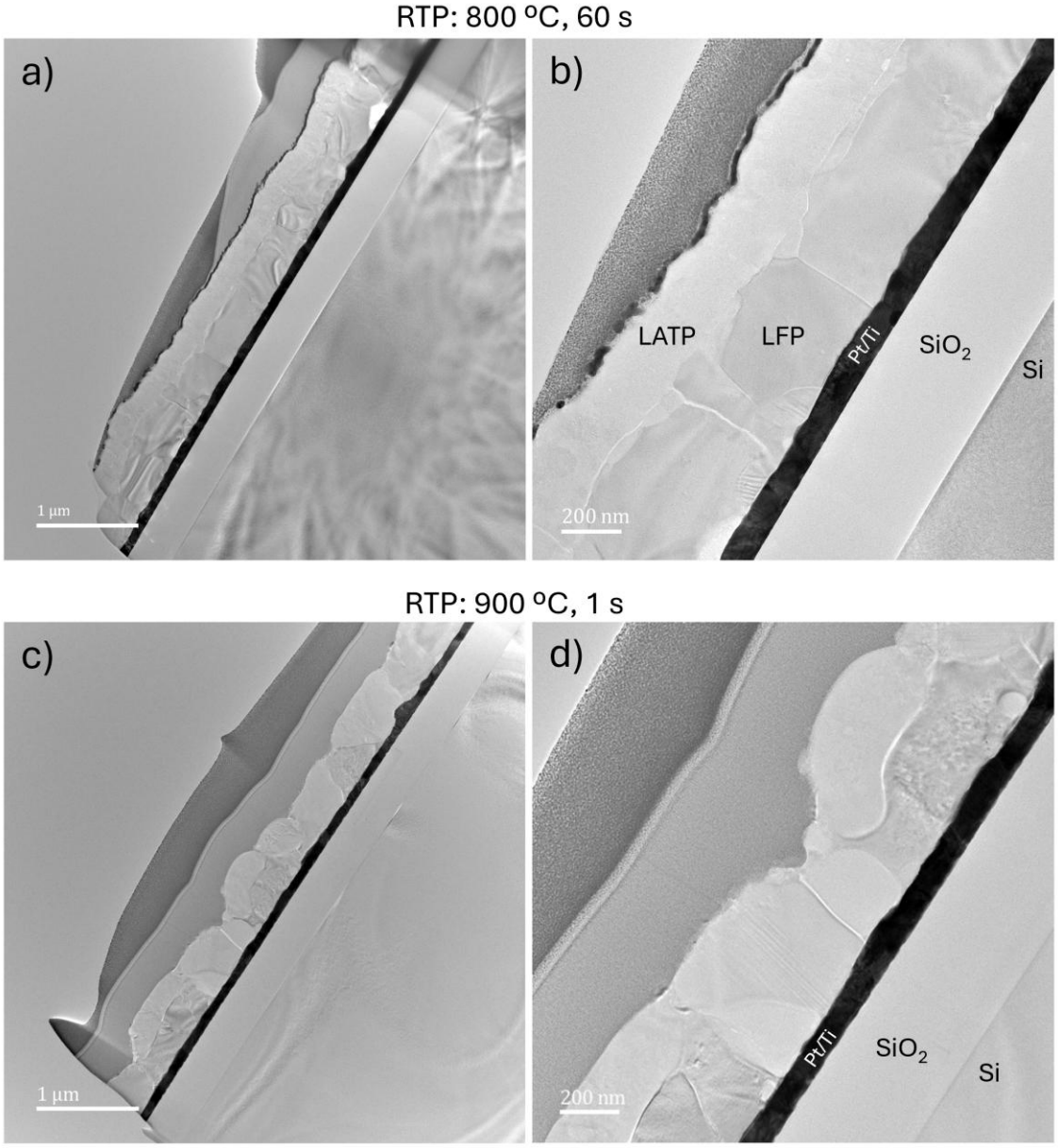


Figure 4.21 - Overview BF-TEM images of FIB lamellas prepared from RTP-annealed LATP/LFP bilayers deposited on Pt/Ti/SiO_2/Si and treated at (a,b) 800 ºC for 60 s and (b,d) 900 ºC for 1 s.

The HRTEM image in **Figure 4.22a** shows the interface between the upper LATP layer and the underlying LFP film after RTP-annealing at 800 ºC. Although some local contrast variations are observed near the interface, the bilayer architecture remains distinguishable after the thermal treatment, without evidence of extensive structural degradation in the analyzed region. Lattice fringes are clearly visible in the LFP, indicating that the LFP layer preserves a crystalline structure after the RTP step. The corresponding FFT pattern obtained from the LFP region (**Figure 4.22b**) , displays well-defined diffraction spots. The symmetry and relative position of the reflections are

consistent with orthorhombic $LiFePO_4$ viewed along the [001] zone axis, as supported by comparison with the simulated diffraction pattern.

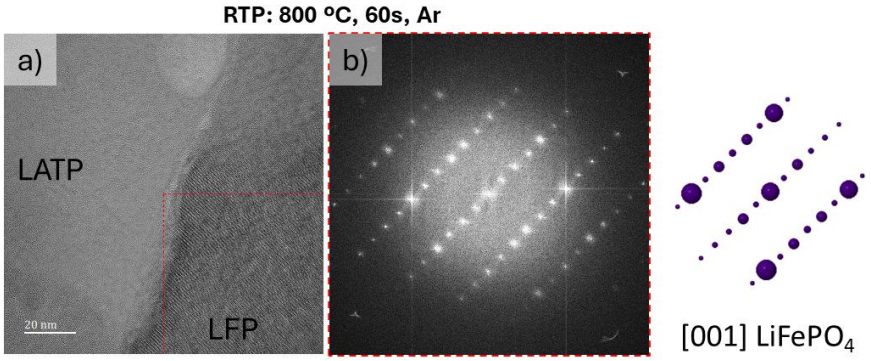


Figure 4.22 - (a) Cross-sectional HRTEM image showing the interface between the LATP layer and the underlying LFP film. The red dashed square indicates the LFP region selected for Fourier analysis. (b) FFT pattern obtained from the selected LFP region, The simulated [001] $LiFePO_4$ diffraction pattern is shown for comparison.

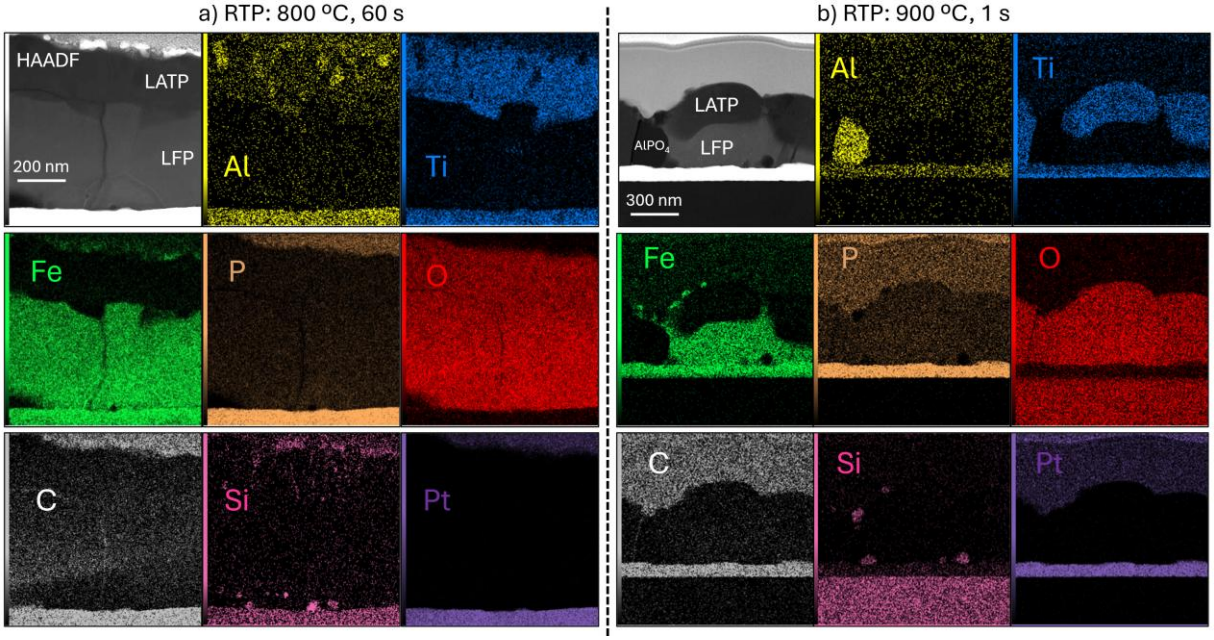


Figure 4.23 - HAADF-STEM images and corresponding EDX elemental maps of LFP/LATP bilayers deposited on Pt/Ti/SiO_2/Si substrates and treated by RTP in Ar at (a) 800 °C for 60 s and (b) 900 °C for 1 s.

4.8 Electrochemical Performance of LFP/LATP Bilayer

After the structural and morphological characterization discussed in the previous section, the electrochemical behavior of the LFP/LATP bilayer annealed at 800 ºC for 60s in Ar was investigated in liquid electrolyte by galvanostatic charge-discharge tests at currents between 0.1 and

2 µA (0.5 - 10.3 µA cm^{-2}). The thickness of the LFP layer is ~420 nm, and the area in contact with the aqueous electrolyte is 19.4 mm^2. The potential (V vs. Ag/AgCl) versus specific capacity (mAh g^{-1}) curves (**Figure 4.24**) confirm that the bilayers remain electrochemically active after fabrication, showing reversible charge and discharge profiles across the investigated current range. The accessible discharge capacity decreases from 113.2 to 50.5 mAh g^{-1}, at 0.5 and 10.3 µA cm^{-2} respectively.

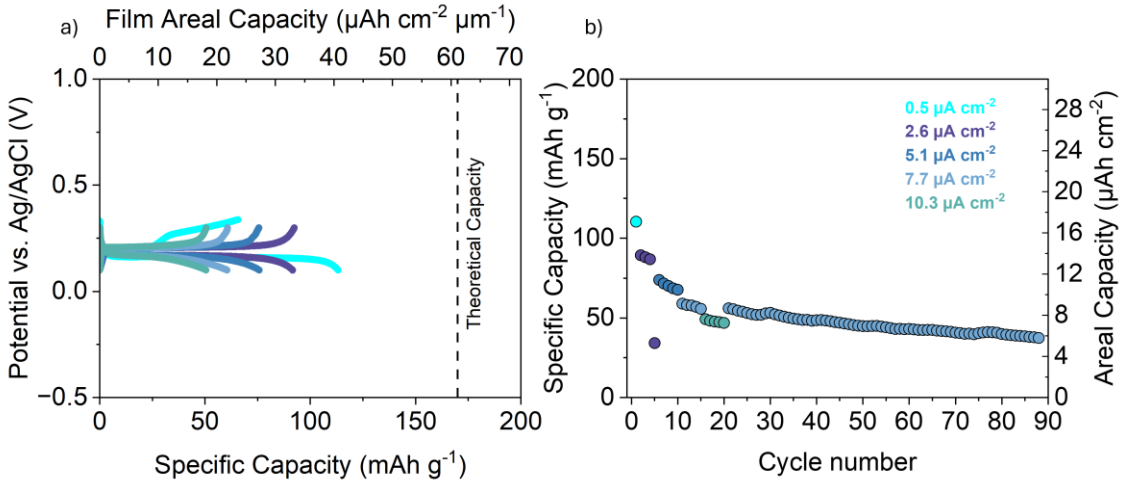


Figure 4.24 - Galvanostatic charge and discharge cycles of the bilayer at different current densities.

The capacity normalization was performed using the LFP thickness of approximately 420 nm. However, after annealing, it cannot be excluded that part of the LFP layer could have interacted with the LATP, which makes the exact electrochemically active mass uncertain. In addition, within the narrow potential window accessible in aqueous electrolyte, it is not possible to determine whether secondary phases such as Fe_2O_3 or $Li_3Fe_2(PO_4)_3$ are present in the system, likely at the solid electrolyte/cathode interface. A broader potential window would be required to verify the presence of additional electrochemically active phases by identifying possible plateaus at other voltages. This point will be further addressed in the next chapter through all-solid-state device measurements. Overall, these results indicate that the bilayer processing preserves electrochemical activity, while the interpretation of the absolute capacity values remains limited by phase complexity and interfacial effects.

After charge/discharge cycling, the bilayer treated at 800 °C for 60 s shows a more damaged microstructure, especially around grain boundaries and pre-existing defects in the LFP active layer (**Figure 4.25**). The LATP layer also retains the cracks already observed in the fresh state as mentioned in previous sections. These results indicate that electrochemical operation does not generate a completely new degradation mechanism, but rather aggravates defects already introduced during bilayer fabrication and RTP treatment. After exposure to the aqueous electrolyte and electrochemical cycling, these regions become more evident, possibly due to the dissolution/removal of amorphous material initially trapped within cracks and grain boundaries.

The corresponding HAADF-STEM/EDX maps (**Figure 4.26**) indicate that the overall elemental distribution remains broadly preserved after cycling, with Ti and Al mainly associated with the LATP layer and Fe predominantly located in the LFP cathode. Hence, cycling does not induce large-scale intermixing between the two layers. Nevertheless, local chemical variations are observed around cracks and grain/domain boundaries, confirming that degradation is spatially localized and preferentially develops in structurally defective regions.

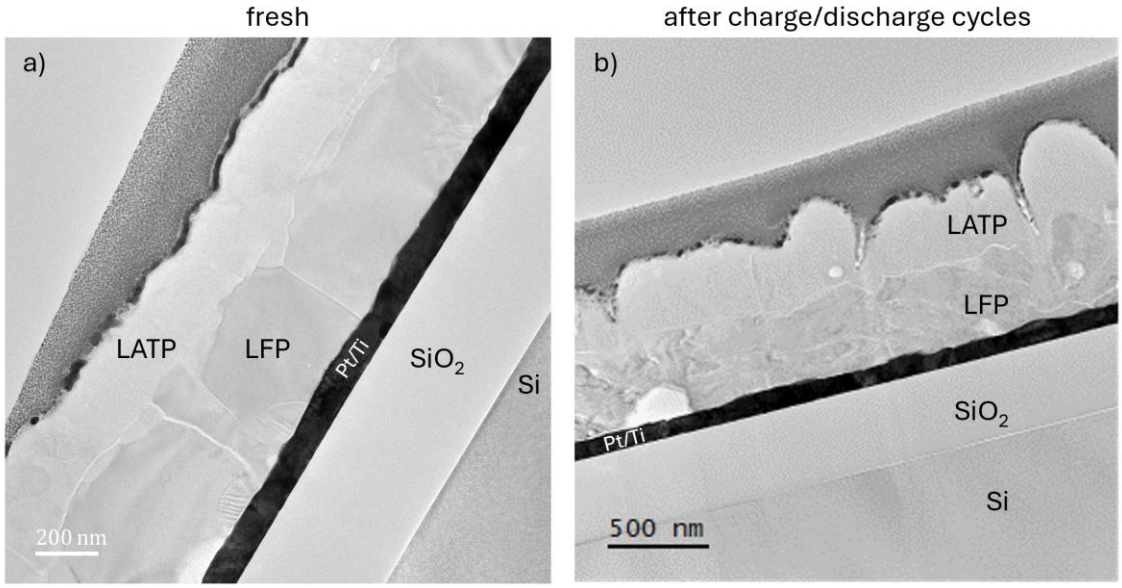


Figure 4.25 - Cross-sectional TEM images of the LATP/LFP bilayer treated at 800ºC for 60 s, showing (a) a fresh region prior to electrochemical testing and (b) a region after charge/discharge cycling.

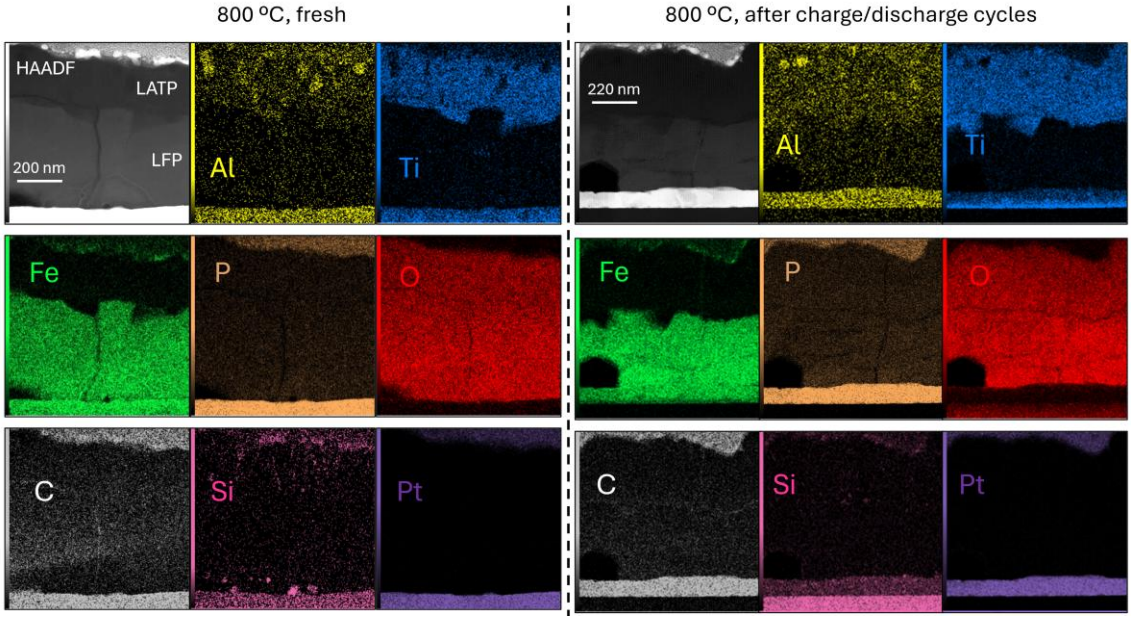


Figure 4.26 - HAADF-STEM images and corresponding EDX elemental maps of the LATP/LFP bilayer treated at 800ºC for 60 s, comparing fresh and cycled regions.

It should also be noted that some amorphous regions observed during HRTEM may be influenced by beam exposure, as illustrated in **Figure 4.27a**, in which the crack observed is intragranular, as the crystallographic orientation is preserved on both sides of the defect. Nevertheless, the presence of void and amorphous regions around cracks and grain boundaries are not attributed solely to beam effects, but primarily due to the sample processing and electrochemical tests.

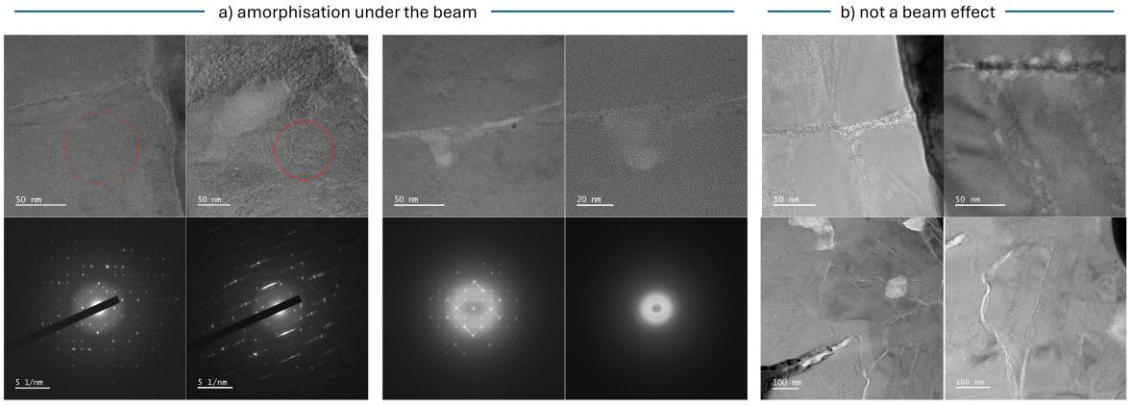


Figure 4.27 - High-resolution TEM images illustrating amorphous regions observed in the LATP/LFP bilayer: (a) local amorphization induced during beam exposure, and (b) void formation/amorphization associated with cracks and grain boundaries, identified as intrinsic to the sample and not caused by the electron beam.

More localized HAADF/EELS analyses around defects (**Figure 4.28**) further show that cracked regions in LFP are associated with oxygen depletion and Fe enrichment, whereas cracks in LATP show a slight Ti enrichment, too small to be clearly resolved by conventional EDX mapping.

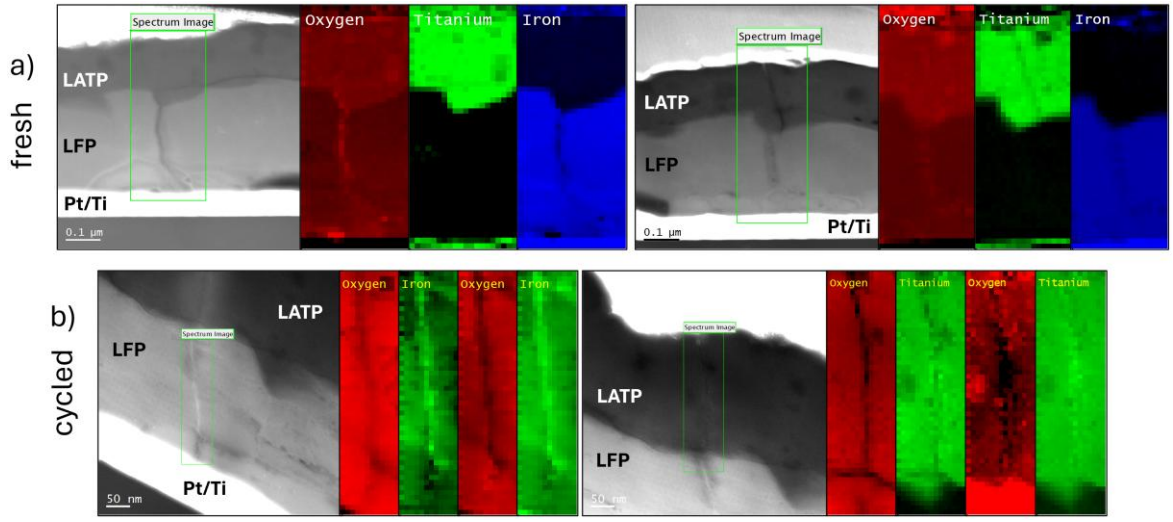


Figure 4.28 - HAADF-STEM images, elemental intensity maps (left) and quantified at.% maps (right) acquired around representative cracks in the LATP/LFP bilayer treated at 800ºC for 60 s (a) before and (b) after electrochemical tests.

Further insight is provided by the 4D-STEM analysis. As shown in **Figure 4.29a**, cycling is associated with strain in the LFP layer and with the appearance of intragranular streak-like defects. These defects follow a preferential direction, identified in **Figure 4.29b** as the [-101] direction, and are therefore contained in the (010) planes. Since the (010) planes are the preferred Li diffusion planes in olivine LFP, this result suggests that defect formation in the cycled bilayer is crystallographically guided and likely coupled to the anisotropic Li^+ transport pathway within the cathode.

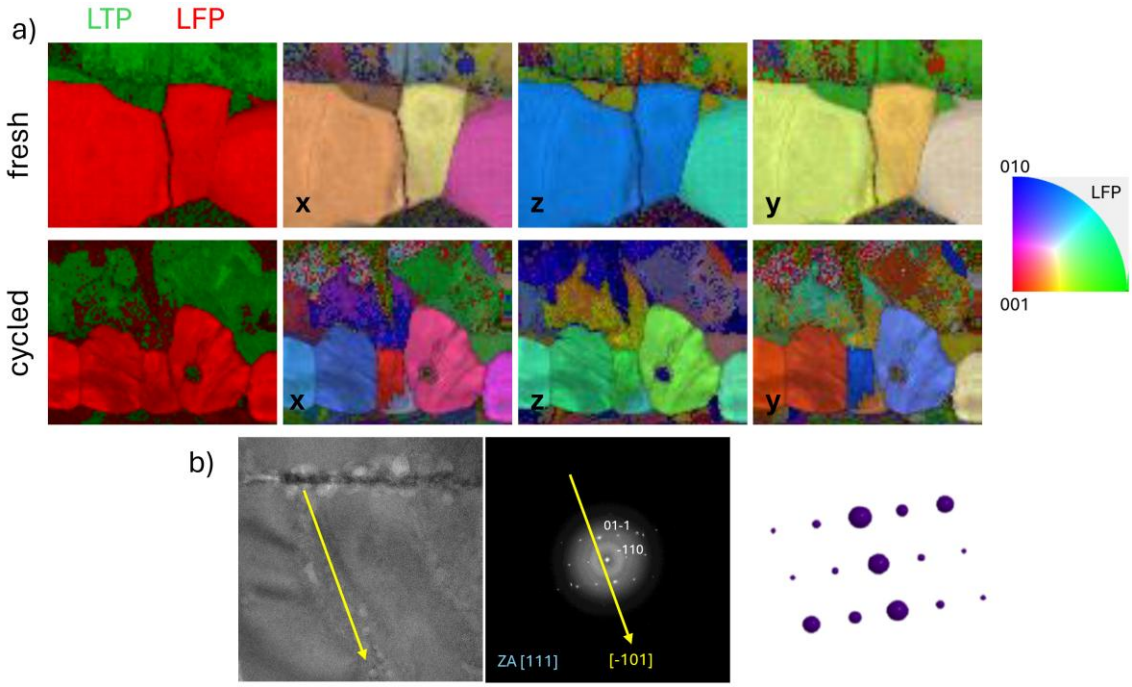


Figure 4.29 – (a) STEM orientation maps of the LATP/LFP bilayer treated at 800ºC for 60 s, comparing fresh and cycled regions. (b) - Crystallographic analysis of the preferential direction of intragranular streak-like defects in LFP.

Overall, the TEM results indicate that the LATP/LFP bilayers already contain mostly intragranular cracks before electrochemical cycling, The pre-existing defects propagate in the direction of the Li diffusion during charge and discharge. In the LFP layer, the evolution of streak-like defects along directions contained in the (010) planes suggests that degradation is linked to crystallographic pathways associated with Li diffusion. At the same time, the increase in the local Fe/O ratio around defects points to additional chemical modification in these damaged regions. Although Li and P could not be reliably quantified in all cases, the combined TEM, EDX, EELS, and 4D-STEM observations consistently support a localized, defect-assisted degradation mechanism in the RTP-annealed LATP/LFP bilayer.

4.9 Conclusions

In this chapter, LATP thin films were fabricated by PLD at reduced temperature and subsequently crystallized by rapid thermal processing (RTP), with the aim of enabling their integration as solid electrolyte layers in LFP-based thin-film battery architectures. The strategy was based on decoupling film growth from crystallization, so that LATP could be deposited under conditions compatible with multilayer fabrication and then crystallized using short high-temperature treatments.

The results demonstrate that low-temperature deposition at 300 ºC leads to dense but structurally amorphous films, which require post-deposition treatment to develop the NASICON crystalline solid electrolyte. RTP was shown to be an effective route to induce LATP crystallization within a very limited thermal budget, strongly reducing the processing time (1-60 s dwell time, 10 ºC s^{-1} heating and cooling rates) compared with conventional long-duration annealing (5h dwell time, 5 ºC min^{-1} heating rate). However, a clear trade-off between crystallization and phase purity was identified in the RTP annealing, particularly under O_2, where the formation of anatase TiO_2 becomes more pronounced at longer dwell times or higher temperatures, which explains the high amount of secondary phases in reported LATP thin films annealed by conventional long routes under oxidizing atmospheres.

The annealing atmosphere was found to be a decisive parameter. While O_2 promotes LATP crystallization more strongly, it also favors TiO_2 formation and is not suitable for integration with LFP because of the risk of cathode oxidation. In contrast, RTP under Ar provides a more favorable compromise for bilayer processing. Although crystallization appears more gradual under Ar, the formation of TiO_2 is strongly reduced and the resulting LATP films still reach room-temperature ionic conductivities in the 10^{-6} - 10^{-7} S cm^{-1} range, close to values commonly reported for LiPON thin-film electrolytes. Therefore, from the point of view of intrinsic electrolyte resistance, RTP-treated LATP is not expected to be the main limiting component in a thin-film microbattery. However, this conclusion is strongly constrained by the mechanical integrity of the electrolyte layer. In practical cross-plane devices, even if the LATP phase exhibits adequate ionic conductivity, crack propagation, or local discontinuities may dominate the effective device response by interrupting ionic pathways or creating leakage/contact pathways across the stack.

These cracks are already present in thick low-temperature-deposited films and are mainly associated with thickness-related stress accumulation. After RTP, the pre-existing crack initiators become preferential paths for further crack propagation, driven by densification, thermal expansion mismatch, and constrained shrinkage during heating and cooling. This represents one of the main limitations of the present LATP films, since cracks can interrupt in-plane percolation pathways, increase the effective resistance, and, in a cross-plane device configuration, potentially act as leakage paths or direct-contact pathways between adjacent layers. Thus, although RTP successfully activates ionic transport, further optimization of film thickness and stress management is required to obtain mechanically robust LATP electrolyte layers.

The integration of LATP with LFP in bilayer architectures demonstrated that sequential PLD deposition is feasible. The LATP layer could be deposited at 300 ºC on top of LFP without destroying the underlying cathode, and subsequent RTP under Ar partially crystallized the electrolyte layer while preserving the electrochemical activity of the stack. Among the tested conditions, annealing at 800 ºC for 60s in Ar provided the best compromise between LATP crystallization and preservation of the multilayer architecture with 250 nm thick LATP. In contrast, treatment at 900 ºC for only 1s led to stronger structural degradation, chemical heterogeneity, and partial loss of the well-defined LFP/LATP bilayer configuration. This indicates that the processing window for integrated bilayers is narrower than for standalone LATP films.

Electrochemical testing of the LFP/LATP bilayer treated at 800 ºC in Ar confirmed that the cathode remains active after LATP deposition and RTP treatment. Reversible charge and discharge profiles were obtained in aqueous electrolyte, with the accessible capacity decreasing with increasing current density. However, the absolute capacity values must be interpreted with caution, since the effective electrochemically active LFP mass may be affected by interfacial reactions, phase redistribution, or the possible formation of secondary phases during annealing.

Post-cycling TEM, STEM-EDX, EELS, and 4D-STEM analyses showed that the bilayers already contain structural defects before electrochemical testing, especially intragranular cracks and defective regions in the LFP layer. Cycling does not induce large-scale intermixing between LATP and LFP, but it amplifies pre-existing defects and promotes localized chemical and structural modifications around cracks and grain/domain boundaries. In particular, oxygen-depleted regions with enhanced Fe-related contrast/signals are observed around damaged LFP areas. However, this local contrast should not be interpreted simply as Fe enrichment within pristine LFP; it may also reflect the formation of Fe-containing reaction products, including possible iron silicide phases. In parallel, streak-like defects develop along directions contained in the (010) planes, suggesting that this defect propagation is crystallographically guided and coupled to the anisotropic Li^+ transport pathways of olivine LFP.

Overall, this chapter establishes RTP as a suitable approach to crystallize low-temperature-deposited LATP thin films and recover ionic transport while reducing the thermal exposure compared with conventional annealing. For LFP/LATP bilayers, the results identify RTP in Ar at moderate temperature, particularly around 800 ºC, as the most promising processing condition among those investigated. Nevertheless, the main limitation is no longer only LATP crystallization or ionic conductivity, but the mechanical integrity of the multilayer stack. Future optimization should therefore focus on reducing stress accumulation and crack formation through thinner electrolyte layers, optimized ramp-down profiles, improved substrate or current collector selection. These guidelines provide the basis for the next step toward all-solid-state thin-film devices, where the LFP/LATP stack will be integrated with additional solid-electrolyte and lithium layers, as addressed in **Chapter 5**.

Chapter 5

All-solid-state thin-film batteries based on phosphates

5 All-solid-state thin-film batteries based on phosphates 128

5.1 Scope and motivation of the chapter 128

5.2 Sample description and experimental overview 129

5.3 Electrochemical characterization of LFP/LiPON/Li all-solid-state thin-film batteries 130

5.4 Electrochemical characterization of LFP/LATP/LiPON/Li all-solid-state thin-film battery 140

5.5 Conclusions 144

5 All-solid-state thin-film batteries based on phosphates

5.1 Scope and motivation of the chapter

The previous chapters established the phosphate-based materials and processing framework for the fabrication of individual LFP and LATP thin films, as well as LFP/LATP bilayers, with the ultimate aim of integrating them into all-solid-state battery (ASSB) architectures. In Chapter 3, LFP thin-film cathodes were fabricated by pulsed laser deposition and shown to be electrochemically active in liquid-electrolyte half-cell configuration. These results demonstrated that crystalline LFP films can be obtained directly during deposition at 600 ºC, without the need for post-deposition annealing, and that they exhibit reversible Li^+ insertion/extraction associated with the Fe^{2+}/Fe^{3+} redox couple. However, the electrochemical utilization of the active material remained limited by the intrinsic transport properties of carbon-free LFP and by the polycrystalline nature of the films.

In Chapter 4, the work progressed toward the integration of LFP with NASICON-type LATP solid electrolyte layers. The use of low-temperature LATP deposition followed by rapid thermal processing made it possible to develop LATP-related structural features while, for selected processing conditions, maintaining the electrochemical response of the LFP layer. However, the LFP/LATP bilayer results also revealed that the interpretation of electrochemical capacity becomes more complex once additional interfacial reactions, secondary-phase formation, cracking, and possible cathode/electrolyte interactions are introduced. These observations highlight that the transition from individual thin-film cathodes and electrolytes to complete all-solid-state devices requires not only the preservation of the functional properties of each layer, but also careful control of the full multilayer stack and its buried interfaces.

Considering these previous results, this chapter investigates the electrochemical behavior of LFP-based all-solid-state thin-film batteries. The discussion first focuses on the LFP/LiPON/Li system, in which LiPON is used as a benchmark solid electrolyte due to its established compatibility with lithium metal, low electronic conductivity, and widespread use in thin-film battery architectures. This configuration provides a well-defined all-solid-state platform to evaluate the electrochemical response of PLD-grown carbon-free LFP cathodes. The influence of LFP thickness, applied current density, and operating temperature is analyzed through galvanostatic charge–discharge measurements, while complementary impedance spectroscopy is used to correlate the present limitations. The chapter then extends the discussion to more complex LFP/LATP/LiPON/Li stacks, where the LATP layer is introduced between LFP and LiPON as part of the broader objective of developing phosphate-based all-solid-state thin-film batteries.

The comparison between LFP/LiPON/Li and LFP/LATP/LiPON/Li devices is used to assess whether the incorporation of LATP preserves the characteristic LFP redox response, modifies the accessible capacity, or introduces additional polarization in the complete solid-state system. Overall, this chapter connects the structural and electrochemical findings of the previous chapters with the performance of complete all-solid-state thin-film cells.

5.2 Sample description and experimental overview

Two multilayer all-solid-state thin-film battery configurations were prepared and investigated in this chapter. In both architectures, the electrochemical devices were fabricated on Pt-coated substrates with lateral dimensions of 10 × 10 mm², with Pt acting as the current collector. This section describes the ASSB configurations studied, which are schematically summarized in **Figure 5.1**.

The first device architecture was LFP/LiPON/Li, that consisted of a PLD-grown crystalline $LiFePO_4$ cathode, an approximately 1 μm-thick LiPON electrolyte deposited by RF sputtering, and a thermally evaporated Li metal anode with a thickness of about 2 μm. The LFP layers were deposited using the optimized condition established in Chapter 3, namely 600 ºC under 1 mTorr Ar. Cathode thicknesses of 120, 200, and 300 nm were selected to examine how the amount of active material affects both capacity utilization and rate response. LiPON was selected as the solid electrolyte because of its well-established stability against Li metal due to a stable interface formed. Although reports specifically addressing carbon-free LFP/LiPON thin-film interfaces remain limited, the phosphate-based nature of both materials and the wide use of LiPON with other oxide cathodes make it a suitable reference electrolyte for assessing the electrochemical behavior of the LFP cathode. The LiPON layer was sputtered over the entire cathode area of 8 × 8 mm², while the final Li evaporation step was patterned by shadow masks, defining active cell areas of either 5 mm² or 0.79 mm².

The second architecture was LFP/LATP/LiPON/Li cells, in which a NASICON-type LATP layer was introduced between the LFP cathode and the LiPON electrolyte. In this architecture, ~250 nm-thick LFP cathode and ~230 nm-thick LATP interlayer were fabricated by PLD under conditions explored in chapter 4. As in the previous configuration, the LFP layer was deposited at 600 ºC under 1 mTorr Ar. The LATP layer was subsequently deposited at low temperature, 300 ºC, under 80 mTorr O_2, in order to reduce thermal exposure of the underlying LFP layer before electrolyte crystallization. The LFP/LATP bilayers were then subjected to rapid thermal processing in Ar at 800 ºC for 1 min, using heating and cooling ramps of 10 ºC s^{-1}. The use of an inert atmosphere during RTP was chosen to promote structural ordering of the LATP layer while minimizing oxidation and interfacial degradation of the LFP cathode. LiPON and Li deposition steps were kept identical to those used for the LFP/LiPON/Li cells, i.e. 1 μm-thick LiPON electrolyte, and a 2 μm-thick Li metal anode.

This configuration was designed to assess the electrochemical response of the LFP/LATP bilayer within a complete all-solid-state thin-film battery architecture. LiPON has an additional function: it separates LATP from Li metal. This is necessary because Ti-containing NASICON electrolytes can be reduced at low potential through Ti^{4+}/Ti^{3+} redox processes when placed in direct contact with lithium. Thus, in the LFP/LATP/LiPON/Li stack, LATP is evaluated on the cathode side, whereas LiPON acts as the Li-compatible electrolyte/buffer layer adjacent to the anode.

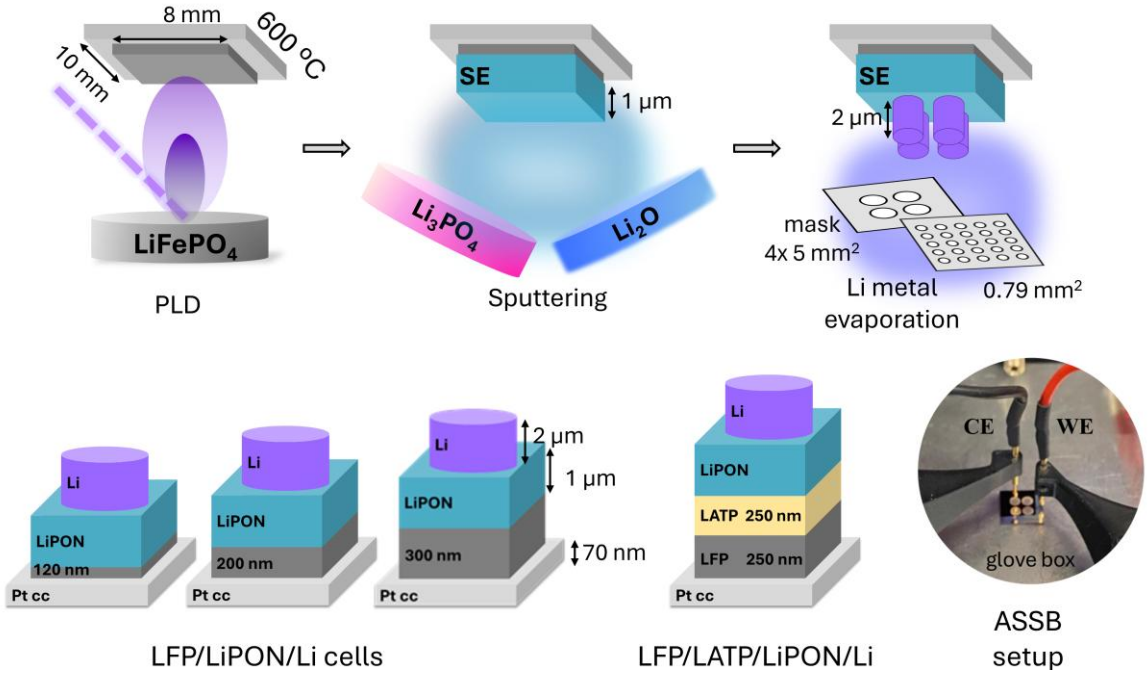


Figure 5.1 - Schematic overview of sequential deposition steps for the fabrication of the all-solid-state thin-film batteries studied in this chapter (top). The final different stack architectures, including LFP/LiPON/Li and LFP/LATP/LiPON/Li, all fabricated on Pt current collectors, are illustrated in the bottom. Schematics are not drawn to scale. The photograph of the electrochemical measurement configuration inside an Ar-filled glovebox.

5.3 Electrochemical characterization of LFP/LiPON/Li all-solid-state thin-film batteries

The LFP/LiPON/Li multilayer ASSB was successfully fabricated combining different methods of deposition. **Figure 5.2** compares devices containing 120, 200, and 300 nm-thick LFP cathodes, imaged in fresh regions that were not subjected to current flow. In all cases, the deposited layers can be distinguished across the stack, confirming that the sequential combination of PLD, RF sputtering, and thermal evaporation produced continuous thin-film cell architectures. The samples were briefly exposed to ambient air before SEM chamber evacuation; therefore, minor surface changes of air-sensitive layers cannot be fully excluded.

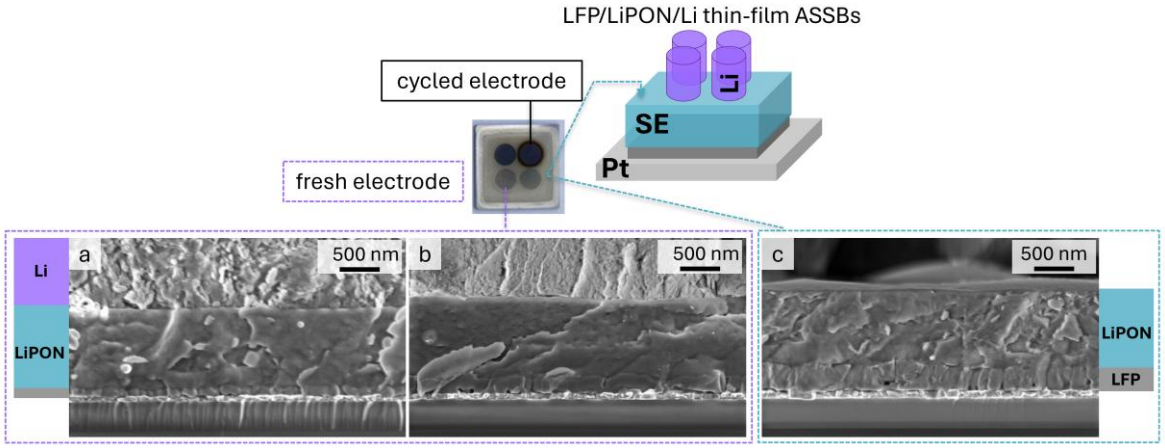


Figure 5.2 - Cross-sectional (a-c) SEM microphotographs of the all-solid-state cells with LFP thin-film cathodes grown by PLD with different thicknesses: 120nm (left), 200 nm (middle) and 300 (right). Schematics are not drawn to scale and are shown for clarity of the layered structures.

The galvanostatic response at room temperature of the LFP/LiPON/Li cells is summarized in **Figure 5.3** for cathode thicknesses of 120, 200, and 300 nm. In **Figure 5.3a-c**, the voltage profiles show the characteristic LFP plateau near 3.45 V vs. Li/Li^+, corresponding to reversible lithium extraction/insertion through the Fe^{+2}/Fe^{+3} redox couple. This feature is maintained over current densities between 2 and 100 μA cm^{-2}. Importantly, no clear additional plateaus appear at approximately 2.8, 2.9, or 3.1 V, which are commonly associated with electrochemically active iron phosphate-related impurity phases such as $Li_3Fe_2(PO_4)_3$, $LiFeP_2O_7$, and $Fe_4(P_2O_7)_3$, respectively, in contrast with previous reports.[157] This observation aligns with the GIWAXS results in chapter 3, which supports the structural evidence that the main electrochemically active phase is olivine $LiFePO_4$. If minor interfacial or secondary phases are present, they either remain electrochemically silent within the selected voltage window or contribute only indirectly by reducing the effective active mass.

For all thicknesses, the first charge capacity is larger than the following discharge capacity (not presented). This irreversible excess charge is consistent with processes occurring during the initial conditioning of the full cell rather than with reversible LFP cycling alone. This behavior is attributed to overlithiation resulting from the co-sputtering process of Li_3PO_4 and Li_2O, as previously reported.[158] Additionally, side reactions at the LiPON/Li anode interface, such as the formation of Li_3PO_4, Li_3P, Li_2O and Li_3N, may contribute to the capacity discrepancy in the first cycle. This interpretation is supported by in situ XPS studies, which provide highly surface-sensitive information on the structure and chemical composition of buried interfaces that are difficult to access by conventional ex situ characterization methods.[159]

The effect of cathode thickness becomes evident when comparing the rate behavior. The 120 nm cell delivers 63 mAh g^{-1} in 85 min at 2 μA cm^{-2}. When the current density is increased to 100 μA cm^{-2}, the capacity decreases to 23 mAh g^{-1} but the response remains stable over the five cycles measured at this rate (**Figure 5.3d**). When the current is subsequently reduced to 10 μA cm^{-}

^{2}, the capacity partially recovers to 44 mAh g^{-1}, indicating that the capacity loss at high current is mainly kinetic rather than irreversible. The 200 nm cathode reaches a comparable low-current capacity of 63 mAh g^{-1} at 2 μA cm^{-2}, indicating improved utilization of active material at this low current density compared to the thinner device, but it undergoes a stronger capacity decrease at higher current densities, reaching about 10 mAh g^{-1} at 100 μA cm^{-2}. The 300 nm cathode provides the highest 6 μAh cm^{-2} areal charge storage at very low current, with a specific capacity close to 56mAh g^{-1} at 0.5 μA cm^{-2}, although a complete discharge requires more than 10 hours for full discharge. This behavior highlights the trade-off imposed by thickness: increasing the active-layer volume improves low-rate areal capacity, but it also amplifies the limitations associated with the low intrinsic electronic and ionic conductivities of carbon-free LFP.

These results show that PLD-grown LFP can be integrated into LiPON-based solid-state thin-film cells while retaining its characteristic electrochemical response. The 300 nm cathode had previously reached about 96 mAh g^{-1} in aqueous electrolyte at 1 μA cm^{-2}

but also surpassing LFP/LiPON bilayer systems fabricated via sputtering.[160] Specifically, the 300 nm PLD-deposited $LiFePO_4$ film achieved ~96 mAh g^{-1} in aqueous electrolyte. In all-solid-state LFP/LiPON/Li configuration, the thicker 300 nm cathode reached 53 mAh g^{-1} at 0.5 μA cm^{-2}, while the thinner 120 nm and 200 nm films delivered reversible capacities above 60 mAh g^{-1} at 2 μA cm^{-2}. These values are competitive when compared with sputtered LFP (150 nm)/LiPON bilayers reported in the literature.[160] It is worth mentioning that the bilayers in this thesis were integrated in an all-solid-state thin-film system, with LiPON thickness fixed to 1 μm and evaporated Li as the anode, while the above-mentioned work resulted in ~72 mAh g^{-1} at 2 μA cm^{-2} with 100 nm LiPON layer, tested in liquid electrolyte. Nevertheless, the capacities remain below the theoretical value of LFP, pointing to incomplete cathode utilization. Based on the structural and electrochemical analysis discussed in the previous chapters, one likely contributor is the Fe-depleted region near the LFP/Pt interface, associated with early-stage interfacial reactions and $FePt_3$ formation. Changing the current collector to ITO proved to be an important strategy for increasing the accessible fraction of the LFP layer.

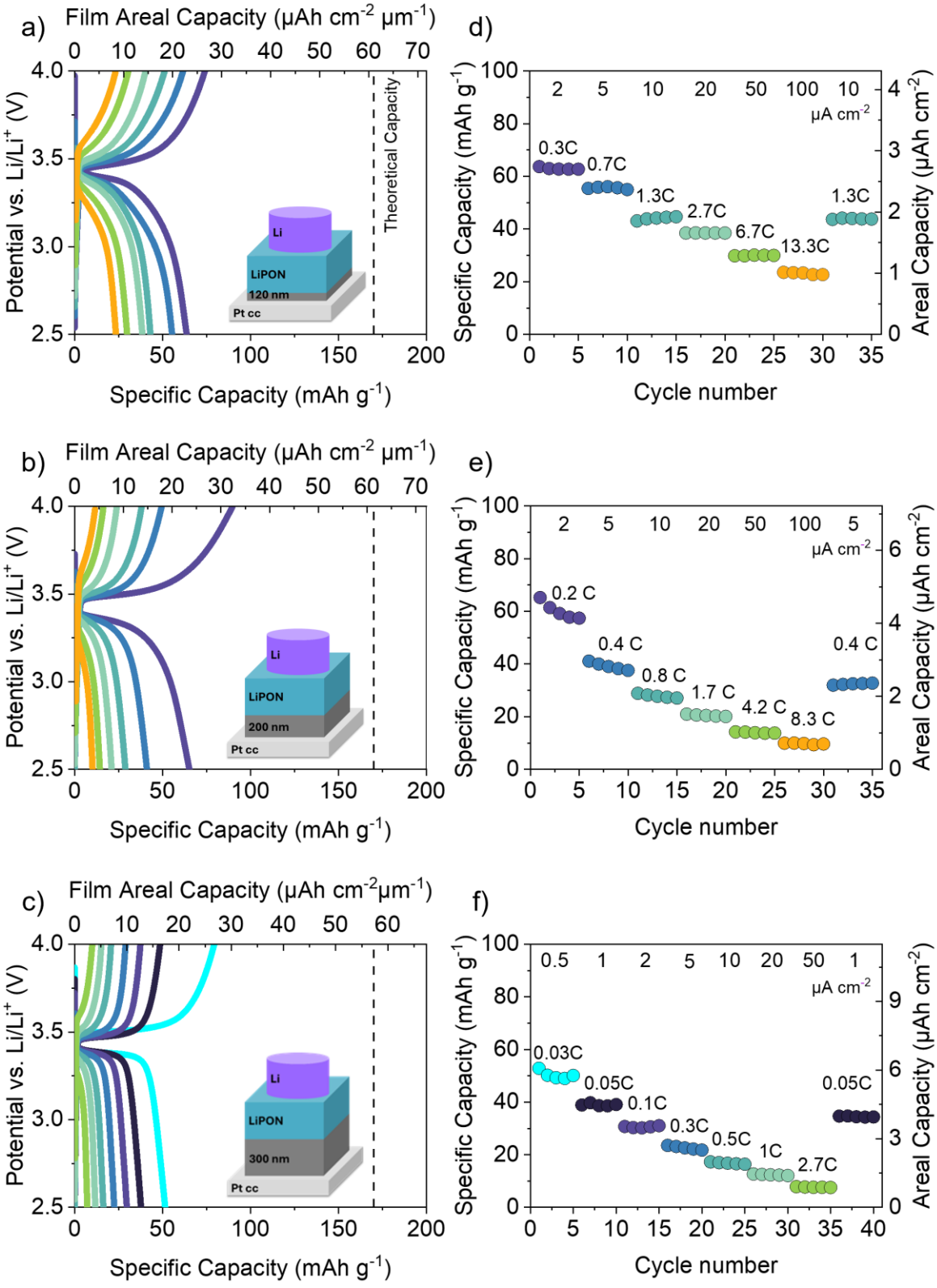


Figure 5.3 - Voltage curves and capacity over cycles of constant-current charge and discharge tests of LFP/LiPON/Li all-solid-state thin-film batteries, with different cathode layer thickness: (a,d) 120 nm, (b,e)

200 nm and (c,f) 300 nm $LiFePO_4$. Schematics shown in a, b, and c are not drawn to scale and serve to provide clarity.

A comparison with recent sputtered Li-Fe-P-O thin films further clarifies the relevance of phase purity. In RF-sputtered porous films annealed at 700 ºC for 1h, film areal capacities close to ~22 $\mu Ah\ cm^{-2}\ \mu m^{-1}$ tested in liquid electrolyte, but the charge storage was mainly associated with a $Li_3Fe_2(PO_4)_3$ secondary phase operating near ~2.8 V.[79] In contrast, the 120 and 200 nm PLD-grown films in the present solid-state cells deliver approximately ~23 and ~22 $\mu Ah\ cm^{-2}\ \mu m^{-1}$ respectively, operating near 3.45 V vs. Li/Li^+. Thus, comparable thickness-normalized capacities are achieved here without post-deposition annealing and without relying on a lower-voltage secondary phosphate phase.

The number of cycles collected in this study was constrained by the long duration of low-current tests. Even within this practical limitation, the cells maintain stable behavior over approximately 35-40 cycles distributed across different current densities. This stability suggests that the stack is not undergoing catastrophic mechanical or electrical failure during the rate tests.

The use of a thin-film geometry reduces ion-transport distances, but it does not remove the influence of buried interfaces. In the LFP/LiPON/Li stack, both the cathode/electrolyte interface and the LFP/current collector interface can contribute to polarization and to the loss of accessible capacity. A direct and specific chemical analysis of the LFP/LiPON interphase would require dedicated operando characterization (e.g., XPS or TEM) because LiPON and Li metal are highly sensitive to H_2O and CO_2. Such an interfacial study is outside the scope of this chapter, but the electrochemical response indicates that interfacial effects remain relevant even in sub-micrometer cells.

Post-cycling backscattered FE-SEM was used to examine how the multilayer morphology changed after electrochemical operation. In the fresh cells (**Figure 5.4a-c**), the LFP cathode, LiPON electrolyte, Li anode, and Pt-coated substrate are clearly distinguishable. After cycling (**Figure 5.4d-f**), the stack shows localized morphological changes, especially near the lower part of the electrolyte/cathode interface, where roughening is observed in the SE. Nevertheless, the LiPON layer remains largely continuous in most analyzed regions and the layered architecture is still recognizable. These observations indicate that cycling may modify the buried interfaces locally, but the overall LFP/LiPON/Li structure remains mechanically preserved over the tested conditions.

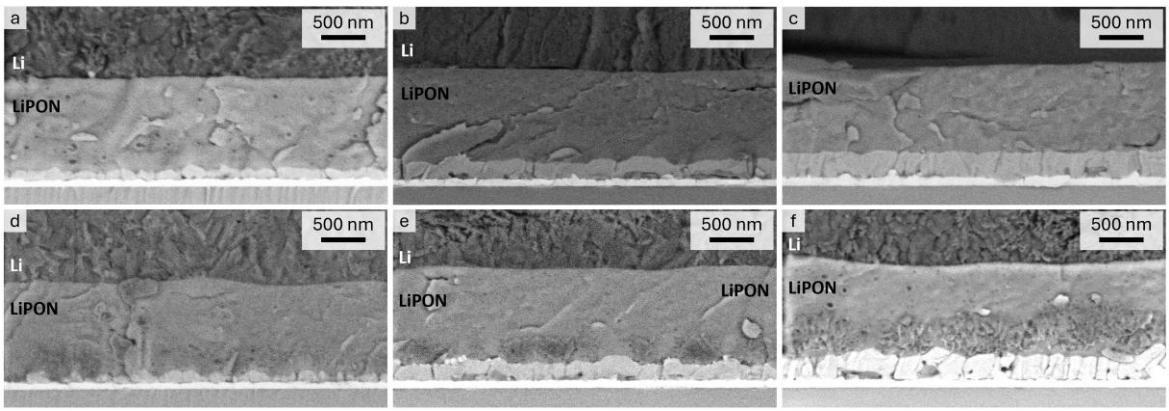


Figure 5.4 - FE-SEM images with ESB detector showing LFP/LiPON interfaces (a-c) before and (d-f) after many constant current cycles of charge-discharge.

The temperature dependence of the LFP (200 nm)/LiPON/Li cell response was evaluated using an active area of 0.79 mm^2 (**Figure 5.5**). Raising the operating temperature to 50 ºC markedly improves the delivered capacity at all tested currents. At 5 µA cm^{-2}, the cell reaches approximately ~100 mAh g^{-1}, almost twice the room-temperature value for comparable conditions. At 98 µA cm^{-2}, the device still delivers about ~46 mAh g^{-1}, roughly three times the capacity obtained at room temperature. This improvement is consistent with thermally activated ionic transport and faster interfacial kinetics in the multilayer stack.

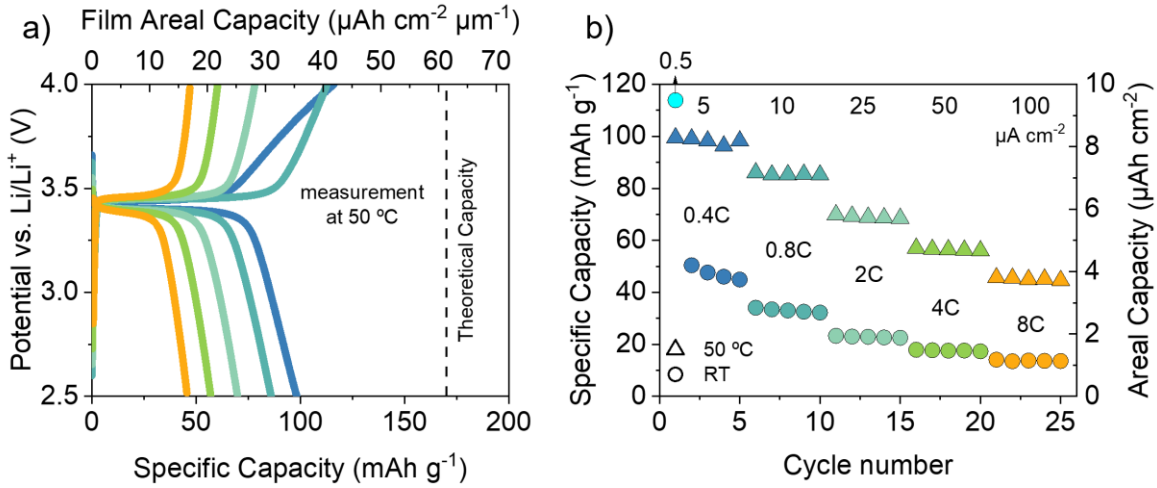


Figure 5.5 - (a) Charge and discharge cycles of LFP (200 nm)/LiPON/Li all-solid-state battery measured at 50 ºC. (b) Comparison of the specific capacity over the cycles at room temperature and 50ºC.

To quantify the degree of cathode utilization, the measured specific capacity at each C-rate was converted into an approximate active thickness (t_{active}). This estimate assumes that the nominal LFP layer is 200 nm thick and that full utilization would correspond to the theoretical capacity, 170 mAh g^{-1}. The effective thickness is therefore obtained by scaling the nominal thickness by the ratio between the measured and theoretical capacities:

$$t_{active} = \left(\frac{\text{Capacity}}{170\ \text{mAh g}^{-1}}\right) \times 200\ \text{nm} \quad (5.1)$$

The values obtained from this calculation are listed in **Table 5.1** for room-temperature and 50 ºC measurements.

Table 5.1 - Experimental discharge capacities and corresponding estimated active thicknesses for the 200 nm $LiFePO_4$ cathode in LFP/LiPON/Li cells measured at room temperature and at 50 ºC.

	RT		50 ºC	
Nominal C-rate	Capacity (mAh g^{-1})	t_{active} (nm)	Capacity (mAh g^{-1})	t_{active} (nm)
0.04C	114.1	134.2	-	-
0.4C	47.3	55.6	100.8	118.6
0.8C	33.2	39	87.6	103.1
2C	22.9	26.9	70.9	83.4
4C	17.6	20.7	58.0	68.3
8C	13.7	16.2	46.3	54.4

At room temperature, the largest capacity measured under very low current conditions, 114.1 mAh g^{-1} at approximately 0.04C, corresponds to an active thickness of about 134 nm. Increasing the current rapidly decreases this value: at 0.4C only about 56 nm are effectively accessed, and at 8C the value falls to approximately 16 nm. At 50 ºC, the same analysis gives significantly larger active thicknesses, with about 119 nm at 0.4C and 54 nm even at 8C. These values provide a simple quantitative picture of the inactive or poorly accessed fraction of the film under different kinetic conditions.

For comparison, an order-of-magnitude Li^+ diffusion length (L) was estimated with use of the relation below based on Fick's diffusion length equation: [115,161]

$$L \sim \sqrt{Dt} \quad (5.2)$$

where *D* is the average chemical diffusion coefficient obtained from cyclic voltammetry for our PLD-grown LFP film on Pt-coated substrate (2.8×10^{-12} cm^2 s^{-1}), and t is the nominal time of discharge. At 8C (450 s), this approximation gives a diffusion length of about 355 nm, which is larger than the nominal cathode thickness and much larger than the experimentally inferred active thickness. This discrepancy between L and t_{active} indicates that the real accessed mass fraction is not determined by diffusion length alone. The simplified diffusion-length estimate does not account for the anisotropic Li^+ migration in the olivine lattice,[67] the two-phase nature of LFP, or the blocking effect of misoriented grains and interfacial regions. In addition, the chemical diffusion coefficient is known to depend strongly on lithium concentration and phase fraction.[66,162] In the present polycrystalline films, Li^+ pathways are therefore expected to be interrupted by grain orientation mismatch promoted by the LFP/Pt interfacial region. This interpretation also explains why the

capacity drop is sharper when moving from low to intermediate rates than when moving from already high rates: once only a near-surface fraction of the cathode is active, the deeper inactive region contributes less to the additional rate-dependent loss.

Electrochemical impedance spectroscopy was used to analyze the resistive contributions of the LFP(200 nm)/LiPON/Li all-solid-state cell at room temperature and at 50 °C. The spectra were fitted with the equivalent circuit shown in **Figure 5.6a**, where R represents the resistive contributions, CPE denotes constant phase elements accounting for non-ideal capacitive behavior, and W corresponds to the Warburg element that describes the low-frequency diffusion-related contribution.

Two depressed semicircles can be distinguished in the high- and intermediate-frequency regions (**Figure 5.6b**). At room temperature, the area-normalized resistances are R_1 = 64.5 Ω cm^2 and R_2 = 194.2 Ω cm^2. Upon increasing the temperature to 50 °C, these values decrease to R_1 = 21.0 Ω.cm^2 and R_2 = 41.0 Ω.cm^2, respectively. This pronounced decrease indicates that the dominant impedance contributions are thermally activated. Based on the characteristic capacitances, time constants, and effective conductivities summarized in Tables **Tables 2** and **3**, the first semicircle ($R_1 \| CPE_1$) is assigned to the bulk ionic transport in LiPON, whereas the second ($R_2 \| CPE_2$) is attributed to the effective transport resistance within the LFP layer, including both ionic and electronic contributions, and possibly the influence of adjacent interfaces.

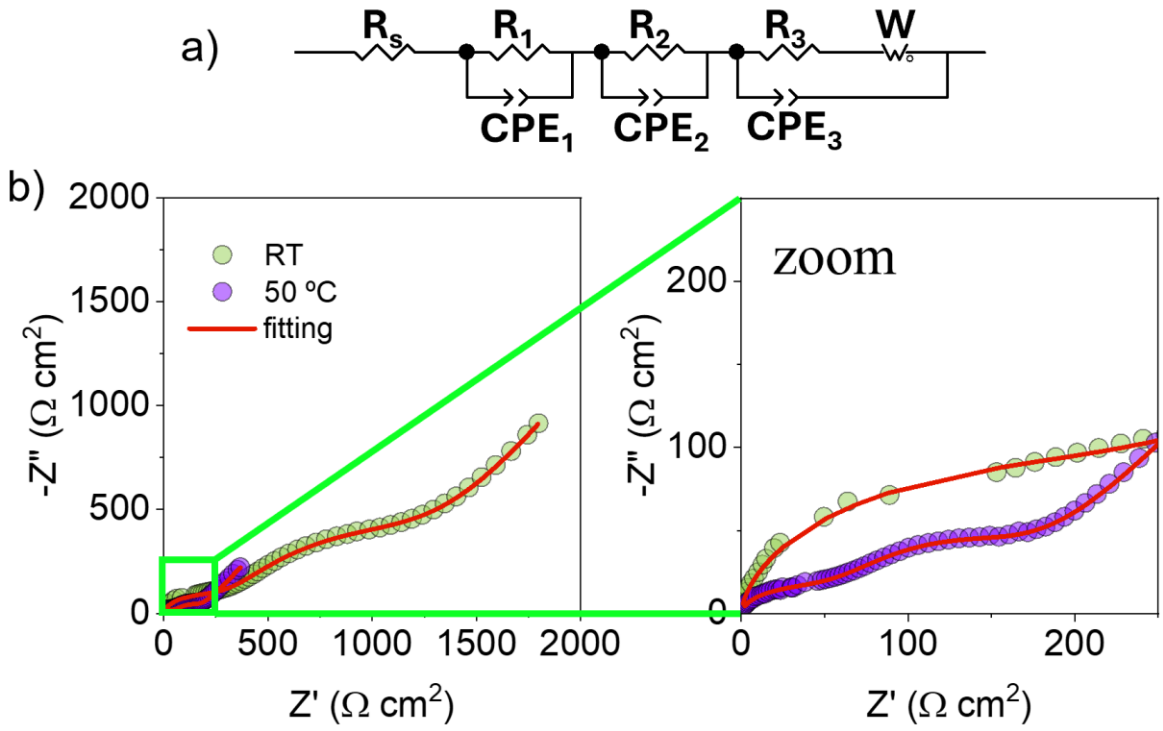


Figure 5.6 - (a) Equivalent circuit employed to fit the PEIS spectra of the LFP (200 nm)/LiPON/Li all-solid-state cell with electrochemically active area of 0.79 mm². (b) Experimental impedance data measured

at room temperature (RT) and 50 ºC together with the corresponding fits. (c) Enlarged view of the higher-frequency region.

The fitting parameters extracted at room temperature and 50 ºC are summarized in **Table 2**. The resistances were normalized by the active area of the cell (0.0079 cm^2), the fitting parameters extracted at room temperature and 50 ºC. The effective areal capacitances and time constants were calculated using the following equations:

$$C = (QR^{1-n})^{1/n} \tag{5.3}$$

$$\tau = RC \tag{5.4}$$

where Q and n are the CPE parameters, R is the corresponding area-normalized resistance, C is the effective areal capacitance, and τ is the characteristic time constant.

Table 5.2 - Area-normalized resistances (R), effective areal capacitances (C), and time constants (τ) derived from PEIS fitting of the LFP(200 nm)/LiPON/Li cell at room temperature and 50 ºC.

	RT			**50 ºC**		
	$R_1 \| CPE_1$	**$R_2 \| CPE_2$**	**$R_3 \| CPE_3$**	**$R_1 \| CPE_1$**	**$R_2 \| CPE_2$**	**$R_3 \| CPE_3$**
R (Ω cm^2)	64.5	194.2	689.7	21.0	41.0	116.0
C (F cm^{-2})	2.5×10^{-8}	1.5×10^{-7}	4.9×10^{-6}	2.9×10^{-8}	3.7×10^{-7}	8.1×10^{-6}
τ (s)	1.6×10^{-6}	2.9×10^{-5}	3.4×10^{-3}	6.1×10^{-7}	1.5×10^{-5}	9.4×10^{-4}

To assess whether the fitted resistances are compatible with the expected transport properties of the individual layers, approximate effective conductivities(σ_{eff}) were calculated assuming a parallel-plate geometry as follows in the equation derived from Ohm's Second Law:

$$\sigma_{eff} = \frac{l}{RA} \tag{5.5}$$

where l is the thickness of the corresponding layer (200 nm for LFP and 1000 nm for LiPON), R is the fitted resistance, and A is the electrochemically active area.

Because the fitted resistance of the second semi-circle may include coupled ionic/electronic transport, interfacial contributions, and possible microstructural limitations, rather than a purely ionic or purely electronic bulk transport resistance, the calculated value is treated as effective conductivity rather than intrinsic material constants. The resulting σ_{eff} values are summarized in **Table 5.3**.

Table 5.3 - Effective conductivities (σ_{eff}) estimated from the impedance resistive contributions at room temperature and 50 ºC.

Contribution	σ_{eff} at RT (S cm^{-1})	σ_{eff} at 50 ºC (S cm^{-1})
LiPON (R_1)	1.5×10^{-6}	4.7×10^{-6}
LFP (R_2)	1.0×10^{-7}	4.9×10^{-7}

To further validate the assignment of the high-frequency contribution, a Cu/LiPON(1 μm)/Li (2 μm) reference stack was measured by PEIS at room temperature using the same active area of 0.0079 cm^2. Although the measurement was collected from 2 MHz to 0.2 Hz, the fitting was restricted to the frequency range between 2 MHz and 56.96 Hz in order to avoid forcing the model to describe the strongly dispersive low-frequency electrode-polarization response. The selected region was fitted using an Rs + ($R_{LiPON} \| CPE_{LiPON}$) + ($R \| CPE$) equivalent circuit (**Figure 5.7**). In this model, the second contribution was included only to account for the onset of the low-frequency response. The second $R \| CPE$ was included to account for the low-frequency contribution; however, it was not used for quantitative interpretation of ionic transport in the LiPON layer. Therefore, the LiPON resistance was extracted exclusively from R_{LiPON}. The high-frequency contribution is well resolved, yielding R_{LiPON} = 7821 Ω or 61.8 Ω cm^2, with a relative fitting error below 1%. This resistance is therefore assigned to the LiPON electrolyte contribution. Assuming through-plane transport across the 1 μm-thick LiPON layer, the effective ionic conductivity is estimated as $\sigma_{eff} = 1.6 \times 10^{-6}$ S cm^{-1} at room temperature.

These values, R_{LiPON} = 61.8 Ω cm^2 and $\sigma_{eff} = 1.6 \times 10^{-6}$ S cm^{-1}, obtained for the Cu/LiPON/Li reference stack are in excellent agreement with the high-frequency R_1 contribution extracted from the complete LFP(200 nm)/LiPON/Li cell at room temperature, namely, 64.5 Ω cm^2 and 1.5×10^{-6} S cm^{-1}. This agreement confirms that the first semicircle observed in the complete cell is mainly associated with LiPON bulk ionic transport. Consequently, the additional intermediate-frequency contribution observed in the LFP/LiPON/Li cell can be assigned to the $LiFePO_4$ layer and/or adjacent interfacial processes.

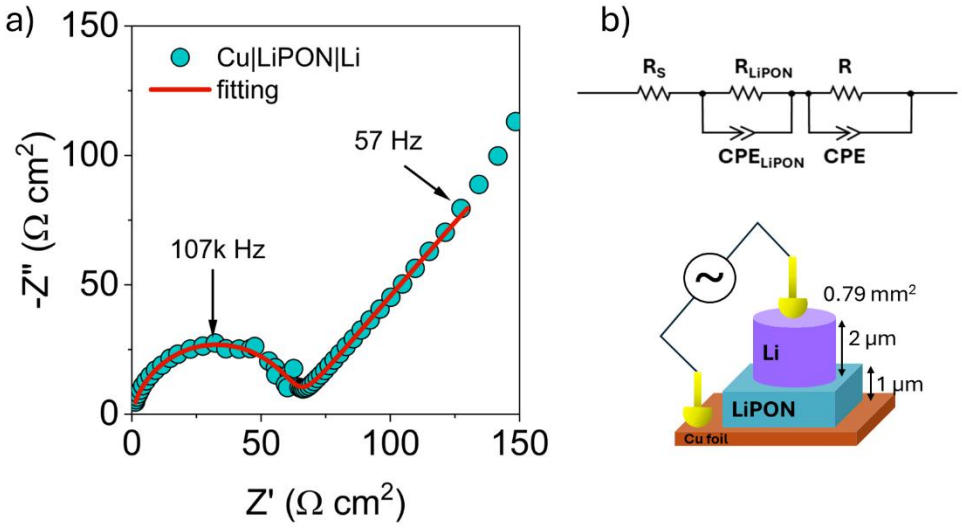


Figure 5.7 – (a) Room-temperature PEIS spectrum of the Cu/LiPON(1 µm)/Li stack and fitting result from 2 MHz to 57 Hz. (b) Equivalent circuit used for the fitting, Rs + (R1 ‖ CPE1) + (R2 ‖ CPE2), together with a schematic illustration of the reference stack and their contacts.

Overall, the impedance results are consistent with the galvanostatic data. Moderate heating substantially reduces the resistive contributions of the solid-state stack and increases cathode utilization. Although all resistances decrease at 50 °C, the LFP-related contribution remains the dominant limitation in the fitted spectra.

From the perspective of thin-film batteries for autonomous microsystems, this behavior is relevant because encapsulated devices can operate above room temperature and moderate heating is often used to reduce interfacial and transport losses in solid-state microbatteries. The 50 °C measurements therefore provide both mechanistic insight into the thermally activated limitations of the stack and a practical estimate of performance under slightly elevated operating temperature.

5.4 Electrochemical characterization of LFP/LATP/LiPON/Li all-solid-state thin-film battery

The electrochemical response of the LFP/LATP/LiPON/Li cells was investigated using a stack composed of approximately 250 nm LFP, 230 nm LATP, 1 µm LiPON, and Li metal (**Figure 5.8**). The active cell area was defined by the evaporated Li electrode, corresponding to 0.79 mm2². Since the voltage profiles show contributions beyond the main $LiFePO_4/FePO_4$ plateau, the electrochemical response is discussed in terms of areal capacity (µAh cm^{-2}) and apparent thickness-normalized areal capacity (µAh cm^{-2} μm^{-1}), rather than gravimetric capacity (mAh g^{-1}). This approach is more appropriate for this configuration because the accumulated charge cannot be assigned exclusively to the nominal LFP layer.

Figure 5.8a and **Figure 5.8b** show galvanostatic charge–discharge profiles obtained under fixed-current conditions but using different voltage windows. In **Figure 5.8a**, the cell was cycled at 0.05 µA, corresponding to 6.4 µA cm^{-2}, between cut-off voltage limits of 2.5 and 4.5 V. The first

three cycles were affected by unstable electrical contact in the setup and were therefore not considered in the graphic. From cycles 4 to 10, the profiles become more reproducible and display the characteristic plateau associated with the LiFePO4/$FePO_4$ redox reaction, together with an additional lower-voltage contribution mear 2.8 V. After stabilization, the discharge capacity remains nearly constant at approximately 5.7–5.8 μAh cm^{-2}, corresponding to an apparent thickness-normalized value of about 23 μAh cm^{-2} μm^{-1} when normalized by the nominal LFP thickness.

Figure 5.8b shows a second LFP/LATP/LiPON/Li cell cycled at 0.1 μA, corresponding to 12.8 μA cm^{-2}, between wider cut-off voltage limits of 2.0 and 4.5 V. In this case, only two cycles were recorded due to experimental time constraints. The broader voltage window activates a more pronounced low-voltage contribution, leading to higher apparent discharge capacities of approximately 10.2 and 9.6 μAh cm^{-2} in the first and second cycles, respectively. These values correspond to apparent thickness-normalized capacities of approximately 41 and 38 μAh cm^{-2} μm^{-1}. The higher capacity obtained in this voltage window, despite the higher applied current, confirms that the additional charge arises from electrochemical processes activated below 2.5 V, and therefore the values should not be interpreted as pure LFP capacity.

Although the full discharge capacity increases when the lower cut-off voltage is extended from 2.5 to 2.0 V, a more direct comparison of the LFP contribution can be obtained by considering only the discharge capacity accumulated down to 3.0 V, i.e., before the onset of the lower-voltage plateau. Under this criterion, the apparent thickness-normalized capacity associated mainly with the LFP plateau is approximately 7.6 μAh cm^{-2} μm^{-1} and 6.4 μAh cm^{-2} μm^{-1} for 6.4 μA cm^{-2} and 12.8 μA cm^{-2}. Therefore, when the current density is doubled, the LFP-related contribution decreases only moderately. These values are lower than those obtained for the LFP/LiPON/Li reference cells at comparable current densities. For the 200 nm LFP/LiPON/Li configuration, the capacity at room temperature corresponds to approximately 17.0 and 12.0 μAh cm^{-2} μm^{-1} at 5 and 10 μA cm^{-2}, respectively. This comparison suggests that the insertion of the LATP interlayer and the associated LFP/LATP interface reduce the effective utilization of the LFP material, even though the broader voltage window activates additional low-voltage capacity. Therefore, the larger total capacity observed in the 2.0–4.5 V experiment should not be interpreted as improved LFP utilization, but rather as the superposition of the LFP response with additional electrochemical processes occurring below 3.0 V.

To further evaluate the current-density dependence of this more complex response, a third cell was cycled between 2.0 and 4.0 V using stepwise current densities from 2 to 100 μA cm^{-2}, followed by a return to 5 μA cm^{-2}. Representative charge–discharge profiles are shown in **Figure 5.8c**, while the corresponding capacity evolution is summarized in **Figure 5.8d**. Several cycles were affected by unstable electrical contact, particularly cycles 5, 6–10, and 32–35, and were therefore excluded from the graphic. Although this instability is likely related to contact issues in the experimental setup, it may also reflect the higher complexity of this multilayer system, where the insertion/extraction process can involve not only the LFP cathode but also interfacial or LATP-derived phosphate phases.

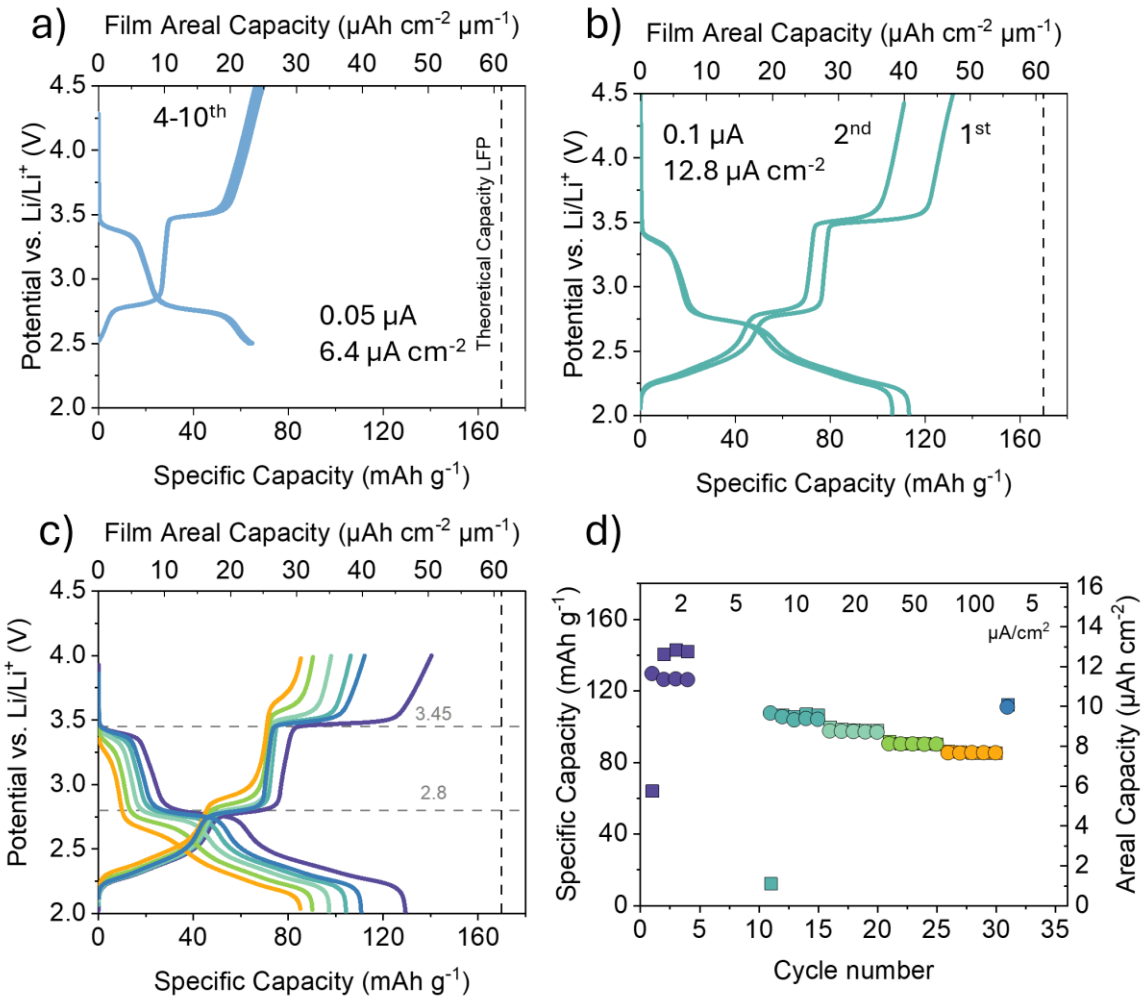


Figure 5.8 - Galvanostatic cycling of similar LFP/LATP/LiPON/Li all-solid-state thin-film cells. Charge–discharge profiles of the (a) first cell with fixed-current at 6.4 µA cm^{-2}, between 2.5 and 4.5 V, (b) second cell with fixed-current at 12.8 µA cm^{-2}, between 2.0 and 4.5 V and (c) third cell cycled between 2.0 and 4.0 V at increasing current densities from 2 to 100 µA cm^{-2}, followed by a return to 5 µA cm^{-2}. (d) Evolution of the apparent specific discharge capacity and apparent thickness-normalized discharge capacity as a function of cycle number.

Nevertheless, the stable cycles reveal a clear current-dependent response. The apparent areal discharge capacity decreases from approximately 11.4 µAh cm^{-2} at 2 µA cm^{-2} to 9.4, 8.7, 8.1, and 7.7 µAh cm^{-2} at 10, 20, 50, and 100 µA cm^{-2}, respectively. When the current density is returned to 5 µA cm^{-2}, the capacity partially recovers to approximately 10.0 µAh cm^{-2}, although only one reliable cycle was obtained in this final step. Expressed as apparent thickness-normalized values, these capacities correspond to approximately 45.7, 37.7, 34.9, 32.4, 30.6, and 39.8 µAh cm^{-2} µm^{-1}, respectively. These values are higher than those obtained for the simpler LFP/LiPON/Li cells at comparable current densities, indicating that the LFP/LATP-containing stack stores additional charge beyond the conventional LFP plateau. This behavior is consistent with the possible formation and electrochemical participation of Fe-containing phosphate or NASICON-type secondary phases

generated during stack fabrication and/or cycling. Therefore, the enhanced apparent capacity should not be interpreted as improved utilization of pristine LFP alone, but rather as evidence that the bilayer architecture introduces additional active redox contributions within the broader 2.0–4.0 V voltage window.

The voltage profiles consistently show a contribution near 3.4-3.5 V vs Li/Li^+, assigned to the Fe^{2+}/Fe^{3+} redox reaction in olivine $LiFePO_4$. However, the lower-voltage plateau observed near 2.7-2.8 V indicates the presence of additional electrochemically active processes. This feature is particularly relevant in the LFP/LATP-containing stack and may be related to Fe-containing NASICON-type phosphate phases formed at or near the LFP/LATP interface. Previous studies on LFP-LATP compatibility reported that secondary phases can form depending on atmosphere and thermal history, including $Li_2FeTi(PO_4)_3$, Fe-substituted LATP-type phases or orthorhombic $Li_{1+x}Fe_xTi_{2-x}(PO_4)_3$ ($1 < x < 2$) and consequently $AlPO_4$ under inert or reducing conditions,[81] while $Li_3Fe_2(PO_4)_3$-type phases are favored under more oxidative conditions.[83]

The assignment of the lower-voltage process is further supported by the work of Beaupain *et al.*, who investigated oxide solid-state battery cathodes based on co-sintered LATP–LFP composite tapes.[84] In that study, the cathode was not a thin-film stack but a porous composite cathode prepared by tape casting from a mixture of carbon-coated $LiFePO_4$ and LATP, followed by debinding and co-sintering under N_2 between 650 and 850 ºC. Electrochemical measurements were performed in Li-metal half-cells, using either a conventional liquid electrolyte configuration, with a Whatman glass-fiber separator infiltrated with 1 M $LiPF_6$ in EC/DEC, or a PEO-based polymer electrolyte separator. Importantly, the voltage window was extended down to 2.0 V to probe not only the LFP response, but also LATP and LATP–LFP reaction products. In this configuration, Beaupain *et al.* observed redox features at 2.75–2.78 V, which were attributed to Fe^{3+}/Fe^{2+} reactions in Fe-containing NASICON-type phases, comparable to $Li_3Fe_2(PO_4)_3$, while features below 2.4 V were assigned to $Ti^{4+/}Ti^{3+}$ redox activity in LATP-derived phases. Therefore, although the geometry and electrochemical setup differ from the present thin-film LFP/LATP/LiPON/Li cells, their results provide a useful reference for interpreting the additional low-voltage plateau as evidence of electrochemical contributions from interfacial or LATP-derived phosphate phases.

Overall, these measurements demonstrate that the LFP/LATP/LiPON/Li architecture is electrochemically active and can sustain reversible cycling over a range of current densities. However, the response is clearly more complex than that of the LFP/LiPON/Li reference cells. The presence of additional low-voltage plateaus, together with the sensitivity of the measurements to contact stability, indicates that these results should be considered as a preliminary proof-of-concept for the LFP/LATP/LiPON/Li configuration. Further cycling experiments, combined with post-mortem structural and chemical analyses, will be necessary to better understand the different contributions and limitations of the bilayers submitted to RTP process.

5.5 Conclusions

This chapter demonstrated the fabrication and electrochemical evaluation of complete all-solid-state thin-film batteries based on phosphate materials, connecting the individual LFP and LATP thin-film studies developed in the previous chapters with full multilayer device architectures. Two configurations were investigated: LFP/LiPON/Li cells, used as a reference all-solid-state platform to assess the behavior of PLD-grown carbon-free LFP cathodes, and LFP/LATP/LiPON/Li cells, designed to evaluate the incorporation of a NASICON-type LATP layer between the cathode and the LiPON electrolyte.

The LFP/LiPON/Li cells confirmed that PLD-grown LFP cathodes can be successfully integrated into solid-state thin-film batteries while preserving the characteristic electrochemical response of olivine LFP. For cathode thicknesses between 120 and 300 nm, the voltage profiles displayed the expected plateau near 3.45 V vs. Li/Li^+, associated with the Fe^{2+}/Fe^{3+} redox couple, without clear additional plateaus from lower-voltage iron phosphate impurity phases. This result confirms that the main electrochemically active phase in the solid-state cells is $LiFePO_4$, in agreement with the structural characterization discussed in Chapter 3.

The comparison between cathode thicknesses revealed a clear trade-off between areal capacity and rate capability. The thinnest 120 nm cathode showed better stability at high current density and partial capacity recovery when the current was reduced, indicating that the capacity loss is mainly kinetic. The 200 nm cathode provided a balanced response, with comparable low-current specific capacity and more representative behavior for temperature-dependent and impedance studies. The 300 nm cathode stored the highest areal charge at very low current density, but required long discharge times and exhibited stronger rate limitations. These results show that increasing the LFP thickness increases the amount of active material available at low rate, but also amplifies the limitations associated with the low intrinsic ionic and electronic conductivities of carbon-free LFP.

Although the thin-film geometry reduces transport distances, the accessible capacity remained below the theoretical value of $LiFePO_4$. The analysis of the effective active thickness showed that, for the 200 nm cathode at room temperature, only about 134 nm were accessed under very low-current conditions, decreasing to approximately 56 nm at 0.4C and 16 nm at 8C. This limited utilization cannot be explained by diffusion length alone, since the estimated Li^+ diffusion length at 8C is larger than the nominal cathode thickness. Instead, the results indicate that cathode utilization is controlled by a combination of phase-boundary kinetics, anisotropic Li^+ transport in the olivine structure, grain-orientation mismatch in the polycrystalline film, and buried interfacial limitations. In particular, the $FePt_3$-containing region previously identified at the LFP/Pt interface likely reduces the accessible fraction of the cathode and contributes to the deviation from the theoretical capacity.

Temperature-dependent measurements provided further evidence that the dominant limitations are thermally activated. When the LFP(200 nm)/LiPON/Li cell was operated at 50 ºC, the delivered capacity increased markedly over the full current-density range. At 5 $\mu A\ cm^{-2}$, the

capacity reached approximately 100 mAh g^{-1}, while at 98 μA cm^{-2} the cell still delivered around 46 mAh g^{-1}. The corresponding active-thickness estimation showed that moderate heating substantially increases the accessible fraction of the cathode, reaching about 119 nm at 0.4C and 54 nm at 8C. Therefore, operation at slightly elevated temperature improves both transport and interfacial kinetics, leading to enhanced cathode utilization.

Electrochemical impedance spectroscopy supported this interpretation. The impedance response of the LFP(200 nm)/LiPON/Li cell showed two main semi-circles contributions. Even though all resistive contributions decreased at 50 ºC, the LFP-related resistance remained the dominant limitation, confirming that the cathode layer governs the overall performance of the LFP/LiPON/Li cells.

The LFP/LATP/LiPON/Li architecture was also shown to be electrochemically active, demonstrating the feasibility of integrating the RTP-treated LFP/LATP bilayer into a complete all-solid-state thin-film battery. The voltage profiles retained a contribution near 3.4–3.5 V vs. Li/Li^+ confirming that the LFP redox process remains accessible after LATP incorporation. However, the response became more complex than that of the LFP/LiPON/Li reference cells, with an additional plateau near 2.7–2.8 V and larger apparent capacities when the lower cut-off voltage was extended to 2.0 V. These low-voltage contributions are consistent with electrochemical activity from interfacial or LATP-derived Fe-containing phosphate phases, rather than with improved utilization of pristine LFP alone.

Consequently, the LFP/LATP/LiPON/Li results should be considered a preliminary proof-of-concept for the integration of LATP into phosphate-based all-solid-state thin-film batteries. The insertion of LATP preserves part of the LFP electrochemical response, but also introduces additional redox contributions and likely increases the complexity of the buried cathode/electrolyte interface. The apparent capacity enhancement observed in wider voltage windows must therefore be interpreted with caution, since it reflects the superposition of the LFP plateau with additional interfacial or LATP-derived processes.

Overall, this chapter confirms that phosphate-based thin films can be integrated into functional all-solid-state battery architectures, while also highlighting the central role of buried interfaces in determining electrochemical performance. The LFP/LiPON/Li system provides a useful reference platform for evaluating carbon-free PLD-grown LFP cathodes, showing stable cycling behavior, thermally activated capacity improvement, and clear impedance signatures associated with LiPON and LFP transport. The LFP/LATP/LiPON/Li configuration extends this approach toward all-phosphate cathode/electrolyte integration, but reveals that further optimization of LATP processing, interfacial stability, and post-mortem chemical analysis will be required. Future improvements should focus on suppressing LFP/current-collector reactions, optimizing cathode texture and grain orientation, and controlling the LFP/LATP interface in order to increase the accessible active fraction and advance phosphate-based all-solid-state thin-film batteries toward practical microbattery applications.

Chapter 6

Conclusions of the thesis

6 Conclusions of the thesis

The present thesis has addressed the development of phosphate-based thin films and their integration into all-solid-state lithium battery architectures. The work establishes a processing-performance relationship in which cathode crystallinity, current-collector chemistry, electrolyte transport, mechanical integrity and buried interfaces jointly determine the electrochemical response. The most relevant results and perspectives are summarized in the following.

The first relevant outcome is the successful deposition of electrochemically active, carbon-free LFP on ITO-coated substrates by PLD. This configuration was developed as an alternative to the route commonly adopted for PLD-grown LFP, where the cathode is deposited directly on metallic Pt-coated substrates under low-oxygen-activity, usins Ar protective atmospheres to preserve Fe^{2+} in the olivine structure. Although Pt is widely used as a current collector, the present results show that direct LFP/Pt contact promotes interfacial reactivity under the fabrication conditions, Fe-Pt alloying or intermetallic formation, and partial electrochemical blocking close to the substrate. The insertion of the ITO oxide interlayer mitigates these effects and increases the accessible cathode volume.

- The benefit of this interfacial strategy was quantified in aqueous three-electrode measurements. A 300 nm LFP film on Pt delivered about 92 mAh g^{-1} at 2 μA cm^{-2} (0.11 C), while a nearly 200 nm LFP film on ITO/Pt reached about 163 mAh g^{-1} at the same current density, close to the theoretical capacity of LFP. The apparent Li^+ diffusion coefficient also increased from approximately 2.8 x 10^{-12} cm^2 s^{-1} for the Pt-based reference to about 1.2 x 10^{-11} cm^2 s^{-1} for optimized LFP/ITO. These values are in the superior compared to the broad 10^{-14} to 10^{-12} cm^2 s^{-1} range values reported in the literature for LFP thin films.
- RTP was further demonstrated as a proof-of-concept route to activate films deposited at lower temperature while limiting the overall thermal budget. After short annealing at 700 ºC, the capacities of films deposited at 400 and 500 ºC increased to 118 and 148 mAh g^{-1} at 2 μA cm^{-2}, respectively, whereas the already optimized 600 ºC film decreased from 163 to 127 mAh g^{-1}. RTP is therefore most useful for under-crystallized films in the set of samples investigated.

The second contribution is the development of LATP thin films as NASICON-type phosphate solid electrolytes compatible with LFP deposition conditions. Since high-temperature oxidative growth, although effective for crystallizing standalone LATP, is not directly compatible with LFP cathodes, this thesis established a low-temperature PLD route followed by short RTP treatments to decouple film deposition from electrolyte crystallization.

- In-plane PEIS showed that as-deposited LATP films at 300 ºC were poorly conducting, with room-temperature conductivities around 10^{-11} S cm^{-1}, whereas RTP increased the conductivity of 250-730nm layers to the 10^{-7} S cm^{-1}, by exposing the samples for short 1s

dwell-time at 800 - 900ºC, in both Ar or O_2 low pressure atmospheres. The achieved conductivities approach to the values of as-deposited LATP thin films at 700 ºC and are also in the order of magnitude of LiPON solid electrolyte. In this thesis, it demonstrated a route to promote LATP Li^+ transport under thermal conditions compatible with LFP/LATP integration.

- The principal limitation of this route is pointed to the mechanical continuity rather than ionic transport alone. RTP promotes densification and crystallization of LATP deposited on LFP cathode, but it also widens pre-existing cracks, which can interrupt lateral percolation and may become leakage paths for Li dendrites in cross-plane devices. Nevertheless, sequential LFP/LATP bilayers remained active, after low-temperature LATP deposition and short RTP treatment at 800 ºC for 60s in Ar, the bilayer delivered 113 mAh g^{-1} at 0.5 μA cm^{-2}, about 0.02 C for the 420 nm LFP film, confirming that the LFP/LATP interface can remain functional after processing.

The transfer from materials to complete all-solid-state thin-film cells was successful and confirmed both the potential and the limitations of the proposed architectures.

- LFP/LiPON/Li cells, with 120 and 200 nm LFP cathodes at room temperature, delivered specific capacities of 60 mAh g^{-1} at 2 μA cm^{-2}, corresponding to about 2.7 and 4.5 μAh cm^{-2}, respectively. By contrast, the thicker 300 nm cathode provided the highest areal charge storage, reaching approximately 6 μAh cm^{-2}, although with a lower specific capacity of about 56 mAh g^{-1} at 0.5 μA cm^{-2}. This comparison evidences the classical trade-off imposed by cathode thickness in pure LFP dense thin-films. As demonstrated in the half-cell studies, replacing the direct LFP/Pt contact with an ITO-coated current collector markedly improves the utilization of the LFP volume, indicating that substrate/interface engineering is an effective route to increase the capacity of dense LFP thin-film cathodes.
- The temperature-dependent response of the 200 nm LFP/LiPON/Li cell further confirmed the thermally activated nature of the limiting processes in dense carbon-free LFP cathodes. At 5 μA cm^{-2} (0.4 C) the discharge capacity increased from 47 mAh g^{-1} at room temperature to 100 mAh g^{-1} (7.2 μAh cm^{-2}) at 50 ºC. This improvement indicates that moderate heating facilitates Li^+ transport and interfacial charge-transfer kinetics within the LFP/LiPON/Li stack, while preserving the functionality of LiPON.
- LFP/LATP/LiPON/Li architecture further demonstrated that a NASICON-type phosphate layer can be incorporated on the cathode side of an all-solid-state thin-film battery. Its highest apparent areal capacity was about 11.4 μAh cm^{-2} at 2 μA cm^{-2} (0.13 C) for a 250 nm-thick LFP, when cycled between 2.0 and 4.0 V. However, the additional plateau near 2.7-2.8 V indicates that part of this capacity arises from interfacial or LATP-derived Fe-containing phosphate phases. LATP integration should therefore be understood as a functional but chemically active interface, rather than as the simple insertion of an inert electrolyte layer.

Overall, the thesis establishes a quantitative processing-performance framework for phosphate-based thin-film batteries: LFP performance is governed by current-collector chemistry, cathode thickness, crystallinity and interfacial stability; LATP performance by the compromise between crystallization, conductivity and crack formation; and full-cell operation by the combined stability of LiPON and the chemically active LATP cathode-side interlayer. The evidence obtained in this thesis points to several relevant directions.

For LFP thin films, future work should systematically decouple deposition temperature from RTP or other fast/ultrafast post-treatments, determining how thermal energy penetrates through films of different thicknesses and how it modifies crystallization, surface chemistry, interfacial reactivity and charge-transfer resistance in final all-solid-state devices. Such studies would define practical thickness limits for dense LFP cathodes deposited on ITO substrates, which are significant better for this material than Pt.

Similarly, the LATP fabrication process should be optimized to retain the conductivity gains achieved by RTP while suppressing defects in thicker layers. Multistep deposition, thinner repeated layers, graded compositions, controlled cooling and stress-relief steps are particularly relevant strategies. At the same time, the present results show that even defective LATP can remain functional as a LiPON-assisted cathode-side interlayer after reaction with LFP, making the LFP/LATP interface an active object of study rather than only a degradation site.

A particularly promising perspective is the engineering of structured phosphate composites. Since Li^+ transport in olivine LFP is intrinsically anisotropic and mainly one-dimensional, dense planar films supplied only from the top electrolyte are geometrically limited. Architectures based on LATP pillars, lateral ionic pathways or interpenetrating LFP/LATP networks could provide Li^+ access from multiple directions and reduce the effective diffusion length. Combined theoretical modelling with in-plane and cross-plane measurements would directly test how phosphate solid-electrolyte structuring modifies transport in thin LFP cathodes.

The most realistic route toward improved devices is therefore the rational combination of complementary electrolytes and interfaces: LATP at the cathode side to provide a crystalline phosphate pathway, LiPON at the anode side to maintain stable contact with Li metal, and diffusion-barrier current collectors such as ITO to suppress LFP/Pt reactions. This hybrid architecture offers a promising basis for safer and more sustainable LFP-based thin-film microbatteries.

References

(1) Whang, G.; Chen, R.; Yu, J. T. T.; Choi, C.; McNeil, P.; Chaillou, J.; Loyez, C.; Lethien, C.; Dunn, B. Do Micropower Sources Meet the Needs of the Internet of Things? *Adv. Energy Mater.* **2025**, *03921*, 1–19. https://doi.org/10.1002/aenm.202503921.

(2) Xia, Q.; Zan, F.; Zhang, Q.; Liu, W.; Li, Q.; He, Y.; Hua, J.; Liu, J.; Xu, J.; Wang, J.; Wu, C.; Xia, H. All-Solid-State Thin Film Lithium/Lithium-Ion Microbatteries for Powering the Internet of Things. *Advanced Materials* **2023**, *35* (2), 2200538. https://doi.org/10.1002/adma.202200538.

(3) Janek, J.; Zeier, W. G. A Solid Future for Battery Development. *Nat. Energy* **2016**, *1* (9), 16141. https://doi.org/10.1038/nenergy.2016.141.

(4) Mauger, A.; Julien, C. M. Critical Review on Lithium-Ion Batteries: Are They Safe? Sustainable? *Ionics (Kiel).* **2017**, *23* (8), 1933–1947. https://doi.org/10.1007/s11581-017-2177-8.

(5) Mauger, A.; Julien, C. M.; Paolella, A.; Armand, M.; Zaghib, K. Building Better Batteries in the Solid State: A Review. *Materials* **2019**, *12* (23), 1–86. https://doi.org/10.3390/ma122333892.

(6) Waldmann, T.; Wilka, M.; Kasper, M.; Fleischhammer, M.; Wohlfahrt-Mehrens, M. Temperature Dependent Ageing Mechanisms in Lithium-Ion Batteries - A Post-Mortem Study. *J. Power Sources* **2014**, *262*, 129–135. https://doi.org/10.1016/j.jpowsour.2014.03.112.

(7) Armand, M.; Tarascon, J.-M. Building Better Batteries. *Nature* **2008**, *451*, 652–657. https://doi.org/10.1038/451652a.

(8) Goodenough, J. B.; Kim, Y. Challenges for Rechargeable Li Batteries. *Chemistry of Materials* **2010**, *22* (3), 587–603. https://doi.org/10.1021/cm901452z.

(9) Zhu, Y.; Gonzalez-Rosillo, J. C.; Balaish, M.; Hood, Z. D.; Kim, K. J.; Rupp, J. L. M. Lithium-Film Ceramics for Solid-State Lithionic Devices. *Nat. Rev. Mater.* **2021**, *6* (4), 313–331. https://doi.org/10.1038/s41578-020-00261-0.

(10) Famprikis, T.; Canepa, P.; Dawson, J. A.; Islam, M. S.; Masquelier, C. Fundamentals of Inorganic Solid-State Electrolytes for Batteries. *Nat. Mater.* **2019**, *18* (12), 1278–1291. https://doi.org/10.1038/s41563-019-0431-3.

(11) Randau, S.; Weber, D. A.; Kötz, O.; Koerver, R.; Braun, P.; Weber, A.; Ivers-Tiffée, E.; Adermann, T.; Kulisch, J.; Zeier, W. G.; Richter, F. H.; Janek, J. Benchmarking the Performance of All-Solid-State Lithium Batteries. *Nat. Energy* **2020**, *5* (3), 259–270. https://doi.org/10.1038/s41560-020-0565-1.

(12) Moitzheim, S.; Put, B.; Vereecken, P. M. Advances in 3D Thin-Film Li-Ion Batteries. *Adv. Mater. Interfaces* **2019**, *6* (15), 1–17. https://doi.org/10.1002/admi.201900805.

(13) Maier, J. Size Effects on Mass Transport and Storage in Lithium Batteries. *J. Power Sources* **2007**, *174* (2), 569–574. https://doi.org/10.1016/j.jpowsour.2007.06.246.

(14) Padhi, A. K.; Nanjundaswamy, K. S.; Goodenough, J. B. Phospho-Olivines as Positive-Electrode Materials for Rechargeable Lithium Batteries. *J. Electrochem. Soc.* **1997**, *144* (4), 1188–1194.

(15) Padhi, A. K.; Nanjundaswamy, K. S.; Masquelier, C.; Okada, S.; Goodenough, J. B. Effect of Structure on the Fe3 + / Fe2 + Redox Couple in Iron Phosphates. *J. Electrochem. Soc.* **1997**, *144* (5), 1609–1613. https://doi.org/10.1149/1.1837649.

(16) Morgan, D.; Van der Ven, A.; Ceder, G. Li Conductivity in LixMPO4 (M = Mn, Fe, Co, Ni) Olivine Materials. *Electrochemical and Solid-State Letters* **2004**, *7* (2), 2003–2005. https://doi.org/10.1149/1.1633511.

(17) Chung, S. Y.; Bloking, J. T.; Chiang, Y. M. Electronically Conductive Phospho-Olivines as Lithium Storage Electrodes. *Nat. Mater.* **2002**, *1* (2), 123–128. https://doi.org/10.1038/nmat732.

(18) Arbi, K.; Bucheli, W.; Jiménez, R.; Sanz, J. High Lithium Ion Conducting Solid Electrolytes Based on NASICON Li 1+x Al x M 2−x (PO 4) 3 Materials (M = Ti, Ge and $0 \leq x \leq 0.5$). *J. Eur. Ceram. Soc.* **2015**, *35* (5), 1477–1484. https://doi.org/10.1016/j.jeurceramsoc.2014.11.023.

(19) Siller, V. Thin Film Based All-Solid-State Lithium-Ion Batteries and Operando Characterization Methods. **2021**.

(20) Christen, T.; Carlen, M. W. Theory of Ragone Plots. *J. Power Sources* **2000**, *91* (2), 210–216. https://doi.org/10.1016/S0378-7753(00)00474-2.

(21) Van den Bossche, P.; Vergels, F.; Van Mierlo, J.; Matheys, J.; Van Autenboer, W. SUBAT: An Assessment of Sustainable Battery Technology. *J. Power Sources* **2006**, *162* (2 SPEC. ISS.), 913–919. https://doi.org/10.1016/j.jpowsour.2005.07.039.

(22) Simon, P.; Gogotsi, Y. Materials for Electrochemical Capacitors. *Materials for Sustainable Energy: A Collection of Peer-Reviewed Research and Review Articles from Nature Publishing Group* **2010**, 138–147. https://doi.org/10.1142/9789814317665_0021.

(23) Yang, X.; Rogach, A. L. Electrochemical Techniques in Battery Research: A Tutorial for Nonelectrochemists. *Adv. Energy Mater.* **2019**, *9* (25), 1–10. https://doi.org/10.1002/aenm.201900747.

(24) Goodenough, J. B.; Park, K. S. The Li-Ion Rechargeable Battery: A Perspective. *J. Am. Chem. Soc.* **2013**, *135* (4), 1167–1176. https://doi.org/10.1021/ja3091438.

(25) Kurzweil, P. Gaston Planté and His Invention of the Lead-Acid Battery-The Genesis of the First Practical Rechargeable Battery. *J. Power Sources* **2010**, *195* (14), 4424–4434. https://doi.org/10.1016/j.jpowsour.2009.12.126.

(26) Morioka, Y.; Narukawa, S.; Itou, T. State-of-the-Art of Alkaline Rechargeable Batteries. *J. Power Sources* **2001**, *100* (1–2), 107–116. https://doi.org/10.1016/S0378-7753(01)00888-6.

(27) The Nobel Prize in Chemistry 2019. NobelPrize.Org. Nobel Prize Outreach AB. Https://Www.Nobelprize.Org/Prizes/Chemistry/2019/Summary/.

(28) Xie, J.; Lu, Y. C. A Retrospective on Lithium-Ion Batteries. *Nature Communications*. Nature Research December 1, 2020. https://doi.org/10.1038/s41467-020-16259-9.

(29) Janek, J.; Zeier, W. G. A Solid Future for Battery Development. *Nat. Energy* **2016**, *1* (9), 16141. https://doi.org/10.1038/nenergy.2016.141.

(30) Gray, F. M. *POLYMER ELECTROLYTES*; Connor, J. A., Ed.; RSC Materials Monographs; Royal Society of Chemistry: United Kingdom, 1997.

(31) Schmaltz, T.; Hartmann, F.; Wicke, T.; Weymann, L.; Neef, C.; Janek, J. A Roadmap for Solid-State Batteries. *Adv. Energy Mater.* **2023**, *13* (43). https://doi.org/10.1002/aenm.202301886.

(32) Li, C.; Wang, Z. yu; He, Z. jiang; Li, Y. jiao; Mao, J.; Dai, K. hua; Yan, C.; Zheng, J. chao. An Advance Review of Solid-State Battery: Challenges, Progress and Prospects. *Sustainable Materials and Technologies* **2021**, *29* (May), e00297. https://doi.org/10.1016/j.susmat.2021.e00297.

(33) Whittingham, M. S. Electrical Energy Storage and Intercalation Chemistry. *Science (1979).* **1976**, *192* (4244), 1126–1127. https://doi.org/10.1126/science.192.4244.1126.

(34) Mizushima, K.; Jones, P. C.; Wiseman, P. J.; Goodenough, J. B. LixCoO2 (0<x<-1): A New Cathode Material for Batteries of High Energy Density. *Mater. Res. Bull.* **1980**, *15* (6), 783–789. https://doi.org/10.1016/0025-5408(80)90012-4.

(35) Yoshino, A., Sanechika, K., & Nakajima, T. Secondary Battery. US 4,668,595, 1987.

(36) Newman, J.; Thomas-Alyea, K. E. *Electrochemical Systems*, 3rd ed.; Wiley-Interscience: Hoboken, NJ, USA, 2004.

(37) Balaish, M.; Gonzalez-Rosillo, J. C.; Kim, K. J.; Zhu, Y.; Hood, Z. D.; Rupp, J. L. M. Processing Thin but Robust Electrolytes for Solid-State Batteries. *Nat. Energy* **2021**.

(38) Kim, K. J.; Balaish, M.; Wadaguchi, M.; Kong, L.; Rupp, J. L. M. Solid-State Li–Metal Batteries: Challenges and Horizons of Oxide and Sulfide Solid Electrolytes and Their Interfaces. *Adv. Energy Mater.* **2021**, *11* (1), 1–63. https://doi.org/10.1002/aenm.202002689.

(39) Alsaç, E. P.; Nelson, D. L.; Yoon, S. G.; Cavallaro, K. A.; Wang, C.; Sandoval, S. E.; Eze, U. D.; Jeong, W. J.; McDowell, M. T. Characterizing Electrode Materials and Interfaces in Solid-State Batteries. *Chem. Rev.* **2025**, *125* (4), 2009–2119. https://doi.org/10.1021/acs.chemrev.4c00584.

(40) Lin, D.; Liu, Y.; Cui, Y. Reviving the Lithium Metal Anode for High-Energy Batteries. *Nature Nanotechnology*. Nature Publishing Group March 7, 2017, pp 194–206. https://doi.org/10.1038/nnano.2017.16.

(41) Khan, M.; Yan, S.; Ali, M.; Mahmood, F.; Zheng, Y.; Li, G.; Liu, J.; Song, X.; Wang, Y. Innovative Solutions for High-Performance Silicon Anodes in Lithium-Ion Batteries: Overcoming Challenges and Real-World Applications. *Nano-Micro Letters*. Springer Science and Business Media B.V. December 1, 2024. https://doi.org/10.1007/s40820-024-01388-3.

(42) Yan, W.; Mu, Z.; Wang, Z.; Huang, Y.; Wu, D.; Lu, P.; Lu, J.; Xu, J.; Wu, Y.; Ma, T.; Yang, M.; Zhu, X.; Xia, Y.; Shi, S.; Chen, L.; Li, H.; Wu, F. Hard-Carbon-Stabilized Li–Si Anodes for High-Performance All-Solid-State Li-Ion Batteries. *Nat. Energy* **2023**, *8* (8), 800–813. https://doi.org/10.1038/s41560-023-01279-8.

(43) Richards, W. D.; Miara, L. J.; Wang, Y.; Kim, J. C.; Ceder, G. Interface Stability in Solid-State Batteries. *Chemistry of Materials* **2016**, *28* (1), 266–273. https://doi.org/10.1021/acs.chemmater.5b04082.

(44) Murugan, R.; Thangadurai, V.; Weppner, W. Fast Lithium Ion Conduction in Garnet-Type Li 7 La 3 Zr 2 O 12. *Angew. Chem. Int. Ed.* **2007**, *46* (41), 7778–7781. https://doi.org/10.1002/anie.200701144.

(45) Inaguma, Y.; Liquan, C.; Itoh, M.; Nakamura, T.; Uchida, T.; Ikuta, H.; Wakihara, M. High Ionic Conductivity in Lithium Lanthanum Titanate. *Solid State Commun.* **1993**, *86* (10), 689–693. https://doi.org/10.1016/0038-1098(93)90841-A.

(46) Bachman, J. C.; Muy, S.; Grimaud, A.; Chang, H.-H.; Pour, N.; Lux, S. F.; Paschos, O.; Maglia, F.; Lupart, S.; Lamp, P.; Giordano, L.; Shao-Horn, Y. Inorganic Solid-State Electrolytes for Lithium Batteries: Mechanisms and Properties Governing Ion Conduction. *Chem. Rev.* **2016**, *116* (1), 140–162. https://doi.org/10.1021/acs.chemrev.5b00563.

(47) Xiao, W.; Wang, J.; Fan, L.; Zhang, J.; Li, X. Recent Advances in Li1+xAlxTi2−x(PO4)3 Solid-State Electrolyte for Safe Lithium Batteries. *Energy Storage Mater.* **2019**, *19* (August 2018), 379–400. https://doi.org/10.1016/j.ensm.2018.10.012.

(48) Kamaya, N.; Homma, K.; Yamakawa, Y.; Hirayama, M.; Kanno, R.; Yonemura, M.; Kamiyama, T.; Kato, Y.; Hama, S.; Kawamoto, K.; Mitsui, A. A Lithium Superionic Conductor. *Nat. Mater.* **2011**, *10* (9), 682–686. https://doi.org/10.1038/nmat3066.

(49) Asano, T.; Sakai, A.; Ouchi, S.; Sakaida, M.; Miyazaki, A.; Hasegawa, S. Solid Halide Electrolytes with High Lithium-Ion Conductivity for Application in 4 V Class Bulk-Type All-Solid-State Batteries. *Advanced Materials* **2018**, *30* (44), 1–7. https://doi.org/10.1002/adma.201803075.

(50) Boaretto, N.; Garbayo, I.; Valiyaveettil-SobhanRaj, S.; Quintela, A.; Li, C.; Casas-Cabanas, M.; Aguesse, F. Lithium Solid-State Batteries: State-of-the-Art and Challenges for Materials, Interfaces and Processing. *J. Power Sources* **2021**, *502* (November 2020). https://doi.org/10.1016/j.jpowsour.2021.229919.

(51) Bates, J. B.; Dudney, N. J.; Gruzalski, G. R.; Zuhr, R. A.; Choudhury, A.; Luck, C. F.; Robertson, J. D. Fabrication and Characterization of Amorphous Lithium Electrolyte Thin Films and Rechargeable Thin-Film Batteries. *J. Power Sources* **1993**, *43* (1–3), 103–110. https://doi.org/10.1016/0378-7753(93)80106-Y.

(52) Bates, J. B.; Dudney, N. J.; Gruzalski, G. R.; Zuhr, R. A.; Choudhury, A.; Luck, C. F.; Robertson, J. D. Electrical Properties of Amorphous Lithium Electrolyte Thin Films. *Solid State Ion.* **1992**, *53–56* (part 1), 647–654. https://doi.org/10.1016/0167-2738(92)90442-R.

(53) Qi, Z.; Wang, H. Advanced Thin Film Cathodes for Lithium Ion Batteries. *Research* **2020**, *2020*. https://doi.org/10.34133/2020/2969510.

(54) Mizushima, K.; Jones, P. C.; Wiseman, P. J.; Goodenough, J. B. LixCoO2 (0<x<-1): A New Cathode Material for Batteries of High Energy Density. *Mater. Res. Bull.* **1980**, *15* (6), 783–789. https://doi.org/10.1016/0025-5408(80)90012-4.

(55) Li, W.; Erickson, E. M.; Manthiram, A. High-Nickel Layered Oxide Cathodes for Lithium-Based Automotive Batteries. *Nat. Energy* **2020**, *5* (1), 26–34. https://doi.org/10.1038/s41560-019-0513-0.

(56) Manthiram, A.; Chemelewski, K.; Lee, E.-S. A Perspective on the High-Voltage LiMn1.5Ni0.5O4 Spinel Cathode for Lithium-Ion Batteries. *Energy Environ. Sci.* **2014**, *7* (4), 1339. https://doi.org/10.1039/c3ee42981d.

(57) Goodenough, J. B.; Hong, H. Y.-P.; Kafalas, J. A. Fast Na+-Ion Transport in Skeleton Structures. *Mater. Res. Bull.* **1976**, *11* (2), 203–220. https://doi.org/10.1016/0025-5408(76)90077-5.

(58) Aono, H.; Sugimoto, E.; Sadaoka, Y.; Imanaka, N.; Adachi, G. Ionic Conductivity of Solid Electrolytes Based on Lithium Titanium Phosphate. *J. Electrochem. Soc.* **1990**, *137* (4), 1023–1027. https://doi.org/10.1149/1.2086597.

(59) Lang, B.; Ziebarth, B.; Elsässer, C. Lithium Ion Conduction in LiTi2(PO4)3 and Related Compounds Based on the NASICON Structure: A First-Principles Study. *Chemistry of Materials* **2015**, *27* (14), 5040–5048. https://doi.org/10.1021/acs.chemmater.5b01582.

(60) Monchak, M.; Hupfer, T.; Senyshyn, A.; Boysen, H.; Chernyshov, D.; Hansen, T.; Schell, K. G.; Bucharsky, E. C.; Hoffmann, M. J.; Ehrenberg, H. Lithium Diffusion Pathway in Li1.3Al0.3Ti1.7(PO4)3 (LATP) Superionic Conductor. *Inorg. Chem.* **2016**, *55* (6), 2941–2945. https://doi.org/10.1021/acs.inorgchem.5b02821.

(61) Rettenwander, D.; Welzl, A.; Pristat, S.; Tietz, F.; Taibl, S.; Redhammer, G. J.; Fleig, J. A Microcontact Impedance Study on NASICON-Type Li1+xAlxTi2-x(PO4)3 ($0 \leq x \leq 0.5$) Single Crystals. *J. Mater. Chem. A Mater.* **2016**, *4* (4), 1506–1513. https://doi.org/10.1039/C5TA08545D.

(62) Mariappan, C. R.; Gellert, M.; Yada, C.; Rosciano, F.; Roling, B. Grain Boundary Resistance of Fast Lithium Ion Conductors: Comparison between a Lithium-Ion Conductive Li-Al-Ti-P-O-Type Glass Ceramic and a Li 1.5Al0.5Ge1.5P3O12 Ceramic. *Electrochem. commun.* **2012**, *14* (1), 25–28. https://doi.org/10.1016/j.elecom.2011.10.022.

(63) Hupfer, T.; Bucharsky, E. C.; Schell, K. G.; Senyshyn, A.; Monchak, M.; Hoffmann, M. J.; Ehrenberg, H. Evolution of Microstructure and Its Relation to Ionic Conductivity in Li1+xAlxTi2-x(PO4)3. *Solid State Ion.* **2016**, *288*, 235–239. https://doi.org/10.1016/j.ssi.2016.01.036.

(64) Giarola, M.; Sanson, A.; Tietz, F.; Pristat, S.; Dashjav, E.; Rettenwander, D.; Redhammer, G. J.; Mariotto, G. Structure and Vibrational Dynamics of NASICON-Type LiTi2(PO4)3. *Journal of Physical Chemistry C* **2017**, *121* (7), 3697–3706. https://doi.org/10.1021/acs.jpcc.6b11067.

(65) Siller, V.; Morata, A.; Eroles, M. N.; Arenal, R.; Gonzalez-Rosillo, J. C.; López del Amo, J. M.; Tarancón, A. High Performance LATP Thin Film Electrolytes for All-Solid-State Microbattery Applications. *J. Mater. Chem. A Mater.* **2021**, *9* (33), 17760–17769. https://doi.org/10.1039/d1ta02991f.

(66) Tang, M.; Belak, J. F.; Dorr, M. R. Anisotropic Phase Boundary Morphology in Nanoscale Olivine Electrode Particles. *Journal of Physical Chemistry C* **2011**, *115* (11), 4922–4926. https://doi.org/10.1021/jp109628m.

(67) Delmas, C.; Maccario, M.; Croguennec, L.; Le Cras, F.; Weill, F. Lithium Deintercalation in LiFePO4 Nanoparticles via a Domino-Cascade Model. *Nat. Mater.* **2008**, *7* (8), 665–671. https://doi.org/10.1038/nmat2230.

(68) Malik, R.; Zhou, F.; Ceder, G. Kinetics of Non-Equilibrium Lithium Incorporation in LiFePO4. *Nat. Mater.* **2011**, *10* (8), 587–590. https://doi.org/10.1038/nmat3065.

(69) Delmas, C.; Maccario, M.; Croguennec, L.; Le Cras, F.; Weill, F. Lithium Deintercalation in LiFePO4 Nanoparticles via a Domino-Cascade Model. *Nat. Mater.* **2008**, *7* (8), 665–671. https://doi.org/10.1038/nmat2230.

(70) Sauvage, F.; Baudrin, E.; Morcrette, M.; Tarascon, J. M. Pulsed Laser Deposition and Electrochemical Properties of LiFePO4 Thin Films. *Electrochemical and Solid-State Letters* **2004**, *7* (1), 15–18. https://doi.org/10.1149/1.1630411.

(71) Iriyama, Y.; Yokoyama, M.; Yada, C.; Jeong, S. K.; Yamada, I.; Abe, T.; Inaba, M.; Ogumi, Z. Preparation of LiFePO4 Thin Films by Pulsed Laser Deposition and Their Electrochemical Properties. *Electrochemical and Solid-State Letters* **2004**, *7* (10), 340–342. https://doi.org/10.1149/1.1795052.

(72) Sauvage, F.; Baudrin, E.; Gengembre, L.; Tarascon, J. M. Effect of Texture on the Electrochemical Properties of LiFePO4 Thin Films. *Solid State Ion.* **2005**, *176* (23–24), 1869–1876. https://doi.org/10.1016/j.ssi.2005.05.012.

(73) Lu, Z.; Cheng, H.; Lo, M.; Chung, C. Y. Pulsed Laser Deposition and Electrochemical Characterization of LiFePO4-Ag Composite Thin Films. *Adv. Funct. Mater.* **2007**, *17* (18), 3885–3896. https://doi.org/10.1002/adfm.200700390.

(74) Lu, Z. G.; Lo, M. F.; Chung, C. Y. Pulse Laser Deposition and Electrochemical Characterization of LiFePO4-C Composite Thin Films. *Journal of Physical Chemistry C* **2008**, *112* (17), 7069–7078. https://doi.org/10.1021/jp0744735.

(75) Legrand, C.; Dupont, L.; Tang, K.; Li, H.; Huang, X. J.; Baudrin, E. Structural and Textural Characterization of LiFePO4 Thin Films Prepared by Pulsed Laser Deposition on Si Substrates. *Thin Solid Films* **2010**, *518* (19), 5447–5451. https://doi.org/10.1016/j.tsf.2010.04.011.

(76) Tang, K.; Sun, J.; Yu, X.; Li, H.; Huang, X. Electrochemical Performance of LiFePO4 Thin Films with Different Morphology and Crystallinity. *Electrochim. Acta* **2009**, *54* (26), 6565–6569. https://doi.org/10.1016/j.electacta.2009.06.030.

(77) Tang, K.; Yu, X.; Sun, J.; Li, H.; Huang, X. Kinetic Analysis on LiFePO4 Thin Films by CV, GITT, and EIS. *Electrochim. Acta* **2011**, *56* (13), 4869–4875. https://doi.org/10.1016/j.electacta.2011.02.119.

(78) Zhu, X. J.; Cheng, L. Bin; Wang, C. G.; Guo, Z. P.; Zhang, P.; Du, G. D.; Liu, H. K. Preparation and Characteristics of LiFePO4 Thin Film by Radio Frequency Magnetron Sputtering for Lithium Microbatteries. *Journal of Physical Chemistry C* **2009**, *113* (32), 14518–14522. https://doi.org/10.1021/jp902560q.

(79) Sugiawati, V. A.; Vacandio, F.; Perrin-Pellegrino, C.; Galeyeva, A.; Kurbatov, A. P.; Djenizian, T. Sputtered Porous Li-Fe-P-O Film Cathodes Prepared by Radio Frequency Sputtering for Li-Ion Microbatteries. *Sci. Rep.* **2019**, *9* (1), 11172. https://doi.org/10.1038/s41598-019-47464-2.

(80) Ke, B.; Zhang, C.; Cheng, S.; Li, W.; Deng, R.; Zhang, H.; Lin, J.; Xie, Q.; Qu, B.; Peng, D.; Wang, X. Tape-casting Electrode Architecture Permits Low-temperature Manufacturing of All-solid-state Thin-film Microbatteries. *Interdisciplinary Materials* **2024**, *3* (4), 621–631. https://doi.org/10.1002/idm2.12174.

(81) Gellert, M.; Dashjav, E.; Grüner, D.; Ma, Q.; Tietz, F. Compatibility Study of Oxide and Olivine Cathode Materials with Lithium Aluminum Titanium Phosphate. *Ionics (Kiel).* **2018**, *24* (4), 1001–1006. https://doi.org/10.1007/s11581-017-2276-6.

(82) Yu, C. Y.; Choi, J.; Anandan, V.; Kim, J. H. High-Temperature Chemical Stability of Li1.4Al0.4Ti1.6(PO4)3Solid Electrolyte with Various Cathode Materials for Solid-State Batteries. *Journal of Physical Chemistry C* **2020**, *124* (28), 14963–14971. https://doi.org/10.1021/acs.jpcc.0c01698.

(83) Malaki, M.; Haust, J.; Beaupain, J. P.; Auer, H.; Beyer, A.; Wätzig, K.; Kusnezoff, M.; Volz, K. Probing the Interface Evolution in Co-Sintered All-Phosphate Cathode-Solid Electrolyte Composites. *Adv. Mater. Interfaces* **2023**, *10* (35). https://doi.org/10.1002/admi.202300513.

(84) Beaupain, J. P.; Waetzig, K.; Auer, H.; Zapp, N.; Nikolowski, K.; Partsch, M.; Kusnezoff, M.; Michaelis, A. Composite Cathodes for Oxide Solid-State Batteries. **2023**, *7*.

(85) Norton, D. P. Pulsed Laser Deposition of Complex Materials: Progress Toward Applications. In *Pulsed Laser Deposition of Thin Films*; Wiley, 2006; pp 1–31. https://doi.org/10.1002/9780470052129.ch1.

(86) Eason, R. *Pulsed Laser Deposition of Thin Films*; Wiley, 2006. https://doi.org/10.1002/0470052120.

(87) Shepelin, N. A.; Tehrani, Z. P.; Ohannessian, N.; Schneider, C. W.; Pergolesi, D.; Lippert, T. A Practical Guide to Pulsed Laser Deposition. *Chem. Soc. Rev.* **2023**, *52* (7), 2294–2321. https://doi.org/10.1039/d2cs00938b.

(88) Lowndes, D. H.; Geohegan, D. B.; Puretzky, A. A.; Norton, D. P.; Rouleau, C. M. Synthesis of Novel Thin-Film Materials by Pulsed Laser Deposition. *Science (1979).* **1996**, *273* (5277), 898–903. https://doi.org/10.1126/science.273.5277.898.

(89) Krebs, H.-U.; Weisheit, M.; Faupel, J.; Süske, E.; Scharf, T.; Fuhse, C.; Störmer, M.; Sturm, K.; Seibt, M.; Kijewski, H.; Nelke, D.; Panchenko, E.; Buback, M. Pulsed Laser Deposition

(PLD) - A Versatile Thin Film Technique; 2003; pp 505–518. https://doi.org/10.1007/978-3-540-44838-9_36.

(90) Indrizzi, L.; Ohannessian, N.; Pergolesi, D.; Lippert, T.; Gilardi, E. Pulsed Laser Deposition as a Tool for the Development of All Solid-State Microbatteries. *Helv. Chim. Acta* **2021**, *104* (2). https://doi.org/10.1002/hlca.202000203.

(91) Loss, L.; Deposited, V.; Films, T. Lithium Loss in Vacuum Deposited Thin Films. **2024**, 0–5. https://doi.org/10.1021/acsenergylett.4c00153.

(92) Ojeda-G-P, A.; Döbeli, M.; Lippert, T. Influence of Plume Properties on Thin Film Composition in Pulsed Laser Deposition. *Adv. Mater. Interfaces* **2018**, *5* (18). https://doi.org/10.1002/admi.201701062.

(93) Groenen, R.; Smit, J.; Orsel, K.; Vailionis, A.; Bastiaens, B.; Huijben, M.; Boller, K.; Rijnders, G.; Koster, G. Research Update: Stoichiometry Controlled Oxide Thin Film Growth by Pulsed Laser Deposition. *APL Mater.* **2015**, *3* (7). https://doi.org/10.1063/1.4926933.

(94) Kelly, P. J.; Arnell, R. D. *Magnetron Sputtering: A Review of Recent Developments and Applications*.

(95) Safi, I. Recent Aspects Concerning DC Reactive Magnetron Sputtering of Thin Films: A Review. *Surf. Coat. Technol.* **2000**, *127* (2–3), 203–218. https://doi.org/10.1016/S0257-8972(00)00566-1.

(96) Wang, B.; Chakoumakos, B. C.; Sales, B. C.; Kwak, B. S.; Bates, J. B. Synthesis, Crystal Structure, and Ionic Conductivity of a Polycrystalline Lithium Phosphorus Oxynitride with the γ-Li3PO4 Structure. *J. Solid State Chem.* **1995**, *115* (2), 313–323. https://doi.org/10.1006/jssc.1995.1140.

(97) Berthou, W.; Legallais, M.; Sorieul, S.; Yildirim, G.; Bousquet, B.; Motto-Ros, V.; Le Cras, F. High-Throughput Experimentation Unveils Composition – Structure – Conductivity Relationships in the Extended LiPON System. *Adv. Energy Mater.* **2024**, *14* (36). https://doi.org/10.1002/aenm.202400656.

(98) Basappa, R. H.; Ito, T.; Yamada, H. Contact between Garnet-Type Solid Electrolyte and Lithium Metal Anode: Influence on Charge Transfer Resistance and Short Circuit Prevention. *J. Electrochem. Soc.* **2017**, *164* (4), A666–A671. https://doi.org/10.1149/2.0841704jes.

(99) Ho, A. S.; Westover, A. S.; Browning, K.; Maslyn, J. A.; Parkinson, D. Y.; Sahore, R.; Dudney, N.; Balsara, N. P. Comparing the Purity of Rolled versus Evaporated Lithium Metal Films Using X-Ray Microtomography. *ACS Energy Lett.* **2022**, *7* (3), 1120–1124. https://doi.org/10.1021/acsenergylett.2c00255.

(100) Acebedo, B.; Cid, R.; de Lasen-Tejada, M.; Morant-Miñana, M. C.; Fallarino, L.; Goikolea, E.; Rikarte, J.; Gonzalo, E.; Ruiz de Larramendi, I. On the Role of Ultrathin Lithium Metal Anodes Produced by Thermal Evaporation. *J. Power Sources* **2024**, *618*. https://doi.org/10.1016/j.jpowsour.2024.235218.

(101) Bates, J. B.; Dudney, N. J.; Neudecker, B.; Ueda, A.; Evans, C. D. Thin-Film Lithium and Lithium-Ion Batteries. *Solid State Ion.* **2000**, *135*, 33–45.

(102) Tsai, C.-H.; Aboy, M.; Pelaz, L.; Hsu, Y.-H.; Woon, W.-Y.; Timans, P. J.; Lee, C.-K. *Rapid Thermal Process Driven Intra-Die Device Variations*.

(103) Fiory, A. T. *Recent Developments in Rapid Thermal Processing*; 2002.

(104) Kao, M. C.; Chen, H. Z.; Wang, C. M.; Chen, Y. C.; Lee, M. S. Rapid Thermal Processing of Lithium Tantalite Thin Films Prepared by a Diol-Based Sol–Gel Process. *Applied Physics A* **2004**, *79* (1), 103–108. https://doi.org/10.1007/s00339-003-2493-x.

(105) Park, H. Y.; Nam, S. C.; Lim, Y. C.; Choi, K. G.; Lee, K. C.; Park, G. B.; Kim, J. B.; Kim, H. P.; Cho, S. B. LiCoO2 Thin Film Cathode Fabrication by Rapid Thermal Annealing for Micro Power Sources. *Electrochim. Acta* **2007**, *52* (5), 2062–2067. https://doi.org/10.1016/j.electacta.2006.08.026.

(106) Buzi, F.; Bernadet, L.; Orrit-Prat, J.; Bonet, R.; Caro, J.; Montinaro, D.; Ouweltjes, J. P.; Baiutti, F.; Torrell, M.; Morata, A.; Tarancón, A. Advanced Manufacturing for Efficient GDC Diffusion Barrier Layer by Rapid Thermal Processing for Large-Area Solid Oxide Cells. *J. Power Sources* **2025**, *652*. https://doi.org/10.1016/j.jpowsour.2025.237629.

(107) Steele, J. A.; Solano, E.; Hardy, D.; Dayton, D.; Ladd, D.; White, K.; Chen, P.; Hou, J.; Huang, H.; Saha, R. A.; Wang, L.; Gao, F.; Hofkens, J.; Roeffaers, M. B. J.; Chernyshov, D.; Toney, M. F. How to GIWAXS: Grazing Incidence Wide Angle X-Ray Scattering Applied to Metal Halide Perovskite Thin Films. *Adv. Energy Mater.* **2023**, *13* (27). https://doi.org/10.1002/aenm.202300760.

(108) FERRARO, J. R.; NAKAMOTO, K.; BROWN, C. W. *Introductory Raman Spectroscopy*, 2nd ed.; Academic Press, Ed.; Elsevier: Amsterdam, 2003. https://doi.org/10.1016/B978-0-12-254105-6.X5000-8.

(109) Gavara, N. A Beginner's Guide to Atomic Force Microscopy Probing for Cell Mechanics. *Microsc. Res. Tech.* **2017**, *80* (1), 75–84. https://doi.org/10.1002/jemt.22776.

(110) ERDMAN, N.; BELL, D. C.; REICHELT, R. Scanning Electron Microscopy. In *Springer Handbook of Microscopy*; Springer International Publishing, Ed.; Cham, 2019; pp 229–318.

(111) Goldstein, J.; Newbury, D. E.; Michael, J. R. ; R. N. W. M.; Scott, J. H. J.; Joy, D. C. *Scanning Electron Microscopy and X-Ray Microanalysis*, 2nd ed.; Springer: New York, 2018.

(112) Williams, D. B.; Carter, C. B. *Transmission Electron Microscopy: A Textbook for Materials Science*, 2nd ed.; Springer.: New York, 2009.

(113) Takahara, H.; Shikano, M.; Kobayashi, H. Quantification of Lithium in LIB Electrodes with Glow Discharge Optical Emission Spectroscopy (GD-OES). *J. Power Sources* **2013**, *244*, 252–258. https://doi.org/10.1016/j.jpowsour.2013.01.109.

(114) Gonzalez-Rosillo, J. C.; Morzy, J.; Romanyuk, Y. E.; Futscher, M. H.; Taranc, A.; Morata, A. Pulsed-Laser-Deposited LiMn2O4 Thin-Film Solid-State Microbatteries with Extended Voltage Window Cycling. *ACS Appl. Energy Mater.* **2026**, *9* (7), 3893−3900. https://doi.org/10.1021/acsaem.5c03983.

(115) Bard, A. J.; Faulkner, L. R. *Electrochemical Methods: Fundamentals and Applications*, 2nd ed.; Wiley, 2001.

(116) Choi, W.; Shin, H. C.; Kim, J. M.; Choi, J. Y.; Yoon, W. S. Modeling and Applications of Electrochemical Impedance Spectroscopy (Eis) for Lithium-Ion Batteries. *Journal of Electrochemical Science and Technology* **2020**, *11* (1), 1–13. https://doi.org/10.33961/jecst.2019.00528.

(117) Lazanas, A. C.; Prodromidis, M. I. Electrochemical Impedance Spectroscopy─A Tutorial. *ACS Measurement Science Au* **2023**, *3* (3), 162–193. https://doi.org/10.1021/acsmeasuresciau.2c00070.

(118) Hu, J.; Huang, W.; Yang, L.; Pan, F. Structure and Performance of the LiFePO4cathode Material: From the Bulk to the Surface. *Nanoscale* **2020**, *12* (28), 15036–15044. https://doi.org/10.1039/d0nr03776a.

(119) Yuan, L. X.; Wang, Z. H.; Zhang, W. X.; Hu, X. L.; Chen, J. T.; Huang, Y. H.; Goodenough, J. B. Development and Challenges of LiFePO4 Cathode Material for Lithium-Ion Batteries. *Energy Environ. Sci.* **2011**, *4* (2), 269–284. https://doi.org/10.1039/c0ee00029a.

(120) Huang, H.; Yin, S. C.; Nazar, L. F. Approaching Theoretical Capacity of LiFePO4 at Room Temperature at High Rates. *Electrochemical and Solid-State Letters* **2001**, *4* (10). https://doi.org/10.1149/1.1396695.

(121) Chrisey, D. B. .; Hubler, G. K. . *Pulsed Laser Deposition of Thin Films*; J. Wiley, 1994.

(122) Aziz, M. J. Film Growth Mechanisms in Pulsed Laser Deposition. *Appl. Phys. A Mater. Sci. Process.* **2008**, *93* (3), 579–587. https://doi.org/10.1007/s00339-008-4696-7.

(123) Wu, J.; Dathar, G. K. P.; Sun, C.; Theivanayagam, M. G.; Applestone, D.; Dylla, A. G.; Manthiram, A.; Henkelman, G.; Goodenough, J. B.; Stevenson, K. J. In Situ Raman Spectroscopy of LiFePO4: Size and Morphology Dependence during Charge and Self-

Discharge. *Nanotechnology* **2013**, *24* (42), 424009. https://doi.org/10.1088/0957-4484/24/42/424009.

(124) Burba, C. M.; Frech, R. Raman and FTIR Spectroscopic Study of LixFePO4 (0≤x≤1). *J. Electrochem. Soc.* **2004**, *151* (7), 1032–1038. https://doi.org/10.1149/1.1756885.

(125) Laurenti, B.; Gonzalez-Rosillo, J. C.; Chiabrera, F.; Fiocco, A.; Monteiro Freitas, F.; Chaigneau, M.; Morata, A.; Tarancón, A. Unraveling Nanoscale Interfacial Kinetics in Battery Cathodes through Operando Tip-Enhanced Raman Spectroscopy. *EES Batteries* **2025**, *1*, 1147–1157. https://doi.org/10.1039/d5eb00094g.

(126) Kowada, Y.; Tatsumisago, M.; Minami, T. Raman Spectra of Rapidly Quenched Glasses in the Systems Li3BO3-Li4SiO4-Li3PO4 and Li4B2O5-Li6Si2O7-Li4P2O7. *J. Phys. Chem.* **1989**, *93* (5), 2147–2151. https://doi.org/10.1021/j100342a085.

(127) Liu, H.; Xie, J.; Wang, K. Synthesis and Characterization of LiFePO4/(C + Fe2P) Composite Cathodes. *Solid State Ion.* **2008**, *179* (27–32), 1768–1771. https://doi.org/10.1016/j.ssi.2008.01.065.

(128) Yu, F.; Zhang, J.; Yang, Y.; Song, G. Reaction Mechanism and Electrochemical Performance of LiFePO4/C Cathode Materials Synthesized by Carbothermal Method. *Electrochim. Acta* **2009**, *54* (28), 7389–7395. https://doi.org/10.1016/j.electacta.2009.07.071.

(129) He, L.; Xu, S.; Zhao, Z. Suppressing the Formation of Fe2P: Thermodynamic Study on the Phase Diagram and Phase Transformation for LiFePO4 Synthesis. *Energy* **2017**, *134*, 962–967. https://doi.org/10.1016/j.energy.2017.06.036.

(130) Shebanova, O. N.; Lazor, P. Raman Spectroscopic Study of Magnetite (FeFe2O4): A New Assignment for the Vibrational Spectrum. *J. Solid State Chem.* **2003**, *174* (2), 424–430. https://doi.org/10.1016/S0022-4596(03)00294-9.

(131) Jubb, A. M.; Allen, H. C. Vibrational Spectroscopic Characterization of Hematite, Maghemite, and Magnetite Thin Films Produced by Vapor Deposition. *ACS Appl. Mater. Interfaces* **2010**, *2* (10), 2804–2812. https://doi.org/10.1021/am1004943.

(132) Saleh, S. A.; Ibrahim, A. A.; Mohamed, S. H. Structural and Optical Properties of Nanostructured Fe-Doped SnO2. *Acta Phys. Pol. A* **2016**, *129* (6), 1220–1225. https://doi.org/10.12693/APhysPolA.129.1220.

(133) Deng, Y.; Eames, C.; Chotard, J. N.; Laleìre, F.; Seznec, V.; Emge, S.; Pecher, O.; Grey, C. P.; Masquelier, C.; Islam, M. S. Structural and Mechanistic Insights into Fast Lithium-Ion Conduction in Li4SiO4-Li3PO4 Solid Electrolytes. *J. Am. Chem. Soc.* **2015**, *137* (28), 9136–9145. https://doi.org/10.1021/jacs.5b04444.

(134) Murayama, M.; Kanno, R.; Irie, M.; Ito, S.; Hata, T.; Sonoyama, N.; Kawamoto, Y. Synthesis of New Lithium Ionic Conductor Thio-LISICON—Lithium Silicon Sulfides System. *J. Solid State Chem.* **2002**, *168* (1), 140–148. https://doi.org/10.1006/jssc.2002.9701.

(135) de Faria, D. L. A.; Venâncio Silva, S.; de Oliveira, M. T. Raman Microspectroscopy of Some Iron Oxides and Oxyhydroxides. *Journal of Raman Spectroscopy* **1997**, *28* (11), 873–878. https://doi.org/10.1002/(SICI)1097-4555(199711)28:11<873::AID-JRS177>3.0.CO;2-B.

(136) Sauvage, F.; Laffont, L.; Tarascon, J. M.; Baudrin, E. Factors Affecting the Electrochemical Reactivity vs. Lithium of Carbon-Free LiFePO4 Thin Films. *J. Power Sources* **2008**, *175* (1), 495–501. https://doi.org/10.1016/j.jpowsour.2007.09.085.

(137) Zaghib, K.; Dontigny, M.; Charest, P.; Labrecque, J. F.; Guerfi, A.; Kopec, M.; Mauger, A.; Gendron, F.; Julien, C. M. Aging of LiFePO4 upon Exposure to H2O. *J. Power Sources* **2008**, *185* (2), 698–710. https://doi.org/10.1016/j.jpowsour.2008.08.028.

(138) He, P.; Zhang, X.; Wang, Y.-G.; Cheng, L.; Xia, Y.-Y. Lithium-Ion Intercalation Behavior of LiFePO[Sub 4] in Aqueous and Nonaqueous Electrolyte Solutions. *J. Electrochem. Soc.* **2008**, *155* (2), A144. https://doi.org/10.1149/1.2815609.

(139) Gordon, D.; Wu, M. Y.; Ramanujapuram, A.; Benson, J.; Lee, J. T.; Magasinski, A.; Nitta, N.; Huang, C.; Yushin, G. Enhancing Cycle Stability of Lithium Iron Phosphate in Aqueous Electrolytes by Increasing Electrolyte Molarity. *Adv. Energy Mater.* **2016**, *6* (2), 1501805. https://doi.org/10.1002/aenm.201501805.

(140) Prosini, P. P.; Lisi, M.; Zane, D.; Pasquali, M. *Determination of the Chemical Diffusion Coefficient of Lithium in LiFePO 4*. www.elsevier.com/locate/ssi.

(141) Xie, J.; Imanishi, N.; Zhang, T.; Hirano, A.; Takeda, Y.; Yamamoto, O. Li-Ion Diffusion Kinetics in LiFePO4 Thin Film Prepared by Radio Frequency Magnetron Sputtering. *Electrochim. Acta* **2009**, *54* (20), 4631–4637. https://doi.org/10.1016/j.electacta.2009.03.007.

(142) Waetzig, K.; Rost, A.; Langklotz, U.; Matthey, B.; Schilm, J. An Explanation of the Microcrack Formation in Li 1.3 Al 0.3 Ti 1.7 (PO 4) 3 Ceramics. *J. Eur. Ceram. Soc.* **2016**, *36* (8), 1995–2001. https://doi.org/10.1016/j.jeurceramsoc.2016.02.042.

(143) Wu, P.; Zhou, W.; Su, X.; Li, J.; Su, M.; Zhou, X.; Sheldon, B. W.; Lu, W. Recent Advances in Conduction Mechanisms, Synthesis Methods, and Improvement Strategies for Li1+xAlxTi2−x(PO4)3 Solid Electrolyte for All-Solid-State Lithium Batteries. *Adv. Energy Mater.* **2022**, *2203440*, 1–25. https://doi.org/10.1002/aenm.202203440.

(144) Waetzig, K.; Rost, A.; Heubner, C.; Coeler, M.; Nikolowski, K.; Wolter, M.; Schilm, J. Synthesis and Sintering of Li1.3Al0.3Ti1.7(PO4)3 (LATP) Electrolyte for Ceramics with

Improved Li+ Conductivity. *J. Alloys Compd.* **2020**, *818*, 153237. https://doi.org/10.1016/j.jallcom.2019.153237.

(145) Eddahaoui, K.; Benmokhtar, S.; Manoun, B.; Belaaouad, S.; Lazor, P. Vibrational Spectra and Factor Group Analysis of M0.50TiOPO4 Oxyphosphates (M=Mg, Zn, Ni, Co, Fe and Cu). *Spectrochim. Acta A Mol. Biomol. Spectrosc.* **2012**, *99*, 81–89. https://doi.org/10.1016/j.saa.2012.08.033.

(146) Cîntă Pînzaru, S.; Onac, B. P. Raman Study of Natural Berlinite from a Geological Phosphate Deposit. *Vib. Spectrosc.* **2009**, *49* (2), 97–100. https://doi.org/10.1016/j.vibspec.2008.05.003.

(147) Hofmann, P.; Walther, F.; Rohnke, M.; Sann, J.; Zeier, W. G.; Janek, J. LATP and LiCoPO4 Thin Film Preparation – Illustrating Interfacial Issues on the Way to All-Phosphate SSBs. *Solid State Ion.* **2019**, *342* (August). https://doi.org/10.1016/j.ssi.2019.115054.

(148) Simmen, F.; Lippert, T.; Novák, P.; Neuenschwander, B.; Döbeli, M.; Mallepell, M.; Wokaun, A. The Influence of Lithium Excess in the Target on the Properties and Compositions of Li1+x Mn2O4−δ Thin Films Prepared by PLD. *Applied Physics A* **2008**, *93* (3), 711–716. https://doi.org/10.1007/s00339-008-4701-1.

(149) Arbi, K.; Bucheli, W.; Jiménez, R.; Sanz, J. High Lithium Ion Conducting Solid Electrolytes Based on NASICON Li 1+x Al x M 2−x (PO 4) 3 Materials (M = Ti, Ge and $0 \leq x \leq 0.5$). *J. Eur. Ceram. Soc.* **2015**, *35* (5), 1477–1484. https://doi.org/10.1016/j.jeurceramsoc.2014.11.023.

(150) Key, B.; Schroeder, D. J.; Ingram, B. J.; Vaughey, J. T. Solution-Based Synthesis and Characterization of Lithium-Ion Conducting Phosphate Ceramics for Lithium Metal Batteries. *Chemistry of Materials* **2012**, *24* (2), 287–293. https://doi.org/10.1021/cm202773d.

(151) Lei, J.; Li, L.; Kostecki, R.; Muller, R.; McLarnon, F. Characterization of SEI Layers on LiMn[Sub 2]O[Sub 4] Cathodes with In Situ Spectroscopic Ellipsometry. *J. Electrochem. Soc.* **2005**, *152* (4), A774. https://doi.org/10.1149/1.1867652.

(152) McArthur, M. A.; Trussler, S.; Dahn, J. R. In Situ Investigations of SEI Layer Growth on Electrode Materials for Lithium-Ion Batteries Using Spectroscopic Ellipsometry. *J. Electrochem. Soc.* **2012**, *159* (3), A198–A207. https://doi.org/10.1149/2.004203jes.

(153) Morata, A.; Siller, V.; Chiabrera, F.; Nuñez, M.; Trocoli, R.; Stchakovsky, M.; Tarancón, A.; Tarancón, A. Operando Probing of Li-Insertion into LiMn2O4cathodes by Spectroscopic Ellipsometry. *J. Mater. Chem. A Mater.* **2020**, *8* (23), 11538–11544. https://doi.org/10.1039/c9ta12723b.

(154) Le Van-Jodin, L.; Ducroquet, F.; Sabary, F.; Chevalier, I. Dielectric Properties, Conductivity and Li+ Ion Motion in LiPON Thin Films. *Solid State Ion.* **2013**, *253*, 151–156. https://doi.org/10.1016/j.ssi.2013.09.031.

(155) Robertson, A. D.; West, A. R.; Ritchie, A. G. Review of Crystalline Lithium-Ion Conductors Suitable for High Temperature Battery Applications. *Solid State Ion.* **1997**, *104* (1–2), 1–11. https://doi.org/10.1016/s0167-2738(97)00429-3.

(156) Forsyth, M.; Wong, S.; Nairn, K. M.; Best, A. S.; Newman, P. J.; MacFarlane, D. R. NMR Studies of Modified Nasicon-like, Lithium Conducting Solid Electrolytes. *Solid State Ion.* **1999**, *124* (3), 213–219. https://doi.org/10.1016/S0167-2738(99)00213-1.

(157) Yada, C.; Iriyama, Y.; Jeong, S. K.; Abe, T.; Inaba, M.; Ogumi, Z. Electrochemical Properties of LiFePO4 Thin Films Prepared by Pulsed Laser Deposition. *J. Power Sources* **2005**, *146* (1–2), 559–564. https://doi.org/10.1016/j.jpowsour.2005.03.117.

(158) Warecki, Z.; Ferrari, V. C.; Robinson, D. A.; Sugar, J. D.; Lee, J.; Ievlev, A. V.; Kim, N. S.; Stewart, D. M.; Lee, S. B.; Albertus, P.; Rubloff, G.; Talin, A. A. Simultaneous Solid Electrolyte Deposition and Cathode Lithiation for Thin Film Batteries and Lithium Iontronic Devices. *ACS Energy Lett.* **2024**, *9* (5), 2065–2074. https://doi.org/10.1021/acsenergylett.4c00674.

(159) Schwöbel, A.; Hausbrand, R.; Jaegermann, W. Interface Reactions between LiPON and Lithium Studied by In-Situ X-Ray Photoemission. *Solid State Ion.* **2015**, *273*, 51–54. https://doi.org/10.1016/j.ssi.2014.10.017.

(160) Hamedi Jouybari, Y.; Berkemeier, F.; Schäfer, A.; Schmitz, G. The Influence of Sputter Conditions on the Properties of LiPON and Its Interfaces. *J. Power Sources* **2018**, *394*, 160–169. https://doi.org/10.1016/j.jpowsour.2018.05.023.

(161) Crank, J. *The Mathematics of Diffusion*, 2nd ed.; Oxford University Press, 1975.

(162) Churikov, A. V.; Ivanishchev, A. V.; Ivanishcheva, I. A.; Sycheva, V. O.; Khasanova, N. R.; Antipov, E. V. Determination of Lithium Diffusion Coefficient in LiFePO4 Electrode by Galvanostatic and Potentiostatic Intermittent Titration Techniques. *Electrochim. Acta* **2010**, *55* (8), 2939–2950. https://doi.org/10.1016/j.electacta.2009.12.079.

(163) Butt, G.; Sammes, N.; Tompsett, G.; Smirnova, A.; Yamamoto, O. Raman Spectroscopy of Superionic Ti-Doped Li3Fe 2(PO4)3 and LiNiPO4 Structures. *J. Power Sources* **2004**, *134* (1), 72–79. https://doi.org/10.1016/j.jpowsour.2004.01.053.

(164) Bih, H.; Bih, L.; Manoun, B.; Azdouz, M.; Benmokhtar, S.; Lazor, P. Raman Spectroscopic Study of the Phase Transitions Sequence in Li3Fe2(PO4)3 and Na3Fe2(PO4)3 at High Temperature. *J. Mol. Struct.* **2009**, *936* (1–3), 147–155. https://doi.org/10.1016/j.molstruc.2009.07.035.

Appendices

Appendix A. Complementary processing and control experiments

A.1. Influence of deposition pressure on film structure

Complementary depositions were performed to evaluate the influence of Ar pressure on the structural formation of LFP thin films grown on Pt substrates (**Figure A.1**). At 1 mTorr Ar, the Raman spectrum is dominated by the characteristic $LiFePO_4$ phosphate vibration at ~948 cm^{-1}, confirming the formation of the olivine phase. In contrast, increasing the Ar pressure to 80 mTorr suppresses this feature and gives rise to broader bands in the 900–1200 cm^{-1} and 400–500 cm^{-1} regions, suggesting the stabilization of a predominantly amorphous phosphate environment, tentatively assigned to a NASICON-type $Li_3Fe_2(PO_4)_3$-like phase. [163,164]

This pressure-induced change is attributed to modified plume dynamics during PLD. At higher Ar pressure, plume-gas collisions reduce the kinetic energy of the ablated species and limit surface mobility, thereby affecting phase selection during growth.[87,121] These results justify the use of low-pressure Ar, 1 mTorr, as the standard condition for obtaining olivine $LiFePO_4$ thin films in this chapter.

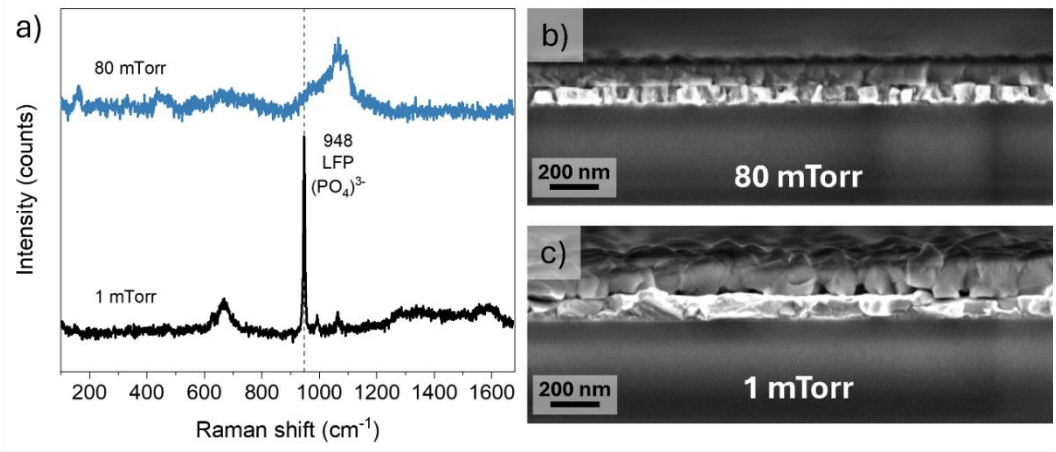


Figure A.1 – (a)Raman spectra of $LiFePO_4$ thin films deposited on Pt substrates by PLD at 600 ºC under 1 mTorr and 80 mTorr Ar background pressures. Cross sectional SEM images of the as-deposited samples at (b)80 mTorr and (c)1 mTorr.

A.2. Influence of target pre-ablation and reproducibility of depositions on Pt substrates

The influence of target conditioning was evaluated by comparing sequential LFP films deposited on Pt under identical PLD conditions, 600 ºC and 1 mTorr Ar (**Figure A.2**). The first film, deposited without effective polishing and target pre-ablation, exhibits a rough morphology formed by gains with apparent lateral size of approximately 220 ± 70 nm, and RMS roughness of ~35.6 nm (**Figure A.2c**). In contrast, the second deposited film shows a finer and more homogeneous surface, with apparent features of approximately 100 ± 35 nm, and reduced RMS roughness of ~6.0 nm (**Figure A.2d**). This morphological difference is also visible in cross-section, where the first

film presents a more irregular microstructure, while the second film forms a more compact and uniform layer (**Figure A.2a,b**).

Raman spectra collected from the first, second, and third sequentially deposited films show a progressive change in the film response with continued use of the target. The first film presents a stronger carbon-related contribution, identified by the D and G bands, that decrease in the following depositions. This behavior indicates that the initial target surface contained carbonaceous contamination, which was progressively removed during laser exposure. Therefore, target pre-ablation was adopted as an essential step to improve the reproducibility, surface homogeneity, and chemical purity of PLD-grown LFP thin films.

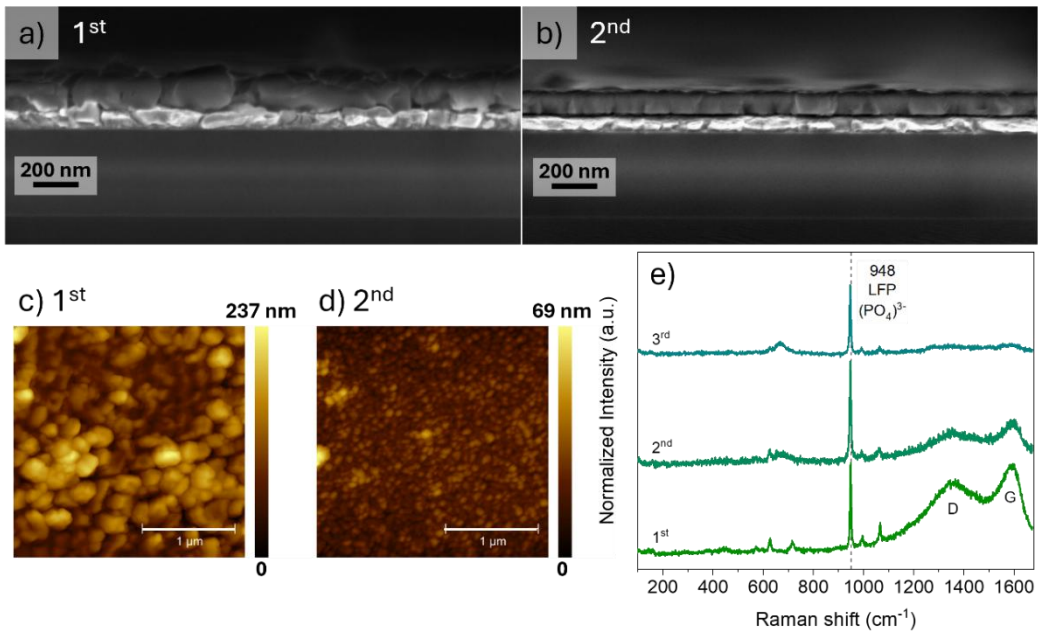


Figure A.2 - Morphological and Raman characterization of sequential $LiFePO_4$ thin films deposited on Pt substrates under the same PLD conditions, 600 ºC and 1 mTorr Ar. Cross-sectional SEM images of the (a) first and (b) second deposited films. AFM topography images of the corresponding (c) first and (d) second deposited films. (e) Raman spectra of the first, second, and third sequentially deposited films. AFM scale bars correspond to 1 µm.

A.3. Early-stage growth morphology of LFP thin films

The early-stage growth morphology of thinner LFP films was investigated by top-view and cross-sectional SEM for films deposited for 15 min under the same conditions, namely 20 Hz, 1 mTorr Ar, and 600 ºC, on ITO- and Pt-based substrates (**Figure A.3**). The LFP film on ITO shows a relatively homogeneous surface composed of fine, irregular and partially coalesced nanoscale features, with apparent lateral dimensions of approximately 50–120 nm and occasional coalesced regions reaching 150–200 nm. In contrast, the film deposited on Pt exhibits a markedly different morphology, where regions of the substrate remain visibly exposed and are interrupted by darker rounded or elongated domains extending over 100–200 nm, locally reaching 200–500 nm. Based

on contrast segmentation of the SEM image, these darker regions occupy approximately 41% of the surface, indicating incomplete surface coverage at this early deposition stage.

These observations suggest that the substrate strongly influences the initial nucleation and coalescence behavior of LFP. Under the same deposition conditions, the ITO-based substrate appears to favor a finer and more uniform distribution of early LFP surface features, whereas Pt leads to a more heterogeneous island-like growth morphology with incomplete coalescence. Since individual grain boundaries are not clearly resolved in these early-stage films, the reported dimensions are referred to as apparent lateral surface feature sizes rather than true crystallographic grain sizes.

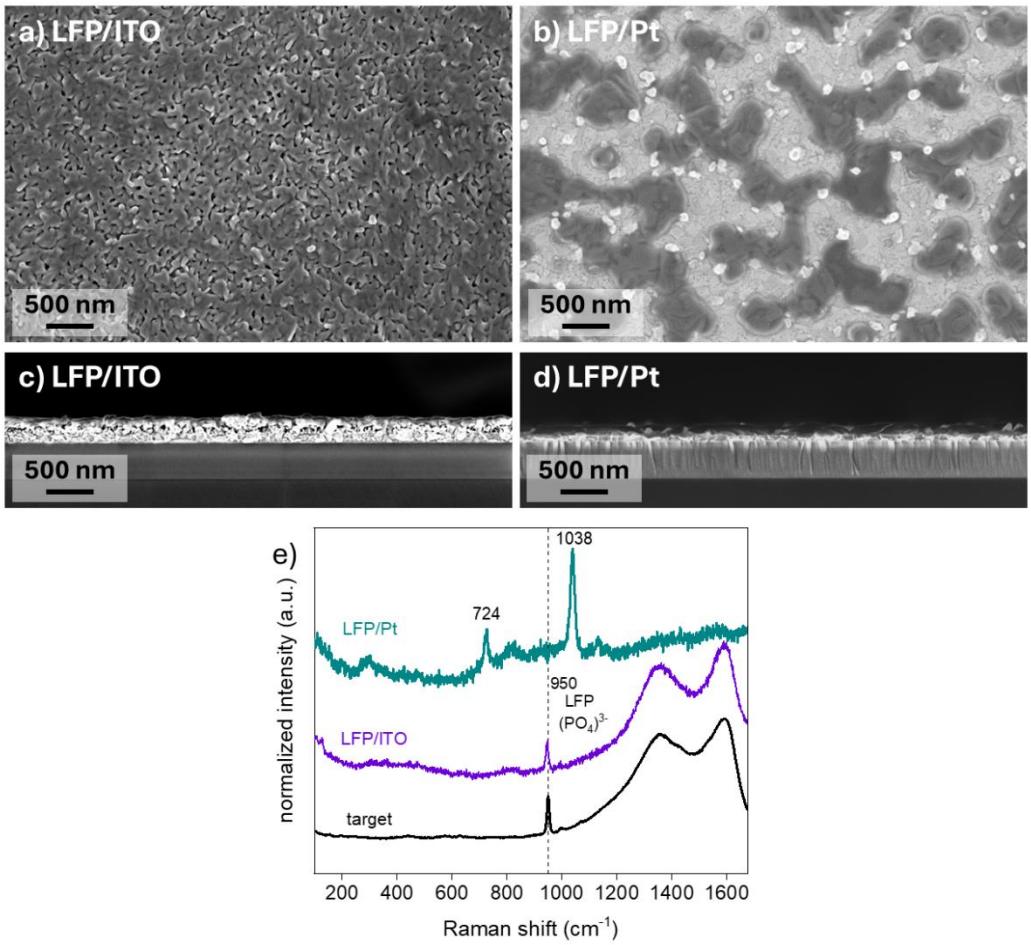


Figure A.3 - Top-view SEM images of LFP deposited for 15 min on (a) ITO and (b) Pt under the same PLD conditions: 600 ºC, 1 mTorr Ar, and 20 Hz. Cross-sectional SEM images of the corresponding films deposited on (c) ITO and (d) Pt. (e) Raman spectra of the corresponding samples.

These preliminary results are included in the Appendix because the ITO substrate used in this specific study had not yet been fully optimized. Therefore, the intrinsic morphology and surface condition of the ITO layer may also influence the nucleation and subsequent growth of the LFP film deposited on top. Nevertheless, the pronounced difference observed between the ITO- and

Pt-based substrates provides relevant evidence of substrate-dependent early-stage growth behavior. This observation is important because similar effects may also occur for other current collectors or substrate configurations, highlighting the need to consider the substrate surface morphology when evaluating the growth and final microstructure of PLD-grown LFP thin films.

A.4. Thickness evolution of LFP films on Pt

Cross-sectional SEM images of LFP films deposited on Pt at 600 ºC show the gradual evolution of the film microstructure with increasing deposition time (33 min – 150 min) /number of laser pulses (20k-90k, 10Hz) (**Figure A.4**). The thinner films exhibit a discontinuous and rough morphology, composed of separated grains and partially coalesced islands, consistent with the early stages of LFP growth on Pt. As the deposition proceeds, the film becomes progressively thicker and more continuous. Grain coalescence reduces the open gaps between islands, leading to a denser and more compact layer. This evolution supports the interpretation that LFP growth on Pt starts through island-like nucleation **Figure A.3**(Error! Reference source not found.**b,d**) and progressively transitions toward a more continuous microstructure as the film thickness increases.

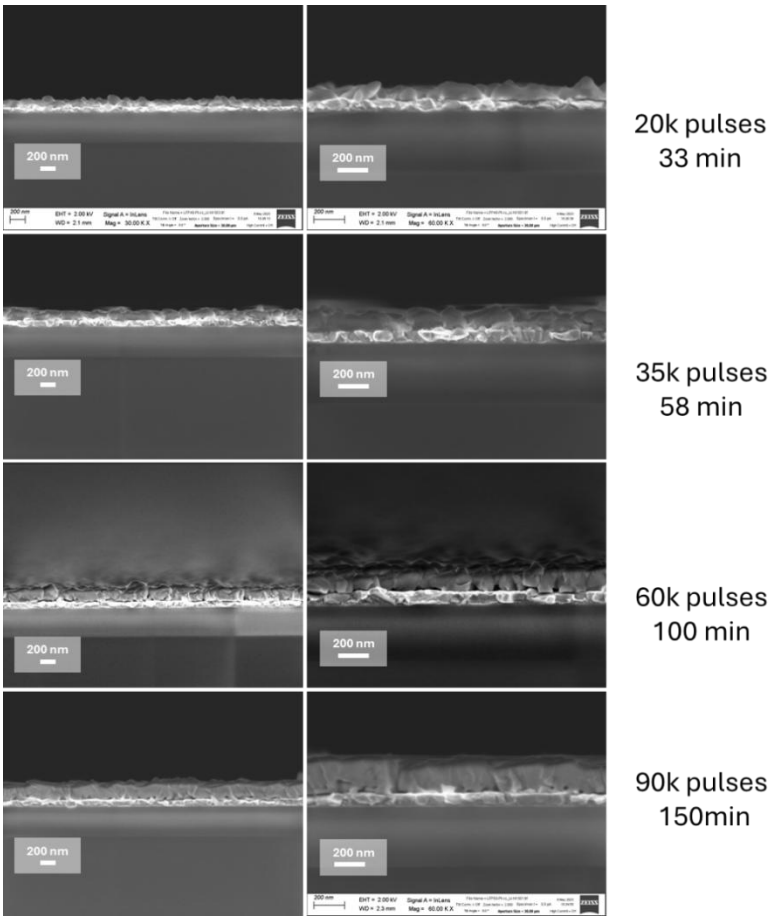


Figure A.4 - Cross-sectional SEM images of $LiFePO_4$ thin films deposited on Pt substrates by PLD at 600 ºC and 1 mTorr Ar with increasing deposition time/number of laser pulses.

A.5. Additional RTP tests at higher temperature

Additional RTP treatments were performed on LFP films deposited on Pt in order to evaluate the thermal stability of the layers outside the optimized annealing window. Films deposited at 300 ºC and annealed at 800 ºC under O_2, as well as films deposited at 600 ºC and annealed at 900–1000 ºC under Ar, show pronounced morphological changes after treatment, including surface restructuring, grain coarsening, and partial loss of film uniformity.

These observations support the selection of milder RTP conditions for the main study, namely 700 ºC for 60 s under Ar. This condition was chosen as a compromise between promoting crystallization in poorly ordered LFP films and avoiding the severe morphological degradation observed after higher-temperature annealing. the severe morphological degradation observed after higher-temperature annealing.

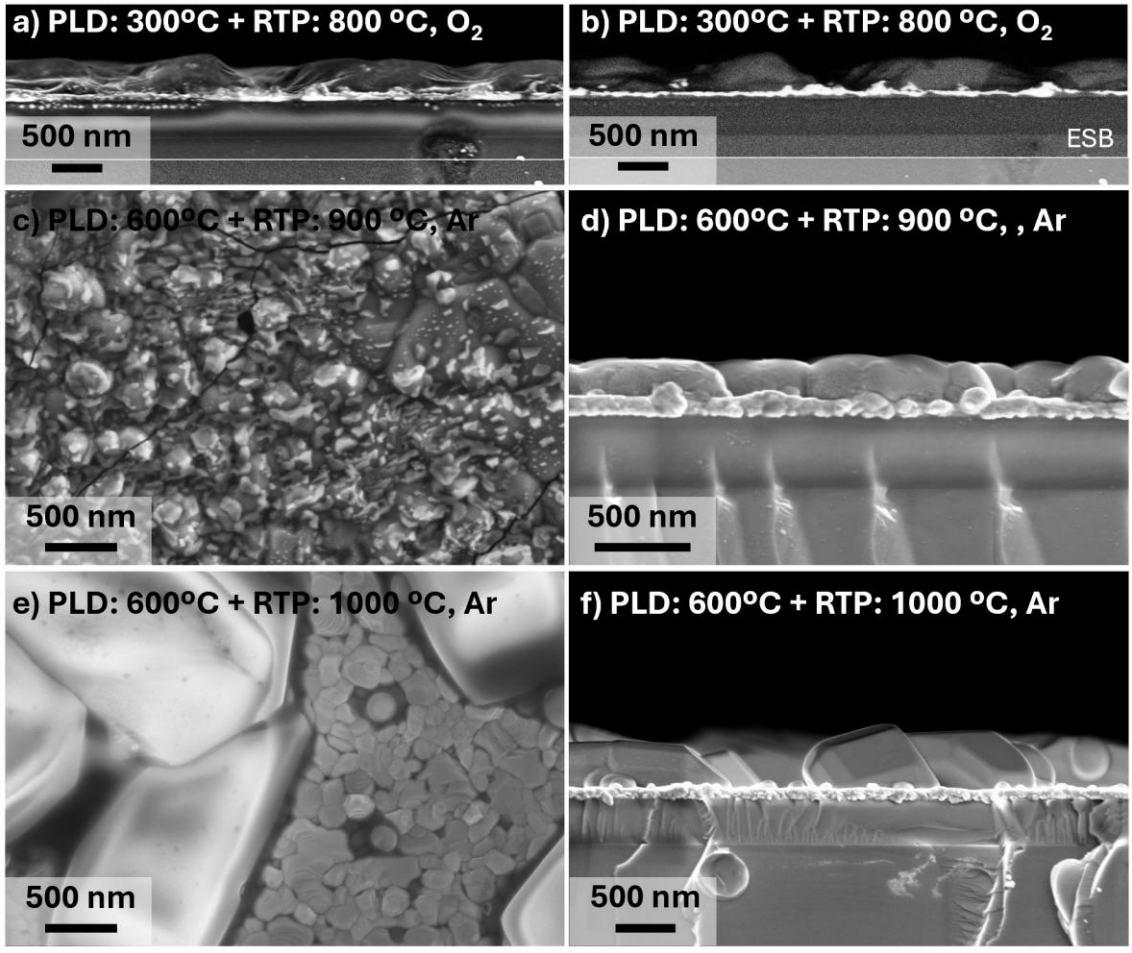


Figure A.5 - Cross-sectional SEM images of a film deposited at 300 ºC and subsequently annealed by RTP at 800 ºC under O_2 atmosphere, acquired using (a) InLens and (b) ESB detectors. Top-view and cross-sectional SEM images of a film deposited at 600 ºC and annealed by RTP under Ar atmosphere at (c,d) 900 ºC and (e,f) 1000 ºC for 60s.

Appendix B. Alternative substrate strategies

B.1. Pre-thermal cleaning of Pt-coated substrates

Considering that residual carbon contamination on Pt substrates could influence the early stages of LFP growth during PLD under non-oxidizing atmosphere, an additional substrate preparation strategy was evaluated. Pt substrates were pre-treated by RTP at 600 ºC under O_2 atmosphere before LFP deposition, and their behavior was compared with standard solvent-cleaned Pt substrates. Raman spectra of the bare substrates exposed to the deposition conditions and of the corresponding LFP films deposited at 500 ºC are shown in **Figure B.1ab**. In both cases, no clear D or G carbon bands are detected, indicating that detectable carbon residues are not present after the deposition process. The LFP films show the characteristic phosphate-related Raman band at approximately 948 cm^{-1}, suggesting that the pre-treatment does not significantly modify the main vibrational signature of the deposited LFP layer.

Cross-sectional SEM of the LFP film grown on pre-treated Pt-coated substrate shows a thickness of approximately 180 nm, comparable to films deposited without previous thermal treatment (**Figure B.1c**). However, the electrochemical response does not improve after the pre-heating step. At constant 2 μh cm^{-2}, this sample gives only ~25 mAh g^{-1} of discharge capacity (**Figure B.1d**). This indicates that the limited performance of LFP/Pt electrodes is not primarily related to residual carbon contamination on the substrate surface.

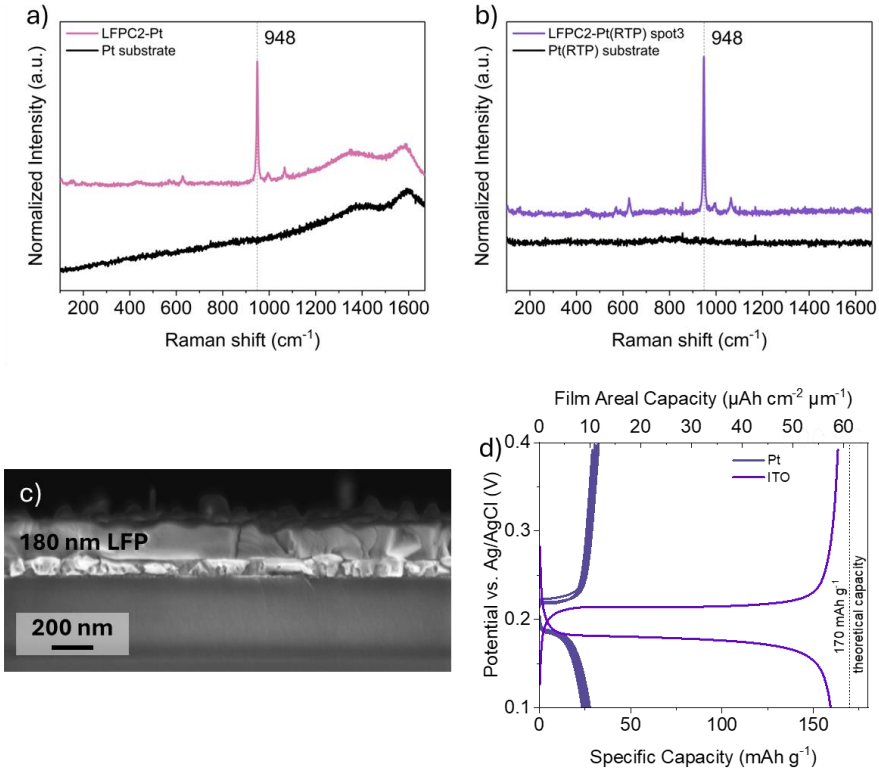


Figure B.1 -Raman spectra of LFP thin films and bare Pt substrates after exposure to the PLD deposition conditions at 500 ºC in Ar: (a) with standard solvent-cleaned Pt substrate; (b) with Pt substrate previously heat-treated by RTP at 600 ºC under O_2 atmosphere. (c) Cross-sectional SEM image of the LFP film deposited on pre-treated Pt (d) Galvanostatic charge–discharge profiles comparing LFP films deposited on pre-treated Pt with optimized LFP films deposited on ITO-based substrates, at same constant density current of 2 μh cm^{-2}.

B.2. LFP deposition on thin ITO-coated Si substrates

As an alternative current-collector configuration, LFP thin films were deposited directly onto 100 nm-thick ITO-coated Si substrates, without the Pt/Ti interlayers used in the reference architecture. This approach was explored to evaluate whether a thinner and simpler oxide current collector. The cross-sectional SEM image confirms the formation of a continuous 300 nm-thick LFP layer on top of the 100 nm ITO layer, with intimate contact. However, the ITO/Si interface does not present similar compatibility in the observed region (**Figure B.2**). The surface morphology reveals a polycrystalline microstructure formed by interconnected grains, with local surface roughness and small bright features (**Figure B.2b**). The elemental depth profile further confirms the expected LFP/ITO/Si sequence, although some accumulation of Li and Fe is observed at the ITO/Si interface (**Figure B.2c**) The structural and spectroscopic analyses indicate that the LFP phase can be formed on the thin ITO-coated Si substrate; however, Raman signal is strongly affected by the intense contribution of the Si substrate (**Figure B.2f**).

Electrochemical testing in **Figure B.2e** shows that voltage profiles of the charge–discharge tests over different current densities. Nevertheless, the profiles are relatively sloping and polarized, suggesting that the simplified current collector architecture is less favorable than the thicker ITO/Pt-based configuration.

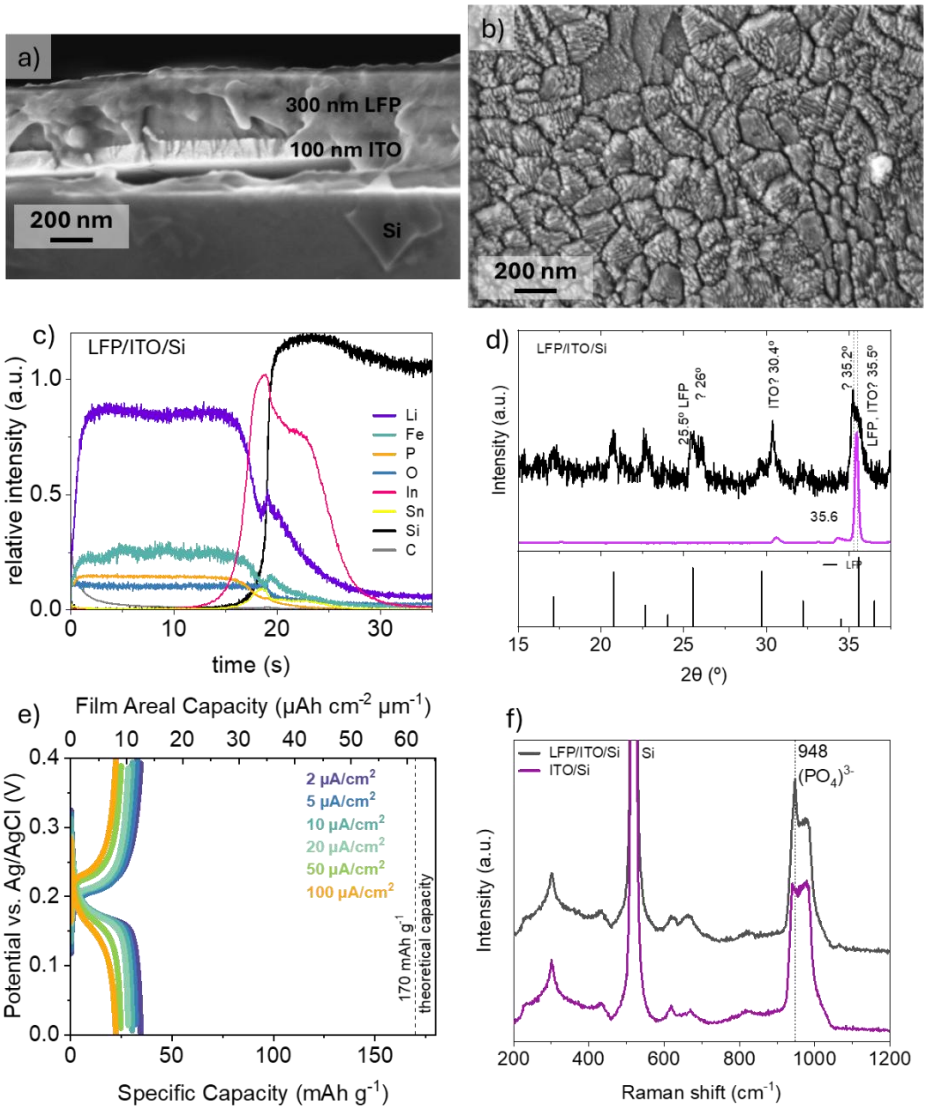


Figure B.2 - Characterization of LFP thin films deposited directly on 100 nm ITO-coated Si substrates (a) Cross-sectional and (b) Top-view SEM images. (c) GDOES depth profile of the LFP/ITO/Si layer sequence. (d) XRD pattern. (e) Galvanostatic charge–discharge curves measured at different current densities from 2 to 100 µA cm^{-2}. (f) Raman spectra.

Scientific contributions

Peer-reviewed scientific journals

Freitas, F. M.; Gonzalez-Rosillo, J. C.; Casella, J.; Laurenti, B.; Solano, E.; Morzy, J.; Futscher, M. H.; A.; Romanyuk, Y.; Tarancon, A.; Morata, A. $LiFePO_4$ Cathode Fabricated by Pulsed Laser Deposition for All-Solid-State Thin-Film Batteries. *J. Phys. Energy* 2026, 8, 025011. https://doi.org/https://doi.org/10.1088/2515-7655/ae6a6f.

Mejia-Centeno, K. V.; Alarcon-Cabrera, C. C.; Chacón-Borrero, J.; Gong, L.; Yang, L.; **Freitas, F. M.**; Yu, J.; Rauret, D. L.; Manjón, A. G.; Carreón-Castro, M. del P.; Tarancón, A.; Llorca, J.; Arbiol, J.; Martinez-Alanis, P. R.; Cabot, A. Chloroplasts-derived Ni-based electrocatalyst for efficient electrochemical ethanol oxidation to acetate with hydrogen cogeneration. *Electrochim. Acta* 2026, 545, 147704. https://doi.org/10.1016/j.electacta.2025.147704.

Castellví Barnés, M.; Ramos Lozano, S.; Mejía-Centeno, K. V.; **Freitas, F. M.**; Biset-Peiró, M.; Martínez-Alanis, P.; Cabot, A.; Jacas Biendicho, J. From Material Synthesis to Electrode Processing, a Holistic Approach to Enhance $LiFePO_4$ Sustainability. *Next Materials* 2025, 9, 101312. https://doi.org/10.1016/j.nxmate.2025.101312.

Laurenti, B., Gonzalez-Rosillo, J. C., Chiabrera, F., Fiocco, A., **Freitas, F. M.**, Chaigneau, M., Morata, A., Tarancón, A. Unraveling Nanoscale Interfacial Kinetics in Battery Cathodes through Operando Tip-Enhanced Raman Spectroscopy. *EES Batteries* 2025, 1, 1147 1157. https://doi.org/10.1039/d5eb00094g.

Conference contributions

Juan Carlos Gonzalez-Rosillo, **Fernanda Monteiro Freitas**, Jędrzej Morzy, Yaroslav E. Romanyuk, Moritz H. Futscher, Alex Morata, Albert Tarancón. Development of PLD-grown $LiMn_2O_4$ and $LiFePO_4$ cathodes for solid-state thin film batteries with LiPON and NASICON electrolytes. **Oral presentation**. E-MRS Spring Meeting 2025. Strasbourg, France. 2025.

Beatrice Laurenti, Juan Carlos Gonzalez-Rosillo, Francesco Chiabrera, Alice Fiocco, **Fernanda Monteiro Freitas**, Marc Chaigneau, Alex Morata, Albert Tarancón. Unraveling Nanoscale Interfacial Kinetics in Battery Cathodes through Operando Tip-Enhanced Raman Spectroscopy. **Oral presentation**. E-MRS Spring Meeting 2025. Strasbourg, France. 2025.

Fernanda Monteiro Freitas, Juan Carlos Gonzalez-Rosillo, Alex Morata and Albert Tarancón. Towards rapid thermal processed all-phosphate solid-state thin film batteries. **Oral presentation**. E-MRS Spring Meeting 2024. Strasbourg, France. 2024.

Juan Carlos Gonzalez-Rosillo, Beatrice Laurenti, **Fernanda Monteiro Freitas**, Francesco Chiabrera, Alex Morata, Albert Tarancón. Towards operando characterization of electroceramics via Tip-Enhanced Raman Spectroscopy. Oral presentation. Power of Interfaces Workshop. Palma de Mallorca, Spain. 2024.

Fernanda Freitas, Juan Carlos Gonzalez-Rosillo, Alex Morata and Albert Tarancón. Poster presentation. Towards all-phosphate solid-state lithium batteries. E-MRS Spring Meeting 2023. Strasbourg, France. 2023.

Fernanda Monteiro Freitas, Juan Carlos Gonzalez-Rosillo, Alex Morata and Albert Tarancón. Towards rapid thermal processed all-phosphate solid-state thin film batteries. Poster presentation. LEAPS-INNOV battery research forum. Barcelona, Spain. 2023.